Investigation of Reactive Oxygen Species Management in Biological and Pathological Processes by Fluorescence Imaging

By

Bocheng Yin

BS, Wuhan University, 2008

Submitted to the Graduate Faculty of the

Dietrich School of Arts and Sciences in partial fulfillment

of the requirements for the degree of

Doctor of Philosophy

University of Pittsburgh

2015

UNIVERSITY OF PITTSBURGH

Dietrich School of Arts and Sciences

This dissertation was presented

by

Bocheng Yin

It was defended on

November 23rd, 2015

and approved by

Adrian C. Michael, PhD, Professor

Xinyu Liu, PhD, Assistant Professor

Germán Barrionuevo, MD, Professor

Dissertation Advisor: Stephen G. Weber, PhD, Professor

Investigation of Reactive Oxygen Species Management in Biological and Pathological Processes by Fluorescence Imaging

Bocheng Yin, PhD

University of Pittsburgh, 2015

Investigation of Reactive Oxygen Species Management in Biological and Pathological Processes by Fluorescence Imaging

Bocheng Yin, PhD

University of Pittsburgh, 2015

Neural damage caused by ischemia/stroke is initiated by excess reactive oxygen species (ROS). Different cell types and even same cell type, but in different regions in hippocampus are found to have differential susceptibility to ischemia/stroke. ROS levels have been found to be different in different cell types or neurons in different regions of hippocampus. However, the mechanism behind this scenario has not been fully understood.

We, for the first time, used a roGFP2 based GSH sensor to monitor the OGD-RP induced redox change of GSH system in mitochondria and cytoplasm from 3 different cell types (HeLa cell culture, pyramidal cells and astrocytes found in OHSC) in real-time. We observed that GSH in cytoplasm was insensitive to OGD-RP, while noticeable changes were found in mitochondria. Mitochondrial GSH get more reduced in OGD, but more oxidized in RP, and that the magnitude of change either in OGD or RP is larger in pyramidal cells than in astrocytes, not significant in HeLa cells. Heterogeneities in ROS production, antioxidant capacity of GSH and mitochondria membrane potential are responsible for the redox changes of GSH system under contrasting pathological conditions, different cellular compartments and various cell types.

In order to understand the differential susceptibility to OGD-RP in hippocampal CA1 and CA3, we study on ROS related critical molecules such NAD(P)H, H_2O_2 and GSH. During OGD-RP, NAD(P)H consumption is higher in CA3 because it is used more rapidly as reducing

equivalents to maintain larger antioxidant pool in this subfield. Mitochondrial H_2O_2 and the oxidation degree of mitochondrial GSH are both lower in CA3 during OGD-RP. This can be ascribed to larger Trx2 pool in CA3 since Trx2 can scavenge H_2O_2 more fast and efficient than GSH system and is able to maintain lower H_2O_2 and GSH at lower oxidation degree.

TABLE OF CONTENTS

LIST OF TABLES

LIST OF FIGURES

LIST OF EQUATIONS

PREFACE

I would like to take a moment to acknowledge the people who have contributed to my success in completing this dissertation.

First and foremost, I would like to express my gratitude to my research advisor and mentor, Professor Stephen Weber, who has given me tremendous help and support in academic research. I cannot finish any of work without his mentorship. I am very grateful for all the members in Dr. Weber's group, especially Yangguang Ou, and Anthony Horner. I really appreciate all of them for many nice helps along the way.

I had a good fortune to work with our collaborator, Professor Germán Barrionuevo, from Department of Neuroscience, University of Pittsburgh. He is also in my PhD committee. He gave me enormous help on the instrument support and thoughtful discussion on research and paper writing. I would like to thank Mr. Thomas Harper (Department of Biological Science) for access and help on the confocal fluorescent microscope.

I really appreciate. Professor Adrian Michael and Assistant Professor Xinyu Liu to be the members in my PhD committee. In addition, I would like to thank all the faculty, staff, and fellow students in the Department of Chemistry. Their kindness and help give a good life in University of Pittsburgh.

Last, but certainly not least, I appreciate all the support from my family members and friends. I extremely acknowledge my father, Zhenkun Yin, my mother, Chun Zhang and my sister, Qin Yin for their everlasting support to me.

1.0 INTRODUCTION

1.1 REACTIVE OXYGEN SPECIES

Neuronal damage in stroke[1-3], trauma[4-6], hypoxia[7], Alzheimer's disease[8-12], Parkinson's disease[13,14], Huntington's disease[15,16], psychiatric conditions[17-19] and other diseases[3,20-22] is in part caused by oxidative stress due to excessive production of reactive oxygen species (ROS)[23-25]. Proper amounts of ROS play a critical role in cell signaling[26-31], but excessive ROS leads to short-term effects in cellular function, and longer-term changes which ultimately cause neuronal death[32-34].

Stroke is a disease with a high risk of causing adult disability and even death[35]. Ischemic stroke is caused by the blockage of blood vessels and the decrease in blood supply to the brain, leading to cell death in brain since cells are deprived of oxygen and glucose[36]. The sequence of an ischemic episode during ischemic stroke followed by reperfusion (RP) is mimicked by oxygen glucose deprivation (OGD) and RP *in vitro* [37-39]. Transient ischemic attack (TIA) is a short-term ischemia without permanent cerebral infarction. TIA had been defined as ischemic events occurring within 24 h until recently[40]. It has now been recognized that the 24-h threshold defining TIA is somewhat arbitrary as it does not consider the level of tissue injury[40]. The latest definition of TIA requires the evaluation of the level of injury in a clinic scale[40]. Most studies have found that ischemia with a duration less than 1 h is TIA[40]. Increased ROS have been found in cerebral cortex in the animal model (rat)[41], rat hippocampal slices[42] and isolated hippocampal and cortical neurons in transient ischemia with a duration less than 1h[43].

The hippocampus, the critical region in brain for developing short term and long term memory, is subject to neuronal damage as are other parts of brain during ischemia[44]. There are two ROS related observations corresponding to the hippocampus. One is that neurons are more susceptible to ischemia/RP than other cell types such as astrocytes[45]. The antioxidant, glutathione (GSH) is believed to be important for the protection of cells from excessive ROS[46]. The consumption of H_2O_2 is much faster in astrocytes compared to neurons[47], which could be ascribed to the fact that the intracellular GSH level is higher in astrocytes than in neurons[46]. Astrocytes have a higher activity of glutathione peroxidase (GPx) which facilitates the reduction of ROS by GSH[46,47]. Accumulating evidence[46,48-52] show that astrocytes are endowed with a greater GSH system in order to support neurons during ROS insult by maintaining the GSH level of neurons. Dringen et al.[52] proposed a mechanism by which astrocytes feed neurons with GSH: astrocytes release GSH, which is degraded to CysGly by γ-glutamyl-transpeptidase (γGT); then CysGly is taken up by neurons and used to synthesize GSH. Griffin et al. [49] observed that astrocytes help prevent a significant decrease of GSH concentration in neurons after OGD, supporting Ringen et al.'s[52] mechanism. The other ROS related observation is that pyramidal cells in hippocampal area CA1 are much more prone to death than those in CA3 after ischemia[53]. Wang et al.[54-56] found that more superoxide and H_2O_2 generation are accompanied with more cell death in CA1 compared to CA3. They attempted to explain the scenario by comparing the transcriptional levels of several ROS related enzymes and proteins in CA1 and CA3. They found that both transcriptional levels of pro-oxidants (e.g. superoxide dismutase (SOD) and xanthine oxidase (XO)) and pro-antioxidants (e.g. nuclear factor E2-related factor 2 (Nrf2) and NAD(P)H quinone oxidoreductase 1(Nqo1)) are higher in CA1 than in CA3[55]. Compared to CA3, The significantly higher mRNA

levels of SOD, XO, Nrf2 and Nqo1 responds to the higher ROS level in CA1[55]. The oxidative stress exerts the differential post-regulation in CA1 and CA3.

About the ischemia-induced cell injury, we know that 1) the ROS level determines the extent of cell/tissue damage; 2) GSH is very important against ROS induced by ischemia-RP; 3) there is intrinsic regulation in the expression of pro-oxidant and antioxidant genes initiated by the excessive ROS. There are also a lot of things that we don't know. We note that there is very little research aimed at revealing the instantaneous effects of ischemia-RP by monitoring the real-time changes of related molecules. Real time profiles of ROS have been reported in neurons during ischemia-RP[43], but the particular types of ROS such as superoxide and H_2O_2 have not been studied separately. Moreover, there is no report about the real-time changes of the GSH system in neurons to study the ROS induced by ischemia-RP from the perspective of antioxidants. We can obtain a better understanding of ROS management during ischemia-RP if we monitor the concomitant changes of superoxide, H_2O_2, the relative molecules participating in ROS generation and removal such as NAD(P)H[57], GSH[58-61] and thioredoxin (Trx)[62-64] by fluorescence imaging. Upon a comprehensive view of these molecules during ischemia-RP or other pathological treatments, we hope to reveal the key factors causing the differential ROS levels and susceptibility to these ROS inducing conditions in different cell types and different hippocampal areas.

In order to understand why NAD(P)H, GSH and Trx are correlated with ROS, we discuss the metabolism of these molecules in the next section. Currently developed fluorescent sensors of these molecules are also introduced to help understand our experimental design, operation and data analysis in the following sections.

1.2 CRITICAL MOLECULES IN REACTIVE OXYGEN SPECIES (ROS) MANAGEMENT

1.2.1 The redox couples, NADH/NAD$^+$ and NADPH/NADP$^+$

NADH/NAD$^+$ and NADPH/NADP$^+$ redox couples are critical important in ROS generation and removal[57]. These redox couples both exist in mitochondria and cytosol segregated by the inner mitochondrial membrane (IMM)[57], but communicate through NADH or NADPH shuttle systems.

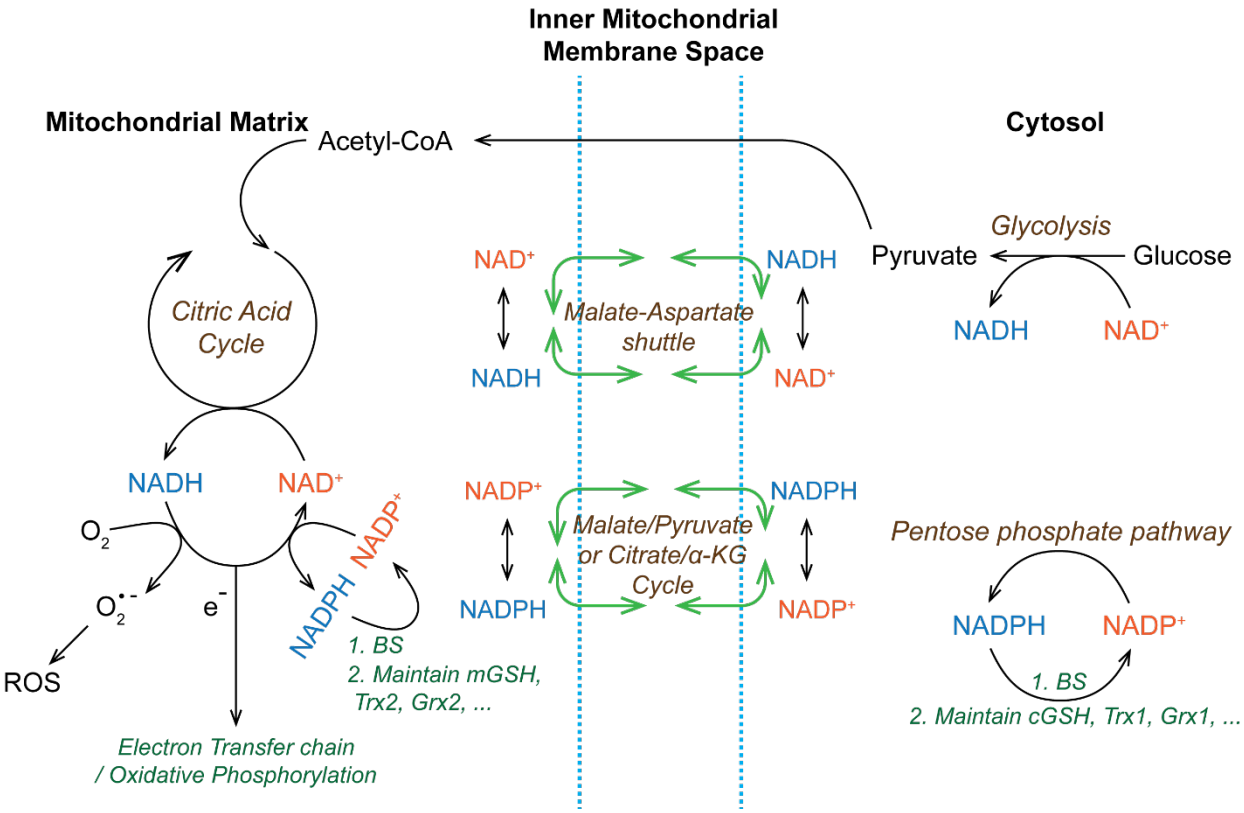

Figure 1-1. The oxidation and reduction of NADH/NAD$^+$ and NADPH/NADP$^+$ couples.

NADH/NAD$^+$ and NADPH/NADP$^+$ redox couples serve as electron carriers for critical biological processes in different cellular compartments. These redox couples in mitochondria (left) and cytosol (right) are not strictly

segregated by IMM space (Middle), but communicate through NADH or NADPH shuttle systems. Abbreviations: α-KG, α-ketoglutarate; BS, biosynthesis; mGSH, mitochondrial glutathione; Trx2, thioredoxin 2; Grx2, glutaredoxin 2; cGSH, cytosolic glutathione; Trx1, thioredoxin 1; Grx1, glutaredoxin 1; NAD(H), nicotinamide adenine dinucleotide; NADP(H), nicotinamide adenine dinucleotide phosphate.

As shown in Fig. 1-1, in cytosol, NADH is generated from NAD^+ via glycolysis[65] with glucose as substrate, and transported into mitochondria via malate-aspartate shuttle[66]. NADH is mainly generated in mitochondria from the citric acid cycle, and participates several important pathways[67] such as being an electron donor to the electron transfer chain (ETC) and used in oxidative phosphorylation for energy generation[67]. When the ETC is blocked, oxygen molecules turn into superoxide by taking over the electron from NADH, then degrade into less energetic reactive oxygen species (ROS) such as H_2O_2[68]. NADH in mitochondria can also act as reducing agent to regenerate NADPH via transhydrogenase[69]. In contrast to NADH, which is used as fuel molecule for cellular respiration, NADPH mainly participates in biosynthesis and maintains the reducing powers of glutathione and thioredoxin in mitochondria and cytosol[70]. Pentose phosphate pathway is the main pathway to generate NADPH in cytosol, while other possible pathways exist[65]. There is no physiological passage allowing NADP(H) to be transported between mitochondria and cytosol, but electron carriers via malate/pyruvate[71] or citrate/α-ketoglutarate cycles[72] could balance the ratio of $NADPH/NADP^+$ from the two sides. Because of the complicated network of the metabolism mentioned above, the respective pool of $NAD(P)H/NAD(P)^+$ in mitochondria and cytosol are spatially separated, but balanced dynamically in redox potential through their shuttle systems. Moreover, we have to emphasize that $NAD(P)H/NAD(P)^+$ is involved in ROS generation and antioxidant maintenance and plays an indispensable role to maintain redox homeostasis.

1.2.2 The metabolism of superoxide and H_2O_2

There are different types of ROS including superoxide, H_2O_2, hydroxyl radical (·OH), nitric oxide radical (NO·) and peroxynitrite ($ONOO^-$) and hypochlorite (OCl^-)[35]. Here we are going to focus on superoxide and H_2O_2.

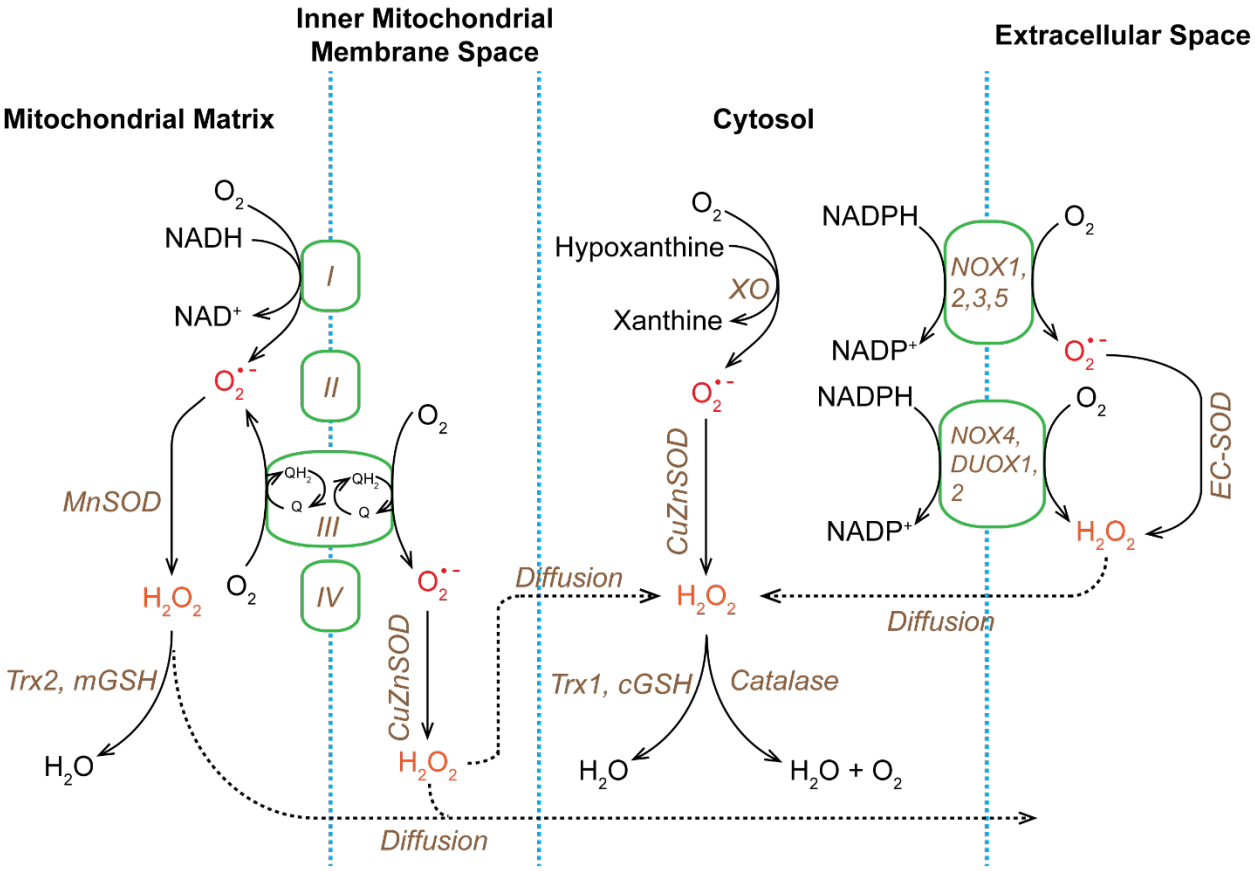

Figure 1-2. The metabolism of superoxide and H_2O_2 within intracellular compartments and extracellular space.

The scheme details the generation and removal of superoxide and H_2O_2 in mitochondrial matrix, inner mitochondrial membrane space, cytosol and extracellular space. Abbreviations: MnSOD, manganese superoxide dismutase; CuZnSOD, copper, zinc containing superoxide dismutase; EC-SOD, extracellular superoxide dismutase; XO, xanthine

oxidase; NOX, NADPH oxidase; DUOX, dual oxidase; QH2, ubiquinol; Q, ubiquinone; see the definitions of mGSH, Trx2, cGSH, Trx1, NAD(H), and NADP(H) in Figure 1-1.

As shown in Fig. 1-2, superoxide and H_2O_2 are generated in different intracellular compartments and the extracellular space (ECS). In mitochondria, the major site of superoxide generations are complex I and complex III, which are embedded in the inner mitochondrial membrane[73]. When ETC is inhibited at Complex I, NADH passes an electron to oxygen and releases superoxide into the mitochondrial matrix (MM). When inhibition of ETC occurs at complex III, the electron from ubiquinol (reduced form of ubiquinone) combines with oxygen and releases superoxide into both of MM and IMM space[74]. The new formed superoxide does not have a long lifetime, but is rapidly converted into H_2O_2 via MnSOD (in MM) and CuZnSOD (in IMM space)[74,75]. The metabolism of cytosolic superoxide and H_2O_2 generation is different. Superoxide in cytosol can be directly generated on XO by using hypoxanthine and oxygen as substrates[76] and then degraded into H_2O_2 via CuZnSOD[75]. NOX and DUO are transmembrane enzymes with NADPH binding sites in the intracellular side[77]. The isoforms 1, 2, 3 and 5 of NOX are the major sites for extracellular superoxide generation, whereas isoform 4 of NOX and isoforms 1 and 2 of DUO are the major sites for extracellular H_2O_2 generation. The negative charge on superoxide impedes its pass through the cellular membrane, but it can be dismutated by EC-SOD into H_2O_2, which can diffuse through the cell membrane. Mitochondrial and cytosolic H_2O_2 can be removed by Trx2[78] and mGSH[79] (in mitochondria) and Trx1[78] and cGSH[79] (in cytosol), respectively. Cytosolic H_2O_2 can also be removed via catalase[80].

1.2.3 Antioxidants: glutathione and thioredoxin

There are two critical types of antioxidants in cells, GSH[58-61], a tripeptide, and Trx, a small 12 kD protein[62-64].

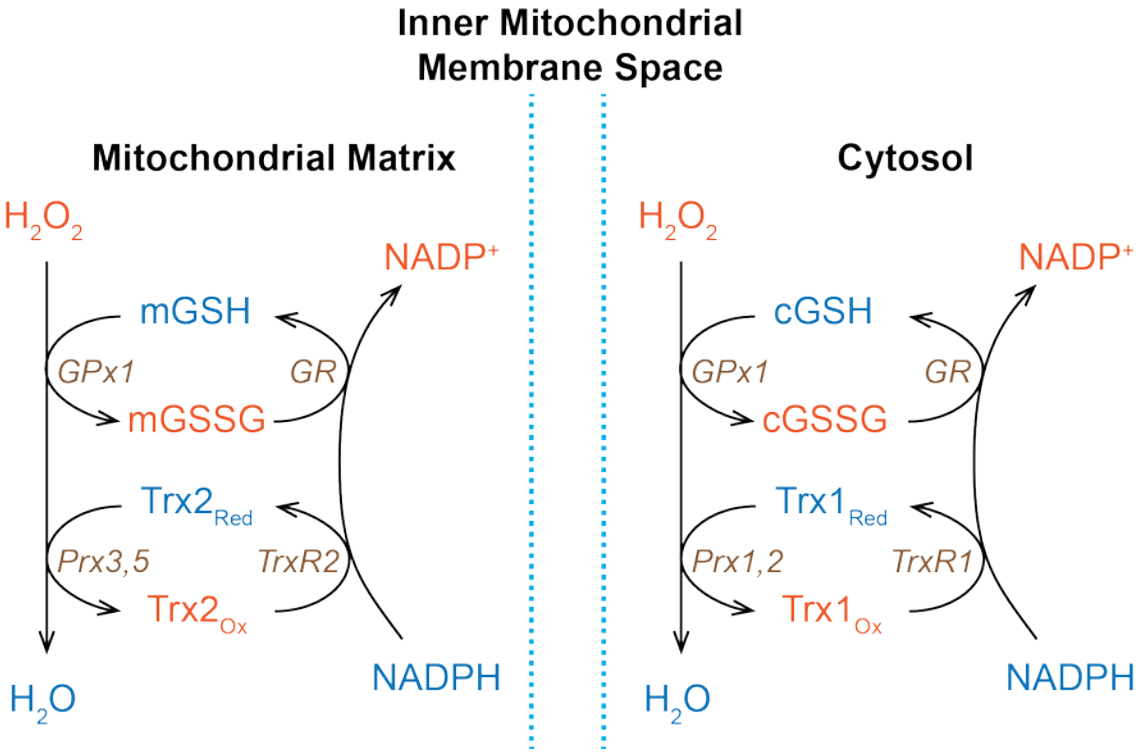

Figure 1-3. GSH and thioredoxin serve as H_2O_2 scavengers and their regeneration by NADPH.

The scheme details the oxidation and reduction of GSH and thioredoxin in mitochondrial matrix and cytosol. Abbreviations: GPx, glutathione peroxidase; GR, glutathione reductase; Prx, peroxiredoxin; TrxR, thioredoxin reductase. mGSSG, mitochondrial glutathione disulfide; cGSSG, cytoplasmic glutathione disulfide. Subscript: Ox, oxidized form; Red, reduced form. See the definitions of mGSH, Trx2, cGSH, Trx1 and NADP(H) in Figure 1-1.

As shown in Fig. 1-3, GSH and Trx are oxidized while scavenging H_2O_2 via respective enzymes, Gpx[81] and Prx[82], and are regenerated by NADPH via GR[81] and TrxR[82], respectively. NADPH acts as a reducing agent to maintain the antioxidant capability of GSH and Trx

systems[81,82]. There are mitochondrial or cytoplasmic specific isoforms of Prx, TrxR and Trx, but not for GR[73,74]. Mitochondria and cytoplasm contain the same GPx isoform, GPx1, whereas the other GPx isoforms are not selectively localized to any cellular compartments, but have various roles in regulating cellular process[83]. In mitochondria, the Trx system contains Trx2, Prx3/Prx5 and TrxR2; and in cytosol, the Trx system consists of Trx1, Prx1/Prx2 and TrxR1. The GSH system contains GSH, GPx1 and GR, in both mitochondria and cytosol. The reaction between Trx2 /Trx 1 and H_2O_2 or GSH and H_2O_2 is catalyzed by Prx isoforms or GPx1, respectively, while their direct reactions are very slower with rate constant, ~ 1 $M^{-1}\cdot s^{-1}$ without the catalysts[84] (Fig. 1-3). Cox et al. summarized the kinetic parameters (concentration in μM/second order rate constant in reaction with H_2O_2, $\mu M^{-1}\cdot s^{-1}$) of these enzymes in mitochondria (e.g. Prx3, ~ 60/20; Prx5, 20/0.3; GPx1, 2/60) and proposed that Prx3 is responsible for 90% of H_2O_2 scavenging in mitochondria since Prx3 has much higher concentration than GPx1with similar reaction constant with H_2O_2[84]. In cytosol, the second order rate constant[85] in reaction with H_2O_2 for Prx1 and Prx2 is 1 ~ 4 $\mu M^{-1}\cdot s^{-1}$ and their intracellular concentration is relatively high, ~ 250 μM[85,86], whereas cytosolic GPx1 with concentration (2 μM) reacts with H_2O_2 with a second rate constant[84] of 60 $\mu M^{-1}\cdot s^{-1}$. After doing the math, Prx1/2 have larger pseudo-first order reaction constant than GPx1 in the reaction with H_2O_2 indicating that Prx1 and Prx2 can scavenge H_2O_2 more rapidly than GPx1 in cytosol. Oxidized Prx and GPx will be reduced by Trx and GSH, respectively. The second order rate constant[86,87] of reaction between Prx3/Prx5 and Trx2 ~1 $\mu M^{-1}\cdot s^{-1}$ is much higher than that of reaction between GPx1 and GSH[88], 0.01 – 0.1 $\mu M^{-1}\cdot s^{-1}$. The rate constant of reaction between Prx1/2 and Trx1[89] is predicted to be ~ 0.1 $\mu M^{-1}\cdot s^{-1}$. The concentration of mGSH is similar to that of cGSH, 1~10 mM[23]. The concentrations of Trx2[84] and Trx1[90] are similar at 10 μM. If we assume that all Prx isoforms and GPx1 are oxidized and all GSH and Trx2/Trx1 are reduced, the final

reaction rates turn out to be: 600 $\mu M \cdot s^{-1}$ (Prx3/Trx2), 200 $\mu M \cdot s^{-1}$ (Prx5/Trx2), 250 $\mu M \cdot s^{-1}$ (Prx1,2/Trx1) and 100 ~ 2000 $\mu M \cdot s^{-1}$ (GPx1/GSH). There is currently no report about the concentration of mitochondrial H_2O_2. The concentration of cytosolic H_2O_2 is predicted to be in the range of nM and only 18 nM H_2O_2 can be generated in cytosol when cell is exposed to 100 μM from model simulations[89]. If this is true, the reaction rate of physiological H_2O_2 and Prx or GPx will be ~ 1- 10 $\mu M \cdot s^{-1}$ or 0.1 - 1 $\mu M \cdot s^{-1}$, respectively. The Trx system can scavenge H_2O_2 ten times faster than GSH system both in mitochondria and cytosol. Oxidized GSH and Trx can be regenerated by NADPH. Unfortunately, the kinetic parameters of GR and TrxR are not known, so this step in the overall process cannot be factored in to this analysis quantitatively. The regeneration of Trx could be faster than that of GSH since the second order rate constants for Trx/NADPH and GSSG/NADPH are 20 $\mu M^{-1} \cdot s^{-1}$ and 3.2 $\mu M^{-1} \cdot s^{-1,}$ respectively[89].

By comparing the kinetic parameters of the Trx and GSH system, we believe that Trx is more important than GSH to remove transient increased H_2O_2 because Trx is more reactive in reaction with H_2O_2.

By mapping the metabolism about NAD(P)H, ROS (e.g. superoxide and H_2O_2) and antioxidants (e.g. GSH and Trx), we find that all of them are inter-connected. We need to follow the network of their activities during ischemia, and the feasible methods for obtaining their transient or real-time profiles are required.

1.3 FLUORESCENCE IMAGING FOR MONITORING THE ROS RELATED CRITICAL MOLECULES

Fluorescence imaging allows us to look inside cell at molecular level[91]. Here we detail fluorescent probes used for detecting NAD(P)H, ROS (emphasize on superoxide and H_2O_2) and GSH, Trx and other thiols involved in ROS management.

1.3.1 Fluorescence imaging of NAD(P)H

NADH and NADPH exhibit auto-fluorescence and have very similar absorbance and emission spectra, thus confocal or two-photon imaging cannot differentiate them[92-94]. Recently, fluorescence lifetime imaging (FLIM) is reported to separate NADH from NADPH by correlating the ratio of NADPH/NADH with their fluorescence decay parameters[95]. However, this technique demands extremely high time resolution in nanoseconds, and is only effective in enzyme-bound NAD(P)H, not the free ones[95]. A NADH/NAD^+ redox sensitive sensor, Peredox, is constructed in Yellen group[96]. This sensor responds to [NADH]/[NAD^+] and is pH sensitive[96]. It cannot be used in the mitochondria as the mitochondrial [NADH]/[NAD^+] is too high and beyond its detection range[96]. The other NADH sensor, Frex, is highly selective for NADH, and has no response to NAD^+, NADP(H), ATP and other abundant adenine nucleotides. However, The signal of Frex is unstable over time upon its binding with NADH[97]. Frex is also pH sensitive and its application needs pH control[97]. There are more details in Appendix A.1. We will image NAD(P)H directly by using two-photon microscope in this manuscript.

1.3.2 Fluorescence imaging of superoxide and H_2O_2

Both superoxide and H_2O_2 can be measured in real time by using non-specific ROS dyes. 2',7'-Dichlorodihydrofluorescein ($DCFH_2$) is a commonly used in biological research for more than 50 years[98,99]. Its detection for ROS is based on the oxidation of the nonfluorescent $DCFH_2$ to yield fluorescent 2',7'-Dichlorofluorescein (DCF)[98]. The ester version of $DCFH_2$, 2',7'-Dichlorofluorescein diacetate ($DCFH_2$-DA), is designed to increase its membrane permeability and cellular retention[99]. $DCFH_2$ and its derivative are reported to have pharmacological effects. For instance, $DCFH_2$-DA can inhibit the upregulation of oxygenase-1 by arsenite, cadmium and hemin[100], and $DCFH_2$ can be used as an alternative substrate for xanthine oxidase[101]. Moreover, we cannot ignore interference in the oxidation of $DCFH_2$ and its derivative from ROS related enzyme systems, such as iron/H_2O_2[101], hypoxanthine/xanthine oxidase (XO)[101], superoxide dismutase (SOD)[102] and catalase (CAT)[102]. Moreover, the evaluation of these interferences is controversial since the effects on $DCFH_2$ vary depending on cell types and pharmacological conditions[98]. $DCFH_2$ is not suitable for application in $pH < 5$ as DCF will exist as its lactonic form, which is non-fluorescent[103]. Three ROS-reactive fluorescent protein sensors have been constructed since 2001: redox sensitive yellow fluorescent protein (rxYFP), redox sensitive green fluorescent protein 1 (roGFP1) and roGFP2. These sensors are developed to sense the redox change in intracellular environment upon the oxidation of two spatially adjacent cysteines causing consequential configuration change in their chromophores[104-106]. The benefit for using genetically coded protein sensor is that it can reflect the dynamic redox change upon its reversible oxidation/reduction, and they can be easily engineered to be selective for cellular compartments with appropriate targeting sequences (roGFP1 and roGFP2 have their mitochondrial and cytosolic versions[105,106]). rxYFP is the first genetically coded redox sensor, which responds slowly (~2 min)

to the reductant, DTT after been treated with oxidant 4-DPS[104]. It equilibrates with H_2O_2, GSH/GSSG and other disulfide compounds very slowly[107]. A fusion protein sensor with incorporated glutaredoxin (Grx), rxYFP-Grx1p, has been designed to make the sensor selective to the redox change of GSH/GSSG with a boosted reaction rate, over 3000 ~25000 fold increase compared to rxYFP[107]. However, rxYFP is very pH sensitive and has a small spectroscopic dynamic range (the ratio of fluorescence at its fully reduced form over its fully oxidized form) of 1.2~1.5[104], which limits its application in biological research. In contrast to rxYFP, roGFP1 and roGFP2 are pH insensitive. roGFPs can provide ratiometric readouts (the ratio of fluorescence from excitation at 405 nm over 488 nm, $R = F_{405}/F_{488}$). The FIs of two excitation channels (405 & 488 nm) change oppositely: F_{405} increases and F_{488} decreases upon oxidation; F_{405} decreases and F_{488} increases upon reduction. Because ~95% roGFPs remained in their reduced forms in cells, roGPFs usually move to a more oxidized status, not a more reduced status in the occurrence of most biological events[105,106]. roGFP1 has stronger F_{405} than F_{488}, which is different from roGFP2 with weaker F_{405} than F_{488}[105,106]. In practical term, roGPF2 is preferred over roGFP1 because 1) when imaging oxidation events, roGFP1 is unfavorable since FIs of its two excitation channels change divergently (the weaker F_{405} becomes weaker and the stronger F_{488} becomes stronger), which makes it difficult to set an appropriate imaging thresholds at the beginning. What's more, more systematic errors can be found in F_{405} since it is weak and becomes weaker during measurement; 2) roGFP2 has a larger dynamic range (DR; the ratio of R at full oxidation over that at full reduction, R_{Ox}/R_{Red}; DR= ~ 4) than roGFP1 with DR, ~ 2.7 in cells[105,106]. However, it's important to note that roGFPs have slow responses (> 15 min) to the different oxidants at 100 μM such as menadione, diamide and H_2O_2[106], which requires more improvement on its dynamic performance.

Any non-specific ROS dye or genetically coded protein sensor has advantages and disadvantages. In practical term, $DCFH_2$ and roGFP2 are preferred.

Dihydroethidium (DHE) and its mitochondrial verison, MitoSox, have been used for detecting superoxide since 1980s[108,109]. The detection of superoxide is based on the measurement of the DNA/ethidium complex (Exi/Emi: 510/580 nm). However, it has been reported that DHE and MitoSox can also be oxidized by H_2O_2[110] and cytochrome c[111]. What's more, ethidium is not the only one oxidized product upon the oxidation of DHE or MitoSox. There are two additional products, nonfluorescent dimers and fluorescent 2-hydroxyl-ethidium (Exi/Emi: 396/580 nm, proved to be superoxide specific product[112]) after the oxidation of DHE and MitoSox[108]. Thus selectively imaging of 2-hydroxyl-ethidium with the excitation at 396 nm instead of ethidium with the excitation at 510 nm is promising to selectively detect superoxide[108,109]. However, Kalyanaraman and his colleagues pointed out that there are other concerns about 2-hydroxyl-ethidium[113]. For instance, 2-hydroxyl-ethidium could be unstable with the presence of peroxidase in some biological samples[113]. There is still no satisfactory protocol for using DHE and MitoSox to selectively detect superoxide. What's more, DHE and MitoSox are irreversible sensors. They cannot be used in long-term imaging since they are consumed by accumulative oxidation over time. A genetically coded protein superoxide sensor, mito-cpYFP is reported[114] and can be used for long term imaging (see more details in Appendix A.2). However, it has been strongly questioned to be a superoxide or pH sensor[115]. We should be cautious to apply these claimed superoxide sensors.

There are several H_2O_2 selective dyes, which have not been commonly used in biological research (see more details in Appendix A.2). We focused on several novel genetically coded protein sensors here. Two different types of genetically coded protein sensor are constructed for

sensing H_2O_2 reversibly: circularly permuted yellow fluorescent protein (cpYFP) and redox sensitive green fluorescent protein (roGFP). HyPer is a fusion cpYFP with OxyR regulatory region (OxyR-RD)[116]. The oxidation/reduction of HyPer causes its chromophore to convert between its oxidized form (deprotonated/anionic form, Exi: 500 nm) and reduced form (protonated/neutral form, Exi: 420 nm)[116]. $R = F_{500}/F_{420}$ is used to indicate the H_2O_2 level. This sensor has fast reaction constant, 10^5 $M^{-1}\cdot s^{-1}$, with $t_{1/2} \approx 0.7\sim7$ s in reaction with $1 \sim 10$ μM H_2O_2[116]. However, HyPer is pH sensitive because its chromophore can undergo proton exchange with its surrounding environment which mimics redox effects[116]. Two advanced versions of HyPer are constructed: HyPer-2[117] and HyPer-3[118]. HyPer-2 has a larger DR (R_{Ox}/R_{Red}) = 6~7 compare to HyPer with DR = 3 but has slower H_2O_2 reaction rate[117]. Hyper-3 has advantages from both HyPer and Hyper-2, with high reaction rate and large DR, but neither HyPer-2 nor HyPer-3 can escape the effect of pH on its redox sensing[117,118]. roGFP2-Orp1 is a fusion of roGFP2 with peroxidase Orp1[119]. The oxidation/reduction causes its chromophore to convert between its oxidized form (protonated/neutral form, Exi: 400 nm) and reduced form (deprotonated/anionic form, Exi: 490 nm)[120]. Though the redox change of roGFP2 is proton exchange related, the final ratiometric readout is pH insensitive since pH exerts similar influence on F_{400} and F_{490}[119]. In practice, the application of roGFP2-Orp1 is easier than HyPers since it doesn't require internal pH sensitive reference. However, roGFP-Orp1 equilibrates with H_2O_2 (~3.5 min) much slower than HyPers[119].

To sum up, $DCFH_2$, DHE and MitoSox are still the most commonly used dyes for sensing ROS. We will use roGFP2-Orp1 to selectively sense H_2O_2 in this research.

1.3.3 Fluorescence imaging of Glutathione and Thioredoxin

There are many thiol-reactive dyes. First, we choose to not to discuss about the probes that could selectively target particular thiols such as cysteine (Cys), homocysteine (Hcy) and glutathione (GSH). Second we focused on the dyes based on the Michael addition mechanism. More dyes are discussed in Appendix A.3.

N- (4'- (7-diethylamino-4-methylcoumarin-3-yl) phenyl) maleimide (CPM) is one of the first examples of such type of dyes[121]. CPM is also pH sensitive, and its reaction rate with thiols and FI of final thiol derivatives vary with pH[122]. A complete thiol staining with CPM requires ~ 60 min[122]. Corrie et al. reported several maleimide baring probes in 1994: dansyl maleimide 7, coumarin maleimide 11a, b and phthalimide maleimide 30[123]. These probes shows different enhancement of FI upon the addiction of thiols: dansyl maleimide 7 (~31 fold), coumarin maleimide 11a, b (~ 4.2~4.8 fold) and phthalimide maleimid 30 (~ 7.4 fold)[123]. We currently do not have any information about the kinetic parameters of thiol reaction and the pH sensitivity of these probes. Precautions must be taken while using these compounds since they have a half-life of 24 hours at pH =7[123]. Thioglo-1, fabricated in 1991[124], is a trademarked product of MerckMillipore, Inc. This sensor is excellent for its rapid reaction with thiols (reaction constant = 2.1×10^4 $M^{-1} \cdot s^{-1}$, $t_{1/2} \approx 3.3$ s with 10 μM thiol, complete thiol staining in few seconds) and pH stability of FI from its thiol adducts[125]. What's more, no obvious hydrolysis of thioglo-1 has been reported[123]. Like Thioglo-1, Thioglo-3 and Thioglo-5 are naphthopyranone-maleimide based probes and commercially available in Covalent associates Inc. These two probes can react with thiols very quickly, usually in 2-5 min[126]. Thioglo-3/thiol adduct can be kept for several weeks at -80°C without degradation[127]. It reacts with thiols at pH = 7 and is kept and detected at pH =1. what's more, the hydrolysis of free Thioglo-3 cannot be ignored[127]. We do not have direct

information of pH sensitivity about these two probes so far. *o*-Maleimide-BODIPY (BODIPY: boron-dipyrromethene) is an novel probe constructed by Matsumoto et al. in 2007[128]. This probe is claimed to be pH insensitive and requires short time (~ 5 min) to completely react with thiols[128]. Thiol Probe IV[129] is a coumarin-enone based dye. The addition of thiol to enone causes fluorescence[129] or spectral shift[130]. Thiol Probe IV is able to stain thiols very rapidly (rate constant, $4.8 \times 10^3\ M^{-1} \cdot s^{-1}$, $t_{1/2} \approx 14.4$ ms with the presence of 10 mM thiol)[129], but this sensor is pH sensitive and its thiol-adduct shows different FI under different pHs (our unpublished data). Also according our experience, the aqueous solution of free Thiol Probe IV at pH = 7 is unstable after 2 hours. In practical term, Thioglo-1 and Thiol Prove IV are favored because they can react with thiols rapidly. However, both two dyes should be applied with cautious pH control.

There are several GSH selective dyes, but we will not list them out here (see more details in Appendix A.3). Monochlorobimane (mCB) is a highly GSH reactive dye, which has been widely used for more than 30 years. The reaction between mCB and GSH is complete in 5 min[131]. We have not found any information regarding pH sensitivity for mCB so far.

The current available genetically coded protein sensor for monitoring $[GSH]^2/[GSSG]$ is Grx1-roGFP2, which is a fusion of roGFP2 with glutaredoxin 1 (Grx1)[132]. The sensor selectively responds to the redox change of GSH/GSSG. Isolated Grx1-roGFP2 does not respond to oxidants such as H_2O_2, cystine and hydroxyethyl disulfide and reductants such as dithiothreitol, ascorbate and cysteine, but the sensor in cell can responds to oxidant/reductant treatment in the presence of intracellular GSH[132]. Isolated Grx1 has a rapid reaction rate with GSH/GSSG ($k = 10 \sim 13\ s^{-1}$, $t_{1/2} = 0.05 \sim 0.07$s)[133], which indicates that Grx1-roGFP2 is a better candidate for monitoring dynamic changes than HyPer or roGFP2-Orp1 (H_2O_2 protein sensors mentioned above). It is also much faster in detecting redox change than roGFP1 or roGFP2 (redox protein sensor mentioned above).

Because of the catalysis of Grx1, the sensor can monitor the redox change of GSH/GSSG occurring within 1 min[132]. Moreover, due to its pH stability, the sensor has been utilized in monitoring mitochondrial (pH ≈ 8) and cytosolic (pH ≈ 7) GSH system in neurons in hippocampal slice[79]. There are not feasible Trx selective sensors developed in recent years (see more details in Appendix A.3).

To sum up, Thioglo-1 is a good choice for the measurement of the intracellular thiols with pH and fluorescence stability and rapid derivatization. Grx1-roGFP2 is the best developed protein sensor for monitoring the real-time redox change of GSH/GSSG couple so far.

1.4 OBJECTIVE AND MOTIVATION

This dissertation is aimed at gaining fundamental understanding of the real-time redox change of oxidant (mainly H_2O_2 here) and reductant (mainly GSH here) under biological and pathological conditions. Our overall goal is to decipher why pyramidal cells in CA1 and CA3 have differential susceptibility to ischemia? In order to finish this goal, *specific questions that motivated this work* include: 1) How do we make an improvement on the control of the oxygen and glucose delivery to cell/tissue to closely mimic pathological condition, ischemia/stroke? 2) How can we improve the quantitative measurement of roGFP2 based ratiometric imaging for reporting redox change of oxidant and reductant system in real-time? 3) Corresponding to the excessive ROS generation, what does the redox change of the GSH system demonstrate and what are the differential performances of GSH in different cell types? 4) What is the key factor for the ROS management with regard to the critical molecules/systems such as NAD(P)H, GSH and Trx? We designed our experiments aiming at resolving these questions.

Chapter 2.0 details our efforts at establishing optimized protocol for mimicking ischemia in vitro and quantitatively recording the dynamic oxidation/reduction of the GSH sensors under ischemia/model. We developed an optimized superfusion system with the capability of rapid and reproducible exchange of the solution bathing the OHSCs for introducing oxygen/glucose deprivation, an *in vitro* ischemia model. Measurements of pO_2 as a function of tissue depth show that in the region containing the transfected cells, the pO_2 is well-controlled. We also found that the response time of pO_2 changes using our optimized superfusion system is in the same time scale as changes in intracranial pressure, cerebral blood flow, and pO_2 during acute stroke. Single pyramidal neurons in the CA1 subfield of organotypic hippocampal slice cultures (OHSCs) were transfected with a redox-sensitive Grx1-roGFP2 fusion protein. Since determining redox terms such as E_{GSH} from the ratiometric fluorescence signal requires an absolute intensity measurement, we use the signal from co-transfected tdTomato as an internal standard improves quantitative measurements of roGFP2 oxidation and allows E_{GSH} to be determined.

In Chapter 3.0, we monitored the OGD-RP induced redox change of GSH system in mitochondria and cytoplasm from HeLa cell, pyramidal cell and astrocyte with the protocol created in Chapter 2.0 in real-time. This sensor was characterized and verified that its dynamic range (DR; the ratio of R at full oxidation over that at full reduction, R_{Ox}/R_{Red}) is stable in all the six biological models that vary in pH, GSH concentration, and other aspects. By doing so, we are confident to apply this sensor for reporting redox information of GSH system. The redox terms, $R_{405/488}$, OxD_S, $\ln\frac{[GSH]^2}{[GSSG]}$ and E_{GSH} demonstrate consistent information about GSH during OGD-RP. Larger values in them mean more oxidized GSH system, while smaller values indicate more reduced GSH system. We observed that GSH systems differ in mitochondria and cytoplasm as well as in various cell types that we tested here.

Chapter 4.0 aims to answer whether differential management of ROS level is the key factor causing differential susceptibility to ischemia. We monitored ROS generating system (including NADH, H_2O_2) and anti-oxidant systems (including Glutatione (GSH) and thioredoxin (Trx), NADPH) in real time during OGD-RP. Without conclusive understanding of the impact of OGD-RP on relative enzyme systems, it is difficult to make convincing interpretation of the OGD-RP data. Thus, we further designed experiments aiming to selectively target certain enzyme involved in ROS generating and anti-oxidant systems and monitored the consequence reflected from the H_2O_2 and GSH system.

With profound understanding of molecular mechanism of ROS generating and antioxidant system, we can help to provide points of entry for developing potential therapeutic methods for ischemia. Also we can broaden its application to other neuron-degradation associated disease like Parkinson's disease, Alzheimer disease and amyotrophic lateral sclerosis[134,135]

2.0 OPTIMIZE SUPERFUSION SYSTEM AND RATIOMETRIC IMAGING ON ROGFP2 BASED SENSOR TO MONITOR THE REDOX CHANGE IN ORGANOTYPIC HIPPOCAMPUS SLICE CULTURE DURING OGD-RP

Parts of this chapter are adapted from a manuscript "Optimized real-time monitoring of glutathione redox status in single pyramidal neurons in organotypic hippocampal slices during oxygen-glucose deprivation and reperfusion" published in ACS chemical neuroscience.
Weber, S. G. and Yin, B. conceived the study. Yin, B. performed all the experimental work, and wrote the paper under the guidance of Weber, S. G.

2.1 INTRODUCTION

Neuronal damage in stroke[1-3], trauma[4-6], hypoxia[7] is in part caused by oxidative stress due to excessive production of reactive oxygen species (ROS)[23-25]. Neurons and glial cells are endowed with mechanisms for maintaining ROS homeostasis including the glutathione-glutathione disulfide couple (GSH/GSSG) and the thioredoxin system. Hypoxia/ischemia (HI) episodes, such as those that occur during stroke, disrupt ROS homeostasis leading to short-term effects in cellular function, and longer-term changes that ultimately cause cell death[32-34]. Several approaches exist for measuring ROS in real time including those based on voltammetry[136-138] and fluorescence microscopy that relies on fluorogenic small molecule probes[113,139-141]. However, there are no small-molecule redox-sensitive fluorophores that respond to the GSH system. Thus, it is noteworthy that several groups have developed the ability to measure its status in real time. Specifically, different

redox protein-based sensors were developed simultaneously by the Winther (rxYFP[142]) and the Tsien and Remington groups (roGFP[106,143]). The sensor response kinetics were relatively slow and were oxidized to varying degrees by a variety of oxidizing agents[106]. Altering the electrostatic environment of the active disulfide by engineering amino acid substitutions in the region of the modified GFPs increased the rate of reaction of the sensors with GSH/GSSG[143,144]. Meyer et al.[145] discovered that roGFP's reaction with GSH/GSSG was catalyzed by endogenous glutaredoxin (Grx). Gutscher et al.[146] made a chimeric protein, Grx1-roGFP2 that responded rapidly to cytosolic changes in GSH/GSSG status. In addition, they determined that the isolated Grx1-roGFP2 was not oxidized by cystine, hydroxyethyl disulfide, or H_2O_2, and was not reduced by ascorbate, cysteine or the thioredoxin system (thioredoxin, thioredoxin reductase and NADPH). Thus, this sensor is quite selective for the glutathione redox couple."

While these sensors have illuminated redox events in a variety of types of cells, they have not been used extensively in mammalian central nervous system (CNS) tissue. Using primary cultures of hippocampal neurons from rats Funke[147] carefully compared the roGFP1's response against a widely used small molecule sensor hydroethidine. These investigators showed a "proof of principle" that the sensor would respond to exogenous peroxide application to an organotypic hippocampal slice culture (OHSC). However, there was no attempt to infer biological information from the observed response. Grosser et al., using roGFP1, studied OHSCs from a Rett syndrome mouse model[148]. They found that cytoplasmic GSH status was more oxidized in the Rett syndrome hippocampus than controls. Hasel et al.[149] contrasted dendritic and somatic responses of Grx1-roGFP2 to stressors in cultured neurons, finding the dendritic regions more oxidized under resting conditions and changing more dramatically under stress than somatic regions. More recently, Breckwoldt et al.[150] created a mouse that expressed Grx1-roGFP2 in neuronal mitochondria. They

used this model with multiparametric imaging to investigate redox and size changes in mitochondria in explants of neuromuscular junctions and *in vivo* in lesioned spinal axons.

Thus far, the few investigations of the GSH system's status in CNS tissue have employed roGFP1 rather than the more rapidly responding Grx1-roGFP2 sensor. There are no reports that we are aware of that use the latter sensor to determine redox events in cortical CNS tissue. Here we describe a method for investigating redox events during oxygen-glucose deprivation, reperfusion (OGD/RP) in the OHSC[151]. OHSCs subjected to OGD/RP is a useful *in vitro* model of HI[37-39]. We use the rapidly responding Grx1-roGFP2 in single transfected pyramidal neurons in the CA1 subfield. We have validated that the transfection occurs within a narrow range of depths into the culture and that the pO_2 during OGD and RP are reproducible in this range of depths. We have also improved the standard superfusion system so that changes in pO_2 occur on the same timescale as it does in *in vivo* models of stroke. In addition, calibration of Grx1-roGFP2 is improved by cotransfecting with the redox-insensitive tdTomato. Fluorescence from tdTomato is used as a reference during calibration when absolute (not ratiometric) intensities from the Grx1-roGFP2 sensor are needed to report well-defined redox parameters (e.g. degree of oxidation of the sensor (OxD), E_{GSH}) as opposed to the measured ratiometric response only[147-150]. Using this optimized approach, we have found that the GSH system changes rapidly and significantly during OGD/RP in mitochondria but not in cytoplasm.

2.2 EXPERIMENTAL SECTION

2.2.1 Biosample preparation

2.2.1.1 Cloning of plasmids

Plasmids for expressing Mito-Grx1-roGFP2[132], Cyto-Grx1-roGFP2[132] were obtained from Tobias P. Dick as generous gifts. pCMV-tdTomato (Clontech) and pCS2+ (Addgene) were kindly provided by Dr. Zachary P. Wills (University of Pittsburgh). Plasmid Mito-tdTomato was constructed for targeting mitochondria with help from Jihe Liu in Dr. Alexander Deiter's group (University of Pittsburgh). The mitochondria-targeting-sequence from ATP synthase protein 9 (Neurospora crassa) was amplified from Mito-Grx1-roGFP2 using primers 5'-ATT AGG TCT CAC ATG GCC TCC ACT CGT GTC CTC GCC TC-3' and 5'-ATT AGG TCT CAT CAC GGA TCC GGA AGA GTA GGC GCG CTT C-3'. pCMV-tdTomato full-length sequence was amplified using primers 5'-AGT GGT CTC AGT GAG CAA GGG CGA GGA GGT C-3' and 5'-ATT GGT CTC TCA TGG TGG CGA CCG GTG GAT C-3'. Two fragments were assembled to construct pMito-tdTomato by using the Golden Gate Cloning method[152]. All of the plasmids were introduced into One Shot TOP10 Chemically Competent *E.Coli* cells (Invitrogen), selected on ampicillin or kanamycin agar plates, amplified in LB media and purified with a QIAGEN Plasmid Prep Kit (Qiagen).

2.2.1.2 Cell preparation and transfection

HeLa cells were grown in 75 cm^2 cell culture flasks (Corning) and cultured in a 5% CO_2/95% air incubator at 37ºC. Culture medium, made of 90% (v/v) DMEM + 10% (v/v) fetal bovine serum (FBS) purchased from Invitrogen, was replaced every 3-5 days. Before experiments,

the cells were transferred onto 35 mm culture dish (BD bioscience) with 2 mL cell culture medium at a seeding density of 1 x 10^5 cell/ dish. The cells were transfected by using lipofectamine (Invitrogen) according to the manufacturer's suggestions. The optimized amount of lipofectamine/ DNA was obtained to minimize the cell death and maximize the transfection efficiency: 1 μg DNA and 2 μL lipofactamine were dissolved in 100 μL opti-MEM for 5 min separately, then the two solutions were mixed for up for 20 min before adding to the cells. The medium containing lipofectamine/DNA was replaced with fresh cell culture medium after 6 hours. Plasmid expression was usually checked in 1-2 days. All of the tools and solutions were sterile.

2.2.1.3 OHSC preparation, transfection

Organotypic hippocampal slice cultures (OHSC) was prepared according to Gogolla's protocol[153]. All of the surgical tools were autoclaved. The dissection medium contained 75%(v/v) Opti-MEM, 25%(v/v) HBSS with the addition of 45% D-glucose solution (1.0 mL per 100 mL medium). Tissue culture medium was made from 50% (v/v) Opti-MEM, 25% (v/v) HBSS, 25% (v/v) horse serum (Invitrogen) with the addition of 45% D-glucose solution (1mL per 100 mL medium).

Our surgery protocol was approved by the Institutional Animal Care and Use Committee (IACUC) of the University of Pittsburgh. Surgery was done in sterilized hood. The postnatal 7-day old Sprague-Dawley rats (Charles River, Pittsburgh) was sacrificed and the hippocampus was taken out and sliced on a McIIwain tissue chopper (Mickle laboratory Engieering Company Ltd., UK). The slices were suspended in dissection medium for 30 min – 1h at 4 ^{o}C before plating onto Millicell organotypic inserts (Millipore Co.) and cultured with tissue culture medium in the incubator at 37^{o}C for 3~5 days before transfection. Culture medium was replaced every 3 days.

Biolistic transfection or electroporation were applied to transfect cells in OHSCs. Biolistic transfection was based on the Woods's[154] protocol. Slice cultures were transfected by using a Helios Gene Gun (Bio-Rad Laboratories, Inc. CA, USA). The bullets were made by coating gold/DNA particles onto inner wall of Tefzel tubing (Bio-Rad). The optimized recipe for gold/DNA complex was 20 μg roGFP2 mitochondrial or cytoplasmic contruct[132], 10 μg mitochondrial or cytoplasmic tdTomato as internal standard and 20 μg pCS2+ as DNA filler [155] loading to 14 mg gold particle (Φ = 1.6 μm), which could be used to make 40-50 bullets. The gold/DNA particles were blown onto an OHSC under 120 PSI pneumatic pressure with the gene gun. Plasmid expression occurs in about two days.

Single cell electroporation on OHSCs was applied according to Haas's procedure[156]. A 1-second train of 1 ms pulses of -50 V at 200 Hz generated by an isolated pulse stimulator (Model 2100, A-M Systems, WA, USA) through a pulled borosilicate glass pipette (18 MΩ) to deliver plasmid into single cells in OHSCs. Borosilicate glass tubing, OD x ID x L, 1.5 mm x 0.86 mm x 10 cm (Sutter Instrument Co. CA, USA) was pulled on P-97 micropipette puller (Sutter Instrument Co. CA, USA) to tip size 1-2 μm. Pulled pipette was filled with 0.3 μg/μL (total plasmid concentration) DNA in intracellular solution. The intracellular solution recipe[157] contained 145 mM K-gluconate, 10 mM HEPES, 14 mM phosphocreatine, 4 mM Mg-ATP, 2 mM $MgCl_2$, and 0.25 mM EGTA, adjusted to pH = 7.30 with KOH. The plasmid was added in a weight ratio of 2:1:2 (roGFP contruct : tdTomato vector : pCS2+). Pyramidal cells in OHSCs (30-50 μm deep inside) were viewed under ZEISS Axioskop FS (Zeiss, Germany). The pipet on holder (Warner Instruments, LLC, CT, USA) was controlled manually with X7500 micromanipulator (Siskiyou Co. OR, USA). After electroporation, tissue was rinsed with sterilized Hank's buffer solution and

placed back to 37ºC incubator for culturing at least 2 days for plasmid expression. Both of the methods work well in OHSCs.

The pO_2 was measured within OHSCs while the OHSC was superfused with ACSF saturated with 95% O_2/5% CO_2 or with 95% N_2/5% CO_2. The pO_2 profile was generated to help to understand the pO_2 dependent OGD-RP experiment and its relevant oxidation status change inside OHSC.

2.2.2 Fluorescent imaging

All imaging experiments were carried out on a Leica TCS SP5II broadband confocal microscope (Department of Biological Sciences, University of Pittsburgh). Cells were imaged with an HCX PL FLUOTAR 5x objective lens with N.A. = 0.15 and an HCX APO L U-V-I water immersion 63x objective lens with N.A. = 0.90. Only images taken with the 63x lens were used for quantitative analysis. The redox green fluorescent protein (roGFP) sensor is excited at 405 or 488 nm, and emission spectra are acquired between 500 – 530 nm. The red fluorescent protein (RFP), tdTomato, was excited at 561 nm and emission was acquired between 580 – 600 nm.

2.2.2.1 Determine the depths of transfected neurons inside OHSCs

The depth of the transfected cells is measured on a Leica TCS SP5II broadband confocal microscope with imaging under bright field and fluorescence mode, by counting the displacement of a z-stack scan, which starts from the top of an OHSC surface and steps through the OHSC until the equatorial section of the cell soma is found.

2.2.2.2 Real-time imaging on the roGFP2 based sensor

Sequential scans are applied to cells with GFP and RFP proteins by alternately exciting at 488, 405 and 561 nm. The Leica confocal microscope was set up to reduce z-direction shifts with an autofocus algorithm and the Hyper-dynamic detector. Shifts in the x, y plane were corrected by post processing (ImageJ Plugin-Template Matching and Slice Alignment[158]). Image series were acquired every ~8 s. Raw image files were processed by modules in ImageJ (http://imagej.nih.gov/ij/). Slices in the time-lapse videos were re-aligned using ImageJ Plugin-Template Matching and Slice Alignment[158] before extracting numerical data for 405,488 and 561 signals. Cell area changes in the time-lapse video were measured with built in functions in ImageJ as folllows: auto-threshold the images to make the cell area distinguishable from its background, then apply the function module "analyze particle" to measure the cell area within the specified threshold range. Ratiometric images in 'Fire' false-color were created by ImageJ[146].

2.2.3 Processing ratiometric images of roGFP2 sensors

Fluorescence data are processed to obtain the ratio $R_{405/488}$, the oxidation degree of Grx1-roGFP2 (OxDroGFP2), the natural logarithm of the ratio, $\frac{[GSH]^2}{[GSSG]}$ and the redox potential of glutathione (EGSH), according to Eq. 2.1-2.6, which are derived from equations described by Meyer and Dick[159] and Gutscher et al.[146].

Redox information is processed from the fluorescence data of Grx1-roGFP2, $R_{405/488}$ to derive of the oxidation degree of Grx1-roGFP2 (OxD_{roGFP2}), the natural logarithm of the ratio, $\frac{[GSH]^2}{[GSSG]}$ and the redox potential of glutathione (E_{GSH}).

We use tdTomato to correct the signal of 488 from Grx1-roGFP2 for calculation of OxD_{roGFP2}.

$$\hat{I}_{405} = I_{405}/I_{561}, \hat{I}_{488} = I_{488}/I_{561} \quad \text{(Eq. 2.1)}$$

$$R_{405/488} = I_{405}/I_{488} \quad \text{(Eq. 2.2)}$$

$$OxD_{roGFP2} = \frac{R_{405/488} - R_{405/488}^{Red}}{\frac{\hat{I}_{488}^{Ox}}{\hat{I}_{488}^{Red}}\left(R_{405/488}^{Ox} - R_{405/488}\right) + \left(R_{405/488} - R_{405/488}^{Red}\right)} \quad \text{(Eq. 2.3)}$$

$\hat{I}_{405}$, $\hat{I}_{488}$ are Normalized fluorescence intensities excited at 405 and 488 of Grx1-roGFP2 by I_{561}. $R_{405/488}$ is the ratio of the emission intensity excited at 405 nm, I_{405}, to that excited at 488 nm, I_{488}. $R_{405/488}$ at fully oxidized status is often normalized to 1 without special mention. $\hat{I}_{488}^{Ox}$,$\hat{I}_{488}^{Red}$ are $\hat{I}_{488}$ from Grx1-roGFP2 at full oxidation and full reduction, respectively. $R_{405/488}^{Ox}$ and $R_{405/488}^{Red}$ are ratio 405/488 of fully oxidized and reduced Grx1-roGFP2.

The Nernst term, $\ln(\frac{[GSH]^2}{[GSSG]})$, can be derived from OxD_{roGFP2} .

$$In\left(\frac{[GSH]^2}{[GSSG]}\right) = In\left(\frac{1 - OxD_{roGFP2}}{OxD_{roGFP2}}\right) + \frac{ZF}{RT}\left(E_{GSH}^{O} - E_{roGFP2}^{O}\right) \quad \text{(Eq. 2.4)}$$

$$E_{GSH}^{O} = -240\ \text{mV};\ E_{roGFP2}^{O} = -280\ \text{mV};\ Z = 2;\ F = 96485\ \text{C mol}^{-1};$$

$$R = 8.315\ \text{J K}^{-1}\text{mol}^{-1}; T = 309.15\ \text{K}$$

The redox potential of the GSH/GSSG couple in mitochondria and cytoplasm is calculated from the known OxD_{roGFP2}. Different pH values in the two compartments is considered.

$$E_{GSH}^{Cyto} = E_{GSH}^{pH=7} = E_{roGFP2}^{pH=7} = E_{roGFP2}^{O} - \frac{RT}{zF} \ln\left(\frac{1 - OxD_{roGFP2}}{OxD_{roGFP2}}\right) \quad \text{(Eq. 2.5)}$$

In this equation, E_{GSH}^{O}[160] and E_{roGFP2}^{O}[106] are the standard redox potentials of glutathione and Grx1-roGFP2 at pH = 7.00 respectively. z is the number of electrons transferred in the redox reaction,. R is the gas constant, F is the Faraday constant, T is the absolute temperature.

$$E_{GSH}^{Mito} = E_{GSH}^{pH=8} = E_{GSH}^{pH=7} + \frac{RT}{zF} \ln\left(\frac{[H^+]_{pH=8}^2}{[H^+]_{pH=7}^2}\right) = E_{roGFP2}^{O} - \frac{RT}{zF} \ln\left(\frac{1 - OxD_{roGFP2}}{OxD_{roGFP2}} \frac{[H^+]_{pH=7}^2}{[H^+]_{pH=8}^2}\right) \quad \text{(Eq. 2.6)}$$

In this equation, $[H^+]_{pH=8}$ = 10^{-8} mol L^{-1}, $[H^+]_{pH=7}$ = 10^{-7} mol L^{-1}.

Numerical data are processed in MatLab (version R2012b, MathWorks, Inc.) and OrginPro (version 9.0, OriginLab Corp.). Statistical inferences are from SPSS version 20, IBM Corp.)

2.2.4 Oxygen measurement

An oxygen microsensor (OX-25, Unisense, Denmark) was used to measure the oxygen partial pressure in OHSCs. This Clark-type sensor[161] is equipped with three electrodes. +800 mV, 0 mV and 0 mV are applied on the reference electrode, working electrode and guard electrode during O_2 measurement respectively. The existing guard electrode removes O_2 from the internal electrolyte to prevent signal drift (< 0.5% /30 min in ACSF saturated with 95% O_2/5% CO_2). The small tip size (20-30 um in diameter) of the electrode facilitates the measurement in small volumes (e.g. tissue with surface diameter ~ 1 mm, thickness, ~ 180 μm) with useful spatial resolution. An LC-4C amperometric detector (BASi, IN, USA) was used as the potentiostat. Data were recorded through a digital logger (NI USB-6008, National instruments Co. TX, USA). The sensor was polarized at -800 mv (working & guard vs reference) overnight before use. Three-point calibration on the oxygen sensor is performed with zero-oxygen solution (0.1 M NaOH + 0.1M sodium ascorbate), artificial cerebrospinal fluid[162] (ACSF) saturated with 95% air/5% CO_2 and

modifed ACSF (MACSF)[162] saturated with 95% O_2/5% CO_2. Oxygen pressure (pO_2) in solution is calculated with equation 2.7.

$$pO_2 = (\text{atmospheric pressure} - \text{water pressure}) * \text{percentage of pure oxygen} \quad \text{(Eq. 2.7)}$$

O_2% in the three standard solutions mentioned above is 0%, 19.95% and 95% respectively. Atmospheric pressure is measured with a mercurial barometer. Water pressure at 35^{o}C is used here.

pO_2 in OHSCs is measured at different depths while perfusing with ACSF saturated with 95% or 0% oxygen-containing gas. Each run is calibrated with ACSF saturated with 95% O_2/5% CO_2. The tissue is viewed under IX-71 inverted microscope (Olympus, USA), while the electrode is held by a manipulator (MP-285, Sutter Instrument). The electrode was inserted into a culture at an angle of 45^o and the tip resided at a certain vertical depth.

2.2.5 Superfusion system

OHSC or HeLa cells were placed in a homemade stage chamber and superfused at a flow rate of 4 mL/min driven with a peristaltic pump (Sci-Q 400DM2, Watson-Marlow, Inc. MA). Solution temperature was maintained at 35 ^{o}C by an inline solution heater, SH-27B under the control of temperature controller, TC-324B (Warner Instruments, LLC. CT, USA). Solution was gassed by an OX miniature gas exchange oxygenator (Living Systems Instrumentation, VT, USA) or by direct bubbling. Gas flow was set to 1.5 L/min with an OMA-1 gas flowmeter (Dwyer Instruments, Inc.). Artificial cerebrospinal fluid[162] (ACSF) is composed of 125 mM NaCl, 2.5 mM KCl, 1.25 mM NaH_2PO_4, 25 mM $NaHCO_3$, 1 mM $CaCl_2$, 4 mM $MgCl_2$, 10 mM glucose. Modifed ACSF (MACSF) substitutes 10 mM glucose with 10 mM sucrose while maintaining the rest as same as ACSF. The osmolarity of buffer solutions used through the works described in the paper

was adjusted to between 290 and 300 mOsm. ACSF gassed with 95% O_2/5% CO_2 and MACSF gassed with 95% N_2/5% CO_2 were alternately introduced into the stage chamber during the control period, OGD and RP.

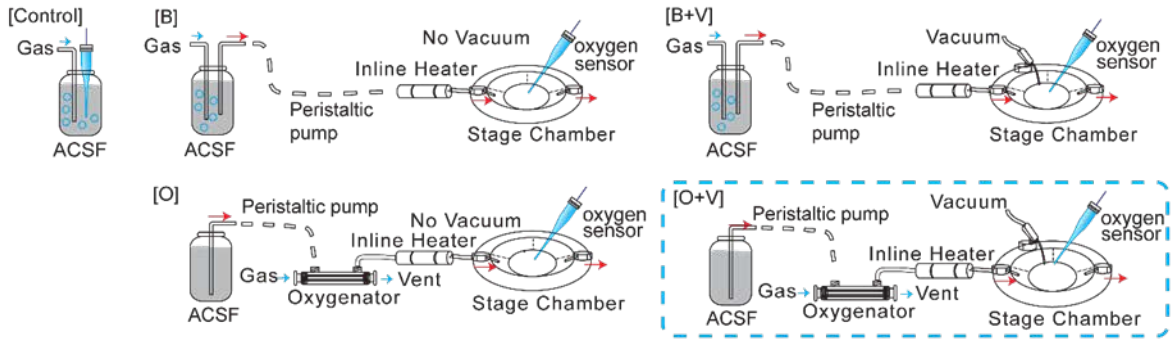

Figure 2-1. Different Superfusion setups.

The conical probe represents the oxygen electrode. [control], oxygen is directly measured in a reservoir with solution continuously bubbled with gas. In the remaining four panels, pO2 is measured in the slice chamber. The solution is driven by a peristaltic pump. Solutions are switched in all cases by pumping from a second reservoir containing the new solution. In the scheme labeled "[B]", solution from a reservoir being bubbled with gas is flowing continuously. [B+V] is as [B] but in addition, when the solution is switched to a new solution, existing solution is removed from the chamber by vacuum suction. In [O], solution is gassed by an oxygenator. [O+V] is as [O] except that solution is removed by suction when the switch is made.

In the [O+V] setup (Figure 2-1), we aspirate the solution in the stage chamber by vacuum at the time that the peristaltic pump begins drawing solution from a new reservoir (e.g. from control to OGD). The oxygen partial pressure was monitored (Supporting Information) with an oxygen sensor (OX-25, Unisense, Denmark) connected to a potentiostat (LC-4C amperometric detector, BASi, IN, USA) with the working and guard electrodes at -800 mV with respect to the OX-25 built-in reference electrode. The oxygen sensor was calibrated with zero-oxygen solution (0.1 M NaOH + 0.1M sodium ascorbate), and ACSF saturated with 95% air/5% CO_2. There is no

difference in the pO_2 measured in MACSF saturated with 95% O_2/5% CO_2 vs. that measured in ACSF. The electrode tip was placed in an OHSC at a particular depth with the aid of a micromanipulator (MP-285, Sutter Instrument). Values of and pO_2 in tissue is recorded at different depths inside OHSC and in different superfusion setups.

2.2.6 OGD-RP experiment

Cells or OHSCs expressing the roGFP2 based sensor are placed in the superfusion setup and imaged under a confocal microscope as shown in Figure 2-2. They are treated with control solution for 10 min, oxygen glucose deprivation (OGD) for 20 min, and reperfusion (RP), 30 min. ACSF gassed with 95% O_2/5% CO_2 is used for the control solution and RP, and MACSF gassed with 95% N_2/5% CO_2 is used in OGD. The use of aspiration by vacuum is preferred during solution switching to assist in the solution exchange in the stage chamber. We run the OGD-RP experiment on pyramidal cells in OHSCs, followed by treating with H_2O_2 and DTT.

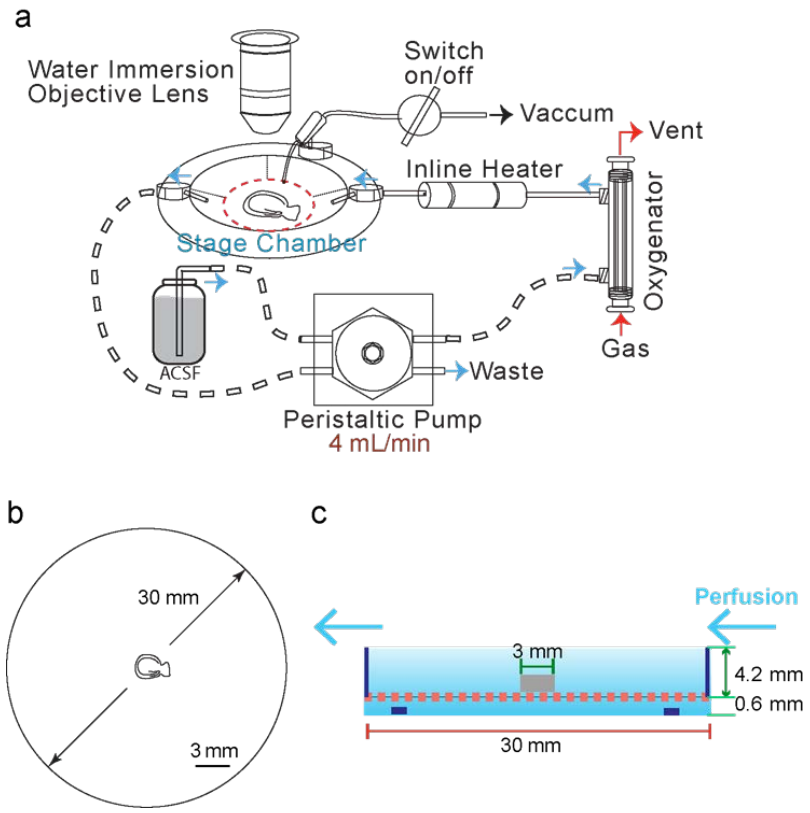

Figure 2-2. Sketch of optimized superfusion system.

(a) An OHSC is placed in the stage chamber of a Leica SP5 upright microscope and imaged with a water immersion objective while being superfused with gassed buffer solution. Solution is driven through the chamber by a two channel peristaltic pump, gassed with an oxygenator and heated with an inline heater placed near the inlet of the chamber. Vacuum is applied to remove solution in the chamber when the reservoir feeding the pump is changed. (b) OHSCs are cultured on a porous membrane insert (Millipore Co.), 30 mm diameter. The OHSC is about 3 mm in the longest dimension. (c) An OHSC (gray) is placed on the porous membrane insert shown (red broken line) held by a plastic frame (purple), and superfused with a buffer solution. The OHSC is positioned 0.6 mm from the base of the stage chamber. The depth and volume of solutions in the chamber above OHSC is 4.2 mm and 2.97 mL.

2.3 RESULTS AND DISCUSSION

2.3.1 Calibration Oxygen sensor

The sensor has a rapid response to oxygen pressure changes ~ 10s as shown in Fig. 2-3a. The current signal acquired with the sensor has a linear relationship with oxygen partial pressure (Fig. 2-3b). The values of pO_2 measured in different solution with variable oxygen level have a very small deviation, which verify that the oxygen sensor is reliable for pO_2 measurement.

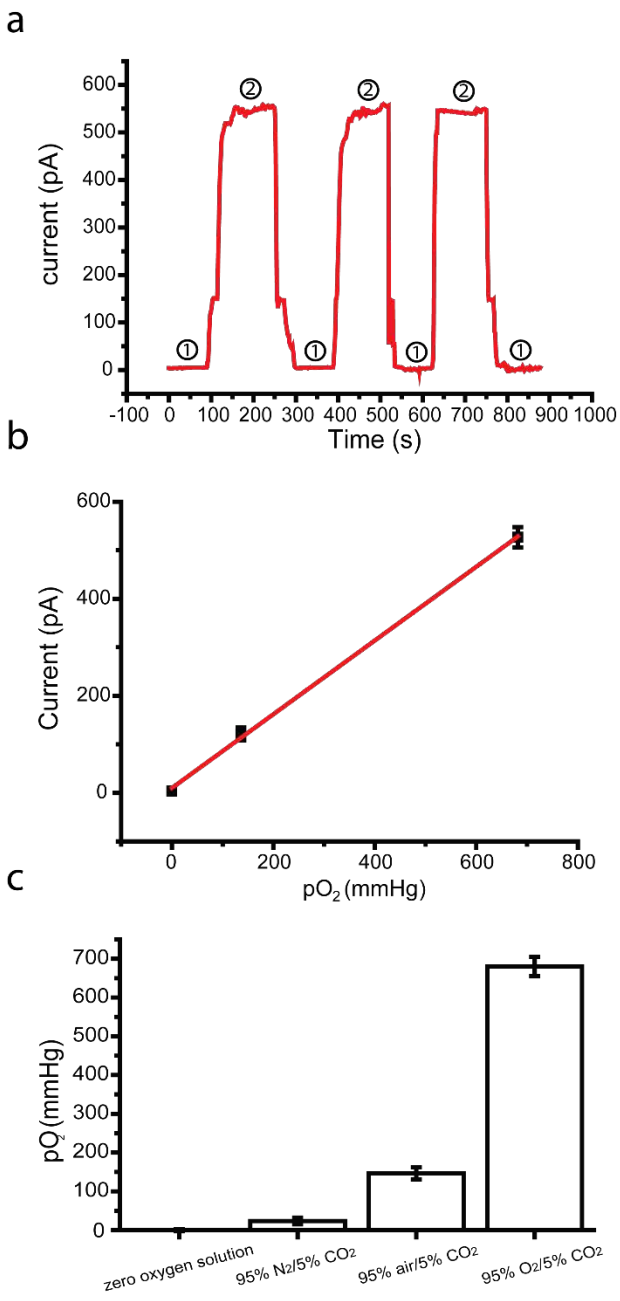

Figure 2-3. Calibrate oxygen sensor (Ox-25) in standard solutions.

a) The sensor is dipped alternately into solutions 1 and 2, which are zero-oxygen solution (0.1 M NaOH + 0.1M sodium ascorbate) and ACSF buffer saturated with 95%O_2/5%CO_2, respectively. b) Three point calibration measured in zero-oxygen solution, 95% air/5%CO_2 saturated ACSF buffer , and 95%O_2/5%CO_2-saturated ACSF buffer. c) pO_2 is measured in four different solutions based on the calibration (n=5).

2.3.2 Optimize superfusion system

The conventional method of slice oxygenation relies on bubbling the superfusion solution, ACSF containing 10 mM D-glucose, with 95% O_2/5% CO_2 and delivering it to the slice chamber with a peristaltic pump ([B], Fig 2-1). OGD is initiated by changing the superfusion solution to ACSF containing 10 mM sucrose (modified ACSF, MACSF) in place of the glucose with 95% N_2/5% CO_2 (see section 2.2.5 for the details of the solution compositions). We measured changes in pO_2 within in the cell dish with no slice culture using four different superfusion systems (Fig. 2-1). In all cases, the tube leading to the pump is manually switched from one reservoir to another to change conditions and the temperature of the incoming fluid is controlled online. In [B] the solution flows continuously while it is bubbled with gas in its reservoir. [B+V] adds a step - the fluid in the slice chamber is removed by vacuum at the time the solutions are switched. In [O] and [O+V] the solution is gassed by an online oxygenator placed near the chamber. The oxygenator uses microfluidic channels with a thin, gas-permeable membrane to introduce oxygen to the solution as it passes through the device. In [O+V] the solution in the chamber is removed by vacuum when the gas supply and the source reservoir are switched. We investigated the four superfusion setups and compared them to the [control] (Fig. 2-4). Clearly setup [O+V] (highlighted in blue box, Fig. 2-1) maintains the desired oxygen level in the stage chamber (Fig. 2-4b). Furthermore, the transition time for complete solution exchange also is dramatically shortened to less than 30 s using the setup [O+V]. In contrast, the other three superfusion systems show significant differences from the control (Fig. 2-4c). The optimized superfusion setup [O+V] will be used in the following experiments without special mention.

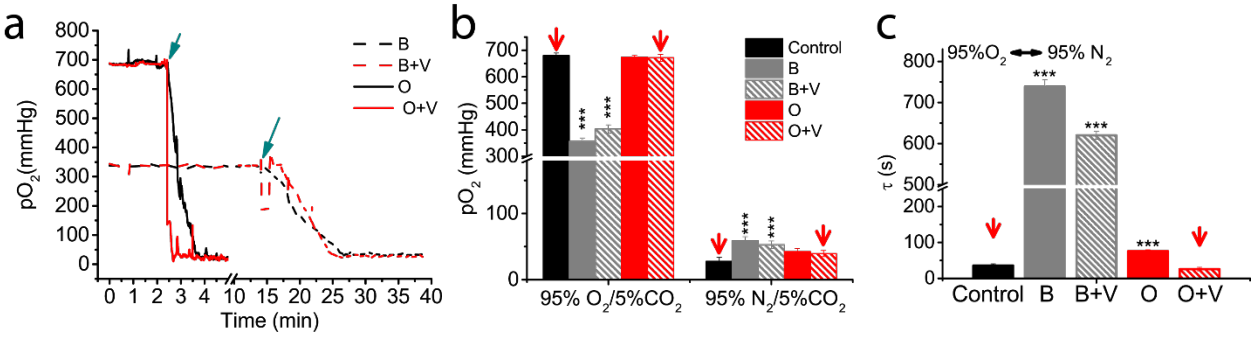

Figure 2-4. Control of pO_2 in different superfusion setups.

Control and the four different setups ([B]. [B+V], [O] and [O+V]) have been described in Figure 2-1. **(a)** Continuous measurement of pO_2 in the slice chamber during superfusion with the four arrangements described in (Figure 2-1). Note the break and the change in the time scale. The solution is switched from 95% O_2/5% CO_2 to 95% N_2 /5% CO_2 (indicated by the green arrow point). τ is the time from the solution switch to the onset of a new steady state pO_2. **(b)** Steady-state pO_2 are measured in control and the four superfusion setups. Arrows indicate control and setup [O+V]. **(c)** τ from the 5 setups. One-way ANOVA with post-hoc test (***, $p < 0.001$, n=6)

2.3.3 Determine the pO_2 and gas exchange efficiency in the depth where transfected neurons located in OHSC placing in our optimized superfusion setup

By controlling the transfection conditions (see section 2.2.1.3), we were able to target pyramidal cells localized within a relatively narrow range of distances below the surface of the OHSC. Half of the transfected cells are confined to 33-40 μm below the surface shown in Fig 2-5. When we treat the tissue with OGD-RP, we need to know if the pO_2 experienced by the neurons expressing roGFP redox sensor is consistent through experiments. Thus, we need to measured pO_2 at various depths within OHSC in our optimized superfusion setup [O+V].

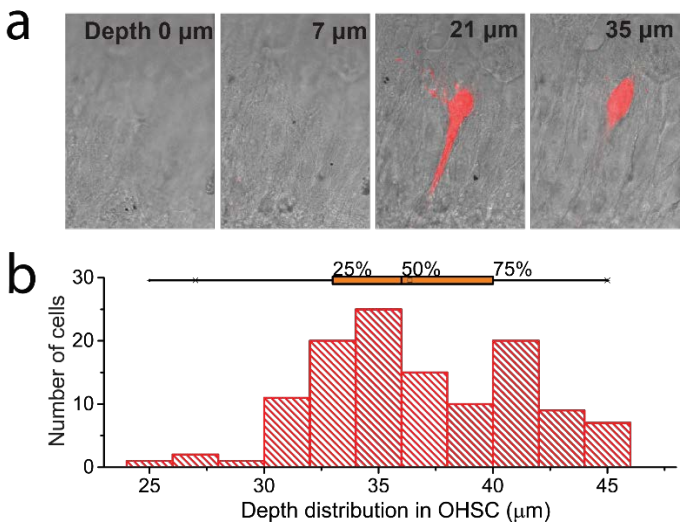

Figure 2-5. The transfected neurons located in a narrow range of depth in OHSCs.

(a) Scan deep into OHSC, the equatorial section of the neuron expressing tdTomato (red fluorescent protein) is found at 21 µm depth. **(b)** Transfected cells are mostly located 30-45 µm below the surface of the culture (n=121 cultures).

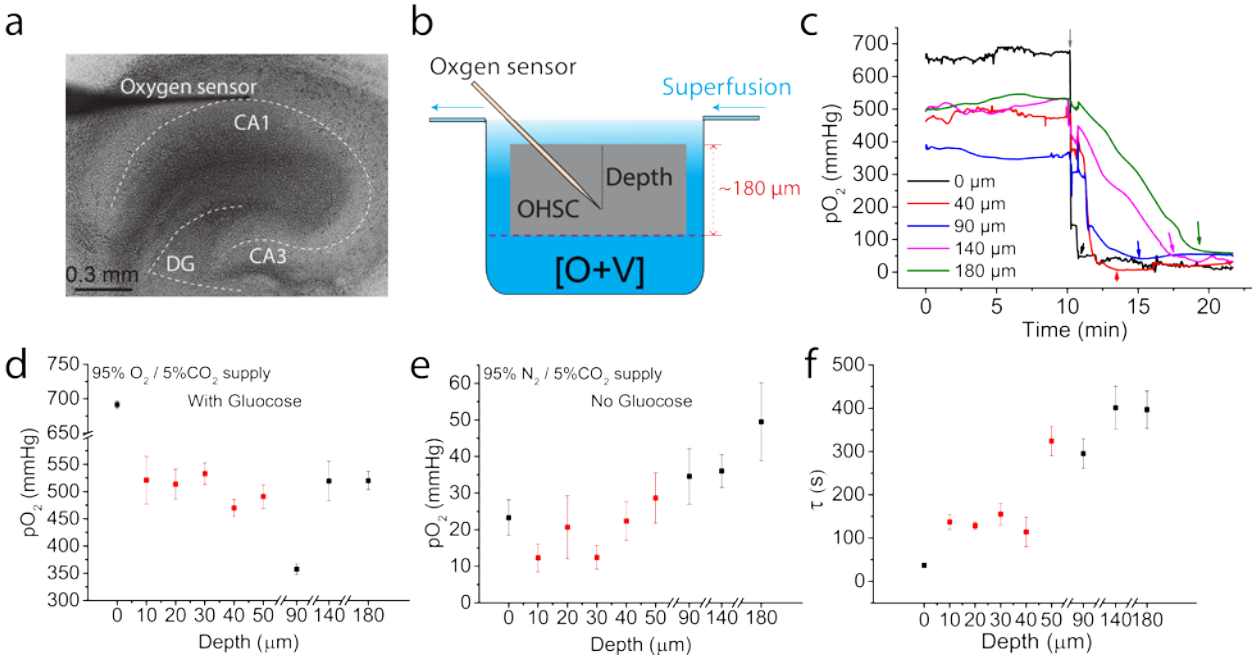

Figure 2-6. pO_2 varies with depth inside OHSC in optimized superfusion setup

(a-f) Measurements made in OHSCs with [O+V], the optimized setup described in Figure 2-1. **(a)** The image of OHSC with an oxygen sensor placed. **(b)** The sketch of OHSC placed in superfusion setup [O+V] and interstitial pO_2 is

measured. (c) pO_2 profile in different depths inside OHSC. Superfusate is switched from 95% O_2/5% CO_2 to N_2/5% CO_2. Gray arrow indicates the switching time. The second arrow (labelled with the same color as relative trace) indicates point where τ is measured to. (d, e) pO_2 in OHSC vs depth in OHSCs for 95% O_2/5% CO_2 and N_2/5% CO_2. Red symbols are in the range of depths where we transfect cells and make measurements. (f) τ measured at different depths inside the OHSC. Error bars from 6 individual tests in (d) to (f).

As shown in Figure 2-6, we measure pO_2 in depths from 0-180 μm in superfusion setup [O+V]. The condition that ACSF saturated with 95% O_2/5% CO_2 is used in the first 10 min of Fig. 2-6c, 2-6d, and will be used in "control" and "RP" for OGD-RP experiment. The condition that MACSF saturated with 95% N_2/5% CO_2 is used in the later 10 min of Fig. 2-6c, 2-6e, and will be used in "OGD" for OGD-RP experiment. As noted in Fig. 2-6c, the changes in pO_2 in the OHSC at depths less than about 50 μm occurs rapidly. In addition, we have determined the steady-state pO_2 during superfusion with ACSF saturated with 95% O_2/5% CO_2 (Fig. 2d). pO_2 within the OHSC ranges from 691 ± 6 mmHg at the top surface to a minimum of 358 ± 10 mmHg in the middle, and 520 ± 17 mmHg at the bottom surface. This is consistent with two facts. One is that oxygen takes time to diffuse into the OHSC and that is consumed on the way[163]. The other is that the culture is maintained with the interface method, so the lower surface of the culture is exposed to the medium underneath which is in equilibrium with air. The pO_2 distribution during superfusion with MACSF saturated with 95% N_2/5% CO_2 and transition times (τ) show similar trends (Fig. 2e,f) indicating that the depth is a significant factor in controlling tissue oxygenation.

2.3.4 The oxidation status of mitochondrial GSH changes in a concert with pO_2 that OHSC experiences

It is very important to control pO_2, especially in OGD-RP experiment because the redox status of the mitochondrial GSH is sensitive to the oxygen level, and it can be tracked with the Grx1-roGFP2 sensor that we used here. As discussed in section 2.3.3, OHSC experienced different pO_2 conditions by using different superfusion setups (Figure 2-6). We expressed mito-Grx1-roGFP2 in OHSCs, and observe its response during an OGD-RP protocol (described in section 2.2.6) under 4 different superfusion systems (Fig. 2-1). Fig. 2-7 shows that Grx1-roGFP2 signal changes on the same timescale as that of pO2 in the four superfusion setups.

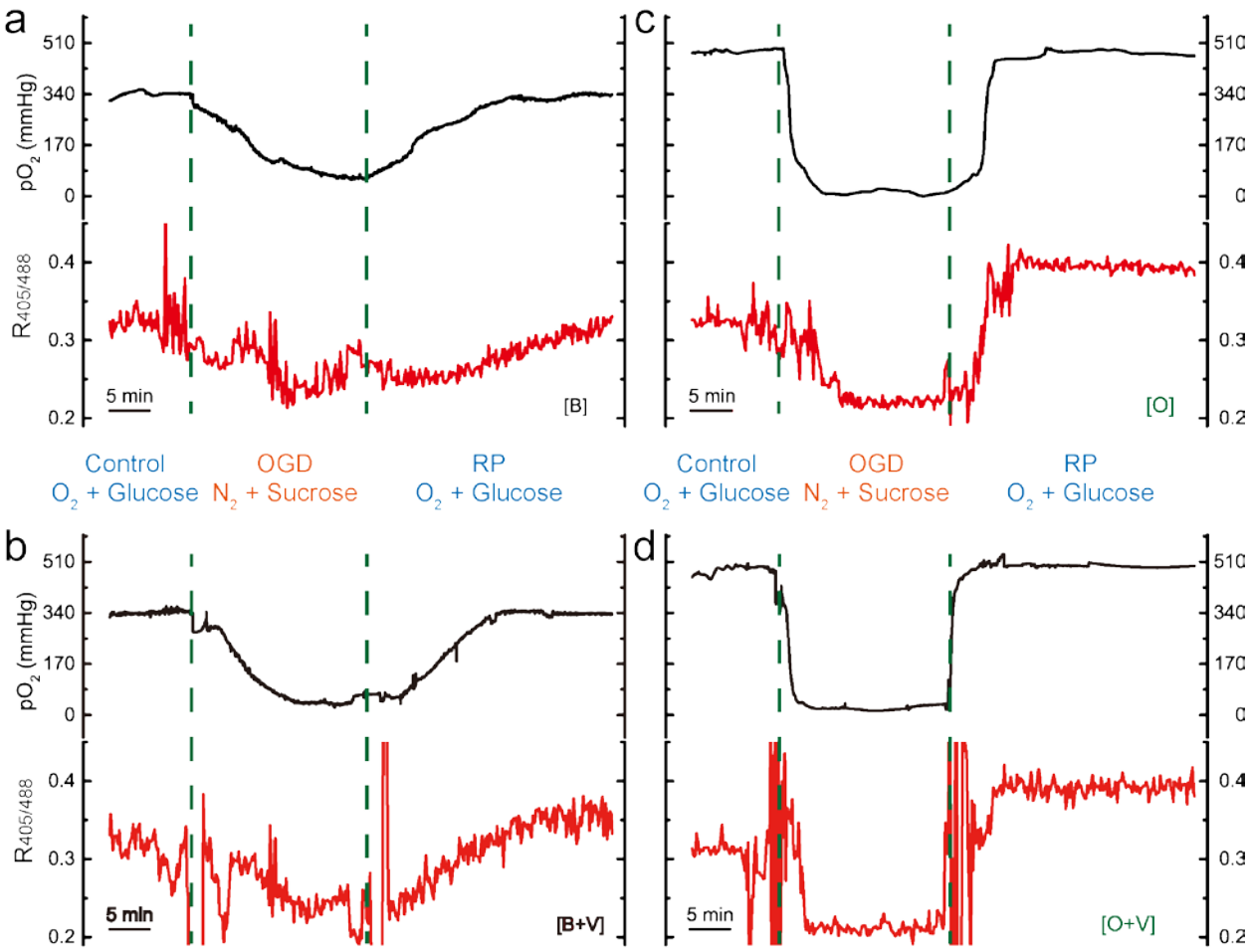

Figure 2-7. mito-Grx1-roGFP2 signal tracks the pO_2 change during OGD/RP.

Each of the four quadrants represents a superfusion method: a: [B], b: [B+V], c: [O], d: [O+V]. In each quadrant there are traces of pO_2 (top) and the mito-Grx1-roGFP2 ratiometric signal, $R_{405/488}$ (bottom) measured simultaneously in OHSCs versus time. "Control", "OGD", "RP" correspond to superfusion with ACSF saturated with 95% O_2/5% CO_2, 95% N_2/5% CO_2 and 95% O_2/5% CO_2, respectively. Each trace is representative of three separate experiments. $R_{405/488}$ (t) reflects the redox status of the GSH system, which changes with extracellular pO_2. The [O+V] configuration significantly improved gas exchange within the OHSC thereby decreasing the response time of the Grx1-roGFP2.

2.3.5 tdTomato corrects signal from Grx1-roGFP2

In OHSCs that have not been subjected to OGD/RP, there are very small or no changes in cell size during exposure to the calibrants (Fig. 2-8a). However, after OGD/RP there are significant changes in cell size (Fig. 2-8b, Fig A-3b in Supporting Information). roGFP2 is ratiometric, so cell size does not change the measured ratio. However, to determine the degree of oxidation of the sensor and redox potentials of the sensor and the GSH/GSSG system we must measure the *absolute* intensities of Grx1-roGFP2 excited at 488 nm in its fully oxidized form, I_{488}^{Ox}, and in its fully reduced form, I_{488}^{Red}. These intensities are influenced by changes in cell size (Fig. 2-8d). We have found that the fluorescence emission intensity of tdTomato[164] is not sensitive to H_2O_2 or DTT (Fig. 2-8a,c and Fig. B-3a,c). In the following discussion, it will be helpful to define some terms. We excite tdTomato at 561 nm, thus we refer to the intensity of the emission from that excitation as I_{561}. We then define ratios of I_{488}^{Ox} and I_{488}^{Red} to I_{561} as $\hat{I}_{488}^{Ox}$ and $\hat{I}_{488}^{Red}$ respectively. More generally, the ratio of the intensity from exciting roGFP2 at 488 nm to the intensity from 561 nm excitation of tdTomato is $\hat{I}_{488}$. See SI for more discussion of these terms and their relationships. Notably, Fig. 2-8b and Fig B-3b show that I_{561} is inversely correlated with the relative changes in cell size. The changes in cell size (ΔS/S) also influence the fluorescence arising from roGFP2 as can be seen in the upper panel of Fig. 2-8d and Fig B-3d. When I_{488}^{Ox} and I_{488}^{Red} (measured during calibration) are divided by I_{561} at each time point, clear steady state values of the ratios $\hat{I}_{488}^{Ox}$ and $\hat{I}_{488}^{Red}$ are obtained making calibration possible.

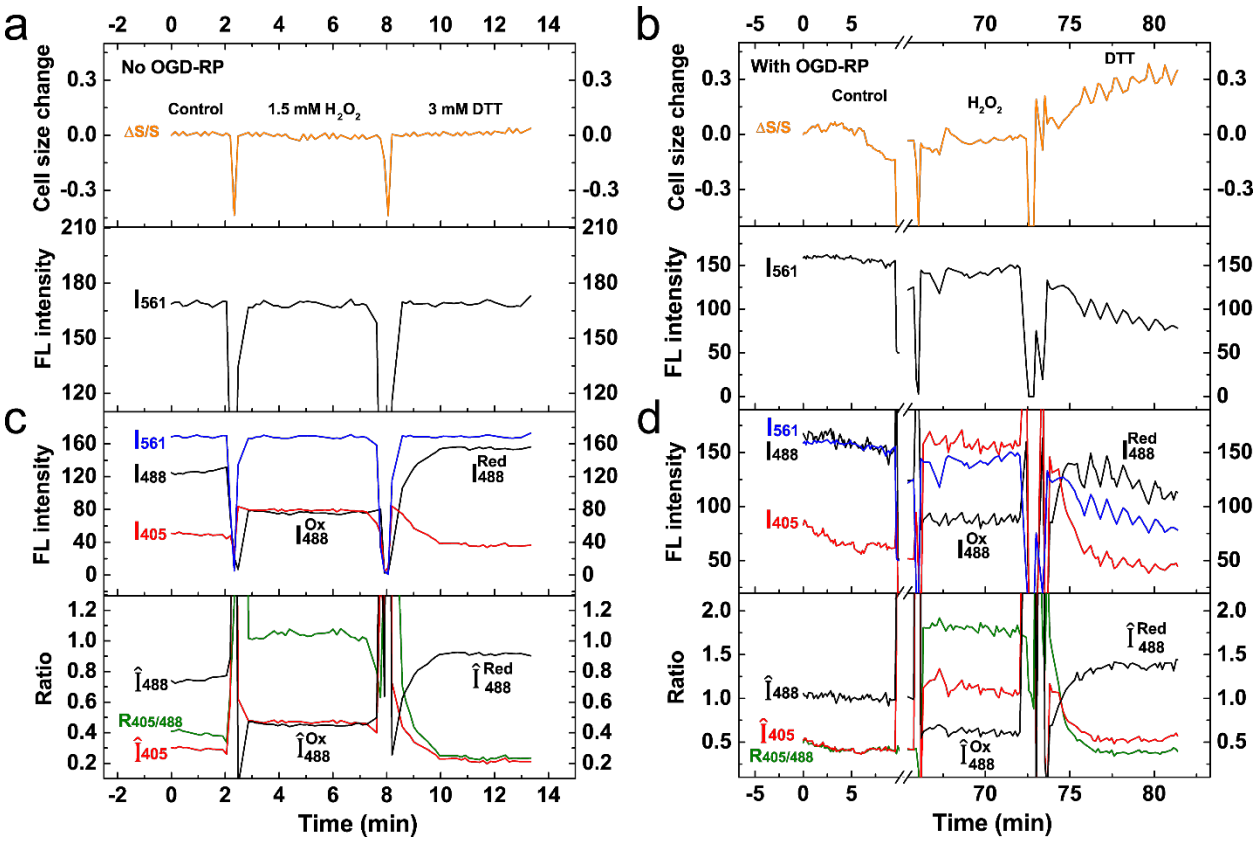

Figure 2-8. tdTomato corrects for changes in cell morphology allowing for stable signal during calibration.

Fluorescence emission of tdTomato (excited at 561 nm) and Grx1-roGFP2 (excited at 405 and 488 nm) recorded from cytoplasm of a CA1 pyramidal cell in an OHSC. **(a)** Top: With no OGD/RP, the cell area does not change during exposure to calibrants H_2O_2 and DTT. Bottom: tdTomato fluorescence emission is not sensitive to H_2O_2 and DTT. **(b)** With OGD/RP, Top: ΔS/S, cell size, changes dramatically, does not reach a steady state, and oscillates. Bottom: Fluorescence signal from tdTomato is inversely correlated with changes in cell size. **(c)** The absolute intensities (Top) and ratios (bottom) from the three channels are obtained when exposed to ACSF, H_2O_2 and DTT with no OGD/RP. The Grx1-roGFP2 fluorescence shows dramatic changes. No difference in trend are observed when comparing absolute intensities (top panel of **c**) and ratios (bottom panel; I_{405} vs. $\hat{I}_{405}$, I_{488} vs. $\hat{I}_{488}$). **(d)** tdTomato calibration is necessary on single channel 405 nm or 488 nm (see the difference in I_{405} vs. $\hat{I}_{405}$, I_{488} vs. $\hat{I}_{488}$ when exposed to DTT) after OHSCs are continuously superfused for ~1.5 h during an OGD/RP experiment with the superfusion setup [O+V] as described in Figure 2-1. Fluorescence traces prior to OGD/RP (control) and during calibration post-OGD/RP with H_2O_2 and DTT are shown (note the break in the time axis). The value of $\hat{I}_{488}^{Red}$ (bottom panel of **d**) is significantly more

stable than the I_{488}^{Red} fluorescent signal in (top). The confounding effects of OGD-induced cell size changes on I_{488} are corrected by I_{561}. $\hat{I}_{488}^{Ox}$ and $\hat{I}_{488}^{Red}$ are used to calculate the degree of oxidation of Grx1-roGFP2, OxD_{roGFP2} (see section 2.2.3 for more details). The curves shown here are representative examples from five sets of measurements on five different OHSCs.

Fekete et al. [165] saw significant swelling/volume changes in acute hippocampus slices during OGD. In an attempt to determine the fluorescence signal from the ROS-reactive dye, dihydrodichlorofluorescein, they used calcein AM (ROS insensitive) to correct for the changing volume. In our case, it was more appropriate to use co-transfection in order to make measurements on single pyramidal neurons in the CA1 region. While the sensor responds rapidly and reproducibly for neuronal mitochondria and cytoplasm in CA1 during the OGD/RP procedure, it was difficult to infer thermodynamically meaningful parameters from the data due to signal instability during the calibration steps following OGD/RP. In other sorts of investigations that do not involve such stressful conditions, changes in cell morphology may not be a problem and the internal standard may not be necessary. Of course, it is often sufficient to just report $R_{405/488}$ as ratiometric measurement which is immune to the volume changes. But introducing tdTomato as an internal standard to correct the fluorescent signal during calibration of mito-Grx1-roGFP2 allowed us to quantify the degree of oxidation of the sensor over time, $OxD_S(t)$, from the ratiometric signal $I_{405}/I_{488}(t)$. With assumptions about the local pH, this in turn can be used to infer E_{GSH}. We can applied this method to the determination of changes in OxD_{GSH} in the cytoplasm and mitochondria of pyramidal neurons in OHSCs.

2.3.6 Quantitative analysis of redox changes in the GSH system in mitochondria and cytoplasm

Fig. 2-9 shows the time-dependent changes in the GSH system in cytoplasm and mitochondria of single pyramidal neurons in the CA1 subfield of OHSCs during OGD/RP. Steady-state values of the Grx1-roGFP2 signal and derived quantities are averages of the last five minutes of each period. The data for pyramidal cells in CA1 (Fig. 2-9) show that the sensor in mitochondria is more oxidized than that in cytoplasm under normal conditions. (OxD_{roGFP2}: Mito/Cyto, 0.297 ± 0.029/0.126 ± 0.023), but E_{GSH} in mitochondria is more negative than that in cytoplasm (Mito/Cyto , -351 ± 2/-305 ± 3 mV) because of the different pHs in mitochondria and cytoplasm (Eq. 2.5-2.6, section 2.2.3). Mitochondrial GSH is notably reduced during OGD, then oxidized to a larger extent in RP than control (OxD_{roGFP2}: Control/OGD/RP, 0.297 ± 0.029/0.101 ± 0.024/0.447 ± 0.002), whereas no significant change is observed in cytoplasmic GSH (OxD_{roGFP2}: Control/OGD/RP, 0.126 ± 0.023/0.156 ± 0.037/0.160 ± 0.026).

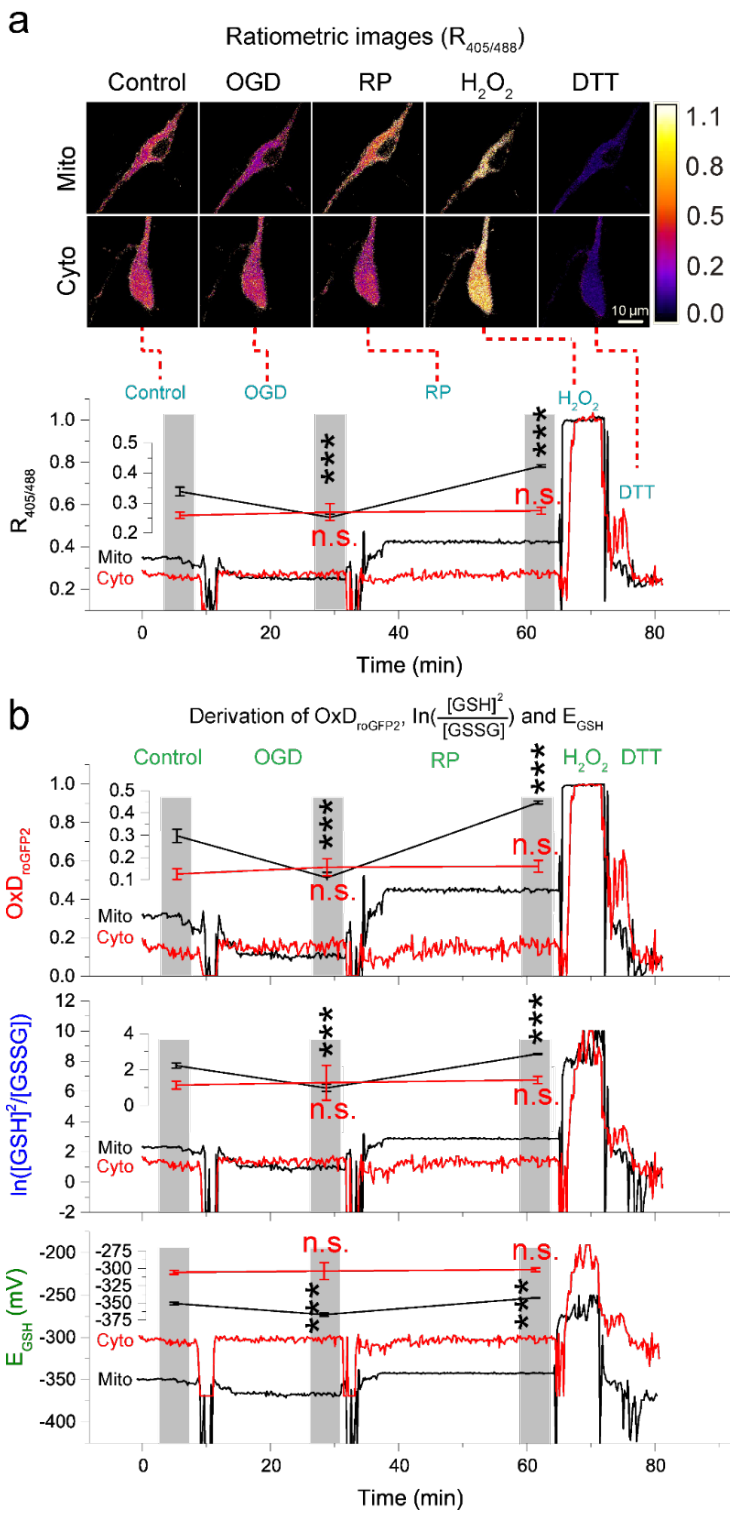

Figure 2-9. Quantitative analysis of GSH redox changes during OGD/RP.

Superfusion setup [O+V] described in Figure 2-1 is used. (a) Ratiometric images of Grx1-roGFP2 in mitochondria (Mito) and cytoplasm (Cyto) at different points in the OGD/RP procedure. (b) Mitochondria (data shown in black)

show a different response during OGD/RP than cytoplasm (data shown in red). Real time data traces are represented. The data in the last 5-minutes of each condition (indicated by the gray bar) from the traces are averaged and plotted with error bars. The data are statistically analyzed and compared to the control data (n.s. (no significant difference), $p > 0.05$; ***, $p < 0.001$, n=30 data points, ANOVA test). All of terms used are defined in Eq. 2.1-2.6 in section 2.2.3. The curves shown here are representative examples from five sets of measurements on five different OHSCs.

Our observation shows that the mitochondrial GSH system becomes more reducing during OGD, and more oxidizing during RP in comparison to the pre-OGD control conditions (Figure 2-9). On the other hand, the cytoplasmic GSH system did not respond to OGD-RP. Abramov et al. recently did a careful investigation of ROS generation during OGD/RP in hippocampal neuron/glia primary co-cultures[43]. They found three sources of ROS occurring in series based on MitoSOX and ethidium fluorescence following application of hydroethidine, HEt. In the first 10-20 min of OGD, ROS production is mitochondrial and correlated with the presence of inner mitochondrial membrane (IMM) depolarization. After about 25 min (longer than our OGD period), Abramov et al. found that there is a phase during which ROS is produced in the cytoplasm by the xanthine/xanthine oxidase system[43]. During RP, ROS generation occurs in the cytoplasm from the NAD(P)H oxidase system. We observed that the mitochondrial GSH system becomes more reducing quite rapidly at the onset of OGD and that this more reducing status is maintained during OGD. A negative shift in E_{roGFP2} could be caused by a number of factors, e.g., import of GSH from cytoplasm[166], reduction of mitochondrial GSSG, or indeed by an increase in local pH. We note that Abramov et al. in primary cultures and others on OHSCs[167-169] have seen rapid IMM depolarization during OGD. This would decrease the local pH in the matrix. Thus, we can be reasonably sure that the response of mito-Grx1-roGFP2 during OGD represents an increase in the ratio $[GSH]^2/[GSSG]$. That is, the GSH system becomes more reduced. Recall that in primary cultures Abramov et al.[43] see a significant increase ROS during OGD which seems in a sense

inconsistent with our observations on GSH. Funke et al.[147] compared the responses of roGFP1 (*i.e.,* the cytoplasm-resident redox responsive GFP with no Grx1) and HEt in primary cultures of hippocampal neurons/glia under various treatments. Indeed, while several treatments led to qualitatively equivalent responses from each sensor, *i.e.*, both indicating more oxidizing conditions or more reducing conditions, exposure to glutamate and (separately) uncoupling with FCCP showed opposite responses – more ethidium fluorescence but a more reduced roGFP. In this same work, a five-min exposure to anoxia led to the same gross changes in roGFP response as we observed though on a much slower timescale. Thus, we are in qualitative agreement with Funke et al.[147] who used the slower, less selective, cytoplasm-resident roGFP1. We conclude that the difference in the ethidium response seen by Abramov et al. and what we have detected during OGD is not likely due a technical issue. While certainly more work is required to understand the contrasting observations, the response of Grx1-roGFP2 may be dominated by increased reducing power during brief OGD rather than by the more oxidizing environment due to excess ROS. There are two contributions to increased reducing power. One is that the pH change from about 8 to about 7 as a result of IMM depolarization increases the difference in redox potentials of the $NADP^+$/NADPH and the GSH systems making the reduction of GSSG by NADPH more thermodynamically favorable (see Appendix A). In addition, the abundance of NADH from the absence of oxidative phosphorylation can lead to more NADPH production by transhydrogenase [73,170] and more GSH from GSSG.

During RP, we find a sharp change in the mitochondrial sensor to more oxidizing potentials. Abramov et al. see an increase in HEt fluorescence as well. This is consistent with the discussion above: the supply of reducing equivalents ultimately derived from fuel and then becoming NADH is a significant factor in mitochondrial GSH status. In the early stages of OGD,

without oxygen present, the mitochondrial matrix concentration of NADH should be relatively high, and during RP with the re-introduction of oxygen it should drop. Thus, the supply of NADPH for acting to reduce GSSG to GSH via glutathione reductase may dictate, at least qualitatively, the GSH system's status.

It is surprising not to find changes in cytoplasmic GSH during OGD/RP. Perhaps cytoplasmic GSH, which has a much larger antioxidant capacity than the mitochondrial GSH system[43,171], can maintain homeostasis when facing increases in ROS generation in the mitochondria and/or the cytoplasm[43]. It might be also reasonable to attribute the lack of response in the cytoplasmic GSH system during OGD/RP to the absence of cytoplasmic ROS. According to Abramov et al.[172], the cytoplasmic sources do not emerge until 25 min of OGD while our OGD time frame is only 20 min. On the other hand, during RP we would expect to see changes in the GSH system if indeed superoxide is being formed from NAD(P)H oxidase[172]. In summary, the time-dependence of the redox status of the GSH system provides new, and perhaps complementary information to that obtained by more classical fluorescence-based techniques. We find that during non-lethal OGD/RP, single CA1 pyramidal neurons show rapid changes in the GSH system in mitochondria during OGD/RP. The mitochondria become more reducing during OGD and more oxidizing during RP. The status of the GSH system is of course a steady state. It is possible that changes in the supply of reducing equivalents, not the supply of oxidizing equivalents, *i.e.*, ROS, is the dominant factor determining the redox status of the GSH system during OGD/RP.

2.4 CONCLUSION

We are not aware of ways to determine the redox status of the GSH system in real time other than by using protein-based sensors[159]. Herein, we choose to use Grx1-roGFP2, which is highly selective and sensitive to GSH system to monitor the redox change in OHSC during OGD-RP. In order to report OxD_{roGFP2} and E_{GSH} in tissue cultures during OGD-RP, we try to optimize our protocol in following aspects: 1) Due to the requirement on well control on pO_2 via superfusion in OGD-RP experiment, we try to optimize the superfusion setup to obtain high gas delivery and exchange efficiency. 2) With a proper transfection protocol, we are able to have a narrow distribution of neurons expressing roGFP2 sensor in depth in OHSC, which enable us to exert consistent experimental conditions on our objects, since we have observed that pO_2 level and transition time varies in different depths. 3) Deriving OxD_{roGFP2} and E_{GSH} requires correction on the fluorescent signal of Grx1-roGFP2, we, for the first time, introduce tdTomato, a redox insensitive fluorescent protein, for the aid to exclude the effect from cell morphology change, vibration, or other non-redox factor.

Our reliable report on OxD_{roGFP2} and E_{GSH}, showing that mitochondrial and cytoplasmic GSH system responds different to OGD-RP in hippocampal neurons, could be broadly applied to study on the systematic pharmacological experiments, like the inhibition assays on GSH related enzymes (e.g. glutathione peroxidase[46], glutathione reductase[46], γ-glutamylcysteine Synthetase[52], GSH synthase[50] and γ-glutamyltranspeptidase[52]), which will influence the GSH system.

2.5 ACKNOWLEDGEMENT

This work is supported by the NIH through grant R01 GM066018. We thank Dr. Zachary P. Wills (University of Pittsburgh) for technical assistance in gene gun transfection. Jihe Liu (University of Pittsburgh) made the plasmid for expressing mito-tdTomato.

3.0 GSH SYSTEM RESPONDS DIFFERENTLY WITHIN DIFFERENT CELL TYPES DURING OGD-RP

3.1 INTRODUCTION

ROS induced by antimycin-A severely inhibited the proliferation of HeLa cells via initiating apoptosis[173]. Imbalanced production of ROS[23-25] has been found to be the main cause of neuronal damage in stroke[1-3]. A proper amount of ROS plays a critical role in cell signaling such as signal transduction and neuronal transmitter releasing[26-31], but excess ROS will leading to short-term effects in cellular function, and longer-term changes that ultimately cause neuronal death[32-34]. Hypoxia/ischemia (HI) episodes, such as those that occur during stroke, disrupt ROS homeostasis in neurons and glial cells. In order to counter against the harmful oxidative stress cuased by ROS, the cells are endowed with mechanisms for maintaining ROS homeostasis. Glutathione (GSH) is an important antioxidant in both abnormal and normal cells for removing ROS generated during oxidative metabolism[52,81,174-179]. HeLa cells are found to have more ROS resistance by enhancing the expression of glucose-6-phosphate dehydrogenase (G6PD) which facilitates the restoration of GSH levels inside[180]. Many anti-tumor drugs are found to cause excessive ROS in HeLa cells that leads to the final cell death[181]. Overexpression of γ-glutamyl-transpeptidase (γGT), which utilizes GSH to create Cys-Gly, helps the survival of HeLa cells under the existence of platinum anti-tumor reagent, cisplatin, the function of which is inhibited by Cys-Gly[182]. Applying exogenous GSH helps to rescue the neurons from the ischemia insult by reducing the ROS generated[183]. Depletion of GSH in the mitochondria of rat cerebellar granule neurons causes neuronal death in 2 hours, but no such phenomenon is found by cytoplasmic GSH

depletion[184]. A more sustained activity of GSH in neurons is the promotion of cell survival by participating in beneficial enzymatically catalyzed reactions[185,186] like those of glutathione peroxidases (GPxs), glutathione S-transferases (GSTs).

The GSH system varies in different cell types. There are very few reports that we are aware of comparing the GSH system of HeLa cells and neuronal cells. HeLa cells show a more robust GSH synthesis system to replenish GSH back to normal levels than rat spleen lymphocytes by utilizing different sulfur amino acid sources, methionine, cysteine and cystine (the oxidized form of cysteine)[187]. The capacity of total GSH in HeLa cells is about 35 fold of that in rat spleen lymphocytes, and the activities of GSH-related enzymes are different in the two types of cells[187]. Astrocytes are found to be more resistant to OGD-induced ROS than pyramidal cells in primary cell cultures[45]. The consumption of H_2O_2 is much faster in astrocytes compared to neurons[47], which could be ascribed to the fact that the intracellular GSH level is higher in astrocytes than in neurons[46]. Astrocytes have a higher activity of glutathione peroxidase (GPx) which facilitates the reduction of ROS by GSH[46,47]. Accumulating evidence[46,48-52] shows that the primary function of astrocytes is to support neurons during ROS insult by maintaining the GSH level in neurons. Ringen et al.[52] proposed a mechanism about how astrocytes feed neuron with GSH: astrocytes release GSH, which is degraded to CysGly by γ-glutamyl-transpeptidase (γGT); then CysGly is uptaken by neurons and used to synthesize GSH inside. Griffin et al. [49] observed that astrocyte cells promote the survivability of neurons after OGD, in which primary cell cultures (neurons or astrocytes) were used. The intracellular GSH level was not affected in astrocytes only cell culture in the 24 h after OGD, but the GSH concentration dropped dramatically in astrocytes when they were co-cultured with neurons, especially with OGD-treated neurons[49]. Meanwhile, the GSH was observed to keep releasing into the culture medium in the 24 h after OGD in the co-culture of

neurons and astrocytes[49]. All of this evidence provided by Griffin et al.[49] directly supports Ringen et al.'s[52] mechanism.

Because oxidation of intracellular GSH leads to the disulfide GSSG and the GSH/GSSG couple is in a dynamic redox status, the redox state of the GSH/GSSH couple is an indicator of oxidative stress. ROS in real time could be measured by voltammetry[136-138,188] and fluorescence imaging with fluorogenic small molecule dyes[113,139-141]. The ROS management inside cells could be investigated through the prospective of its antioxidant pool, GSH system. However, there are not many practical ways to study the GSH/GSSG couples. The concentration of GSH or GSSG could be measured by 5,5′-dithio-bis-2-nitrobenzoic acid (DTNB) assay using spectroscopy or high-performance liquid chromatography (HPLC) with or without the existence of NADPH and glutathione reductase, but it is not practical or efficient for real-time measurement[189]. It is a breakthrough that roGFP1[147] and roGFP2[145] have been used to detect ROS in real-time, even though it is in a relative slow time scope. Real time GSH/GSSG redox status has not been monitored until that Meyer et al.[145] applied exogenous glutaredoxin (Grx) and roGFP2. Gutscher et al.[146] made a chimeric protein (Grx1-roGFP2) to facilitate the measurement of intracellular GSH/GSSG redox status. By now, there are rare reports investigating the GSH system in central neuron system (CNS) tissue. We applies the selective sensors, mito-Grx1-roGFP2[146] and cyto-Grx1-roGFP2[146], in which their advantages over other chemical ROS detecting dyes[113,139-141], and rxYFP[142] or roGFP based protein sensors (roGFP1[147], roGFP2[145]) has been discussed in Chapter 2. HeLa cells are a ubiquitous biological model used in research[190]. We used HeLa cells to test the Grx1-roGFP2 sensor and to help transfection optimizition, fluorescence imaging and calibration for calculation of redox information of GSH system in Chapter 2. In this chapter, HeLa cells were used as an abnormal-cell model, and expected to have different GSH system mediating ROS

homeostasis from normal neuronal cells (pyramidal cells and astrocytes) in OHSC during OGD-RP. The GSH system in mitochondria and cytosol were studied individually since their differences in mediating ROS have been found in rat cerebellar granule neurons[184].

We follow the protocol in Chapter 2 to treat Cells or OHSCs with OGD-RP in optimized superfusion system. Well-defined redox parameters ($R_{405/488}$, OxD_{roGFP2}, $\ln([GSH]^2/[GSSG])$ and E_{GSH}) are reported with Grx1-roGFP2's fluorescence intensity referenced by signal from tdTomato, and compared in six different biological models (two cell compartments × three cell types) as mentioned above.

3.2 EXPERIMENTAL SECTION

3.2.1 Cell and tissue preparation

HeLa cells were cultured and transfected with the plasmids for expressing tdTomato and Grx1-roGFP2 sensor (see Section 2.2.1.2 for more details). Organotypic hippocampal slice cultures (OHSC) were prepared by following Gogolla's protocol[153] from the postnatal 7-day old Sprague-Dawley rats (Charles River, Pittsburgh) with approval by the Institutional Animal Care and Use Committee (IACUC) of the University of Pittsburgh. tdTomato and Grx1-roGFP2 sensor were introduced into OHSC by biolistic transfection or single cell electroporation (see Section 2.2.1.3 for more details). Pyramidal cells (A.K.A. neurons) and astrocytes with tdTomato and Grx1-roGFP2 were found in the treated OHSC.

3.2.2 Ratiometric imaging and characterization of Grx1-roGFP2 in different cell types

Cells were imaged with an HCX PL FLUOTAR 5x objective lens with N.A. = 0.15 and an HCX APO L U-V-I water immersion 63x objective lens with N.A. = 0.90 on a Leica TCS SP5II broadband confocal microscope (Department of Biological Sciences, University of Pittsburgh).

Grx1-roGFP2 was excited at 405 or 488 nm and its emission intensity was acquired in a range of 500 – 530 nm. In Grx1-roGFP2, roGFP2 is the functional fluorescent subunit responding to redox change of GSH/GSSH couple, due to the change of the chromophore from its neutral form to anionic form[105,106]. The part of Grx1[132] is incorporated to accelerate the reaction between roGFP2 and GSH/GSSG couple when countering redox change and it dramatically boosts the response rate. The spectroscopic changes in roGFP at 405 and 488 nm excitation are quantitatively related, which allows them to be used to calculate OxD_{roGFP2} and E_{GSH} [105,106,120].

We examined the response of Grx1-roGFP2 in three different cell types (pyramidal cells, astrocytes in OHSCs and HeLa cells) and two different cell compartments (mitochondria and cytoplasm) in each cell type. I_{405} and I_{488} from Grx1-roGFP2 are firstly divided by I_{561} from tdTomato (normalized I_{405} and I_{488} are represented as $\hat{I}_{405}$ and $\hat{I}_{488}$, respectively). The ratios $\frac{\hat{I}_{405}^{max}}{\hat{I}_{405}^{min}}$ and $\frac{\hat{I}_{488}^{max}}{\hat{I}_{488}^{min}}$ are the dynamic range of channels of Grx1-roGFP2 excited at 405 and 488 nm respectively. $R_{405/488}$, $\frac{\hat{I}_{405}}{\hat{I}_{488}}$, is commonly used to represent the redox change of roGFP2 based sensor [105,106,119,132,191,192]. The ratio $\frac{R_{405}^{max}}{R_{408}^{min}}$ represents the dynamic range of the Grx1-roGFP2 sensor responding to the extreme oxidizing and reducing environment. $\hat{I}_{405}$ and $R_{405/488}$ increase with oxidation and decrease with reduction, but $\hat{I}_{488}$ changes in opposite to them. Thus we can find the maximum value of $\hat{I}_{405}$ and $R_{405/488}$ and minimum value of $\hat{I}_{488}$ from fully oxidized Grx1-roGFP2

sensor, but the minimum value of $\hat{I}_{405}$ and $R_{405/488}$ and maximum value of $\hat{I}_{488}$ from fully reduced Grx1-roGFP2 (Eq. 3.2, 3.4). The dynamic range of each single channel of Grx1-roGFP2, excited at 405 nm ($\frac{\hat{I}_{405}^{max}}{\hat{I}_{405}^{min}}$), 488 nm ($\frac{\hat{I}_{488}^{max}}{\hat{I}_{488}^{min}}$) and dynamic range of R, ($\frac{R_{405}^{\max}}{R_{408}^{\min}}$), are statistically analyzed among the six biological models, mitochondria and cytoplasm in HeLa cells, pyramidal cells and astrocytes in OHSC (Fig. 3-4). The calculations are shown in Equation 3.1-3.6.

$$\hat{I}_{405} = I_{405}/I_{561}, \hat{I}_{488} = I_{488}/I_{561} \quad \text{(Eq. 3.1)}$$

$$\hat{I}_{405}^{Ox} = \hat{I}_{405}^{\max}, \hat{I}_{405}^{Red} = \hat{I}_{405}^{\min}, \hat{I}_{488}^{Ox} = \hat{I}_{488}^{\min}, \hat{I}_{488}^{Red} = \hat{I}_{488}^{\max} \quad \text{(Eq. 3.2)}$$

$$R_{405/488} = I_{405}/I_{488} \quad \text{(Eq. 3.3)}$$

$$R_{405/488}^{\max} = R_{405/488}^{Ox};\ R_{405/488}^{\min} = R_{405/488}^{Red} \quad \text{(Eq. 3.4)}$$

$$DR_{405} = \frac{\hat{I}_{405}^{\max}}{\hat{I}_{405}^{\min}} = \frac{\hat{I}_{405}^{Ox}}{\hat{I}_{405}^{Red}};\ DR_{488} = \frac{\hat{I}_{488}^{\max}}{\hat{I}_{488}^{\min}} = \frac{\hat{I}_{488}^{Red}}{\hat{I}_{488}^{Ox}} \quad \text{(Eq. 3.5)}$$

$$DR_R = \frac{R_{405/488}^{\max}}{R_{405/488}^{\min}} = DR_{405} \times DR_{488} \quad \text{(Eq. 3.6)}$$

In which, I_{405}, I_{488} and I_{561} are fluorescence intensity excited at 405 and 488 nm of Grx1-roGFP2 and excited at 561 nm of tdTomato, respectively. $\hat{I}_{405}$ and $\hat{I}_{488}$ are Normalized I_{405} and I_{488} by I_{561}. $R_{405/488}$ is the ratio of $\hat{I}_{405}$ to $\hat{I}_{488}$. $\hat{I}_X^{Ox}$,$\hat{I}_X^{Red}$, $\hat{I}_X^{max}$, $\hat{I}_X^{min}$ are fully oxidized, reduced, maximum and minimum normalized fluorescence intensity at excitation X nm (405 or 488 nm), respectively. $R_{405/488}^{Ox}$, $R_{405/488}^{Red}$, $R_{405/488}^{max}$ and $R_{405/488}^{min}$ are fully oxidized, reduced, maximum and minimum $R_{405/488}$. DR_{405}, DR_{488} and DR_R are the dynamic range of channels 405, 488 and $R_{405/488}$ of Grx1-roGFP2.

The parameters, DR_{405}, DR_{488} and DR_R are compared among six biological models with one way ANOVA test (no significant difference, $p > 0.05$, *$p < 0.05$, **$p < 0.01$, ***$p < 0.001$, n=12).

In this work, numerical data were processed in MatLab (version R2012b, MathWorks, Inc.) and OrginPro (version 9.0, OriginLab Corp.). Statistical analysis was processed in R (www.r-project.org) and MatLab (version R2012b, MathWorks, Inc.)

3.2.3 Derivation of redox information from Grx1-roGFP2.

The fluorescent intensities of roGFP2 that excited at 405 nm and 488 nm are quantitatively related with its oxidized and reduced form, which allows the calculation of oxidation degree of the sensor, Grx1-roGFP2 (OxD_S) and the redox potential of glutathione (E_{GSH})[105,106,120].

Redox information of OxD_S, the natural logarithm of the ratio, $\frac{[GSH]^2}{[GSSG]}$ and E_{GSH} is derived from $R_{405/488}$, $\hat{I}_{405}^{Ox}$ and $\hat{I}_{405}^{Red}$ as shown below (Eq. 3.7-3.11).

.

$$OxD_S = \frac{R_{405/488} - R_{405/488}^{Red}}{\frac{\hat{I}_{488}^{Ox}}{\hat{I}_{488}^{Red}}\left(R_{405/488}^{Ox} - R_{405/488}\right) + \left(R_{405/488} - R_{405/488}^{Red}\right)} \quad \text{(Eq. 3.7)}$$

In which, $\hat{I}_{405}$, $\hat{I}_{488}$, OxD_S,$R_{405/488}$, $R_{405/488}^{Ox}$ and $R_{405/488}^{Red}$ have been defined above. The necessity to obtain $\hat{I}_{405}^{Ox}$ and $\hat{I}_{405}^{Red}$ by correcting I_{405} and I_{488} from Grx1-roGFP2 with I_{561} from tdTomato has been explicitly discussed in Chapter 2.0[79].

The Eq. 3.6 can be transformed into Eq. 3.7 as $R_{405/488}^{Ox}$ is normalized to 1 and $R_{405/488}$ is normalized to $R_{405/488}^{Ox}$.

$$OxD_S = \frac{R_{405/488} - \frac{1}{DR_R}}{\frac{1}{DR_{488}}\left(1 - R_{405/488}\right) + \left(R_{405/488} - \frac{1}{DR_R}\right)} \quad \text{(Eq. 3.8)}$$

In which, DR_{488}, DR_R, $R_{405/488}$ and OxD_S have been defined above.

The Nernst term, $\ln(\frac{[GSH]^2}{[GSSG]})$, can be derived from OxD_S.

$$\mathrm{In}\left(\frac{[\mathrm{GSH}]^2}{[\mathrm{GSSG}]}\right) = \mathrm{In}\left(\frac{1-\mathrm{OxD_S}}{\mathrm{OxD_S}}\right) + \frac{\mathrm{ZF}}{\mathrm{RT}}\left(\mathrm{E^O_{GSH}} - \mathrm{E^O_{roGFP2}}\right) \quad \text{(Eq. 3.9)}$$

In which, E^O_{GSH} [160] and E^O_{roGFP2} [106] are the standard redox potentials of glutathione and Grx1-roGFP2 at pH = 7.00 respectively; Z is the number of electrons transferred in the redox reaction; R is the gas constant; F is the Faraday constant; T is the absolute temperature. $E^O_{GSH} = -240\ mV$; $E^O_{roGFP2} = -280\ mV$; Z = 2; F= 96485 C/mol; R = 8.315 J·K^{-1}·mol^{-1}; T = 309.15 K.

The redox potential of the GSH/GSSG couple in mitochondria and cytoplasm is calculated from the known OxD_S. Different pH values in the two compartments are considered.

$$\mathrm{E^{Cyto}_{GSH}} = \mathrm{E^{pH=7}_{GSH}} = \mathrm{E^{pH=7}_{roGFP2}} = \mathrm{E^O_{roGFP2}} - \frac{\mathrm{RT}}{\mathrm{ZF}}\mathrm{In}\left(\frac{1-\mathrm{OxD_S}}{\mathrm{OxD_S}}\right) \quad \text{(Eq. 3.10)}$$

$$\mathrm{E^{Mito}_{GSH}} = \mathrm{E^{pH=8}_{GSH}} = \mathrm{E^{pH=7}_{GSH}} + \frac{\mathrm{RT}}{\mathrm{zF}}\mathrm{In}\left(\frac{[H^+]^2_{pH=8}}{[H^+]^2_{pH=7}}\right) = \mathrm{E^{Cyto}_{GSH}} - 61.3\ (\mathrm{mV}) \quad \text{(Eq. 3.11)}$$

In this equation, the same values of E^O_{GSH}, E^O_{roGFP2}, Z, F, R and T are used here; $[H^+]_{pH=8}$ = 10^{-8} mol L^{-1}, $[H^+]_{pH=7}$ = 10^{-7} mol L^{-1}.

3.2.4 OGD-RP experiment

HeLa cell cultures and OHSC were treated with OGD-RP (see Section 2.2.6 for more details), in which optimized superfusion system [O+V] (see Section 2.2.5 for more details) was applied. The purpose of these experiments is to investigate whether the GSH system responds

differently to OGD-RP in these six different biological models (two cellular compartments × three cell types: mitochondria and cytoplasm × HeLa cells, pyramidal cells and astrocytes).

3.3 RESULTS AND DISCUSSION

3.3.1 Expressing tdTomato and Grx1-roGFP2 sensor in HeLa cell culture and OHSC.

As shown in Fig. 3-1, 3-2 and 3-3, Grx1-roGFP2 and tdTomato are introduced into the HeLa cell culture and OHSC successfully. To transfect the HeLa cell culture, lipofectamine (Invitrogen) with plasmids were mixed to form a subtle positively charged complex, which could better fuse with negativly charged cell membrane, sequentially increasing the transfection efficiency[193]. Our recipe was modified based on the manufacture's protocol to minimize the toxicity to the HeLa cell culture. However, the lipofectamine aided transfection does not work on OHSCs according to our experience. The poor case could be due to the extremely low permeability of intense microglial[194] cell layer covering OHSC impeding the delivery of the lipofectamine/plasmid complex. We had to circumvent the microglia cell layer by using gene gun[195]. As shown in Fig. 3-2b, the gold particles fired with gene gun firstly penetrate through the glia cell layer, then get trapped somewhere beneath (~ 30 – 45 μm below[79] the very top of OHSC), and leave the loaded plasmid to its target, pyramidal cell or astrocyte. In order to study the GSH system in mitochondria and cytoplasm individually, mitochondrial targeting sequence[132] was tagged into the normal tdTomato[79] and Grx1-roGFP2[132] that was used for expression in cytoplasm to create their mitochondrial types. The distributions of tdTomato and Grx1-roGFP2 in mitochondria and cytoplasm are observable in Fig. 3-1 and 3-3.

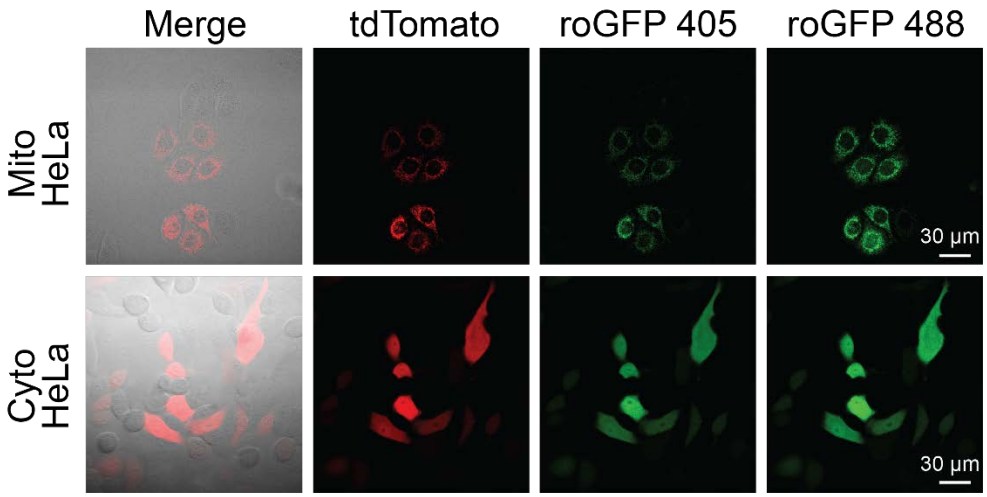

Figure 3-1. Transfection in HeLa cells.

Grx1-roGFP2 and tdTomato co-expressed in mitochondria or cytoplasm of HeLa cells. Images of merge (merge of bright field image and fluorescent image of tdTomato), tdTomato, 405 nm excitation of Grx1-roGFP2 and 488 nm excitation of Grx1-roGFP2 are shown from left to right.

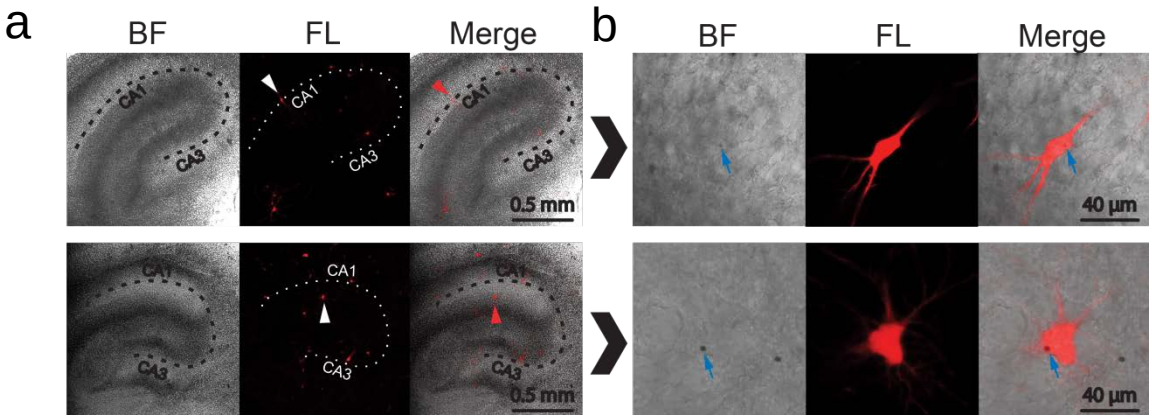

Figure 3-2. Transfection inside OHSC.

Plasmid coding for tdTomato is transfected into cells in OHSCs by gene gun. **(a)** Images are taken with a 5x objective lens to give bright field (BF), fluorescence (FL) and merged images from left to right. The dotted line indicates approximately the Cornu Ammonis (CA). Gene gun-enabled transfection in 10~15 cells per OHSC. Pyramidal cells or astrocytes expressing tdTomato are distributed randomly in OHSC. Cell highlighted by a white arrow in (a) is

imaged under 63x objective lens to show enlarged details in (b). **(b)** Pyramidal cells show a different pattern of alignment and cell shape than astrocytes. Gold particles (indicated by blue arrows) are found left in OHSC after using gene gun.

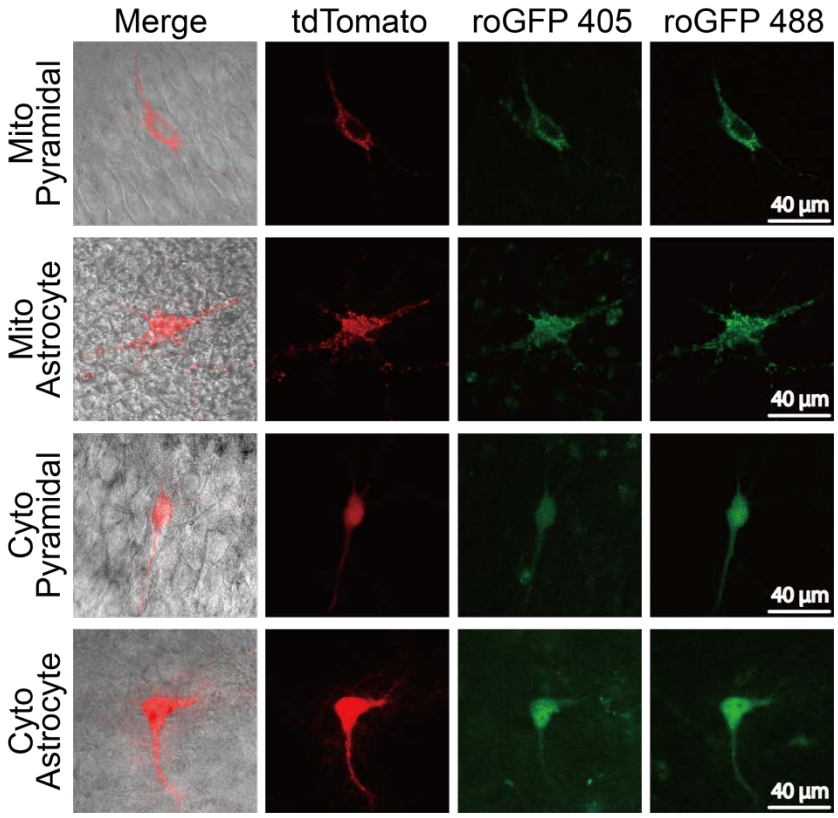

Figure 3-3. Co-expression of tdTomato and Grx1-roGFP2 in mitochondrial or cytoplasmic pyramidal cells and astrocytes and in OHSCs.

Grx1-roGFP2 and tdTomato co-expressed in mitochondria or cytoplasm in pyramidal cells or astrocytes in OHSCs. Images of merge, tdTomato, 405 nm excitation of Grx1-roGFP2 and 488 nm excitation of Grx1-roGFP2 are shown from left to right.

3.3.2 Characterization of Grx1-roGFP2 in six different biological models.

Before applying Grx1-roGFP2 to investigate the GSH system in six different biological models (two cell compartments × three cell types: mitochondria, cytoplasm × HeLa cells, pyramidal cells and astrocytes), we characterized the sensor to see whether its spectroscopic change would vary depending on the biological environment.

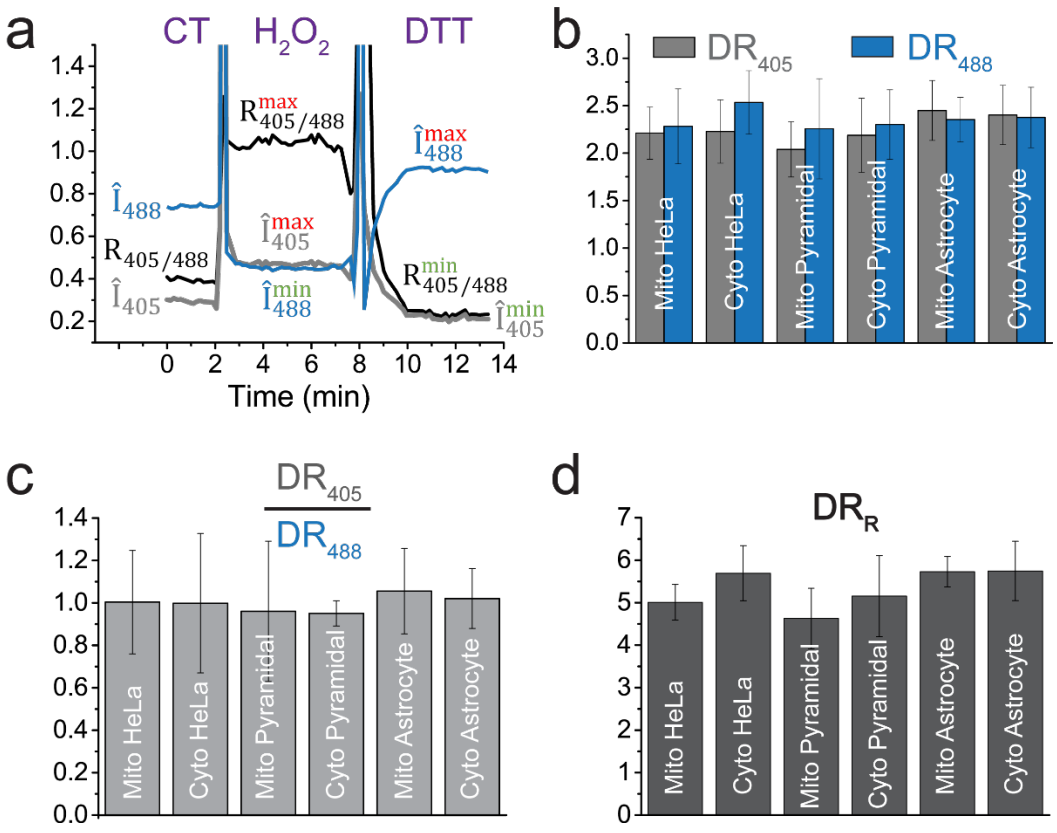

Figure 3-4. Characterization of Grx1-roGFP2 in different cell compartments and cell types.

Grx1-roGFP2 is expressed selectively in 6 biological models (2 cell compartments × 3 cell types; mitochondria or cytoplasm × HeLa cells, pyramidal cells or astrocytes in OHSCs). **(a)** A representative data set from Grx1-roGFP2 expressed in the cytoplasm of pyramidal cell. Cell or OHSC were treated with ACSF in control (CT), then calibrated with oxidant, H_2O_2 and reductant, DTT to reach full oxidation and full reduction. $\hat{I}_{405}$, $\hat{I}_{488}$ are fluorescence intensity from Grx1-roGFP2, exited at 405 nm and 488 nm and normalized by I_{561}, fluorescence intensity from tdTomato,

excited at 561 nm. $R_{405/488}$ is the ratio of $\hat{I}_{405}$ and $\hat{I}_{488}$. **(b)** DR_{405} and DR_{488} are the respective dynamic range of excitation channels, 405 and 488 nm, of Grx1-roGFP2, which are approximately 2.2 ($p>0.05$, n=12 for each case). There is no significant difference found between the two excitation channels **(c)** The ratios of DR_{405}/DR_{488} are ~ 1 ($p>0.05$, n=12 for each case). There is no difference among the 6 biological models. **(d)** DR_R (referred to as dynamic range of $R_{405/488}$) is ~5 ($p>0.05$, n=12 for each case) and similar in the 6 different biological models. Data are shown in mean ± SEM and statistically analyzed by student's t test or one-way ANOVA test. There is no special mentions or labels when there is no significant difference found. All of the terms shown in the figure are defined in Eq. S1 – S6 in Supporting Information.

As represented in Fig. 3-4a, cell culture or OHSC was treated with ACSF, then calibrated sequentially with H_2O_2 and DTT. I_{405} and I_{488} of Grx1-roGFP2 was calibrated by I_{561} from tdTomato, and represented as $\hat{I}_{405}$ and $\hat{I}_{488}$, respectively (Eq. 3.1). It is necessary to make this correction since several confounding factors distort I_{405} and I_{488}, such as the vibration introduced by continuous superfusion during OGD-RP and the noticeable cell-volume changes during H_2O_2 and DTT calibration after OGD-RP experiment (fully discussed in Chapter 2.0[79]). $\hat{I}_{405}$ and $\hat{I}_{488}$ change oppositely, and $R_{405/488}$ changes in the same trend as $\hat{I}_{405}$. $\hat{I}_{405}^{max}$, $R_{405/488}^{max}$ and $\hat{I}_{488}^{min}$ are acquired with H_2O_2 treatment, and $\hat{I}_{405}^{min}$, $R_{405/488}^{min}$ and $\hat{I}_{488}^{max}$ are acquired with DTT treatment. We compared the dynamic range of channel 405, 488 and $R_{405/488}$ of Grx1-roGFP2 (DR_{405}, DR_{488} and DR_R) in the six different biological system and found that all of the terms are not significant different in the tested models (Fig. 3-4b, d). The GSH system varies in different cell types. HeLa cells have stronger capability in synthesizing GSH by utilizing different sulfur amino acid sources (e.g. methionine, cysteine and cysteine) and maintaining much higher GSH level than normal cells such as rat spleen lymphocytes[187]. Astrocytes contain higher intracellular GSH level than neurons[46]. Apparently, the dynamic change of spectrum of Grx1-roGFP2 will not vary with the different GSH levels in HeLa cells, pyramidal cells and astrocytes according to our observation.

The concentration of mitochondrial GSH (mGSH) is similar to that of cytoplasmic GSH (cGSH)[23], but pH is different in mitochondria and cytoplasm[196]. $R_{405/488}$ of Grx-roGFP2 is not sensitive to pH[120]. We also observed that neither DR_{405}, DR_{488} nor DR_R influenced by pH. All of the data in Fig. 3-4 convinces us that the same equation (Eq. 3.8) could be used to derive OxD_S from $R_{405/488}$ in all six tested biological models because the rest of terms, DR_{488} and DR_R in Eq. 3.8 are measured to be constant. Grx1-roGFP2 is verified to be a proper sensor for the redox change of GSH system, which is not influenced by the complex cellular environments differing in many factors such as GSH level and pH.

3.3.3 HeLa cells, pyramidal cells and astrocytes in OHSCs respond differently to OGD-RP.

As shown in Fig. 3-5, the redox terms, OxD_S, $\ln\frac{[GSH]^2}{[GSSG]}$ and E_{GSH} derived from $R_{405/488}$ are obtained from mitochondria and cytoplasm of HeLa cells, pyramidal cells and astrocytes. All of the terms change in a similar trend during OGD-RP, and the values of the redox terms show the similar relationship among HeLa cells, pyramidal cells and astrocytes. In general, larger redox terms represent more oxidized GSH system, and smaller redox terms indicate more reduced GSH system. We found that mitochondrial or cytoplasmic OxD_S are not significant different among HeLa cells, pyramidal cells and astrocytes, but the sensor in the mitochondria is more oxidized than that in the cytoplasm under normal condition (mito: HeLa/Pyra/astro, 0.238 ± 0.046/0.205 ± 0.064/0.229 ± 0.061; cyto: HeLa/Pyra/astro, 0.103 ± 0.006/0.074 ± 0.030/0.065 ± 0.028; mean ± SEM, n=6; CT). Basically, we found larger $R_{405/488}$ and $\ln\frac{[GSH]^2}{[GSSG]}$ in mitochondria under normal conditions. In contrast, E_{GSH} in mitochondria is more negative than that in cytoplasm under normal

conditions (Fig. 3-4, Table. C-1) because the pH difference will shift E_{GSH} by -61.3 mV from cytoplasm to mitochondria even with the same OxD_S (Eq. 3.11). Our data is consistent with the OxD_S and E_{GSH} in HeLa cells reported via rxYFP [197] (OxD_S: mito/cyto, ~ 0.22/~ 0.05; E_{GSH}: mito/cyto, ~ -345mV/~ -345 mV). We did not report the degree of oxidation of the GSH/GSSG couple (OxD_{GSH} = 2[GSSG]/(2[GSSG]+ [GSH])) in this work because that we do not know the accurate concentration of mGSH and cGSH in different cell types. However, with reasonable assumption about mGSH = cGSH ≈ 10 mM[23], our values of these redox terms correspond to a very small degree of oxidation of the GSH/GSSG couple (OxD_{GSH}: mito/cyto, ~5×10^{-4}/~1×10^{-4}) indicating that the majority of GSH (> 99%) exist as its reduced form in different cell types under normal conditions[159].

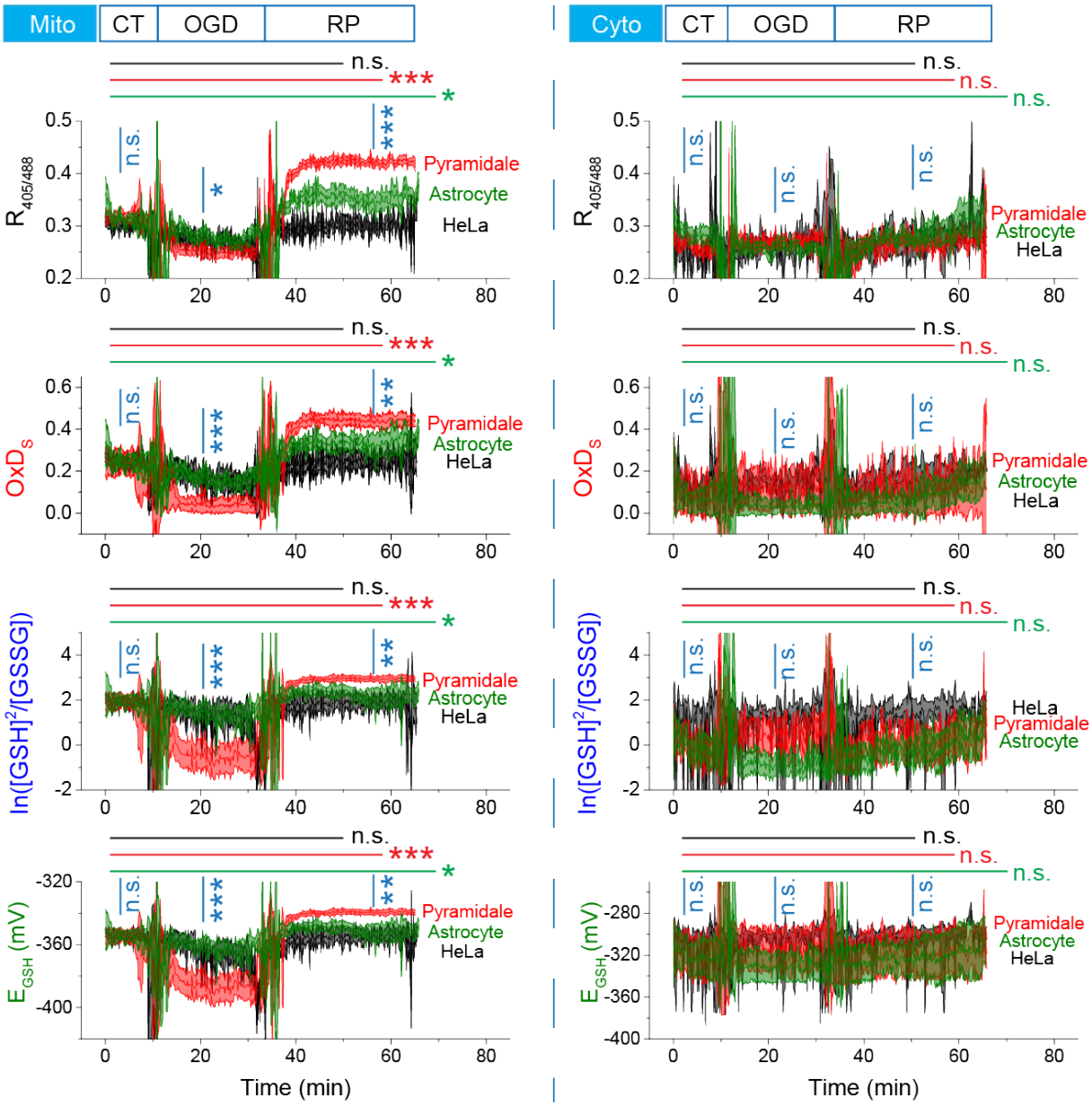

Figure 3-5. GSH systems in variable biological models respond differently to OGD-RP.

Cells or OHSCs were sequentially treated with 10 min control/20 min OGD/30 min RP followed with H_2O_2 and DTT calibration (Data portion for H_2O_2 and DTT calibration are not shown here). Superfusion setup [O+V] described in Figure 2-1 is used. Fluorescence signals from mitochondrial or cytosolic Grx1-roGPF2 and tdTomato were measured. $R_{405/488}$, OxD_{roGFP2}, $ln([GSH]^2/[GSSG])$ and E_{GSH} were calculated from 405 nm, 488 nm and 561 nm signals. $R_{405/488}$ at the fully oxidized period is normalized to 1. OxD_{roGFP2}, $ln([GSH]^2/[GSSG])$, E_{GSH} were calculated from fluorescence signal at excitation 405 and 488 nm of Grx1-roGFP2 with calibration of I_{561} of tdTomato (see Section 2.2.3 for more details). Mean ± SEM for six separate experiments are shown in each subplot. Statistical analysis was applied to

compare among the different cell types at each period during OGD-RP (indicated by blue vertical line with relative blue result symbol), or compare among the different periods of OGD-RP in each biological model (indicated by horizontal line with relative result symbol) with ANOVA analysis (n.s., no significant difference, $p > 0.05$, *$p < 0.05$, **$p < 0.01$, ***$p<0.001$). Data traces, symbols, labels, and lines for HeLa cells, pyramidal cells and astrocytes are colored by black, red and green, respectively.

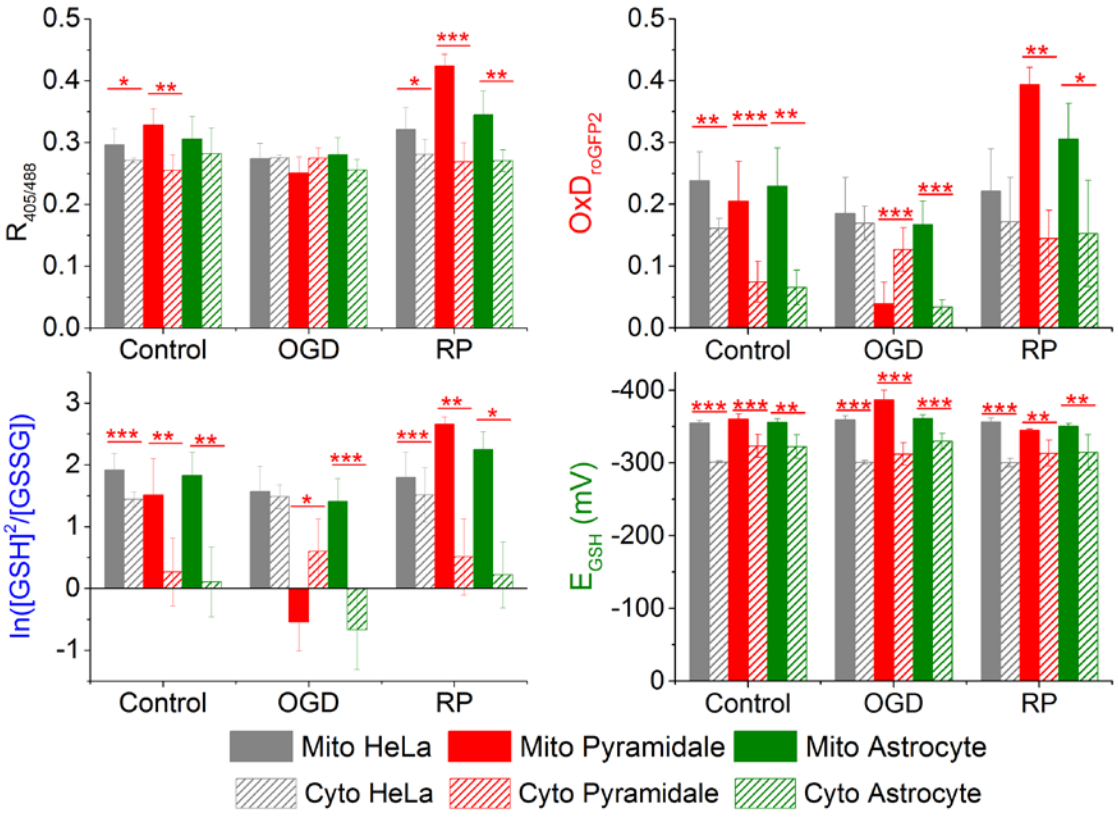

Figure 3-6. GSH systems respond differently in mitochondria and cytoplasm.

Mitochondrial and cytoplasmic GSH systems have a different redox status and response to OGD-RP in three cell types, HeLa cells, pyramidal cells and astrocytes. Steady state values of $R_{405/488}$, OxD_{roGFP2}, $\ln([GSH]^2/[GSSG])$ and E_{GSH} in control, OGD and RP are represented as mean ± SEM in the plots (n=6). Their full data traces in OGD-RP

are shown in Figure 3-5. A one way ANOVA was applied to compare mitochondria and cytoplasm (*$p<0.05$, **$p<0.01$, ***$p<0.001$, n=6). There is no special mentions or labels when there is no significant difference found.

There is no change to the time-dependent redox terms from the cytoplasm during OGD-RP, and the cGSH system performs similarly in HeLa cells, pyramidal cells and astrocytes (Fig. 3-5 (Right)). In contrast, mGSH system changes dramatically in pyramidal cells and astrocytes even though no obvious change is found in the mitochondria of HeLa cells. All of the redox terms differ between mitochondria and cytoplasm in our six biological models under various pathological conditions (Fig. 3-6) indicating the presence of intrinsic differences in their GSH system. In theory, OxD_S, $\ln\frac{[GSH]^2}{[GSSG]}$ and E_{GSH} are balanced by internal ROS generation and reducing power by NADPH[81]. Three sources of ROS were discovered in the investigation of ROS generation in hippocampal neurons during 40 min OGD- 20 min RP conducted by Abramov et al.[43]. According to his observation, the first ROS production occurred at 10-20 min of OGD origins from the mitochondria membrane depolarization, and the additional ROS produced by cytoplasmic xanthine/xanthine oxidase system did not happen until 25 min from the onset of OGD. ROS produced in RP with participation of NAD(P)H oxidase were found both in the mitochondria and the cytoplasm[43]. As pointed out by Abramov et al.[43], the absence of cytoplasmic ROS during 20 min OGD could result in the lack of response of cGSH in our time frame of OGD. To our surprise, we also observed no change of cGSH during RP. A reasonable explanation for this could be that cGSH has enough antioxidant capacity to maintain its oxidation status when facing ROS generated in RP. In contrast to cGSH, mGSH systems in OHSCs (pyramidal cells/astrocytes) respond to the ROS generated in OGD and RP in different ways. mGSH becomes more reduced in OGD, but more oxidized in RP compare to CT. One rational explanation for our observation is that the redox

status of mGSH is regulated mainly by the increased reducing power of NADPH in OGD, but mainly by increased ROS in RP. NADPH is abundant during OGD since it is well maintained (via transhydrogense[73,170]) by NADH, the consumption of which is inhibited due to the absence of oxygen[198]. During RP, the consumption of NADH is resumed, and NADPH is continuously being utilized to replenish reduced GSH[81] and other thiols[82]. The reduction of GSSG by NADPH to produce more mGSH is favored and un-favored in OGD and RP, respectively. In theory, increased proton concentration in mitochondria, $[H^+]_{mito}$, facilitates this reduction (Eq. A1-A6, see Appendix A for more details). The presence of rapid mitochondria membrane (MM) depolarization[166,168,169] evoked during OGD brings up the $[H^+]_{mito}$, while the MM hyperpolarization[199] after RP brings down the $[H^+]_{mito}$. mGSH in RP gets more oxidized due to the increase ROS production and compromised reducing power of NADPH in mitochondria, while opposites changes of mGSH, ROS and NADPH occur in OGD[43,73].

We believe that the different behaviors of mGSH in HeLa cells, pyramidal cells and astrocytes are attributed to the presence of differences in their mitochondria from various aspects. In rat cortical slice, unlike neurons, astrocytes do not exhibit MM depolarization after launching the spreading depression (a spreading MM depolarization), which often occurs in stroke [200]. Campanella et al.[201] observed that inhibitor factor 1 (IF1) is a critical protein for determining the tendency of MM depolarization (more IF1, easier depolarization). The mechanism behind it is complicated. In brief, $[H^+]_{mito}$ is maintained lower than $[H^+]$ outside mitochondria ($[H^+]_{OM}$). The proton gradient (AKA, MM potential) is built up by the continuously outward flow of $[H^+]_{mito}$ powered by electron transfer flow from NADH. The protein gradient can be dissipated by the inward flow of $[H^+]_{mito}$, which powers the ATP generation at F_1F_0 ATP synthase in mitochondrial respiration[201]. When the respiration halts, the original outward flow of $[H^+]_{mito}$ is no longer been

powered, and the original inward flow of $[H^+]_{mito}$ is inverted since F_1F_0 ATP synthase converts into F_0F_1 ATPase to consume ATP and pump $[H^+]_{mito}$ out of mitochondria [201]. IF1, the F_0F_1 ATPase inhibitor, stops the inversion of the original inward flow of $[H^+]_{mito}$ and allows the proton gradient to dissipate[201]. Campanella et al.[201] treated different cell types with 1 mM NaCN (an efficient inhibitor of cellular respiration) and monitored their MM potential. In their experiment, FCCP, an uncoupler, was used to induce 100% MM depolarization. Mitochondria in pyramidal cells depolarized up to 90% in 15 min, but astrocytes showed much smaller MM depolarization (~ 40%) in 15 min, due to higher IF1 in neurons (vs. astrocytes). Incredibly, HeLa cells showed more stable MM potential in that their mitochondria only depolarized by ~13 % in 15 min with low concentrated IF1 compare to pyramidal cells and astrocytes[201]. As mentioned above, increased $[H^+]_{mito}$ in MM depolarization during OGD favors the reduction of mGSH by NADPH. The tendency towards MM depolarization (pyramidal cells > Astrocytes > HeLa cells) is responsible for our observation of the reduction extent of mGSH in the same order (pyramidal cells > Astrocytes ≈ HeLa cells) during OGD (Fig. 3-5 (left)).

HeLa cells have a much lower oxygen consumptions rate in mitochondria (mOCR) compared to cortical primary neuron under normal condition[202]. Upon the MM potential dissipated by FCCP, mOCR increases and ATP generation decreases dramatically in neurons, but mOCR and ATP generation are not affected in HeLa cells[202]. This demonstrates that oxygen dependent ROS generation in compromised mitochondria is higher in neurons compare to HeLa cells. Pyramidal cells in mice are reported to have earlier and more rapid generation of mROS compared to astrocytes after the insult of transient forebrain ischemia[203]. Considering the larger heterogeneity between HeLa cell and rat hippocampal cells than that between different hippocampal cell types (pyramidal cells, astrocytes), we believe that mROS generation ranks in an order (pyramidal cells

> Astrocytes > HeLa cells), which is similar to the order of the oxidation status of mGSH (larger → smaller) during RP (Fig. 3-5 (left)).

The various concentrations of total GSH also corresponds to the variation of redox status of mGSH. HeLa cells have much higher GSH than normal cells (various cell types other than hippocampal cells)[187,204]. After comparing their data of hippocampal neurons with Dooley et al.'s[106] data of HeLa cells, Funke et al.[147] concluded that ROS generation is much easier and more rapid in hippocampal neurons because of their less capable anti-oxidant system. Astrocytes are higher in GSH than pyramidal cells[46]. It is reasonable to rank the GSH concentration in the sequence, HeLa cells > astrocytes > pyramidal cells. Their relative GSH pool size contributes to their relative redox response (smallest in HeLa cells, modest in astrocytes, largest in pyramidal cells) both in OGD (reduction in mGSH) and RP (oxidation in mGSH).

3.4 CONCLUSION

In summary, unobservable OGD-RP induced change in cGSH in any cell type was due to the absence of ROS in cytoplasm during 20 min OGD. cGSH remained well-maintained when facing RP-induced ROS. mGSH showed opposite redox changes in OGD and RP because 1) the reduction of GSH by NADPH is favored in MM depolarization in OGD, but disfavored in MM hyperpolarization in RP; and 2) the oxidizing power by ROS cannot beat the reducing power in OGD, but dominates in RP. The different tendency of MM depolarization (pyramidal cells > astrocytes > HeLa cells) dictate the different mGSH reduction degrees (pyramidal cells > astrocytes > HeLa cells) in OGD. In theory, ROS production and GSH pool size exert opposite impacts on the redox status of GSH. It is very impressive that the opposite tendency in ROS

production (pyramidal cells > astrocytes > HeLa cells) and order in GSH pool size (pyramidal cells < astrocytes < HeLa cells) enhance their overall influence on mGSH oxidation in RP (pyramidal cells > astrocytes > HeLa cells).

3.5 ACKNOWLEDGEMENT

This work is supported by the NIH through grant R01 GM066018. We thank Dr. Zachary P. Wills (University of Pittsburgh) for technical assistance in gene gun transfection. Jihe Liu (University of Pittsburgh) made the plasmid for expressing mito-tdTomato. Tom Harper (University of Pittsburgh) provided technical support for imaging on the confocal microscope.

4.0 THE DIFFERENTIAL SUSCEPTIBILITY BETWEEN CA1 AND CA3 PYRAMICAL CELLS TO OGD-RP DUE TO THEIR DIFFERENCE IN ROS MANAGEMENT

4.1 INTRODUCTION

Observations on the brains of patients suffering from transient global ischemia in the 1980s demonstrated that the hippocampus was more vulnerable than other regions so that cell death was high in that region.[205,206] The phenomenon that pyramidal cells in CA1 have much higher cell death after ischemia than in CA3 in organotypic hippocampal slice cultures (OHSC) was observed decades ago[53,207], and has not yet been fully understood. As early as 1962, a 43 year-old woman suffered from transient ischemia induced by anesthetic during surgery and she died 23 months later[208]. Her hippocampus was found to have more cell loss in CA1 than other CA areas[208]. A famous ischemia case about a patient (R.B.) was reported in 1986[207]. Histological examination after his death showed that the hippocampal lesion was found in CA1, not in CA3[207]. Selective vulnerability to transient global cerebral ischemia had been found in animal experiments. More damage in CA1 than CA3 was found in rat[209,210] and gerbils[211]. A latest study reported in 2015 by using magnetic resonance imaging shows that the selective neuronal damage in hippocampal CA1 after the global ischemia is consistently found in 50 patient cases[212].

Different concerns including Ca^{2+} mediated mechanisms[213,214] and oxidative stress exerted by reactive oxygen species (ROS)[54] are ascribed to the regionally selective vulnerability in OHSC to ischemia. The intracellular Ca^{2+} concentration is regulated by Ca^{2+} permeable N-methyl-D-aspartate (NMDA) receptor and α-amino-3-hydroxy-5-methyl-4-isoxazolepropionic acid (AMPA)

receptor. Both receptors are therapeutic targets to relieve ischemia induced cell damage[214]. Hippocampal lesions after ischemia also can be alleviated when excessive ROS are depressed[215]. The excessive generation of ROS is concomitant with the elevation of Ca^{2+} [213,216]. Both increases of Ca^{2+} and ROS are found to be larger in CA1 than in CA3 under the insults such as ischemia[217-219] and glutamate/NMDA[213,214,216].

Excessive generation of ROS is a critical threat to cellular redox homeostasis during ischemia[215]. Mitochondria with excessive ROS levels undergo membrane depolarization and structural damage[213], accompanied by the release of cytochrome c[220], which triggers a cascade of events with caspase 9 and caspase 3 involved[220], leading to necrosis. In cerebral ischemia, ROS also target the DNA repair enzymes[215], and activate nuclear factor-κB (NF-κB)[221] inducing the expression of pro-oxidant enzymes and functional proteins, such as cyclooxygenase-2 (COX-2, EC 1.14.99.1)[222], metalloproteinase (EC 3.4.24.77)[223] and cytokines[224], which provoke an inflammatory response and propagate the formation of additional ROS leading to neuronal death[221].

There are two particular types of ROS, superoxide and H_2O_2[35]. Superoxide in mitochondria is produced by transferring an electron from NADH to oxygen molecule at NADH:ubiquinone oxidoreductase (complex I, EC 1.6.5.3)[225]. H_2O_2 in mitochondria is converted from superoxide via manganese superoxide dismutase (MnSOD, EC 1.15.1.1)[75]. The mechanism for the generation of superoxide and H_2O_2 is different in cytosol, in which superoxide is formed at xanthine oxidase (EC 1.17.3.2)[76] , and then degraded into H_2O_2 via copper, zinc, superoxide dismutase (CuZnSOD, EC 1.15.1.1)[75].

It is promising to address the importance of the antioxidant systems against ROS to interpret the differential cell death between CA1 and CA3 after ischemia. There are two critical

types of antioxidants in cells, glutathione (GSH)[58-61], a tripeptide, and thioredoxin (Trx), a small 12 kD protein[62-64] (Trx2 is the special type of Trx in mitochondria[226]). GSH and Trx are oxidized while scavenging H_2O_2 via the enzymes, glutathione peroxidase (Gpx, EC 1.11.1.9) [81] and peroxiredoxin (Prx, EC 1.11.1.15)[82], respectively, and are regenerated by NADPH via glutathione reductase (GR, EC 1.8.1.7)[81] and thioredoxin reductase (TrxR, EC 1.8.1.9)[82], respectively. There are other antioxidants that are not enzymes such as ascorbate, vitamin E, carotenoid, flavonoids and selenium[227]. SOD and catalase are claimed to be enzymatic antioxidants to remove superoxide and H_2O_2 (cytosol only), respectively[227]. Of course, SOD is also a ROS generator since it generates H_2O_2 from superoxide[75]. There are is disagreement about the estimate of the relative contributions of the GSH and Trx systems to depress pathological ROS. Mitozi et al.[228] claim that the glutathione system is superior in decomposing hydrogen peroxide with their assays in which separate inhibition of glutathione reductase and thioredoxin reductase were tested in acute hippocampal slices. Meanwhile, Kudin et al.[229] observed a completely different result indicating that the Trx system outperforms the GSH system in H_2O_2 removal.

Wang et al.[54-56] attempted to decipher the mechanism leading to differential vulnerabilities to oxidative stress in CA1 and CA3 by collecting mRNA profiles from several oxidative stress-related enzymes and proteins. They found that both ROS generating proteins (e.g. superoxide dismutase (SOD, EC 1.15.1.1) [230], xanthine oxidase (EC 1.17.3.2)[231]) and ROS depressing proteins (e.g. Gpx, Nuclear factor E2-related factor 2 (Nrf2)[232], NAD(P)H: quinone oxidoreductase 1 (Nqo1, EC 1.6.5.2)[233]) present higher mRNA levels in CA1 than CA3, but mRNA levels for Trx and TrxR (which are anti-oxidants) were found not to be significantly different between CA1 and CA3 under normal conditions[55]. The mRNA levels of Nqo1 are consistently higher in CA1 after different exposure times to duroquinone (a superoxide generator)[56]. Wang et al. did not clarify the

rationale of the co-existence of higher ROS generation and higher expression of antioxidant genes in CA1. Instead, they stated that the higher mRNA levels of antioxidant genes (e.g. *Nrf2* and *Nqo1*) correspond to the demand of scavenging higher ROS concentrations[54-56]. It is clear that more work is required to understand the ROS generating and antioxidant systems, and not just at their transcriptional level. It is more promising to address the real-time activities of critical metabolites and proteins (oxidants and antioxidants) that participate in ROS management in order to find the reasons for different responses to the ischemia in CA1 and CA3.

Here, we focus on the NAD(P)H, superoxide, H_2O_2, GSH and Trx systems to investigate their respective contributions to the marked difference in ROS management between pyramidal cells in areas CA1 and CA3 in oxygen-glucose deprivation/reperfusion (OGD-RP, an *in vitro* ischemia model[234,235]). NAD(P)H was directly monitored with two photon imaging[94], and H_2O_2 and the GSH system were assessed by using roGFP2-based redox sensors[119,132] with confocal fluorescent imaging during OGD-RP,. There are no reliable protocols to monitor either superoxide or Trx by fluorescence imaging, but we designed particular experiments to indirectly monitor their activity by using the H_2O_2 and GSH sensors. ROS generation and removal were studied with a combination of stimulation and inhibition assays. Related protein levels in CA1 and CA3 were compared by Western blots (WB) and immunofluorescence (IF). Our data demonstrate that during the fifty minute OGD-RP, H_2O_2 and GSH changes are confined to the mitochondria. Compared to CA1, pyramidal cells in CA3 have a greater reducing capability because of having a larger pool of Trx2. This is the main reason that CA3 is more resistant to OGD-RP than CA1.

4.2 EXPERIMENTAL SECTION

4.2.1 Chemicals and reagents

All chemicals are purchased from Sigma Aldrich and used as received. Tryptone and yeast extract are from BD bioscience.

Various redox sensors based on roGFP2 construct including Mito-Grx1-roGFP2[132], Cyto-Grx1-roGFP2[132], Mito-roGFP2-Orp1[119], Cyto-roGFP2-Orp1[119] were obtained from Tobias P. Dick as generous gifts, pCMV-tdTomato[236] (Clontech) and pCS2+[155] (Addgene) were kindly provided by the Wills lab (University of Pittsburgh). pMito-tdTomato was constructed in the Deiter lab (University of Pittsburgh): the full-length sequence of tdTomato was amplified from pCMV-tdTomato using primers 5'-AGT GGT CTC AGT GAG CAA GGG CGA GGA GGT C-3' and 5'-ATT GGT CTC TCA TGG TGG CGA CCG GTG GAT C-3'. The mitochondria-targeting-sequence from ATP synthase protein 9 was amplified from Mito-Grx1-roGFP2[132] using primers 5'-ATT AGG TCT CAC ATG GCC TCC ACT CGT GTC CTC GCC TC-3' and 5'-ATT AGG TCT CAT CAC GGA TCC GGA AGA GTA GGC GCG CTT C-3'. Two fragments were assembled to construct pMito-tdTomato by using the Golden Gate Cloning method[152]. One Shot TOP10 Chemically Competent E.Colis (Invitrogen) was used to amplify plasmids. The final plasmid solution was purified with QIAGEN Plasmid Prep Kit (Qiagen), dissolved in 10 mM Tris·HCl + 1 mM EDTA solution (pH = 8.0).

Opti-MEM and HBSS were purchased from Invitrogen. The tissue dissection media contained 75%(v/v) Opti-MEM, 25%(v/v) HBSS with the addition of 45% D-glucose solution (1mL per 100 mL medium). The tissue culture media was made from 50% (v/v) Opti-MEM, 25% (v/v) HBSS, 25% (v/v) horse serum (Invitrogen) with the addition of 45% D-glucose solution

(1mL per 100 mL medium). Intracellular solution (IS) consists of 145 mM K-gluconate, 10 mM HEPES, 14 mM phosphocreatine, 4 mM Mg-ATP, 2 mM $MgCl_2$, and 0.25 mM EGTA, adjust to pH = 7.3 with KOH. Artificial cerebrospinal fluid[162] (ACSF) was composed of 125 mM NaCl, 2.5 mM KCl, 1.25 mM NaH_2PO_4, 25 mM $NaHCO_3$, 10 glucose, 1 mM $CaCl_2$, 4 mM $MgCl_2$, 10 mM glucose. Modifed ACSF (MACSF) substituted 10 mM glucose with 10 mM sucrose.

1.6 µm gold nanoparticles and other accessories used for biolistic transfection[154] were purchased from Bio-Rad Laboratories, Inc. Thiol probe IV[129] was obtained from Invitrogen, dissolved in anhydrous DMSO at 5 mM, stored at -80^{o}C and protected from light. Menadione stock solution was made in anhydrous DMSO at 25 mM, and stored in a dark place at -80^{o}C. Auranofin DMSO stock solution was made by dissolving 10 mg of gold salt into 2 mL DMSO, and was protected from light and store at -80^{o}C. MnSOD mimic ($MnSOD_m$), MnTnBuOE-2-PyP5+[237], was obtained from Ines Batinic-Haberle (Duke University Medical Center) in 5.31 mM aqueous solution, stored at 4 ^{o}C, and protected from light. All of the stock solutions were diluted in ACSF solution to the desired working concentrations.

4.2.2 OHSC preparation and transfection

Organotypic hippocampus slice culture (OHSC) were prepared by following the modification of Gogolla's protocol[153]. The surgery protocol was approved by the Institutional Animal Care and Use Committee (IACUC) of the University of Pittsburgh. Surgery was performed in a sterilized hood. The postnatal 7-day old Sprague-Dawley rats (Charles River, Pittsburgh) were decapitated and the hippocampus was harvested and chopped into slices on a McIlwain tissue chopper (Mickle laboratory Engieering Company Ltd., UK). The slices were first healed in tissue

dissection medium at 4 ºC for at least 30 min, and then plated onto Millicell organotypic inserts (Millipore Co.). Tissue culture medium was used to nourish the tissue and was replaced every 2-3days. Tissue was used after incubating for 5 days.

Either biolistic transfection[154] or single-cell electroporation[156] can be applied to transfect cells in OHSCs. A Helios Gene Gun (Bio-Rad Laboratories, Inc. CA, USA) was used following the Woods[154] protocol. 20 μg roGFP sensor[119,132] + 10 μg tdTomato + 20 μg pCS2+ as DNA filler[155] was loaded onto 14 mg of gold particles (Φ = 1.6 μm) for 40-50 bullets, which were fired toward the OHSC at 120 PSI.

Single cell electroporation on OHSCs was performed based on Haas's[156] procedure. 0.3 μg/μL (total plasmid concentration) plasmid dissolved in IS was used here. The plasmid was added in a weight ratio of 2:1:2, roGFP contruct vs. tdTomato vector vs. pCS2+. Pyramidal cells in OHSC were electroporated with a train of pulses (1 ms pulse width, -50 V voltage, 200 Hz frequency, last for 1s) through a pulled borosilicate glass pipette (18 MΩ after filled plasmid solution, tip size, 1-2 μm). Borosilicate glass tubing, OD x ID x L, 1.5 mm x 0.86 mm x 10 cm (Sutter Instrument Co. CA, USA) was pulled on P-97 micropipette puller (Sutter Instrument Co. CA, USA). Electroporation on OHSCs was performsed under a ZEISS Axioskop FS microscope (Zeiss, Germany) with X7500 micromanipulator (Siskiyou Co. OR, USA). It took 2-3 days to observe the expression of fluorescent protein in OHSC.

4.2.3 OGD-RP experiment in superfusion system

OHSCs were placed in a homemade stage chamber, and perfused with buffer solution at a flow rate of 4 mL/min driven by a peristaltic pump (Sci-Q 400DM2, Watson-Marlow, Inc. MA). One input tube and one output tube were used to fill the stage chamber with ~3 mL flowing buffer

solution, and one vacuum pump (KNF Neuberger. Inc.) was used to rapidly remove solution if needed. The solution flow rate was set to 4 mL /min. A TC-324B temperature controller and a SH-27B inline solution heater (Warner Instruments, LLC.) were used to maintain the solution temperature at 35^{o}C. The solution was gassed by an OX miniature gas exchange oxygenator (Living Systems Instrumentation, VT). The gas flow was adjusted to 1.5 L/min with an OMA-1 gas flowmeter (Dwyer Instruments, Inc.). Isotonic buffer solution (290 - 300 mOsm) was used for perfusion. For the OGD-RP experiment, OHSCs were treated with 10 min control (CT), 20 min oxygen glucose deprivation (OGD) and 30 min re-perfusion (RP), in which ACSF gassed with 95% O_2/5% CO_2 is used in CT and RP, and MACSF gassed with 95% N_2/5% CO_2 is used in OGD. Then OHSC was treated with 3 mM H_2O_2 and 3 mM DTT for 5 min each for calibration.

4.2.4 Fluorescence imaging

All fluorescent images were acquired on a Leica TCS SP5II broadband confocal microscope (Department of Biological Science, University of Pittsburgh). Live tissues were imaged with a 63x water immersion objective lens (model: HCX APO L U-V-I, N.A. = 0.90). Formaldehyde fixed tissues were imaged with a 63x oil immersion objective lens (model: HCX PL APO, N.A. = 1.40-0.60 with variable iris). Images of the whole OHSC were taken with a 5x objective lens (model: HCX PL PLUOTAR, N.A. = 0.15). Quantitative analysis of images was performed in ImageJ (http://imagej.nih.gov/ij/), then the numerical data was processed in MatLab (version R2014b, The MathWorks, Inc.) and OrginPro (version 9.0, OriginLab Corp.). Statistical data was analyzed in SPSS Statistics (version 20, IBM Corp.)

4.2.4.1 Cell death assay: propidium iodide stain and imaging

OHSCs treated with various conditions were stained with 7 μM propidium iodide (PI) overnight. PI can enter dead cells through the compromised cell membranes, bind to DNA and converts to fluorescent complex[238]. PI stained OHSCs were imaged with 561 nm excitation and 600-640 nm emission (Fig. 4-7). The cell death percentage in a particular area of OHSC was calculated by following Eq. 4.1:

$$Death\% = \frac{(I_{sample} - I_{negative})}{(I_{positive} - I_{negative})} \times 100\% \qquad \text{(Eq. 4.1)}$$

I_{sample}, $I_{positive}$ and $I_{negative}$ are fluorescence intensity from tested OHSC, positive control and negative control, respectively. 100% methanol treated OHSCs were used as the positive control (assuming 100% cell death) and healthy OHSCs were used as the negative control (assuming 0% cell death).

4.2.4.2 Two-photon imaging of NAD(P)H

NAD(P)H[239] images of pyramidal cell layer in OHSC were acquired with Mai Tai Ti:Sapphire laser (Spectra-Physics. CA), which excites NAD(P)H at 740 nm with a power output of 2.175 W. NAD(P)H images were detected by a non-descanned detector (NDD), which was equipped with a dichromatic mirror (cut off, 580 nm). Multiple scans (line average and frame accumulation) are applied to capture a NAD(P)H image with a better signal to noise ratio (S/N), but requires a relatively long time to collect one image (~20 s). In order to maintain focus on one pyramidal cell layer in the OHSC, "autofocus (AF)" (a built-in function of Leica confocal microscope) was applied to a pyramidal cell expressing tdTomato [236] to prevent out-of-focus (Fig. D-3). tdTomato (Exi: 561 nm, Emi: 580 – 600 nm) and bright field (BF) image (lighten by 561

nm) were simultaneously recorded with a hyper dynamic detector (Leica-Microsystems). Sequential scan of (tdTomato+BF) and NAD(P)H was operated on one area of OHSC. In order to acquire information from CA1 and CA3 within the same OHSC at the same time frame, the function “Mark & Find and Tile Scan” in the Leica microscope platform was applied to shuttle scans between the area CA1 and CA3 (Fig. D-3).

4.2.4.3 GSH stain and imaging

Glutathione (GSH) can rapidly react with thiol probe IV[129], which is non-fluorescent and cell permeable, and shows strong fluorescence after derivatization (Exi: 405 nm, Emi: 440-480 nm). OHSCs were incubated with 100 μM thiol probe IV and the staining process was monitored over time. Sequential scan of (tdTomato + BF) and GSH stain, was performed. The AF function was applied to the single cell labelled with tdTomato in order to maintain focus during imaging (Fig. D-3). The function “Mark & Find and Tile Scan” was applied to scan between CA1 and CA3 sequentially (Fig. D-3).

4.2.4.4 Ratiometric image of roGFP2 sensor and calculation of oxidation degree

The roGFP2 sensor[119,132] was excited at 405 or 488 nm, and emission spectra are acquired between 500 – 530 nm. tdTomato[236] was excited at 561 nm, acquired between 580 – 600 nm. Sequential scan was operated by exciting fluorescent proteins at 488, 405, and 561 nm in order. The AF function was applied to the 488 nm excitation channel. Image series were acquired every ~8 s. The ImageJ Plugin “Template Matching and Slice Alignment”[158] was used to align slices in time lapse video for removing the location shift in x, y axis. Fluorescence intensities excited at 405, 488 and 561 nm were extracted after the re-alignment. Ratiometric images were represented in ‘Fire’ false-colored mode by ImageJ[132] (see Fig. D-1, S2).

The ratio 405/488 ($R_{405/488}$) and oxidation degree of roGFP2 sensor (OxD_{roGFP2}) are calculated according to Eq. 4.2-4.3[120,132].

$$R_{405/488} = \frac{I_{405}}{I_{488}} \quad \text{(Eq. 4.2)}$$

I_{405}, I_{488} are fluorescence intensities excited at 405 and 488 nm from roGFP2 sensor. $R_{405/488,}$ when it is fully oxidized by H_2O_2, is often normalized to 1 in this paper.

We used tdTomato to correct the signal of 488 nm from roGFP2 sensor for calculation of OxD_{roGFP2} according to the equation shown below. The necessity to apply tdTomato has been fully described in Chapter 2.0[79].

$$OxD_{roGFP2} = \frac{R_{405/488} - R^{Red}_{405/488}}{\frac{I^{ox}_{488}}{I^{Red}_{488}}\left(R^{ox}_{405/488} - R_{405/488}\right) + \left(R_{405/488} - R^{Red}_{405/488}\right)} \quad \text{(Eq. 4.3)}$$

$R^{ox}_{405/488}$ and $R^{Red}_{405/488}$ are $R_{405/488}$ of fully oxidized and reduced roGFP2 sensor. I^{ox}_{488} and I^{Red}_{488} are fluorescence intensity excited at 488 nm of roGFP2 sensor when it is fully oxidized and reduced. The value of $\frac{I^{ox}_{488}}{I^{Red}_{488}}$ is corrected by $\frac{I^{ox}_{488}/I^{ox}_{561}}{I^{Red}_{488}/I^{Red}_{561}}$, where I^{ox}_{561} and I^{Red}_{561} are fluorescence intensity of tdTomato excited at 561 nm, which are simultaneously recorded with I^{ox}_{488} and I^{Red}_{488}, respectively.

The signal of the roGFP2 sensor was calibrated by treating with H_2O_2 (full oxidation) and DTT (full reduction).

4.2.4.5 Quantitative analysis of the protein content in OHSCs by immunofluorescence.

We follow Gogolla's[240] protocol to stain OHSCs. NADH dehydrogenase subunit 4L (ND4L) is a part of complex 1[241]. Anti- (anti-ND4L) produced in rabbit (sc-20665, Santa Cruz Biotechnology, Inc.), anti-SOD2 produced in rabbit (ab13533, Abcam Inc.) and anti-thioredoxin 2 produced in rabbit (ab185544, Abcam Inc.) were used to stain complex I, SOD2 and thioredoxin 2, respectively. Then, they were fluorescent labelled with the secondary antibody, CFTM568 conjugated goat anti-rabbit pre-absorbed antibody with low cross reaction (Cat# 20103-1, Biotium, CA, USA). α-tubulin, used as the internal control, is firstly immune-stained with anti-α-tubulin (DM1A) mouse monoclonal antibody (Cell Signaling Techonology, USA), then labelled by goat anti-mouse with CF™488A antibody (SAB4600387, Sigma-Aldrich, USA). OHSC was first fixed with 4% paraformaldehyde solution for 5 min then permeabilized with 1% Triton X-100 PBS solution at 4°C for 18 h, blocked with 20% BSA for 3 h at room temperature (RT), and then incubated with the primary antibody at 4°C overnight, followed by incubation with the secondary antibody at RT for 4 h. Washing with 5% BSA PBS was needed between the treatments.

Well prepared OHSC on glass slide were imaged with a 63x oil immersion objective lens. Images from CA1 and CA3 within one OHSC were acquired with the same imaging parameters and processed by imageJ with incorporated multi-plugins. Fluorescence ratio, FR, was used to quantify the protein content corresponding to the internal standard, α-tubulin (details shown in Fig. D-7). It is calculated using equation shown below.

$$\mathrm{FR} = \frac{\mathrm{F}_{\mathrm{protein}}}{\mathrm{F}_{\alpha-\mathrm{tubulin}}} \quad \textbf{(}\text{Eq. 4.4}\textbf{)}$$

4.2.5 Western blot after laser capture microdissection (LCM)

The protein content between subfield CA1 and CA3 from OHSC with Western blot[242,243]. To prepare frozen tissue sections, we collected hippocampuses from postnatal 7-day old Sprague-Dawley rats (Charles River, Pittsburgh), froze them in a cryopreservative solution (OCT)[244] matrix and sliced them into frozen sections at 100 μm thickness. Every three frozen sections were transferred to a normal glass slide, then treated with the hematoxylin and eosin stain[244] (but without treating with xylene) to reveal the anatomy of OHSC. The pyramidal cells in the area CA1 or CA3 of OHSC (Fig. 4-6a) were cut out by LCM[244], operated on an Arcturus PixCell IIe LCM device (Molecular Devices, LLC.). In order to collect enough samples, pyramidal cells of CA1 or CA3 were collected from ~ 50 frozen sections to ensure ~ 10 μg of total protein that could be extracted. The harvested sample was lyzed in 10 μL RIPA buffer with phenylmethanesulfonyl fluoride (PMSF) from Cell Signaling Technology, sonicated on ice with 10 rounds of cycles (15 s pulse on and 1 min pulse off) at 15% power with a Fisher Scientific 550 sonic dismembrator, and then loaded to a 12% polyacrylamide gel for separation. In order to detect complex I, SOD2, thioredoxin 2 and α-tubulin (used as internal control), anti-NADH dehydrogenase subunit 4L(Anti-ND4L) rabbit antibody (sc-20665) from Santa Cruz Biotechnology, Inc., anti-SOD2 rabbit anbody(ab13533), anti-Thioredoxin 2 rabbit antibody (ab185544) from Abcam Inc., and anti-α-tubulin mouse monoclonal antibody (DM1A) from Cell Signaling Technology, USA) were used as primary antibodies. Anti-mouse IgG/HRP-linked antibody (#7076) and anti-rabbit IgG/HRP-linked antibody (#7074) from Cell Signaling Technology were used as secondary antibodies. Chem-illuminescence was detected by using SignalFire™ Elite ECL Reagent (#12757, Cell Signaling Technology).

4.2.6 Assays to trigger superoxide generation, dismutation and Trx system inhibition

Menadione (MD) was used to trigger the generation of superoxide by acting on complex I on the mitochondrial inner membrane. Exogenous MnSOD mimic ($MnSOD_m$) was used to complement the catalytic power of endogenous superoxide dismutase. Auranofin acts an inhibitor of the Trx system. All chemicals were tested on OHSCs by monitoring the H_2O_2 (OxD_{HS}) and GSH (OxD_{GS}) systems with ratiometric imaging. ACSF buffer, oxygenated with 95% O_2/5% CO_2 and maintained at 35 ^oC was used for control (CT) or wash out (WO) to recover OHSC from chemical treatment. The proper maximum working concentration of $MnSOD_m$ was found by testing at 10, 20, 30 μM $MnSOD_m$ by co-adding 10 μM MD (Fig. D-5). The effect of $MnSOD_m$ only was tested by treating OHSC with 5 min CT/ 15 min 20 μM $MnSOD_m$/15 min WO in order (Fig. D-4). To manage the superoxide generation and dismutation, a serial assay was applied (Fig. 4-4): OHSC was first stabilized for 5 min in CT, then stimulated with 10 μM or 20 μM MD for 15 min following by 15 min WO; After the redox status of OHSC was recovered, OHSC was treated with 15 min with 10 μM or 20 μM MD + 20 μM $MnSOD_m$ following by 15 min WO. In the assay of Trx system inhibition (Fig. 4-5), OHSC was pre-incubated with 1 μM auranofin (AF) for 1h, then imaged with 5 min CT, 15 min 10 μM MD + 20 μM $MnSOD_m$. All of the assays mentioned above were calibrated with H_2O_2 (full oxidation) and DTT (full reduction).

4.2.7 Fitting and Statistical analysis of curves

4.2.7.1 Peak analysis

The peaks in Fig. 4-3 were analyzed in an open source statistical software, R (www.r-project.org), in four aspects: peak altitude, ascending slope, descending slope and the emerging

time of the peak from the onset of OGD. All of the peak parameters from different peaks were compared with a t-test with bootstrap (no significant difference, n.s., $p > 0.05$, *$p < 0.05$, **$p < 0.01$, ***$p < 0.001$).

4.2.7.2 Linear fitting

Linear data segments were analyzed in the statistical software, R, to extract parameters, mean and slope of the lines with linear regression. In Fig. 4-1g, h, the traces were divided into several portions with a singular linear trend. The linear parameters, mean and slope, were compared according to two subcategories, OGD-RP time period (CT vs. OGD vs. RP; one way ANOVA) and tissue subfield (CA1 vs. CA3; t-test with bootstrap). In Fig. 4-4b, d, the data in I to III with linear trend were fitted and linear parameters were compared according to two subcategories, treat period (CT vs. 10 μM MD vs. WO; one way ANOVA) and tissue subfield (CA1 vs. CA3; t-test with bootstrap). The same criteria (no significant difference, n.s., $p > 0.05$, *$p < 0.05$, **$p < 0.01$, ***$p < 0.001$) were used to present the analysis results.

4.2.7.3 Nonlinear fitting to the first order exponential equation

The theory of pseudo-first order mechanism is shown in Fig. 4-1c, the enzymatic subunit of the H_2O_2 sensor, Orp1 (left), and of GSH sensor, Grx1 (right), catalyze the coupling the sensors with their relative redox couples. The rate equations of OxD_{HS} and OxD_{GS} are derived as below according to Fig. 4-1c:

H_2O_2 sensor

$$[Orp1]_T \frac{dOxD_{HS}}{dt} = \frac{d[Orp1]_{Ox}}{dt} = k_1[H_2O_2][Orp1]_{Red} - k_2[Trx]_{Red}[Orp1]_{Ox} \quad \text{(Eq. 4.5)}$$

$$[Orp1]_T = [Orp1]_{Red} + [Orp1]_{Ox} \quad \text{(Eq. 4.6)}$$

$$OxD_{HS} = \frac{[Orp1]_{Ox}}{[Orp1]_T} \quad \text{(Eq. 4.7)}$$

$$\frac{dOxD_{HS}}{dt} = k_1[H_2O_2] - (k_1[H_2O_2] + k_2[Trx]_{Red})OxD_{HS} \quad \text{(Eq. 4.8)}$$

In which $[Orp1]_T$, $[Orp1]_{Ox}$ and $[Orp1]_{Red}$ are the concentration of total form, oxidized form and reduced form of roGFP2-Orp1, respectively. $[H_2O_2]$ is the concentration of H_2O_2. $[Trx]_{Red}$ is the concentration of reduced form of Trx. H_2O_2 and Trx_{red} are all first order in the their reactions with Orp1 at different redox forms in our H_2O_2 sensor, roGFP2-Orp1[245,246].

GSH sensor

$$[Grx1]_T \frac{dOxD_{GS}}{dt} = \frac{d[Grx1]_{Ox}}{dt} = k_1'[GSSG][Grx1]_{Red} - k_2'[GSH][Grx1]_{Ox} \quad \text{(Eq. 4.9)}$$

$$[Grx1]_T = [Grx1]_{Red} + [Grx1]_{Ox} \quad \text{(Eq. 4.10)}$$

$$OxD_{GS} = \frac{[Grx1]_{Ox}}{[Grx1]_T} \quad \text{(Eq. 4.11)}$$

$$\frac{dOxD_{GS}}{dt} = k_1'[GSSG] - (k_1'[GSSG] + k_2'[GSH])OxD_{GS} \quad \text{(Eq. 4.12)}$$

In which $[Grx1]_T$, $[Grx1]_{Ox}$ and $[Grx1]_{Red}$ are the concentration of total forms, oxidized form and reduced form of Grx1-roGFP2, respectively. $[GSH]$ and $[GSSG]$ are the concentration of GSH and GSSG, respectively. GSH and GSSG are all first order in their reactions with Grx1 at different redox status in our GSH sensor, Grx1-roGFP2[247].

Fitting OxD_{HS} and OxD_{GS} to the pseudo first order reaction model

$$\frac{dx}{dt} = A - kx \quad \text{(Eq. 4.13)}$$

$$x = \frac{A}{k} - (\frac{A}{k} - x_0)e^{-kt} \quad \text{(Eq. 4.14)}$$

In which A is a constant, k is a reaction rate constant for this pseudo first order reaction, and x is the independent variable.

If we organize Eq. 4.8 for H_2O_2 sensor and Eq. 4.12 for GSH sensor into the form of Eq. 4.13 and 4.14. We get the table below.

Table 4-1. Parameters of the equations of OxD_{HS} and OxD_{GS} in terms of x, A, k, x_0 in Eq. 4.13, 4.14.

sensor	x	A	k	x_0
H_2O_2	OxD_{HS}	$k_1[H_2O_2]$	$k_1[H_2O_2] + k_2[Trx]_{Red}$	$OxD_{0_{HS}}$
GSH	OxD_{GS}	$k_1'[GSSG]$	$k_1'[GSSG] + k_2'[GSH]$	$OxD_{0_{GS}}$

OxD_{HS} would change exponentially in first order (Eq. 4.14) when $k_1[H_2O_2]$ and $k_2[Trx]_{Red}$ are stable, and OxD_{GS} would change exponentially in first order (Eq. 4.14) when $k_1'[GSSG]$ and $k_2'[GSH]$ are stable.

The nonlinear regression was coded and operated in MatLab (version R2014b, The MathWorks, Inc.). The curve segments of OxD in Fig. 4-4b (IV), 4-4c (II), 4-4c (IV), 4-4d (IV), 4-4e (II), 4-4e (IV), the curves of OxD in Fig. 4-5b, c during "10 μM MD + 20 μM $MnSOD_m$" and the curves of OxD in Fig. D-5 during "MD + $MnSOD_m$" were fitted to the first order exponential equation (Eq. 4.14). T-test with bootstrap and one way ANOVA were operated in open source statistical software, R (www.r-project.org) and MatLab (version R2014b, The MathWorks, Inc.)

(no significant difference, n.s., $p > 0.05$, *$p < 0.05$, **$p < 0.01$, ***$p < 0.001$) on these fitted parameters (Table 4-1).

4.3 RESULTS AND DISCUSSION

4.3.1 Real-time redox change of the H_2O_2 and GSH systems during OGD-RP

We monitored the real time redox change of H_2O_2 and GSH/GSSG couple in mitochondria or cytosol of pyramidal cells by using roGFP2 based H_2O_2[119] and GSH[132] sensors, respectively (Fig. 4-1a, b, Fig. D-1, S2).

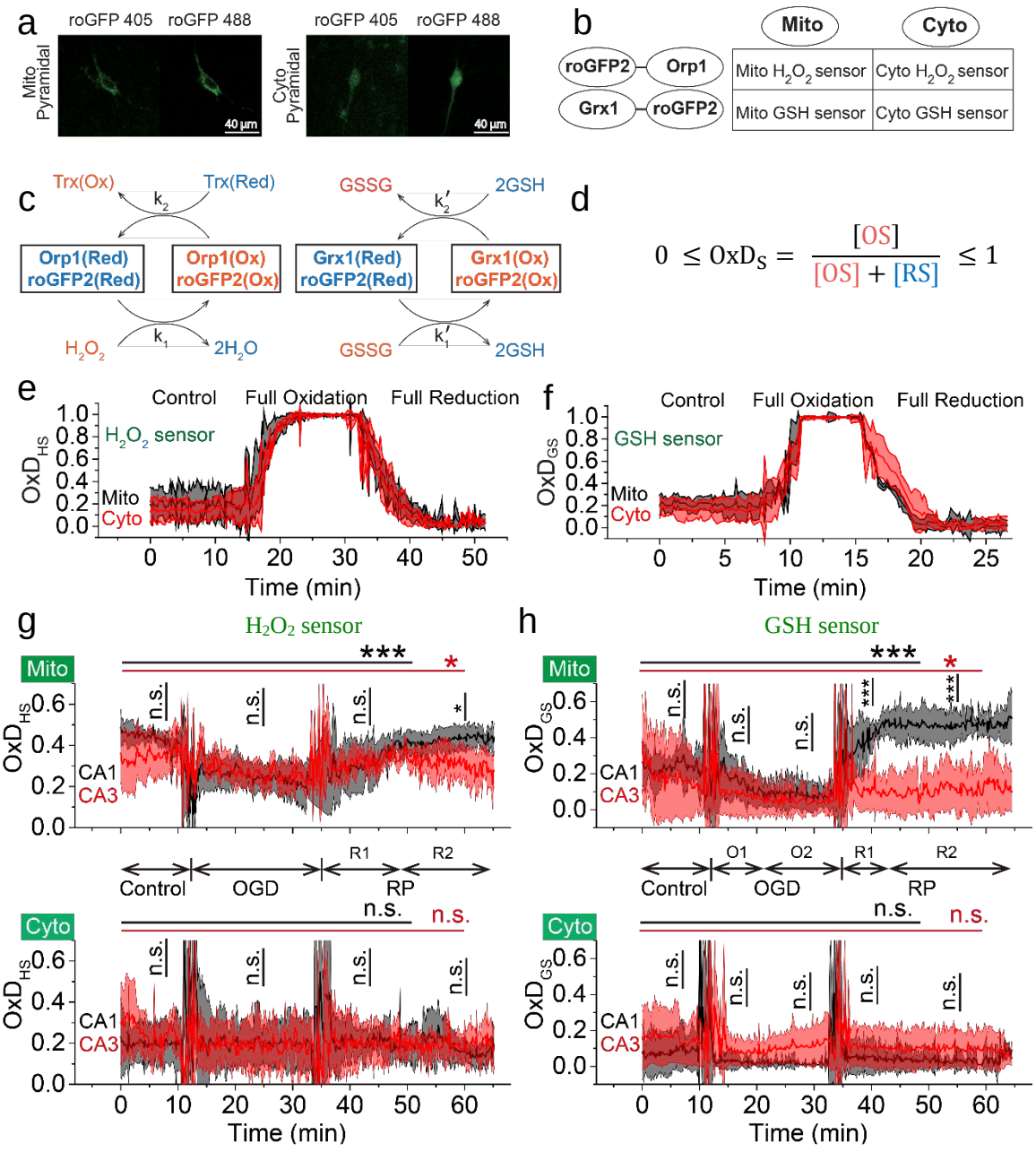

Figure 4-1. Mitochondrial OxD_{HS} and OxD_{GS} show significant differences during OGD-RP in pyramidal cells (stratum pyramidale). OxD_{GS} but not OxD_{HS} is higher during reperfusion in CA1 than CA3.

(a) Grx1-roGFP2 is expressed in mitochondria or cytoplasm in pyramidal cells, imaged with excitation at 405 nm and 488 nm. roGFP2-Orp1 has the similar fluorescence parameters as Grx1-roGFP2. (b) Four chimeric protein sensors are expressed in CA1 and CA3 (Fig. D-1, D-2): Mito-Grx1-roGFP2, Cyto-Grx1-roGFP2 (GSH sensor targeting mitochondria or cytoplasm) and Mito-roGFP2-Orp1, Cyto-roGFP2-Orp1(H_2O_2 sensor targeting mitochondria or cytoplasm). (c) Orp1 in H_2O_2 sensor and Grx1 in GSH sensor regulate the oxidation and reduction of their functional

fluorescent subunit, roGFP2. Orp1 is coupled with H_2O_2/H_2O and Trx_{Ox}/Trx_{Red} and Grx1 is coupled with GSH/GSSG, labelled with k_1, k_2, k_1' and k_2' as the reaction constant in the rate determining step for the respective forwarding reactions. (d) OxD_S is the percentage of oxidized form out of the total sensor molecules, changes in a range of 0 - 1. (e) and (f) OxD_{HS} and OxD_{GS} represent the OxD_S of H_2O_2 and GSH sensor, respectively. The sensors are calibrated with oxidant (H_2O_2) and reductant (DTT). Each trace is representative of 40 individual tests (mean ± SEM). (g) and (h) Data of OxD_{HS} in (g) and OxD_{GS} in (h) in pyramidal cells in OHSC during OGD-RP are presented in mean ± SEM (n=6 for each trace). Data from mitochondria and cytoplasm are shown in the top and bottom, respectively. Statistical analysis was applied with t test with bootstrap and one way ANOVA test (no significant difference, n.s., $p > 0.05$, *$p < 0.05$, ***$p < 0.001$, n=6, see Section 4.2 for more details). The horizontal lines with symbols showing the ANOVA test result indicate the comparison among different periods in OGD-RP in pyramidal cell in CA subfield, CA1 (black) or CA3 (red). The vertical lines with symbols showing the t test result indicate the comparison between CA1 and CA3 at the corresponding period in OGD-RP. While there is little change in the cytoplasmic sensors (n.s., $p > 0.05$, n=6), the mitochondrial sensors change significantly (*$p < 0.05$, ***$p < 0.001$, n=6) during OGD-RP. In (g), there is no significant difference (n.s., $p > 0.05$, n=6) between CA1 and CA3 in mitochondrial OxD_{HS} in OGD-RP except during the later period of RP, R2 (*$p < 0.05$, n=6). Noticeable differences are found in mitochondrial OxD_{GS} between CA1 and CA3 during RP (***$p < 0.001$, n = 6).

The H_2O_2 sensor, roGFP2-Orp1, is oxidized by H_2O_2/H_2O and reduced by thioredoxin (Trx)[119,246] with rates that are first-order in H_2O_2 and Trx, respectively[245,246]. The GSH sensor, Grx1-roGFP2, is oxidized by GSSG and reduced by GSH[132] (Fig. 4-1c) with rates that are first order in GSH and GSSG, respectively[247]. We observe the degree of oxidation, OxD, of each sensor. OxD is the ratio of the oxidized sensor concentration to the total sensor concentration ($0 \leq OxD_s \leq 1$). We report OxD of the H_2O_2 sensor (OxD_{HS}) and of GSH sensor (OxD_{GS}) (see Eq. 4.2, 4.3 in Section 4.2 for more details). In the OGD-RP experiment[248-252], OHSCs were treated with 10 min control (CT), then with 20 min OGD/30 min RP and followed by the calibration of the H_2O_2 or GSH sensor with 5 min H_2O_2 (the oxidant) and 5 min DTT (the reductant) sequentially (see Section 4.2 for more details). OxD_{HS} and OxD_{GS} reach ~ 1 when fully oxidized, and less than ~ 0.01 when

fully reduced both in mitochondria and cytoplasm (Fig. 4-1e, f). Neither OxD_{HS} nor OxD_{GS} in cytoplasm changes during OGD-RP in CA1 and CA3 neurons. In mitochondria, both OxD_{HS} and OxD_{GS} change significantly through the three periods of OGD-RP in CA1 or CA3 neurons (top, Fig. 4-1g, h). The different behaviors of mitochondria and cytoplasm have been fully discussed in Chapter 2.0[234]. In brief, the lack of response of OxD_{HS} and OxD_{GS} in cytoplasm is due to the absence of the cytoplasmic ROS in 20 min of OGD[43], and much more abundant antioxidants[23,253] in cytoplasm (vs. mitochondria) against ROS produced in RP. In mitochondria, lower OxD_{HS} and OxD_{GS} in OGD (vs. CT), but higher OxD_{HS} and OxD_{GS} in RP (vs. CT) indicate a less oxidizing cellular environment in OGD and a more oxidizing cellular environment in RP. Mitochondrial OxD_{HS} and OxD_{GS} are very similar between CA1 and CA3 neurons during the control period and OGD, but not during RP. In the last 15 min of RP, mitochondrial OxD_{HS} increases slightly more in CA1 than in CA3, and is maintained at a high level (top, Fig. 4-1g, Table D-1). During RP, mitochondrial OxD_{GS} in CA1 increases sharply in the first 8 min, then stabilizes at a much higher level than in CA3 (top, Fig. 4-1h, Table D-1). While the difference between mitochondrial H_2O_2 (mH_2O_2) system in CA1 and CA3 (top, Fig. 4-1g) during RP is significant but small, the difference of the mitochondrial GSH (mGSH) system in the two CA subfields during RP is striking (top, Fig. 4-1h), indicating that CA1 and CA3 manage ROS differently and that the which GSH system is involved in that difference.

4.3.2 Reduced thiol concentrations are not different in CA1 and CA3 before OGD-RP, but they are different after OGD-RP measured with thiol stain after OGD treatment

Since GSH is the largest antioxidant pool in cells[175], we examined whether the concentration of GSH corresponds to the different vulnerability to OGD-RP in CA1 and CA3.

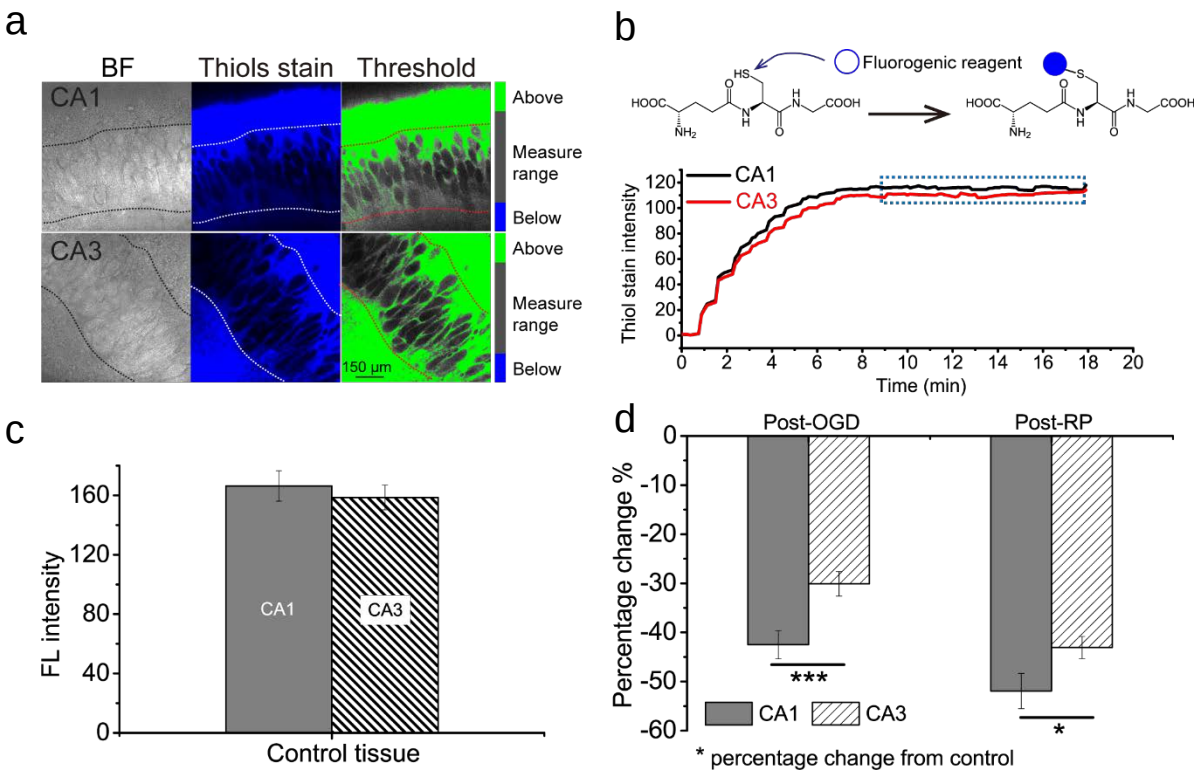

Figure 4-2. Thiol depletion in CA1 is larger than that in CA3 in OHSC after OGD-RP.

(a) Representative images from CA1 (top) and CA3 (bottom) are displayed: (left) Bright field (BF) image, (middle) fluorescence image (exi. 405 nm, emi: 440-480 nm) and (right) threshold image with area of interest (gray), area above threshold (green), and area below threshold (blue). Imaging protocol is optimized as shown in Fig. D-3. (b) Non-fluorescent thiols turn fluorescent after reacting with 100 μM thiol probe IV. The cells in CA1 and CA3 of OHSC spend similar time (~ 8 min) to reach a stable staining with similar fluorescent intensity (see the traces). (c) The absolute contents of reduced thiols are similar between CA1 and CA3 in OHSC (unpaired t-test, no significant difference, $p > 0.05$, $n = 17$) according to the fluorescent intensity of thiols stain. (d) Significant depletion of reduced thiols in OHSCs is found in post OGD and post RP. CA1 shows much larger loss percentage of reduced thiols than CA3 (unpaired t-test, *$p< 0.05$, ***$p<0.001$, $n = 17$).

The total reduced thiol pool can be determined quantitatively via fluorescence imaging after derivatization with thiol probe IV[129] (Fig. 4-2b, Section 4.2). The concentration of total thiols is similar in CA1 and CA3 neurons (Fig. 4-2c). However, the change in total thiol concentration after OGD and RP significantly differs between neurons in those two subfields. Thiol-based

fluorescence decreases by 42.5 ± 2.9 % (n=6) post-OGD, 51.9 ± 3.6 % (n=6) post-RP in CA1. The decreases are 30.1 ± 2.5 % (OGD, n=6) in post-OGD, 43.1 ± 2.3 % (RP, n=6) in CA3. The total thiols can represent the content of intracellular GSH since GSH is the most abundant non-protein thiols inside the cell[181]. This suggests that the GSH system is less effectively maintained in CA1 compared to CA3.

4.3.3 Real-time imaging of NAD(P)H during OGD-RP

Though NADH and NADPH are not distinguishable in two-photon spectra, the analysis of them is simplified since they often respond concurrently to glucose[94] and they are in a dynamic balance either in mitochondria or in cytoplasm through mutual conversions via transhydrogenase[69,94].

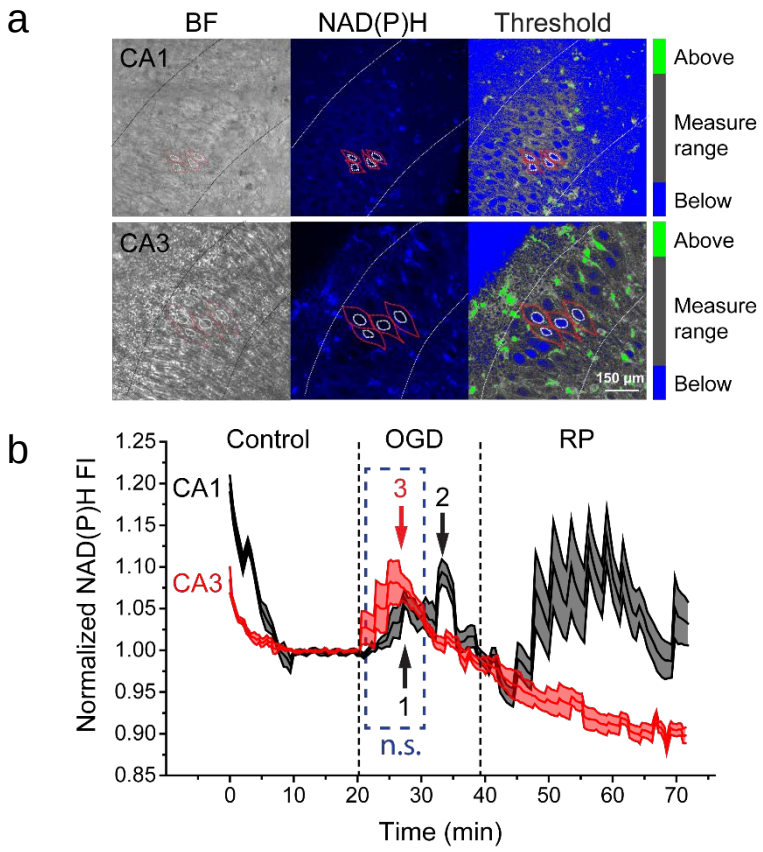

Figure 4- 3. A larger change in NAD(P)H is found in CA1 vs. CA3.

(a) Bright field image (left), two photon image (exi: 740 nm, emi : 580-630 nm) from the pyramidale layer in OHSC (middle) and threshold image (right). The threshold is set with an upper and lower boundary of fluorescence intensity. The area of interest is shown in gray (above in green, below in blue). Several cells are outlined with red closed lines and nuclei are encircled by white closed lines. Nuclei have much lower NAD(P)H content than the rest part of the cells according to the fluorescence intensity. The pyramidal cells are larger in size in CA3 (bottom) than in CA1 (top). Imaging protocol is optimized as shown in Fig. D-3. (b) The normalized fluorescence intensity of NAD(P)H (mean ± SEM, n= 6) changes through OGD-RP (Section 4.2). Fluorescence intensity (FI) is normalized to the stable value during "Control". CA3 shows a different pattern in NAD(P)H change from CA1: During "OGD", two sequential peaks are found in CA1, but only one in CA3. The first peak (labelled 1) in CA1 is not different from the peak (labeled 3) in CA3 after statistical analysis (see Section 4.2 for more details). During "RP", NAD(P)H in CA1 oscillates around a notable higher level than the general level in CA3, and NAD(P)H keeps dropping during RP in CA3.

We measured the content of NAD(P)H by two-photon imaging (Section 4.2, Fig. D-3) over time during OGD-RP. We measured NAD(P)H from mitochondria and cytoplasm of the pyramidal cell (the nucleus is clearly low in NAD(P)H, and excluded from image processing in Fig. 4-3a). NAD(P)H responds differently in CA1 and CA3(Fig. 4-3b). NAD(P)H reaches a steady state after 10 min both in CA1 and CA3 as the OHSC adapts to the pO_2 transition from 19% O_2 during tissue culturing to 95% O_2 in CT. During OGD, one peak emerges between 6-7 min both in CA1 and CA3 (not significantly different (n.s.), see Table D-4, Section 4.2 for more details). An additional peak emerges after 12 min OGD in CA1, but not in CA3. During RP, NAD(P)H slowly decays in CA3 while in CA1, NAD(P)H oscillates around a level that is much higher than in CA3.

4.3.4 Controlled generation of superoxide and H_2O_2 in mitochondria

To address differences in the response of mH_2O_2 and mGSH between CA1 and CA3, we decided to investigate three steps, namely superoxide generation, dismutation to form H_2O_2, and H_2O_2 removal (Fig. 4-4a).

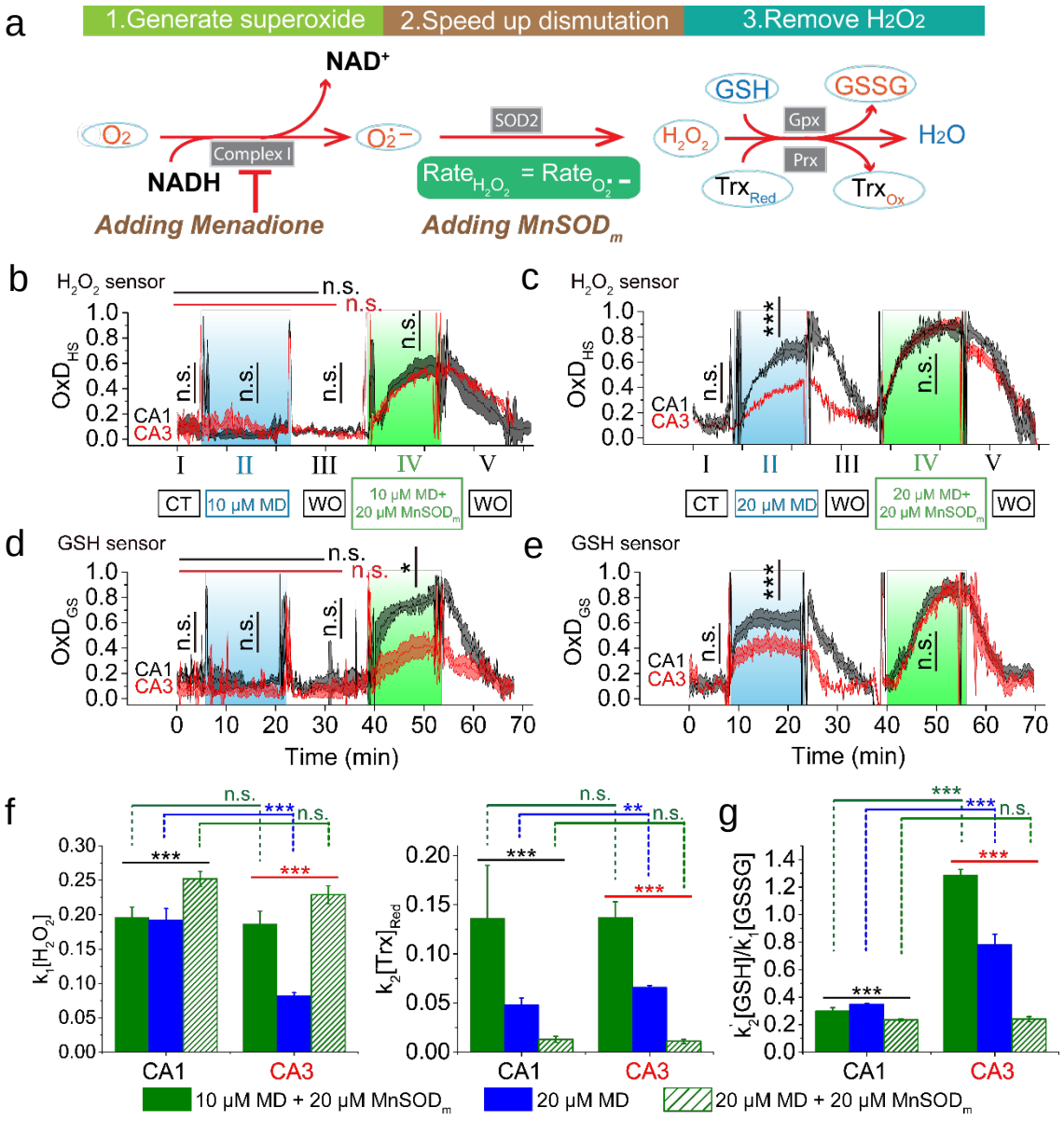

Figure 4-4. Difference between pyramidal cells in CA1 and CA3 in the pathways of ROS management is evidenced by artificially stimulating the generation and removal of superoxide and ROS.

(a) (1) superoxide is generated by inhibiting complex I with menadione; (2) superoxide is dismutated into H_2O_2 via endogenous SOD2 with the absence of ADM. $MnSOD_m$ (a type of ADM) is added to speed up the conversion; $MnSOD_m$ cannot affect complex I, but only affects the dismutation of superoxide (see Fig. D-4 for more details). 20 μM is found to be a proper concentration of $MnSOD_m$ to fully convert superoxide into H_2O_2 (see Fig. D-5 for more details). (3) H_2O_2 is removed by GSH system or Trx system. In (b-e), there are five periods (labelled with I to V) in the treatment. Each trace is represented in mean ± SEM, n= 6. (b) OxD_{HS} of the H_2O_2 sensor is monitored in CA1 and

CA3 during the treatment of 5 min, CT/15 min, 10 μM MD/15 min, wash out (WO) followed by 15 min, 10 μM MD + 20 μM $MnSOD_m$/15 min, wash out (WO). ACSF is used in CT and WO. One way ANOVA test (n.s., $p > 0.05$, n = 6) is applied for period I to III in CA1 and CA3 (indicated by black and red horizontal lines, respectively). T test (n.s., $p > 0.05$, n = 6) is applied to CA1 vs CA3 in period I to IV, indicated by vertical lines. (c) OxD_{HS} is monitored in CA1 and CA3 during the treatment of 5 min, CT/15 min, 20 μM MD/15 min, wash out (WO) followed by 15 min, 20 μM MD + 20 μM $MnSOD_m$/15 min, wash out (WO). ACSF is used in CT and WO. CA1 and CA3 are compared in period I, II and IV with t test (n.s., $p > 0.05$, ***$p < 0.001$, n = 6), indicated by vertical lines. (d) OxD_{GS} of GSH sensor is monitored in CA1 and CA3 when OHSC is treated in the same condition as in (d). Horizontal lines (black for CA1, red for CA3) show the statistical analysis among period I to III with one way ANOVA test (n.s., $p > 0.05$, n = 6). CA1 vs CA3 is compared in period I to IV with t test (n.s., $p > 0.05$, *$p < 0.05$, n = 6), indicated by vertical lines. (e) OxD_{GS} is monitored in CA1 and CA3 treated in the same conditions as in (e). CA1 vs CA3 is compared in period I, II and IV with t test (n.s., $p > 0.05$, ***$p < 0.001$, n = 6), indicated by vertical lines. (f) $k_1[H_2O_2]$ and $k_2[Trx]_{Red}$ were obtained by fitting the data trace in b(IV), c(II) and c(IV). (g) $\boldsymbol{k_2'[GSH]/k_1'[GSSG]}$ was obtained by fitting the data trace in d(IV), e(II) and e(IV). In (f) and (g), one way ANOVA test (***$p < 0.001$, n=6) was applied in CA1 (black) or CA3(red) to compare among different treatment conditions. A t-test (n.s., $p > 0.05$, **$p < 0.01$, ***$p < 0.001$, n=6) was applied under each treatment condition to compare between CA1 and CA3. Curve fitting and statistical analysis are described in Section 4.2. The toxicities of MD, $MnSOD_m$ and MD + $MnSOD_m$ corresponding to the cell death of OHSCs are measured with PI assay (Fig. D-6).

We applied 10 or 20μM menadione (MD)[254] to stimulate superoxide generation at complex I [255,256] in OHSCs. As shown in Fig. 4-4a (I), once superoxide forms in mitochondria (step 1), it can be converted enzymatically into H_2O_2 via endogenous superoxide dismutase (SOD), SOD2 [230] (step 2). The rate of the natural dismutation process is limited by the rates of the uncatalyzed and catalyzed dismutation rates, and the latter is controlled by the amount of endogenous SOD2. Thus, the peroxide sensor's response depends both on the generation rate of superoxide and the rate of its conversion to peroxide. Thus, we obtained a well-designed and effective artificial manganese superoxide dismutase mimic, ($MnSOD_m$, MnTnBuOE-2-PyP^{5+}), from the Batinic-Haberle[237] lab.

Its introduction into mitochondria at a sufficiently high concentration would make the peroxide sensor sensitive to the rate of generation of superoxide in the mitochondria. We characterized $MnSOD_m$ and confirmed that it did not stimulate superoxide generation as MD did (Fig. D-4). But $MnSOD_m$ efficiently dismutates superoxide since OxD_{HS} reaches a higher steady state with the treatment of MD + $MnSOD_m$ than that of MD only (see Fig. 4-4b (II) vs. 4-4b (IV) and Fig. 4-4c (II) vs. 4-4c (IV)). We tested different concentrations of $MnSOD_m$ with 10 μM MD to find a $[MnSOD_m]_{max}$ at which $MnSOD_m$ is enough to maximize the dismutation of superoxide. As shown in Fig. D-5, The steady state values of OxD_{HS} and OxD_{GS} increase from 10 μM $MnSOD_m$ to 20 μM $MnSOD_m$, but no significant changes when increasing $[MnSOD_m]$ from 20 μM to 30 μM. We decided to use $[MnSOD_m]_{max}$ = 20 μM in the following experiments, and assume that the generation rate of superoxide will equal that of H_2O_2 at $[MnSOD_m]_{max}$ ($R_{O_2^{\cdot-}} = R_{H_2O_2}$, Fig. 4-4a (II)).

We ran a serial experiment, 5 min CT/15 min MD/15 min wash out (WO)/15 min MD + $MnSOD_m$/15 min WO (see more details in Section 4.2) in Fig. 4-4 (b-e) to explore how the mH_2O_2 and mGSH systems in pyramidal cells in CA1 and CA3 would respond when the generation and dismutation of superoxide is regulated. As shown in Fig. 4-4b, c, OHSCs are treated with ACSF in CT, and OxD_{HS} and OxD_{GS} are acquired as baselines. WO helps to restore OxD_{HS} and OxD_{GS} back to baseline by removing the agents.

MD at 10 μM does not cause a noticeable increase in OxD_{HS} (Fig. 4-4b (II)) or OxD_{GS} (Fig. 4-4d (II)) in either CA1 or CA3 (see Table D-3 for more details). But when $MnSOD_m$ is also applied, a sharp increase in OxD_{HS} (Fig. 4-4b (IV)) and OxD_{GS} (Fig. 4-4d (IV)) are found both in CA1 and CA3. Fig. 4-4c clearly shows that 20 μM MD alone is capable of influencing OxD_{HS}

(Fig. 4-4c (II)) and OxD_{GS} (Fig. 4-4e (II)), while 20 μM MD + 20 μM $MnSOD_m$ shifts OxD_{HS} (Fig. 4-4c (IV)) and OxD_{GS} (Fig. 4-4e (IV)) close to their fully oxidized status in 15 min.

Note that the traces of OxD_{HS} and OxD_{GS} in Fig. 4-4b (IV), 4-4c (II), 4-4c (IV), 4-4d (IV), 4-4e (II) and 4-4e (IV) all appear to follow a first order exponential rise in OxD (Eq. 4.14). We have thus derived the equation for the change in OxD with time based on first order reactions for the oxidation and reduction of each sensor (Eq. 4.5 – 4.12, see Section 4.2 for more details). Four quantities can be determined from the curves: for the peroxide sensor, we determined the rate parameters of sensor oxidation, $k_1[H_2O_2]$ and reduction, $k_2[Trx]_{Red}$) and for GSH we found the analogous rate parameters, $k_1'[GSSG]$ and $k_2'[GSH]$. Their values are summarized in Tables D-5, D-6, and statistically analyzed and plotted in Fig. 4-4f, g.

We compared OxD_{HS}, OxD_{GS} and the aforementioned rate parameters between CA1 and CA3 to find the difference in each step of the ROS pathway (Fig. 4-4a). **1. Superoxide generation.** OxD_{HS} and $k_1[H_2O_2]$ with treatment of 10 μM MD + 20 μM $MnSOD_m$ (Fig. 4-4b, f) or 20 μM MD + 20 μM $MnSOD_m$ (Fig. 4-4c, f) are not significantly different between CA1 and CA3. As we discuss above, the H_2O_2 sensor can be used as a superoxide sensor since $\text{Rate}_{O_2^{\cdot-}} = \text{Rate}_{H_2O_2}$ at $[MnSOD_m]_{max}$ (Fig. 4-4a (II)). This demonstrates that superoxide generation is similar in CA1 and CA3 with the same concentration of MD. This implies that CA1 has a similar content of complex I as CA3. 2**. Dismutation.** With 20 μM MD only, OxD_{HS} and $k_1[H_2O_2]$ are much higher in CA1 than CA3 (Fig. 4-4c (II), f). The difference could be due to different SOD2 activities, meaning that less H_2O_2 is formed in CA3 than CA1. Or it could be caused by a greater rate of removal of H_2O_2 in CA3 than CA1. eration. The latter conclusion is consistent with the observation that the concentration of SOD2 is higher in CA3 in adult male Sprague-Dawley rats[257]. More work

will be described below to permit an understanding of these contrasting observations. **3. Removal of H_2O_2.** When OHSCs are treated with 20 μM MD or 20 μM MD + 20 μM $MnSOD_m$, there is no significant difference in any of the measured parameters between CA1 and CA3 (Fig. 4-4f and g). In addition combined observations of the two sensors indicate a highly oxidizing environment: H_2O_2 concentration is high (4f, left); Trx2 is oxidized (4f, right) and the GSH system is oxidized (4g). However, the same correlation between H_2O_2 and GSH is absent under the treatment of 10 μM MD + 20 μM $MnSOD_m$. In this case, the parameters related to the H_2O_2 sensor are not significantly different in CA1 and CA3 (Fig. 4-4b (IV), 4-4f) but OxD_{GS} and $k_2'[GSH]/k_1'[GSSG]$ are dramatically different (Fig. 4-4d (IV), 4-4g). Broadly, then, under highy oxidizing conditions, 20 μM MD and $MnSOD_m$, CA1 and CA3 are similarly stressed. With a high superoxide production rate and endogenous SOD2 CA3 maintains a lower concentration of H_2O_2 and a more reduced GSH system than CA1. With a more modest superoxide production rate (10 μM MD) and the same effective dismutation rate (20 mM $MnSOD_m$) we find, remarkably, statistically indistinguishable peroxide sensor response but very different GSH system response with CA3 once again being more reduced. We thus wondered whether the other antioxidant system (Trx) contributes to this scenario. An efficacious way to study the Trx2 system but with the H_2O_2 and GSH redox sensors would be to inhibit TrxR from participating in the regeneration of Trx2, and to monitor the consequential influence on OxD_{HS} and OxD_{GS}.

4.3.5 Inhibition of the Trx system in mitochondria

We decided to study the Trx system to determine its contribution to H_2O_2 removal. The redox changes of the H_2O_2 and GSH systems were monitored with the treatment of 10 μM MD + 20 μM $MnSOD_m$ while 1 μM auranofin (AF)[228] was applied to inhibit the Trx system as shown in

Fig. 4-5a. First order exponential equations for OxD_{HS} (Fig. 4-5b) and OxD_{GS} (Fig. 4-5c) curves were fitted to the data (Eq. 4.14, see Section 4.2 for more details), and the fitted parameters are listed in Table D-7, D-8. The GSH (via Gpx) and Trx2 systems (via Prx) are consistently more oxidized when the Trx system is inhibited: OxD_{HS} and OxD_{GS} become higher after adding AF (Fig. 4-5b, c). The higher $k_1[H_2O_2]$ is accompanied by a smaller $k_2[Trx]_{Red}$ and $k_2'[GSH]/k_1'[GSSG]$ (Fig. 4-5d, e). Fig. 4-5b, c shows changes in OxDs due to auranofin: ΔOxD_{HS}^{CA1} in CA1 (0.241 ± 0.039) is significantly lower than in CA3 . (0.324 ± 0.019). and the changes in the GSH system are very high (ΔOxD_{GS}^{CA1} vs. ΔOxD_{GS}^{CA3}, 0.056 ± 0.034 vs. 0.404 ± 0.067) These data support the idea that CA3 is affected to a much larger extent by Trx inhibition than is CA1. This demonstrates that GSH system in CA3 is maintained at a more reduced status due to its Trx system since the H_2O_2 generated is not significantly different in CA1 and CA3 under normal conditions (no AF here). No difference in GSH system is found between CA1 and CA3 once the Trx system is inhibited (OxD_{GS}: CA1 ≈ CA3 (AF); $k_2'[GSH]/k_1'[GSSG]$: CA1 ≈ CA3 (AF); Fig. 4-5c, e).

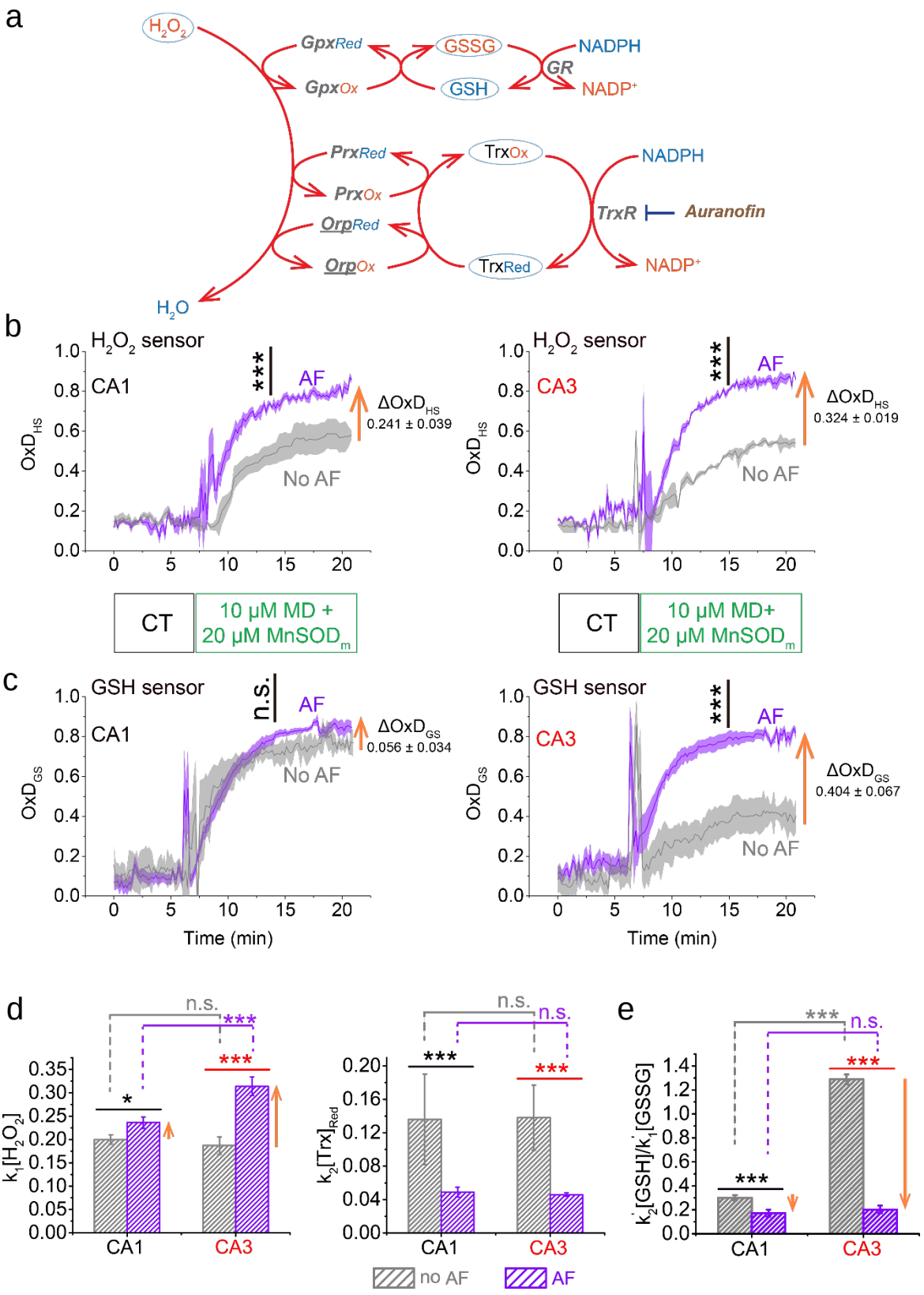
a
H2O2
GpxRed
GpxOx
GSSG
GSH
NADPH
GR
NADP+
PrxRed
PrxOx
OrpRed
OrpOx
TrxOx
TrxRed
TrxR
Auranofin
H2O
b
H2O2 sensor
CA1
CA3
AF
No AF
***
ΔOxDHS
0.241 ± 0.039
0.324 ± 0.019
OxDHS
CT
10 μM MD +
20 μM MnSODm
10 μM MD+
c
GSH sensor
n.s.
ΔOxDGS
0.056 ± 0.034
0.404 ± 0.067
OxDGS
Time (min)
d
k1[H2O2]
k2[Trx]Red
CA1
CA3
no AF
AF
e
k'2[GSH]/k'1[GSSG]

Figure 4-5.The H_2O_2 and GSH systems experience larger redox shifts in CA3 than in CA1 when the Trx system is inhibited by auranofin (AF).

The tissue is pre-treated with or without 1 μM auranofin 1h before imaging. Tissue is superfused with ASCF in control (CT) for ~ 8 min, then with 10 μM menadione + 20 μM MnSOD mimics (10 μM MD+20 μM $MnSOD_m$) for 15 min during image data acquisition. (a) H_2O_2 is consumed by the GSH and Trx systems via several redox enzymes, glutathione peroxidase (Gpx), peroxiredoxin (Prx) and oxidant receptor protein (Orp). roGFP2-Orp1, the H_2O_2 sensor used here, has the subunit, Orp (underlined in a), which is directly coupled with Trx. AF can inhibit the Trx system by deactivating thioredoxin reductase (TrxR). (b) H_2O_2 in CA1 (left) and in CA3 (right) shifts to a more oxidized status when pre-treated with AF. A larger change in OxD_{HS} during 10 μM MD+20 μM $MnSOD_m$ is found in CA3 than in CA1. (c) (left) OxD_{GS} changes subtly during 10 μM MD+20 μM $MnSOD_m$ in CA1 between "with" and "without" AF pre-treatment. (right) OxD_{GS} in CA3 changes noticeably under the conditions from "without" to "with" AF pre-treatment during 10 μM MD+20 μM $MnSOD_m$. In (b) and (c), each trace is represented as mean ± SEM (n=6). Comparison between CA1 and CA3 (indicated by vertical lines) (n.s., $p > 0.05$, ***$p < 0.001$, t test; n=6). ΔOxD is the difference between the steady state values of OxD (AF) and OxD (no AF). (d) $k_1[H_2O_2]$ and $k_2[Trx]_{Red}$ were obtained by fitting the data trace in (b). (e) $\mathbf{k_2'[GSH]/k_1'[GSSG]}$ was obtained by fitting the data trace in (c). In (d) and (e), a t test (***$p < 0.001$, n=6) was applied in CA1 (cyan) or CA3 (purple) to compare between no AF and AF treatment conditions. A t test (n.s., $p > 0.05$, **$p < 0.01$, ***$p < 0.001$, n=6) was applied under each treatment condition to compare between CA1 and CA3. Curve fitting and statistical analysis are described in Section 4.2.

4.3.6 Compare protein content between the pyramidal cells in CA1 and CA3

To compare the relative content of complex 1, SOD2 and Trx2 between CA1 and CA3, We made measurements by Western blot (WB) and immunofluorescence (IF) to OHSCs (see Section 4.2 for more details).

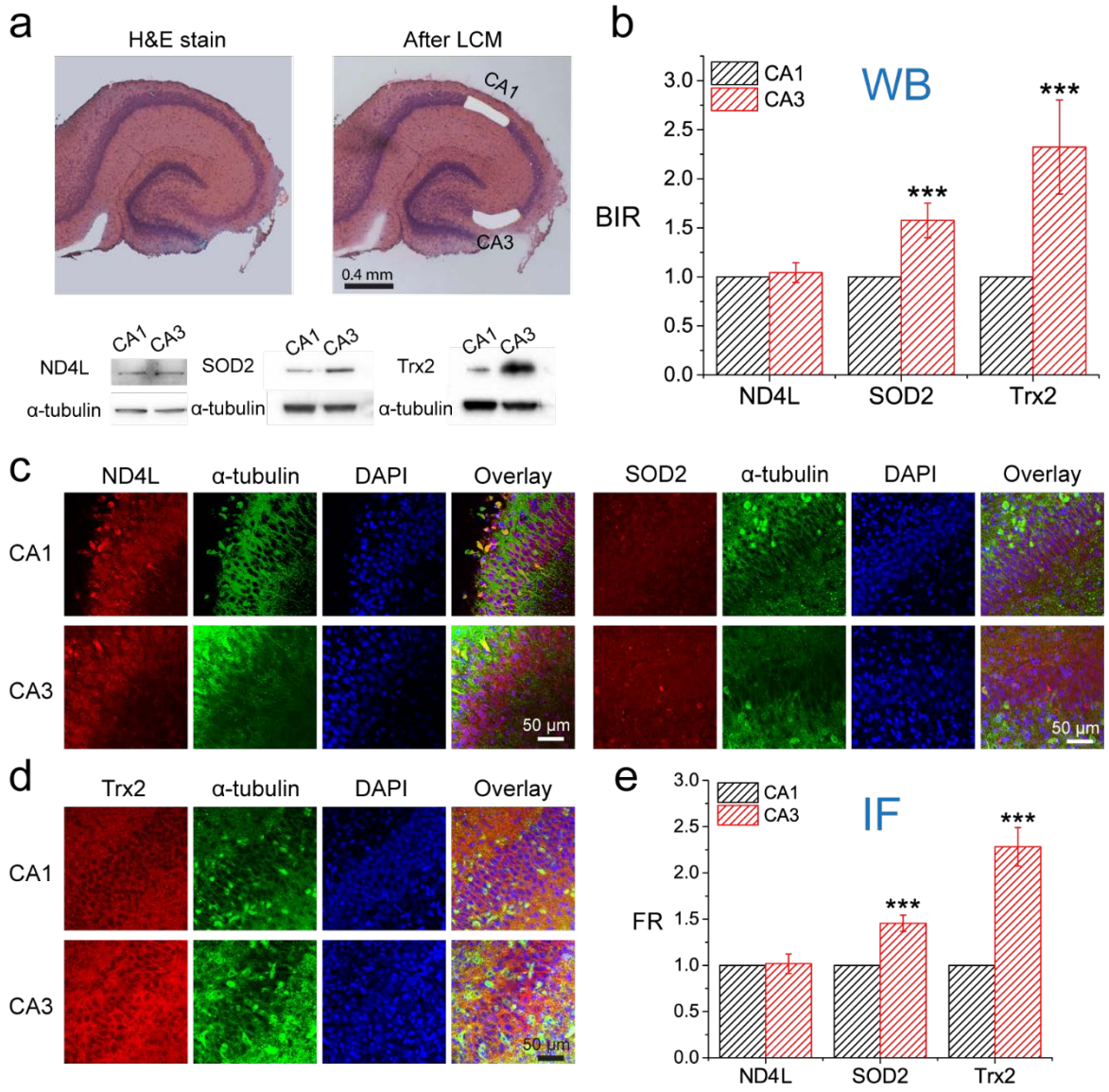

Figure 4-6. The expression of Trx2 and SOD2 is much higher in CA3 pyramidal cells than in CA1, but not for ND4L.

(a) top, The pyramidal cell layers of CA1 and CA3 from the H&E stained OHSC are collected separately by LCM; bottom, Western blot bands of ND4L, SOD2 and Trx2 from CA1 and CA3 subfields of OHSCs are optically read and analyzed. (b) Expression of each protein from CA1 and CA3 is compared quantitatively (***p<0.001, n=3). Band intensity ratio (BIR) is used to refer the targeting protein to internal standard, α-tubulin. (c) and (d) Representative fluorescence images from subfields of CA1 and CA3 from triple stained OHSCs are displayed in three subplots. From left to right in each subplot, ND4L and SOD2 in (c) and Trx2 in (d) are immuno-stained, shown in red; α-tubulin is immuno-stained, shown in green; nuclei are counterstained with DAPI, shown in blue; the final image is the overlay

of the former three. (e) Fluorescence ratio (FR) of the targeting protein to α-tubulin, is quantitatively analyzed and compared between CA1 and CA3 (***$p<0.001$, $n=10$, see Fig S7 and Section 4.2 for more details).

To restrict the measurement to (mostly) pyramidal cells, we used laser capture microdissection (LCM)[244] to capture the pyramidal cell layers from CA1 or CA3 for Western blots (Fig. 4-6a). Only pyramidal cell layers from CA1 and CA3 in OHSCs were imaged in IF (Fig. 4-6c,d). NADH dehydrogenase subunit 4L (ND4L, a subunit of complex I)[241], SOD2 and Trx2 were targeted with their specific antibodies. The band intensity (Fig. 4-6a, WB) and fluorescence (Fig. 4-6c,d, D-7, IF) of each protein was referred to that of the internal standard, α-tubulin. The values obtained from CA3 were normalized to that from CA1 (see Section 4.2 for more details). We obtained consistent information from WB and IF (Fig. 4-6): pyramidal cells in CA1 and CA3 have similar amounts of complex I, which explains why similar amount of superoxide is generated in CA1 and CA3 with a given menadione concentration (Fig. 4-4b (IV), 4-4c (IV)). The amount of SOD2 in CA3 is about 1.5 times that in CA1, which indicates that H_2O_2 generation from superoxide is much more efficient in CA3. We found that Trx2 in CA3 is about 2.3 times that in CA1 in supporting the idea that the GSH system is more reduced in CA3 with similar H_2O_2 levels (Fig. 4-4b (IV), 4-4d (IV), 4-1h(top, RP)) due to the contribution of reducing capacity from Trx2. Considering that CA3 has greater endogenous capabilities to both generate and remove H_2O_2, it would be rational to conclude that maintenance of a lower H_2O_2 level is governed by the greater reducing capacity of CA3, not a lower production rate of ROS (Trx2, CA1 < CA3; GSH, CA1 ≈ CA3) (Fig. 4-4c (II), 4-1g(top, RP)).

4.3.7 Trx2 is critical important for the prevention of the neuronal death.

After we found that CA3 has a higher Trx2 content which contributes to its relatively lower H_2O_2 level and less oxidized GSH system, we also found that Trx2 is critically important to protect the tissue from neuronal damage following OGD-RP as shown in Fig. 4-7. We measured fluorescence from following incubation with propidium iodide (PI) following OGD-RP or exogenous stimulation of ROS production with and without AF. PI intensities were compared to "live" (0%) and "dead" (100%) controls. We used 1 μM AF, which is not toxic, causing less than 10% cell death in CA1 and CA3 (Fig. 4-7). CA1 has more cell death than CA3 with the treatment of OGD-RP or 10 μM MD + 20 μM $MnSOD_m$. When OHSCs were pre-treated with AF, then treated with OGD-RP or 10 μM MD + 20 μM $MnSOD_m$, the cell death increased both in CA1 and CA3, and the difference of cell death disappeared between the two CA areas.

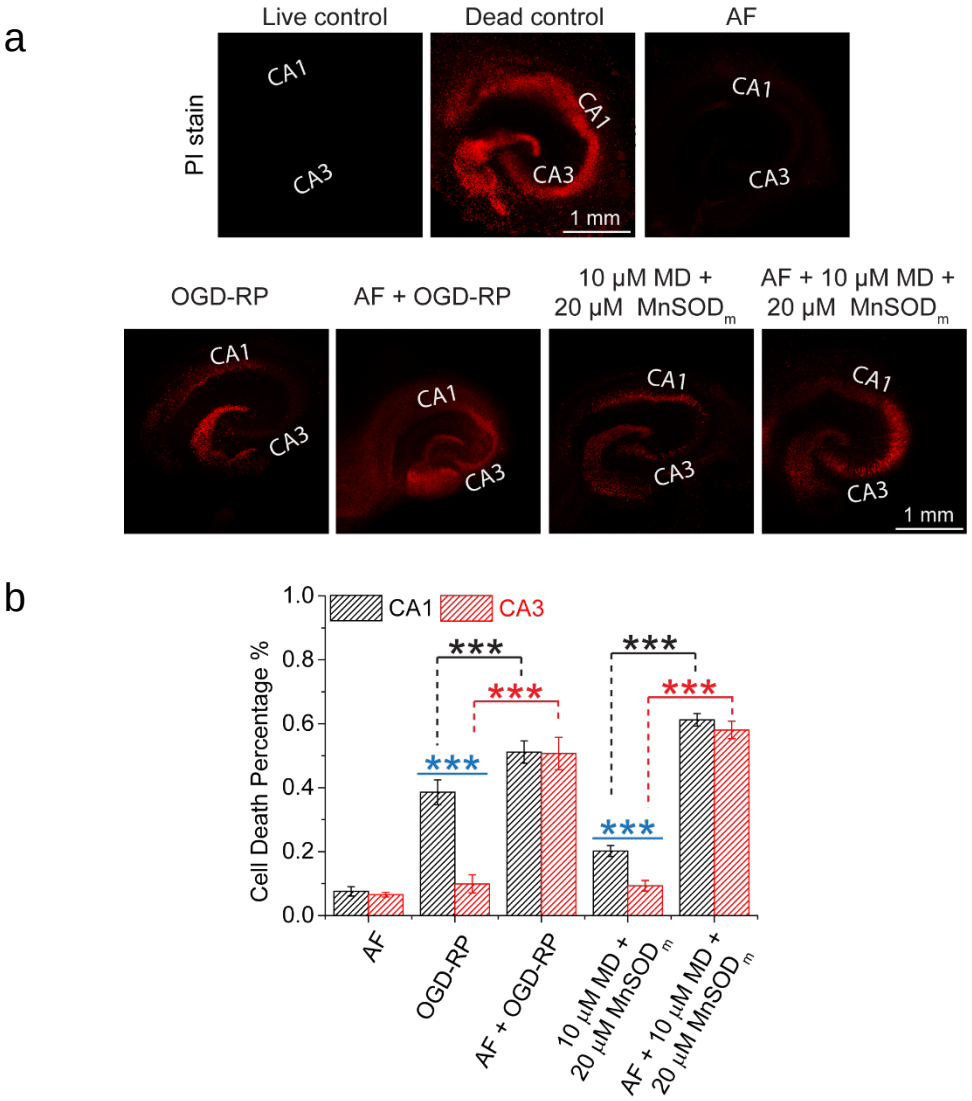

Figure 4-7. Inhibition of the Trx system by AF increases the cell death percentage and remove the difference in cell death between CA1 and CA3.

(a) Fluorescence images of OHSCs after different treatments. (b) Data of cell death under different treatments are represented and compared in CA1 and CA3 (One-Way ANOVA test, ***$p < 0.001$, $n = 10$; no special sign is added if there is no significant difference). The cell death percentage is tested with PI stain (Section 4.2).

4.4 CONCLUSION

Our overall goal is to decipher a decades-old observation that pyramidal neurons of the CA1 region of the hippocampus are less resilient under hypoxia/ischemia than those of the CA3 region[207]. As described earlier, ROS are implicated in this difference, but there is at present no clear evidence of why this is the case. We want to determine the mechanism behind this scenario, and try to correlate the ROS management with the survivability of cells in different CA regions.

In the OGD-RP experiment, H_2O_2, GSH and NAD(P)H were monitored as a function of time. The redox changes of the mitochondrial and cytoplasmic sensors for H_2O_2 and GSH were determined readily by fluorescence microscopy. We found no significant changes in the cytoplasmic responses, but there were significant changes in the mitochondrial matrix-directed sensors during OGD-RP. These changes were different in CA1 and CA3. It is worth mentioning that these sensors have several significant advantages over other widely used fluorogenic reagents[113,119,132,258]. We regulated each step in one branch of the ROS pathway (Fig. 4-4a) by using MD, $MnSOD_m$ and AF, Superoxide is generated at complex I and complex III[259] with certain exogenous reagents. However, superoxide from complex I goes to the mitochondrial matrix, while complex III releases superoxide towards the cytosol[259]. Neuronal production of superoxide mostly occurs at complex I[255].. Thus, we used MD which targets complex I[254,256] to evoke superoxide production in mitochondria[256]. 100 μM MD is toxic to astrocytes, while MD at 10 μM, is non-toxic[260]. We applied 10 or 20 μM MD to create a relatively mild insult to OHSCs. NAD(P)H responds to the chemical insults in seconds[92,261,262]. We found that the fluorescence intensity of NAD(P)H quickly dropped below the detection limit of the confocal microscope during a 15 min exposure to MD or MD + $MnSOD_m$, thus no useful information of NAD(P)H can be acquired (data not shown). As shown in Fig. 4-4b, c, when only MD is applied, superoxide was only partially

converted into H_2O_2. When MD + $MnSOD_m$ at $[MnSOD_m]_{max}$ was introduced, superoxide was maximally converted into H_2O_2. In Fig. 4-4, that the relative values of OxD_{GS} (CA1 vs. CA3) are correlated with that of OxD_{HS} (CA1 vs. CA3) when treating with 20 μM MD or 20 μM MD + 20 μM $MnSOD_m$, but this relationship does not exist when treating with 10 μM MD + 20 μM $MnSOD_m$. However, it is consistent under all MD and MD + $MnSOD_m$ conditions that the relative values of the Trx related term, $k_2[Trx]_{Red}$, are quite correlated with that of H_2O_2 related terms (see Fig. 4-4f). These findings indicate the Trx system may remove H_2O_2 in a different efficiency compared to the GSH system. Several researchers address the relative contribution and importance of the Trx and GSH systems to relieve the oxidative stress. The two antioxidants, the Trx and GSH systems, are relatively independent, and can only be coupled through redox reactions via indirect electron transfer[263]. Greetham et al. claim that only the oxidation of mitochondrial Trx leads to ROS dependent cell death, while the GSH system is not as influential as Trx[264]. Similar statements claim that Trx system, not the GSH system, is required for cell viability of yeast [265]. Kudin et al.[229] demonstrate that Trx2 contributes to remove H_2O_2 to a larger extent than GSH in mitochondria. In the term of kinetics, the Trx system is much more efficient at removing H_2O_2 than the GSH system, and could be more rapidly reduced by NADPH. The rate constants of the reaction of the Trx system with H_2O_2 via Prx[89,266,267] are approximately twice that of the reaction of the GSH system with H_2O_2 via Gpx[89,268]. The rate constant for Trx reduction[89,269] by NADPH is about six times that of NADPH-dependent GSH reduction[89,270]. Based on all the evidence, we hypothesized that 1) The Trx system is preferred to handle the modest amounts of H_2O_2 generated (e.g. with 10 μM MD + 20 μM $MnSOD_m$,) with low participation of the GSH system, but it will need high participation of the GSH system against large amounts of H_2O_2 that overwhelm the whole antioxidant systems (e.g. with 20 μM MD + 20 μM $MnSOD_m$). Inhibiting Trx would force GSH to become the main

reducing agent against H_2O_2; 2) Compared to CA1, Pyramidal cells in CA3 have more Trx in mitochondria to maintain their mGSH at relative reduced status.

AF was applied to inhibit the Trx system, and we found a dramatic influence on the H_2O_2 and GSH systems in CA3. H_2O_2 was generated by adding 10 μM MD + 20 μM $MnSOD_m$. We observed similar OxD_{HS} in CA1 and CA3 (no AF), but larger OxD_{HS} in CA3 (AF). But we should be cautious to believe that larger OxD_{HS} in CA3 indicates a higher H_2O_2 level in CA3 when AF is added. OxD of the H_2O_2 sensor, roGFP2-Orp1, is not only dependent on H_2O_2, but also influenced by Trx (the sensor is coupled with both H_2O_2/H_2O and Trx_{Ox}/Trx_{Red}, Fig. 4-5a)[119,246]. The increase of OxD_{HS} is not purely caused by the increased H_2O_2 level when Trx is inhibited here. The data of OxD_{GS} strongly supports our assumption (1) mentioned above. Similar OxD_{GS} (CA1 vs. CA3) with AF matches with similar OxD_{HS} (CA1 vs. CA3) indicating that the GSH system no longer partially reacts with H_2O_2 once the Trx system is inhibited.

We attempted to find the relative content of complex 1, SOD2 and Trx2 (CA1 vs. CA3) by running WB and IF (Fig. 4-6). There is some evidence about these three proteins measured from similar animal models. It is reported that the concentration of complex I can vary widely among different tissue types[255,271]. The mRNA level for transcription of Complex I is higher in CA3 than CA1 in mouse[93]. Research in adult male rats shows that SOD2 (protein level) is higher in CA3 than CA1[257], but mRNA level for SOD2 is higher in CA1 in 7-day cultured OHSCs collected from postnatal 10 day old Sprague Dawley rats (p10 SD rats)[55,56], and Trx2 (mRNA in p10 SD rat[27,28] or protein level in the adult male rats[63]) is not different between CA1 and CA3. No reports are found to study 7-day cultured OHSCs collected from p7 SD rats so far except our observations reported here. We measured the relative contents of proteins via WB and IF. Pyramidal cell layer in OHSC was selectively collected by using LCM for WB, and selectively imaged for IF. WB and

IF provide consistent information of these proteins (CA1 vs. CA3) in Fig. 4-6. The results match with our deduction about these proteins from OxD_{HS} and OxD_{GS} data in Fig. 4-4, 4-5. We summarized the conclusions about the differences in managing ROS pathway (CA1 vs. CA3) in Fig. 4-8b. In brief, similar protein content of complex I (CA1 vs. CA3) supports that similar amounts of superoxide are generated in CA1 and CA3 when OHSC treated with MD + $MnSOD_m$ (Fig. 4-4b (IV), 4-4c (IV)); CA3 has higher protein content both in SOD2 and Trx2. The extra reducing capacity from more Trx2 allows CA3 to maintain the GSH system at a more reduced state (Fig. 4-4d (IV)) when facing similar amounts of H_2O_2 generated in CA1 and CA3 (Fig. 4-4b (IV)). Compared to CA1, CA3 regulates H_2O_2 at a lower level by its larger Trx2 pool with the similar amounts of superoxide generated and higher efficiency to generate H_2O_2 via its more endogenous SOD2 (Fig. 4-4c (II)).

a

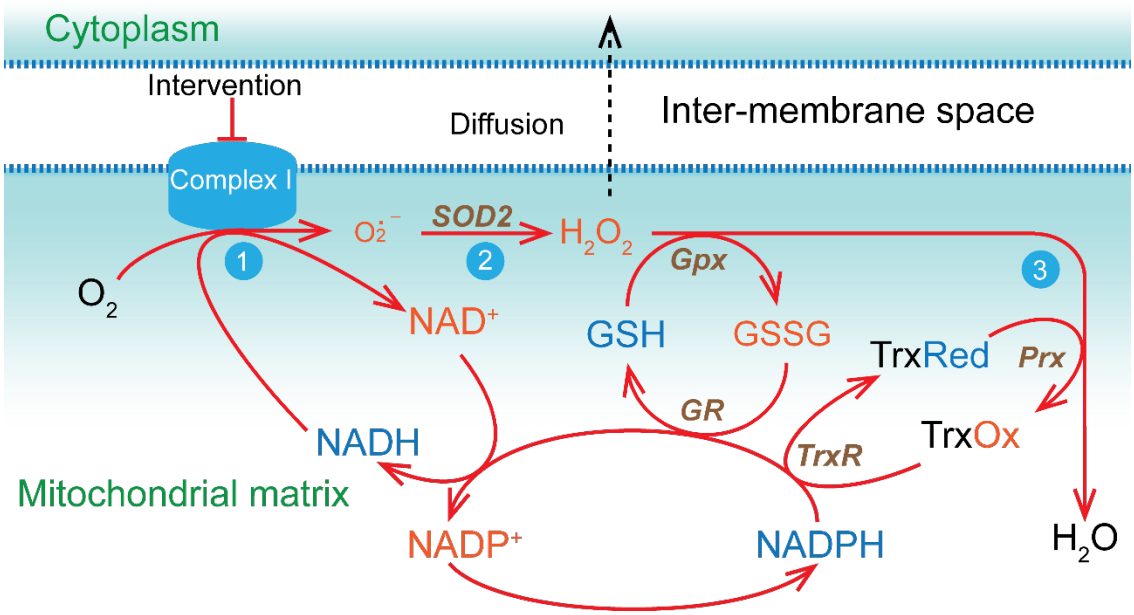

b

Step in ROS pathway	*Key factor*		*CA1 vs. CA3*	*Evidence*
1.Superoxide generation	Complex 1	content	CA1 ≈ CA3	Fig. 4-4 - 4-6
		capacity	CA1 ≈ CA3	Fig. 4-4b (IV) vs. 4-4c (IV)
2.convert from superoxide to H_2O_2	SOD2 system	content	CA1 < CA3	Fig. 4-4 – 4-6
		capacity	CA1 < CA3	Fig. 4-4 – 4-5
3. removal of H_2O_2	GSH system	content	CA1 ≈ CA3	Figure 4-2d
		capacity	CA1 ≈ CA3	Fig. 4-4c (IV) vs. 4-4e (IV) and Fig. 4-5c
	Trx system	content	CA1 < CA3	Fig. 4-4 – 4-6
		capacity	CA1 < CA3	Figure 4-5

Figure 4- 8. Summary of comparison on ROS management between CA1 and CA3.

(a) ROS management in mitochondria. (b) Analysis of the differences in ROS pathway between CA1 and CA3 based on our data. The conclusions with their relative evidences and the deduction process are explicitly discussed in the main text.

Back to the discussion of the OGD-RP data, we by examining the actions of superoxide, H_2O_2, GSH, Trx and NAD(P)H in the ROS pathway in mitochondriawe note that all of them are

redox coupled and connected in a closed loop (Fig. 4-8a). NADH acts as an electron donor to generate superoxide, finally leading to the formation of H_2O_2[225,230]. NADPH, the phosphorylated form of NADH, restores GSH[81] and Trx[272] to their reduced forms, maintaining the reducing capacity of cellular system, while its function in generating ROS is not a main concern in mitochondria[273]; in addition, $NADH/NAD^+$ and $NADPH/NADP^+$ are balanced via transhydrogenase[69,94]. H_2O_2 is in the middle of the ROS pathway, in which $NADH/NAD^+$ and GSH/GSSG & Trx_{Red}/Trx_{Ox} systems located at two opposite terminals for the generation and removal of H_2O_2, respectively.

We find that the OxD_{HS} and OxD_{GS} from OHSCs treated with 15 min 10 μM MD + 20 μM $MnSOD_m$ (Fig. 4-4b (IV), 4-4d (IV)) resemble that in the earlier 15 min of RP (Fig. 4-1g(top), Fig. 4-1h(top)): the H_2O_2 system performs similarly between CA1 and CA3, but the GSH system is less oxidized in CA3. The H_2O_2 levels during RP should be of a similar magnitude as during 10 μM MD + 20 μM $MnSOD_m$. The smaller OxD_{GS} in CA3 during RP can be ascribed to the larger reducing capacity provided by Trx2 in CA3. However, the changes of OxD_{HS} and OxD_{GS} in the neurons during OGD-RP are not first order exponential as during the treatment of MD + $MnSOD_m$. Only complex 1 and SOD2 were regulated in the MD + $MnSOD_m$ treatment. However, more enzymes such as Gpx, GR, Prx and TrxR besides complex 1 and SOD2 could be influenced during OGD-RP. The enzyme activity of SOD2 and Gpx was found to be depressed in neonatal rat hippocampal neurons after 2 h OGD- 24 h RP[274]. In *in vivo* hypoxic exposure (pressure atmosphere = 282 mmHg) assays on adult SD rats, the activity of Gpx in the hippocampus is enhanced, but SOD2 and GR from the hippocampus show lower activity after the experiment[275]. Expression of Prx in mice hippocampus is cut off by ~50% after 1h OGD and 24 h RP[276]. TrxR[277] is de-activated by nitration in myocardial cells from SD rats suffered from 30 min OGD - 3 hr RP. The cellular

metabolism is influenced by OGD-RP in a much more complicated way than by MD + $MnSOD_m$. Despite of the differences in cellular regulation, we still could apply the deduction withdrawn from the experiments with MD, $MnSOD_m$ and AF to interpret the OxD_{HS} and OxD_{GS} data of the OGD-RP experiment. Larger content of Trx2 enables CA3 to remain a lower H_2O_2 level and less oxidized GSH system than CA1 during RP.

In Fig. 4-3, we discover that NAD(P)H is continuing to be consumed in CA3 in OGD-RP after a short temporal elevation in OGD, but NAD(P)H does not change similarly in CA1, in which two elevations of NAD(P)H are found during OGD, and then NAD(P)H oscillates around a relatively higher level in RP than its baseline in the control. A rational explanation for the NAD(P)H elevation in OGD, is that the complex I is suppressed during OGD. Schuchmann et al.[92] described that a transient stimulus of 1 μM rotenone caused an increase in NAD(P)H due to the inhibition of complex 1, and transient bath application of 100 μM glutamate resulted in an increase in NAD(P) due to the activation of citric acid cycle which can replenish NAD(P)H. The elevation of NAD(P)H helps maintain mH_2O_2 and mGSH system at a more reduced state in OGD than CT (Fig. 4-1g, h). Due to the similarity in superoxide generation and complex I content, the consumption of NADH should be similar between CA1 and CA3. The higher requirement of NADPH in CA3 can be attributed to its utilization on restoring the larger pool of Trx2, reducing the depletion of thiols in CA3 (Fig. 4-2d) and maintaining the GSH system at a much more reduced status during RP (OxD_{GS}, CA1 vs. CA3, 0.489 ± 0.020 vs. 0.241 ± 0.035 in Fig. 4-1h). NADPH oscillations in CA1 demonstrates that there are rapid cycles of mitochondrial membrane depolarization/hyperpolarization, evenly matched competition between ROS generation and annihilation[278]. As the oscillation could be diminished with a higher ROS scavenging capability[278],

the absence of oscillation in CA3 indicates its higher reducing capacity to remove ROS by utilizing NADPH.

Our observations support that the Trx system dominates the removal of H_2O_2 under the treatment of 10 μM MD + 20 μM $MnSOD_m$ and RP, and the GSH system only participates to remove a relatively small portion of H_2O_2 until the Trx system is disabled. The more reducing capacity provided by Trx2 in CA3 leads to the higher consumption of NAD(P)H, lower H_2O_2 levels and less oxidation in the GSH system during RP, and results in less susceptibility to OGD-RP.

In order to correlate the regulation of the H_2O_2 level and the oxidation status of the GSH system with the cell death, we measured the cell death in areas CA1 and CA3 under all the treatments that applied in this manuscript (Fig. D-6, 4-7). In general, more cell death is correlated with a higher H_2O_2 level or a more oxidized GSH system. For the MD + $MnSOD_m$ experiments (Fig. 4-4), very little cell death (<10%) with the treatment of 10 μM MD or 20 μM $MnSOD_m$ (Fig. D-6) corresponds to the absence of change in OxD_{HS} and OxD_{GS} with such a treatment in Fig. 4-4b (II) or Fig. D-4; similar or different cell death (CA1 vs. CA3) with the treatment of 10 μM MD + 20 μM $MnSOD_m$, 20 μM MD or 20 μM MD + 20 μM $MnSOD_m$) (Fig. D-6) corresponds to similar or different values (CA1 vs. CA3) of OxD_{GS} and $k_2'[GSH]/k_1'[GSSG]$ (Fig. 4-4d, e, g); with the treatment of 20 μM MD, higher cell death in CA1 (vs. CA3) is correlated with its larger values of OxD_{HS} and $k_1[H_2O_2]$ (Fig. 4-4c, f). For the OGD-RP experiment, compared to CA3, CA1 has more cell death (Fig. 4-4 – 4-7) corresponding to its larger OxD_{HS} and OxD_{GS} (top, Fig. 4-1g, h). A more important correlation that noticed is that the inhibition of Trx by AF increases the cell death (Fig. 4-4 – 4-7), OxD_{HS} (Fig. 4-5b) and OxD_{GS} (Fig. 4-5c) induced by 10 μM MD + 20 μM $MnSOD_m$ and removes the difference of those parameters that once existed in CA1 and CA3. This

indicates that the administration of the Trx system is critical important for regulation of intracellular H_2O_2 and GSH systems. Moreover, we found that applying AF removes the differential cell death in CA1 and CA3 induced by OGD-RP (Fig. 4-4 – 4-7) indicating that the Trx system is the key factor which is contributed to the differential susceptibility to OGD-RP between the two hippocampal areas.

Different from our perspectives, Wang et al.[54-56] attempted to decipher the scenario of the particular sensitivity to oxidative stress of CA1 by collecting transcriptional data of enormous amounts of genes (~174 genes) related with oxidative stress, inflammatory, ion channels, and excitatory and inhibitory responses. They screened out 5 genes such as *Nrf2* and *Nqo1*, which participate in evoking anti-oxidants and have significantly different expression levels in CA1 and CA3[54-56]. However, their statement about higher anti-oxidant related gene expression indicates that higher ROS in CA1 is a little confusing. To our understanding, their focus is that the post-regulation of the expression of anti-oxidant genes responds to the overwhelmed antioxidant systems by the excessive oxidative stress. In contrast, our research focuses on the presence of ROS generating and anti-oxidant capacity when facing ongoing oxidative stress, then extends to the post-insult neuronal damage. It is inappropriate to directly compare our data with Wang et al.'s [54-56]. We are checking into different time scope (us: in ROS stress; Wang: post ROS stress) and causal relationship (us: what → ROS stress; Wang: ROS stress → what). For instance, the higher anti-oxidant capacity of CA3 is in our case likely not due to activation of the Nrf2 system by OGD. The sequence of a putative activation of Nrf2 involves increased ROS in the cytoplasm to a level high enough to activate Nrf2, transport of Nrf2 to the nucleus, transcription of Nrf2-regulated genes, translation in the cytoplasm and then transport to the mitochondria. We found no evidence for an increase in ROS in the cytoplasm where the sequence of Nrf2 activation starts. Even if the

Nrf2 system was activated by OGD-RP the time scale in our experiment (70 min) is too short to allow for substantial elevated Nrf2-driven anti-oxidant capacity. In vivo oxygen deprivation by MCA occlusion causes upregulation of Nrf2-regulated proteins but the maximum and significant upregulation were found after 24h while no increases were reported after 8h[279,280]. In another study on global ischemia an upregulation of HO-1, a Nrf2-regulated protein, was maximal after 72h with a small increase observed after 1h (< 10% of maximum)[281]. In addition, using a similar experimental set-up as ours (OGD in OHSCs followed by reoxygenation for 24h), Parada et al. found no increase in Nrf2-regulated proteins after 24h and no difference in toxicity between OHCs from Nrf2 knock-outs and normal animals[282].

In summary, CA3 is less vulnerable to OGD-RP than CA1 because it maintains its H_2O_2 and mGSH systems at a lower oxidative state when facing the OGD-RP insult, and thus avoids long-term damage initiated by excessive ROS [213,215,220-224]. CA3 can remove excessive H_2O_2 better due to that it has a larger in Trx2 system and utilizes NADPH to replenish its antioxidants more efficaciously. CA3 is also more efficient in producing H_2O_2 from similar superoxide generation (vs.CA1), which does not compromise its capability to keep H_2O_2 at lower level. These indicates that reducing capacity is the determining factor against oxidative stress. In the comparison of the two critical reducing pools, the Trx2 and mGSH systems, our data demonstrate that mGSH is maintained at a relatively reduced state passively by Trx2 rather than participating in H_2O_2 removal. We found that the differential cell death after OGD-RP is dependent on the differential H_2O_2 level and oxidation status of the GSH system in CA1 and CA3. Our evidence show that a larger Trx2 system is proposed to result in less vulnerability of CA3 to OGD-RP.

4.5 ACKNOWLEDGEMENT

This work is supported by NIH Grant R01 GM066018. We thank Tom Harper (Department of Biological sciences, University of Pittsburgh) for advice on imaging; Professor Alexander Deiters, Jihe Liu, Ji Luo and Xinyu Chen (Department of Chemistry, University of Pittsburgh) for help with Western blot experiment; Professor Mona F. Melhem (MD, Veterans' Affairs Medical Center in Pittsburgh) and Krishna Prasadan (Children's Hospital of Pittsburgh) for laser capture microdissection; Prof. Ines Batinic-Haberle (Duke University Medical Center) provided the drug, MnTnBuOE-2-PyP^{5}+. Thanks to the thoughtful and productive discussion with Prof. Satish Lyengar (Department of Statistics, University of Pittsburgh) about the statistical analysis of linear and nonlinear curves comparison. Bowen Yi (Department of Statistics, University of Pittsburgh) generously assisted with coding in the software R.

5.0 SUMMARY AND FUTURE DIRECTIONS

A good model for studying cerebral ischemia is oxygen glucose deprivation (OGD)[37-39]. Abundant evidence supports the damaging nature of excess reactive oxygen species (ROS)[55] in cells, which can be converted into less reactive H_2O_2[81]; then H_2O_2 can be scavenged by glutathione (GSH), which is oxidized to glutathione disulfide (GSSG)[81]. Monitoring H_2O_2 and GSH during OGD-reperfusion is a promising way to investigate the course of ischemic injury. We are unaware of single-cell investigations in tissue though there is a rich literature about this problem. Thus we have developed an approach using the organotypic hippocampal slice culture (OHSC), and employ green fluorescent protein (GFP)-based sensors[119,132], which are selectively sensitive to H_2O_2 or GSH. In order to precisely control OGD/RP experiment condition and report reliable OxD_{roGFP2} and E_{GSH}, we optimized the protocol in several important ways. 1) We improved the delivery of oxygen and glucose to the tissue cultures so that the timescale of the changes reflect those found *in vivo*. 2) We optimized the transfection protocol to yield neurons expressing the Grx1-roGFP2 in a narrow range of depths in OHSCs. The chosen range of depths corresponds to a range in which changes in pO_2 are reproducible. 3) Deriving OxD_{roGFP2} and E_{GSH} requires a redox insensitive marker to act as a reference intensity during the calibration process following OGD/RP. We introduced tdTomato, a redox insensitive fluorescent protein, specifically to exclude the apparent effect of changes in cell size on the fluorescent signal of Grx1-roGFP2.

We tested this optimized protocol on different cell types (HeLa/pyramidal/astrocyte) and cellular compartments (mitochondria/cytosol), and found no observable OGD-RP induced changes in cytoplasmic GSH in any cell type, but obvious changes in mitochondrial GSH in pyramidal cells and astrocytes. Opposite changes in OGD and RP are due to the absence (OGD)/presence (RP) of

ROS and MM depolarization (OGD) and hyperpolarization (RP). The differential performance in their GSH system is due to their differences in tendency of MM depolarization, ROS production and GSH pool size.

In order to understand the differential susceptibility of hippocampal pyramidal cells in CA1 and CA3, we investigated the difference in mitochondrial reactive oxygen species (mROS) management by using roGFP-based fluorescent sensors for peroxide and the GSH system[79,119,132] transfected into individual pyramidal neurons in organotypic hippocampal slice cultures. We controlled three key steps in mROS production and removal: 1) superoxide generation at complex I with menadione (MD)[254]; 2) superoxide dismutation via mitochondrial superoxide dismutase (SOD2)[81] with its mimic (MnTnBuOE-2-PyP^{5+}, $MnSOD_m$)[237] ; 3) thioredoxin (Trx2) activity[81,82] with auranofin[228]. We measured the oxidation degrees of roGFP-based sensors[120] for H_2O_2 (OxD_{HS}) and GSH (OxD_{GS}). Relative quantitation of complex 1, SOD2 and Trx2 was carried out with immunofluorescence and Western blots. We observed similar superoxide generation rates in CA1 and CA3 consistent with our finding of similar complex I levels. However, CA1 has less SOD2 than CA3 which produces less peroxide. Nonetheless, CA1 has a higher steady-state OxD_{HS} and OxD_{GS} than CA3. Inhibition of Trx2 leads to statistically indistinguishable OxD_{HS} and OxD_{GS} in CA1 and CA3.The inferiority of CA1's ROS handling is mainly due to its lower activity of Trx2 in comparison to CA3.

Using this optimized protocol, we found that the time dependence of the redox status of the H_2O_2 and GSH system provides new, and perhaps complementary information to that obtained by more classical fluorescence-based techniques. This method could be broadly applied to other types of studies such as pharmacological investigations of H_2O_2 and GSH-related enzymes[46].

APPENDIX A

1.3 FLUORESCENCE IMAGING FOR MONITORING THE ROS RELATED CRITICAL MOLECULES

This Appendix contains information for section 1.3 *Fluorescence imaging for monitoring the ROS related critical molecules.*

A.1 Fluorescence imaging of NAD(P)H

There are more information about Peredox and Frex.

Table A-1. Fluorescence probes for NAD(P)H.

Name	Exi/Emi	Reversible	pH sensitive [b] (4-9)	*in vivo* Application	REF	Reaction Mechanism
NAD(P)H	340/460	Yes	Yes	Natural molecule	94	Molecule itself
Genetically Coded Protein Sensor						
Peredox	440/510	Yes	Yes	Transfection	96	NADH-binding protein, Rex
Frex® (Mito/Cyto)	400&510 /530	Yes	Yes	Transfection	97	NADH-binding protein, Rex

Superscript b: pH sensitivity of fluorescent spectra (only) of the sensor; Superscript ®: Ratiometric imaging probe

A NADH/NAD^+ redox sensitive sensor, Peredox, is constructed in Yellen group[96]. Its fluorescent intensity (FI) increases with the binding of NADH to its functional subunit, Rex[96]. Normalized fluorescence (NF) is obtained from correcting FI by fluorescence of its incorporated red fluorescent protein, mCherry (Exi/Emi: 587/610 nm, internal standard)[96]. This sensor is pH sensitive. NF[96] responds nonlinearly to the ratio of [NADH] × $[H^+]/[NAD^+]$ in a range of $0 \sim 8\times10^{-11}$. This sensor is sensitive enough to detect the redox change of NADH within 1 min, and its FI

is ~58 times brighter than the auto-fluorescence of NAD(P)H[96]. However, it is not good to work in mitochondria as the mitochondrial [NADH]/[NAD^+] is too high and beyond its detection range[96]. The other NADH sensor, Frex, also contains the NADH-binding unit, Rex[97]. This ratiometric sensor is highly selective for NADH, and has no response to NAD^+, NADP(H), ATP and other abundant adenine nucleotides. Thus its ratio of F_{510}/F_{400} (F_{400} and F_{510} are respective fluorescence at excitation 400 and 510 nm) is not a function of [NADH]/[NAD^+][97]. Frex nonlinearly responses to 0 ~ 40 μM NADH, and can be used in mitochondria (~ 30 μM NADH) and cytosol (~ 0.12 μM NADH)[97]. However, F_{510}/F_{400} of NADH binding Frex is unstable over time when [NADH] ≤ 40 μM, and its signal decays by more than 50% within 14 min after adding NADH, which will compromise its application in real-time measurement of cellular NADH[97]. Moreover, Frex is pH sensitive and its application needs pH control[97].

A.2 Fluorescence imaging of superoxide and H_2O_2

2-Me-TeR is not discussed in section 1.3.2.

Recently a novel ROS sensor, 2-Me-TeR (tellurium containing rhodamine dye), is developed in the Nagano Lab[283]. Its becomes fluorescent once it is oxidized into 2-Me-TeOR[283]. Its advantage over $DCFH_2$ is that it can directly detect the dynamic change of ROS since its oxidation/reduction is reversible[283]. 2-Me-TeOR, have relative pH stability in the range of pH = 5 – 9, and experience sharp FI drop below pH = 4[283]. Its pharmacological effects on cellular system and potential cellular interference on its application have not been reported.

Table A-2. Fluorescence probes for ROS.

Name	Exi/Emi	Reversible	pH sensitive [b] (4-9)	*in vivo* Application	REF	Reaction Mechanism

Small Molecule Probe						
$DCFH_2$	493/521	No	Yes	Staining	[98,99]	Oxidation
2-Me-TeR	669/686	Yes	slightly	Staining	[283]	Oxidation of Tellurium atom
Genetically Coded Protein Sensor						
rxYFP	512/523	Yes	Yes	Transfection	[104]	Thiol-disulfide redox interchange
roGFP1® (mito/cyto)	400 & 475/ 510	Yes	No	Transfection	[105]	Thiol-disulfide redox interchange
roGFP2 ® (mito/cyto)	400 & 490/ 510	Yes	No	Transfection	[106]	Thiol-disulfide redox interchange

Superscript b: pH sensitivity of fluorescent spectra (only) of the sensor; Superscript ®: Ratiometric imaging probe

Table A-3. Selective fluorescence probes for Superoxide.

Name	Exi/Emi	Reversible	pH sensitive [b] (4-9)	*in vivo* Application	REF	Reaction Mechanism
Small Molecule Probe						
DHE	369/580	No	No	Staining	[109]	Oxidation
MitoSOX	369/580	No	No	Staining	[108]	Oxidation
Genetically Coded Protein Sensor						
mito-cpYFP®	405 & 488/>505	Yes	Yes	Transfection	[114]	unclear

Superscript b: pH sensitivity of fluorescent spectra (only) of the sensor; Superscript ®: Ratiometric imaging probe

A putative protein superoxide sensor, mito-cpYFP is a reversible probe, and can be used for long term imaging. However, Schwarzlander and his colleagues strongly questioned whether mito-cpYFP senses superoxide or pH[115]. They pointed out there is no redox sensitive subunit in this protein could direct its reaction with superoxide and cause relative change in its own fluorophore[115] and the sensor failed to represent the right change of superoxide under some classic regulations which have been tested repetitively in past researches[284]. Unlike mito-cpYFP, DHE and MitoSox are unlikely to be pH sensitive and no such records for their pH sensitivity has been found so far.

Table A-4. Selective fluorescence probes for H_2O_2

Name	Exi/Emi	Reversible	pH sensitive [b] (4-9)	*in vivo* Application	REF	Reaction Mechanism
Small Molecule Probe						
Amplex Red	560/590	No	Yes	No	[285]	Oxidation
PX-1; PF-1; PR-1 [a]	350/440; 450/470; 575/585	No	unclear	Staining	[286]	BDM
RPF-1 ® [a]	420/464 &517	No	unclear	Staining	[287]	BDM
PL-1® [a]	410 & 475/540	No	unclear	Staining	[288]	BDM
PY1; MitoPY1 [a]	519/548; 510/528	No	unclear	Staining	[289]	BDM
PY1-ME [a]	515/540	No	unclear	Staining	[290]	BDM
PO1; PF-2; PF-3 [a]	540/565; 475/511; 492/515	No	unclear	Staining	[291]	BDM
PF6-AM [a]	482/517	No	unclear	Staining	[292]	BDM
PN1 [a]	750(TP)/425&525	No	No	Staining	[293]	BDM
QCy7	595/635	No	unclear	Staining	[294]	BDM
SHP-Mito	750(TP)/435&565	No	No	Staining	[295]	BDM
FP-H_2O_2-NO	400/460	No	unclear	Staining	[296]	BDM
Probe 3	400 & 484/566	No	Yes	Staining	[297]	BDM
RF-1 [a]	495/503	Yes	unclear	Staining	[298]	Thiol-disulfide redox exchange
Genetically Coded Protein Sensor						
Hyper® (mito /cyto)	420 & 500/516	Yes	Yes	Transfection	[116]	Thiol-disulfide redox interchange
Hyper 2®	420 & 500/516	Yes	Yes	Transfection	[117]	Thiol-disulfide redox interchange
Hyper 3®	420 & 500/516	Yes	Yes	Transfection	[118]	Thiol-disulfide redox interchange
roGFP2-Orp1® (mito/cyto)	400 & 490/ 510	Yes	No	Transfection	[119]	Thiol-disulfide redox interchange

Superscript a: from the Chang Lab; Superscript b: pH sensitivity of fluorescent spectra (only) of the sensor; Superscript ®: Ratiometric imaging probe
BDM: Boronate deprotection mechanism.

10-Acetyl-3,7-dihydroxyphenoxazine (Amplex red) is a H_2O_2 sensitive dye that is converted to fluorescent resorufin with the aid of Horseradish peroxidase[285]. This sensor is usually used for extracellular H_2O_2 assay with incubation time of ~10 min[285]. Amplex red is pH sensitive , especially in the range of 4 ~ 9[299].

There are a series of small molecule H_2O_2 sensors based on boronate deprotection mechanism developed in Chang Lab in the past ten years[286-293,298,300-303]. Peroxyxanthone-1 (PX1), Peroxyfluor-1 (PF1) and Peroxyresorufin-1 (PR1) are blue, green and red fluorescent probes reported in 2005. The selective H_2O_2 deprotection of two boronic ester groups of the xanthenone scafold induces fluorescence[286]. Ratio-Peroxyfluor-1 (RPF1) is a derivative of PF1, which has a coumarin donor and boronate protected fluorescein acceptor[287]. Fluorescence resonance energy transfer occurs and causes the fluorescence emission shift from 464 nm to 517 nm (Exi: 420 nm) once H_2O_2 removes the boronate groups[287]. The increase in F_{510}/F_{464} indicates the presence of H_2O_2[287]. In 2008, Peroxy Lucifer 1 (PL1) is a green fluorescent aminonaphthalimide with boronate-based carbamate group before H_2O_2 cleavage[288]. Peroxy yellow (PY1), the mitochondrial version of PY1 (MitoPY1) are rhodol derivatives[289]. Its methyl ester form of PY1, PY1-ME, was developed to increase the cellular retention after staining[290]. In 2010 and 2011, Dickinson and his colleagues synthesized several boronate protected H_2O_2 sensors, Peroxy Orange (PO1), Peroxyfluor-2 (PF-2), Peroxyfluor-3 (PF-3), Peroxy Emerald 1 (PE1) and Peroxyfluor-6-acetoxymethyl ester (PF6-AM)[291,292]. PF-2, PF-3, and PF6-AM have similar structures (boronate protected fluorescein analogs) as PF-1, but have different visible fluorescence spectra upon the H_2O_2 deprotection. PE1 is classified as a rhodol derivative like PY1 and PO1, similar to fluorescein in molecular structure[291,292]. Peroxy Naphthalene 1 (PN1) is a ratiometric H_2O_2 sensor with boronate-based carbamate group, which can be excited by near infrared light[293]. The kinetic response of these sensors in 1~5 μM with 1 ~10 mM H_2O_2 is slow at 25°C, pH = 7.4. For instance, the time for ½ full reaction ($t_{1/2}$) with H_2O_2 is ~ 21, 12 and 19 min for PF1, PR1 and PX1, respectively[286]; $t_{1/2}$ for RPF1 is ~60 min[287]; $t_{1/2}$ for PL1 = 13 min[288]; PY1 has $t_{1/2}$ = 6 min, which should be similar in mitoPY1 and PY1-ME[289]; PO1, PF-2, PF-3, and PF6-AM, $t_{1/2}$ = 1.4 ~ 3.5

min[291,292]. PN1 $t_{1/2}$ = 12.1 min[293]. In practical term, PE1 is most favored for its relative rapid reactions with H_2O_2 ($t_{1/2}$ = 1.4 min) among these sensors. PO1, PF-2, PF-3, and PF6-AM would be dyes with acceptable reaction time with H_2O_2, ~ 10 - 20 min. Redoxfluor-1 (RF1) is the only reversible small-molecule H_2O_2 sensor discussed here. It is a fluorescein derivative, can be reversibly oxidized by H_2O_2 and reduced by reducing reagents (e.g. tris(2-carboxyethyl)phosphine, sodium dithionite, and NaBH4)[298]. The sensor has a relative rapid response to H_2O_2 ($t_{1/2}$ = 17 s), which can be used to achieve a H_2O_2 profile with a time resolution of 1 ~ 2 min[298].

Our big concern here is that the pH sensitivity of these sensors from Chang Lab mentioned above have not been tested except that PN1 has been proven to be pH insensitive[286-293,298,300-303]. It is highly possible that these sensors are pH sensitive since they mimic the molecular structure of fluorescein (a pH sensitive dye)[304].

Irreversible H_2O_2 sensors have also been developed in other groups in the past three years. QCy7 is a boronate protected cyanine dye with $t_{1/2}$ for reaction with H_2O_2, ~ 7 min and untested pH sensitivity[294]. SHP-Mito is a ratiometric sensor, which means its yellow and blue fluorescence intensities change upon cleavage of boronate containing carbamate group by H_2O_2 ($t_{1/2}$ = 11.6 min), and it is pH insensitive[295]. FP-H_2O_2-NO is coumarin-rhodamine coupled ratiometric dye with boronate protected hydroxyl group at 7' carbon site of the coumarin subunit[296]. It has three independant fluorescence signals responding to H_2O_2, NO and H_2O_2/NO, respectively, and needs 30 min to equilibrate with H_2O_2[296]. The pH sensitivity of this sensor has not been tested[296]. Probe 3 (informal name by the author) constructed by Kumar et al. is a boronate protected ratiometric sensor[297]. This sensor is not recommened for biological application because it reacts slowly with

H_2O_2 (predicted $t_{1/2}$ > 15 min) and experiences drastic changes in its fluorescence spectra under various pH[297].

Genetically coded protein sensors, Hyper, Hyper-2, Hyper-3 and roGFP2-Orp1 have been discussed in Section 1.3.2.

A.3 Fluorescence imaging of Glutathione and Thioredoxin

Firstly, we choose to not to discuss about the probes that could selectively target particular thiols such as cysteine (Cys), homocysteine (Hcy) and glutathione (GSH). Several general thiol probes have been developed based on different mechanisms. Monobromobimane (mBrB) was first reported in 1981, and it yields a fluorescent thiol adduct by replacing a bromide group with a thiol group[305]. General incubation time for derivatizing thiols is ~ 15 min[306]. mBrB is pH sensitive; metallothionein (a thiol) experiences different derivation efficiency under various pHs[306]. The reaction rate of Cys with mBrB varies with different pHs; faster reaction is often achieved under basic condition (pH > 7), but its thiol-adduct is unstable when pH > 10.

Table A-5. Fluorescence probes for Thiols

Name	Exi/Emi	Reversible	pH sensitive [b] (4-9)	*in vivo* Application	REF	Reaction Mechanism
Small Molecule Probe						
mBrB	380/480	No	Yes	Staining	[305]	nucleophilic substitution
CPM	390/465	No	Yes	Staining	[121]	Michael addition
Thioglo-1	379/513	No	No	Staining	[124]	Michael addition
Dansyl maleimide 7; Coumarin maleimide 11a, b; Phthalimide maleimide 30	342/530; 430/480; 394/458	No	unclear	Staining	[123]	Michael addition
Thioglo-3; Thioglo-5	378/446; 365/536	No	unclear	Staining	[307]	Michael addition
o-Maleimide-BODIPY	505/520	No	No	Staining	[128]	Michael addition

Thiol Probe IV	400/465	No	Yes	Staining	[129]	Michael addition
Probe 1 ®	420/466 &553	No	No	Staining	[130]	Michael addition
Ratio-HPSSC®	350/459 & 658	No	Yes	Staining	[308]	Cleavage of disulfide bond
SSH-Mito®	740 (TP) /462 & 545	No	No	Staining	[309]	Cleavage of disulfide bond
NRFTP ®	488/515&610	No	Yes	Staining	[310]	Cleavage of thioester
Cy-NiSe; Cy-TfSe	635/750; 635/750	No	No	Staining	[311]	Cleavage of Se-N bond
DNBSCy	600/700	No	Yes	Staining	[312]	Cleavage of sulfonate ester
3-HTC®	370 & 448/500	Yes	unclear	Staining	[313]	Thiol-disulfide redox interchange
Cy-O-Eb®	768/794	Yes	unclear	Staining	[314]	Form (Oxidize) and break (reduce) and the Se-N bond

*Any specific-thiol selective probes are not included; Superscript b: pH sensitivity of fluorescent spectra (only) of the sensor; Superscript ®: Ratiometric imaging probe

Most of the thiol dyes based on Michael addition have been discussed in Section 1.3.3. Probe 1 (informal name by the author)[130] are coumarin-enone based thiol sensors. The addition of thiol to enone causes fluorescence[129] or spectral shift[130]. Probe 1 is a slow probe with a reaction rate constant, 6.98×10^{-2} $M^{-1} \cdot s^{-1}$ and $t_{1/2} \approx 16.6$ min under the presence of 10 mM thiol, but its thiol adduct is pH insensitive[130].

Several thiol probes based on other mechanisms have been developed in the past five years. Ratio-HPSSC[308] and SSH-Mito[309] are ratiometric thiol probes. Their detection of thiols upon that cleavage of disulfide bond causes relative changes at two fluorescence channels[308,309]. Both dyes equilibrate with 1 mM thiol slowly (Ratio-HPSSC, $t_{1/2} > 10$ min; SSH-Mito, $t_{1/2} \approx 38.5$ min), but the difference is that Ratio-HPSSC is pH sensitive, but SSH-Mito is not[308,309]. NRFTP contains a rhodamine and a BODIPY dye linked by a thioester group[310]. Cleavage of the thioester by thiol can modulate the energy transfer between the two dye units causing relative changes of F_{510} and F_{590}. Complete reaction between the dye and thiol requires ~ 23 min[310]. The dye after thiol

incubation is pH stable between 7.4 ~ 10, but is sensitive to pH < 7[310]. DNBSCy converts fluorescent heptamethine cyanine (Cy)-quinone after cleavage of sulfonate ester bond. It can react with 2 mM GSH completely less than 1 min, but it is pH sensitive[312]. Similar to DNBSCy, Cy-NiSe and Cy-TfSe also have the Cy scaffold with fluorescence turned on after breaking Se-N bond by thiols[311]. The two sensors (5 μM) completely react with 5 μM GSH in 3 ~ 5 min, and they show excellent pH stability[311]. There are two reversible probes for sensing thiol discussed here: 3-hetaryl-7-thiol coumarin (3-HTC)[313] and heptamethine cyanine-o-ebselen (Cy-o-Eb)[314]. 3-HTC can sense the change of the ratio [GSH]/[GSSG] in the range of 10^{-3} to 10^{3} based on the disulfide exchange[313]. About ten minutes is required to achieve redox equilibrium with [GSH]/[GSSG][313]. Cy-o-Eb is not a pure thiol sensor, which has been evaluated with H_2O_2 (oxidant) and GSH (reductant)[314]. The sensor responds linearly to H_2O_2 (0 ~ 200 μM) and GSH (0 ~ 20 μM), and takes ~ 25 min or 5 min to equilibrate with 200 μM H_2O_2 or 20 μM GSH[314]. The pH sensitivity of 3-HTC and Cy-o-Eb has not been tested.

Table A-6. Selective fluorescence probes for GSH

Name	Exi/Emi	Reversible	pH sensitive [b] (4-9)	*in vivo* Application	REF	Reaction Mechanism
Small Molecule Probe						
mCB	380/470	No	unclear	Staining	[315]	nucleophilic substitution
BODIPY 1a ®	550/556 & 588	No	unclear	Staining	[316]	nucleophilic substitution
Bis-spiropyran 1a	446/643	No	slightly	Staining	[317]	GSH binding
Genetically Coded Protein Sensor						
Grx1-roGFP®	400 & 490/ 510	Yes	no	Transfection	[132]	Thiol-disulfide redox interchange

Superscript b: pH sensitivity of fluorescent spectra (only) of the sensor; Superscript ®: Ratiometric imaging probe

In theory, GSH sensors have the potential to react with all types of thiols such as Cys and Hcy, but they selectively target GSH or have distinguishable signal of their adduct with GSH than

that with other thiols. Monochlorobimane (mCB) and BODIPY 1a are two nucleophilic-substitution type dyes developed in 1981 and 2012, respectively. mCB is a highly active dye, which has been widely used for more than 30 years. In contrast to mBrB, mCB selectively targets GSH . The reaction between mCB and GSH is complete in 5 min[131]. BODIPY 1a is also an active dye with 1st order reaction rate constant, 4.6×10^{-2} s^{-1} and $t_{1/2} \approx 15$ s[316]. Its reaction with GSH can be finished within 2 min, and F_{588}/F_{556} linearly corresponds to GSH in a range of 0 ~ 60 μM[316]. We have not found any information regarding pH sensitivity for mCB and BODIPY 1a. Bis-spiropyran 1a detects GSH upon the binding of GSH with a high affinity constant[317], $K = 7.52 \times 10^4$ M^{-1}. As its reaction with GSH strongly favors association, Bis-spiropyran 1a is unlikely to be a reversible dye[317]. Both this free dye and its-GSH adduct show relative pH stability between pH > 5, but their FI change and get enhanced when pH < 5[317].

Table A-7. Fluorescence probes for Trx

Name	Exi/Emi	Reversible	pH sensitive [b] (4-9)	*in vivo* Application	REF	Reaction Mechanism
Thioredoxin probe 1	430/535	No	unclear	Yes	[318]	Disulfide cleavage
Mito-Naph	428/531	No	unclear	Yes	[319]	Disulfide cleavage

Superscript b: pH sensitivity of fluorescent spectra (only) of the sensor;

There are a very few Trx sensors developed in recent years. Lee et al. constructed two Trx probes, Thioredoxin probe 1 (for use in cytosol)[318] and Mito-Naph (for use in mitochondria)[319]. Trx attacks the disulfide bond to cleave the carbamate group from the naphthalimide unit (fluorescent spectra subject to change). Both of the sensors equilibrate with Trx slowly (~ 30 min incubation time needed). The other drawback is that the severe interference from Cys and Hcy is unavoidable.

APPENDIX B

2.0 OPTIMIZE SUPERFUSION SYSTEM AND RATIOMETRIC IMAGING ON ROGFP2 BASED SENSOR TO MONITOR THE REDOX CHANGE IN ORGANOTYPIC HIPPOCAMPUS SLICE CULTURE DURING OGD-RP

This Appendix contains information for section 2.0 *Optimize superfusion system and ratiometric imaging on roGFP2 based sensor to monitor the redox change in organotypic hippocampus slice culture during OGD-RP*.

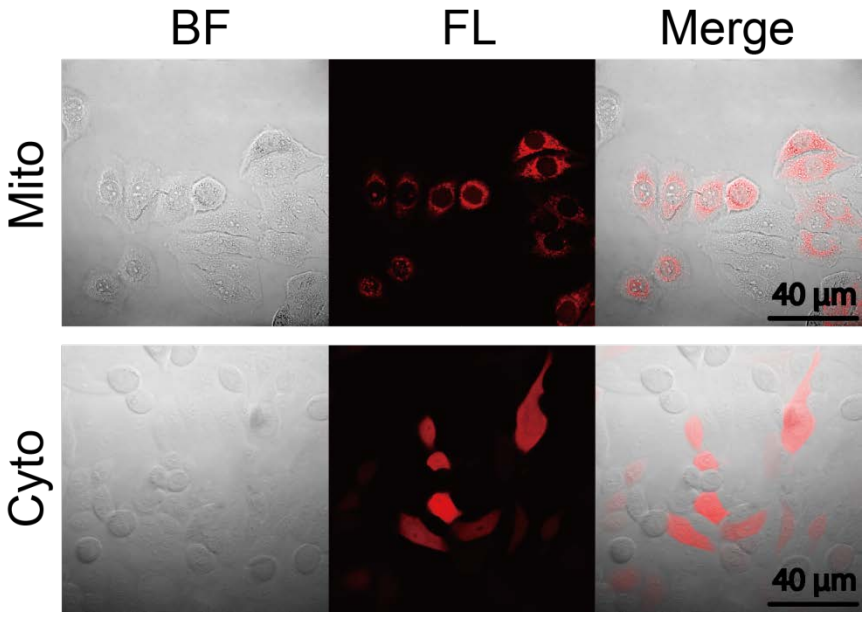

Figure B-1. Lipofectamine-aided transfection in HeLa cells.

Red fluorescence protein (RFP), tdTomato is expressed in mitochondria (top row) or cytoplasm (bottom row) in HeLa cells. Images are bright field (BF), fluorescence (FL) and merged from left to right.

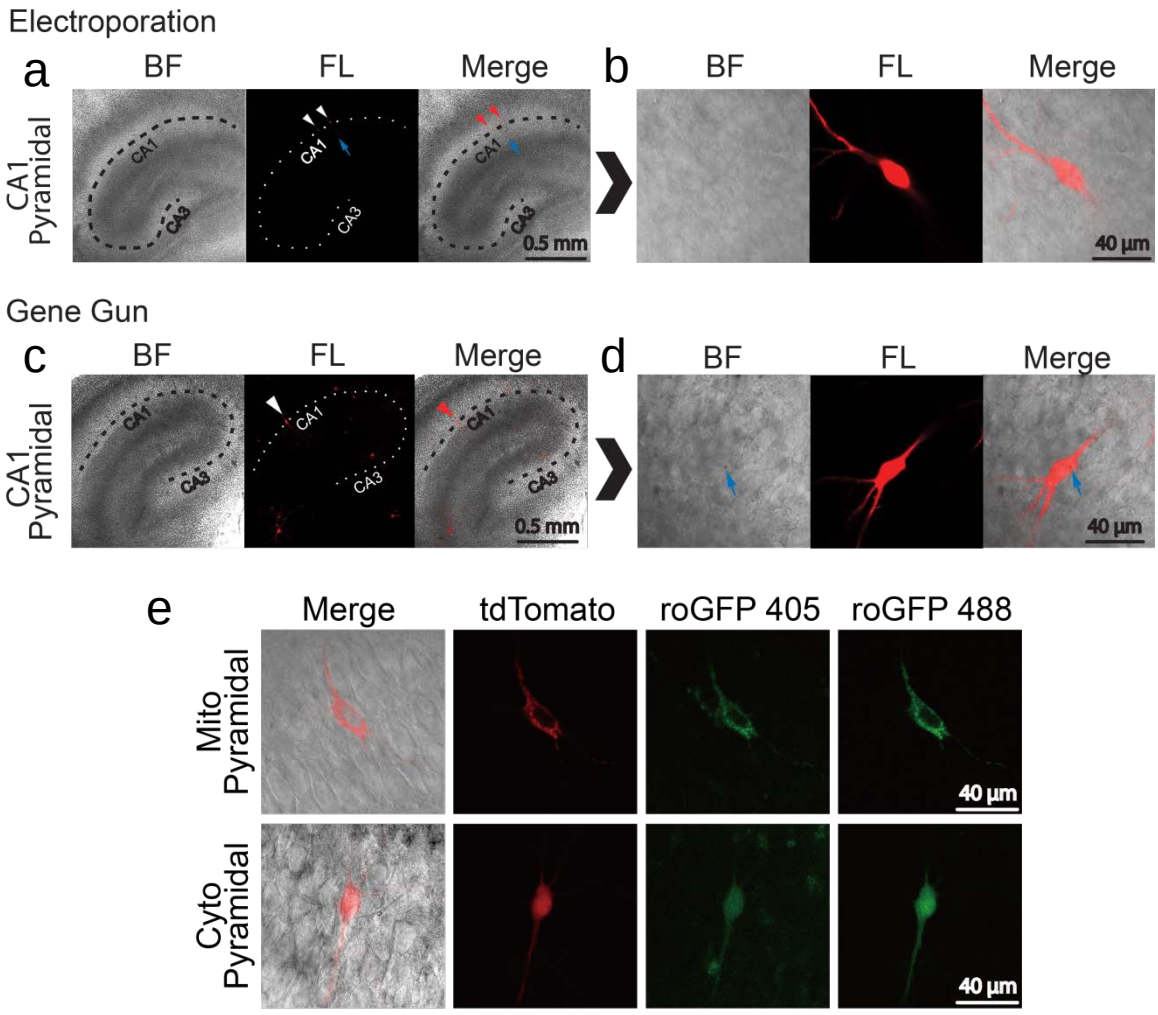

Figure B-2. Plasmid transfection of CA1 pyramidal cells inside OHSCs

Plasmid coding for tdTomato is transfected into cells in OHSCs by single cell electroporation (a and b) or gene gun (c and d). Images in (a) and (c) are taken with a 5x objective lens to give bright field (BF), fluorescence (FL) and merged images. The dotted line indicates approximately the Cornu Ammonis (CA). Electroporation was applied to 2~3 pyramidal cells in region CA1 per OHSC, and succeeded in 1~2 cells (pointed out by red arrows (FL) and white arrows (merge) in (a). Gene gun-enabled transfection on 10~15 cells per OHSC. Cells, highlighted by the blue arrow in (a) or by white in (c), are enlarged in (b) and (d), (63x objective lens). The gene gun will introduce gold particles(blue arrows in d) into the transfected cells. (e) Grx1-roGFP2 and tdTomato co-expressed in mitochondria or cytoplasm in pyramidal cells in OHSCs. Images of merge, tdTomato, 405 nm excitation of Grx1-roGFP2 and 488 nm excitation of Grx1-roGFP2 are shown from left to right.

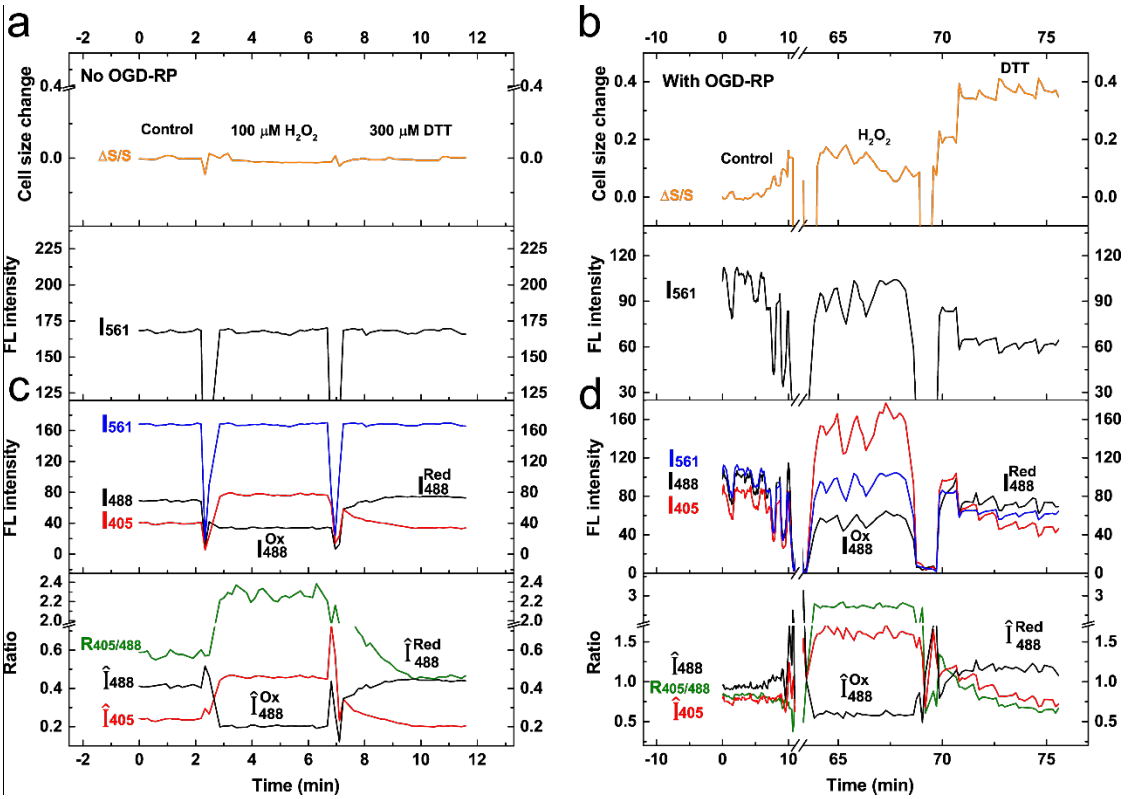

Figure B-3. tdTomato used as internal standard to correct the calibration signal from Grx1-roGFP2 in HeLa cells.

Cytosolic Grx1-roGFP2 and tdTomato are co-expressed in HeLa cells. tdTomato is not sensitive to calibrants in HeLa cells. Fluorescence emission of tdTomato (excited at 561 nm) and Grx1-roGFP2 (excited at 405 and 488 nm) recorded. **(a)** Top: With no OGD/RP, the cell area does not change during exposure to calibrants H_2O_2 and DTT. Bottom: tdTomato fluorescence emission is not sensitive to H_2O_2 and DTT. **(b)** With OGD/RP, Top: cell size changes dramatically, does not reach a steady state, and oscillates. Bottom: Fluorescence signal from tdTomato is inversely correlated with changes in cell size. **(c)** The absolute intensities (Top) and ratios (bottom) from the three channels are obtained when exposed to ACSF, H_2O_2 and DTT with no OGD/RP. The Grx1-roGFP2 fluorescence shows dramatic changes. No difference in trend are observed when comparing absolute intensities and ratios (I_{405} vs. $\hat{I}_{405}$, I_{488} vs. $\hat{I}_{488}$). **(d)** tdTomato calibration is necessary on single channel 405 nm or 488 nm (see the difference in I_{405} vs. $\hat{I}_{405}$, I_{488} vs. $\hat{I}_{488}$ when exposed to DTT) after OHSCs are continuously superfused for ~1.5 h during an OGD/RP experiment with the superfusion setup [O+V] as described in Figure 2-1. Fluorescence traces prior to OGD/RP (control) and during calibration post-OGD/RP with H_2O_2 and DTT are shown (note the break in the time axis). $\hat{I}_{488}^{Red}$ ($I_{488}^{Red}/I_{561}^{Red}$. See Eq. 2.1, section 2.2.3) in (Bottom, d) is significantly more stable than the I_{488}^{Red} fluorescent signal in (Top, d). The

confounding effects of OGD-induced cell size changes on I_{488} are corrected by I_{561} (Equation 2.1, section 2.2.3). $\hat{I}_{488}^{Ox}$ and $\hat{I}_{488}^{Red}$ (the corrected I_{488} at full oxidation and reduction) are used to calculate the oxidation degree of Grx1-roGFP2, OxD_{roGFP2} (see section 2.2.3 for more details).

pH effect on NADPH/NADP+ and GSH/GSSG system

$$NADP^+ + H^+ + 2e^- \rightarrow NADPH \quad \text{(Eq. A.1)}$$

$$\Delta E_{NADPH/NADP+} = \frac{RT}{2F} \ln \frac{[H^+]_e}{[H^+]_s} = -30.65\ \Delta pH\ (mV) \quad \text{(Eq. A.2)}$$

$$GSSG + 2H^+ + 2e^- \rightarrow 2GSH \quad \text{(Eq. A.3)}$$

$$\Delta E_{GSH/GSSG} = \frac{RT}{2F} \ln \frac{[H^+]_e^2}{[H^+]_s^2} = -61.3\ \Delta pH\ (mV) \quad \text{(Eq. A.4)}$$

$$NADPH + GSSG + H^+ \rightarrow 2GSH + NADP^+ \quad \text{(Eq. A.5)}$$

$$\Delta E = \Delta E_{GSH/GSSG} - \Delta E_{\frac{NADPH}{NADP}+} = -30.65\ \Delta pH\ (mV) \quad \text{(Eq. A.6)}$$

In which $R = 8.315\ J\ K^{-1}mol^{-1}; T = 309.15\ K$; $[H^+]_s$ and $[H^+]_e$ are start and end proton concentration with pH change. If pH changes from 8 to 7, ΔE will equal 30.65 mV, indicating the reaction in Eq. A5 is favorable.

APPENDIX C

3.0 GSH SYSTEM RESPONDS DIFFERENTLY WITHIN DIFFERENT CELL TYPES DURING OGD-RP

This Appendix contains information for section 3.0 *GSH SYSTEM RESPONDS DIFFERENTLY WITHIN DIFFERENT CELL TYPES DURING OGD-RP*

Table C-1. Redox information of Grx1-roGFP2 from various cell types.

$Ratio_{405/488}$	Mitochondria			Cytoplasm		
	Control	OGD	RP	Control	OGD	RP
Pyramidal cell in OHSC	0.328 ± 0.027	0.251 ± 0.026	0.424 ± 0.019	0.255 ± 0.024	0.274 ± 0.016	0.268 ± 0.030
Astrocyte in OHSC	0.305 ± 0.036	0.280 ± 0.027	0.345 ± 0.038	0.252 ± 0.042	0.255 ± 0.017	0.277 ± 0.077
HeLa cell	0.296 ± 0.025	0.274 ± 0.024	0.321 ± 0.034	0.271 ± 0.003	0.275 ± 0.005	0.281 ± 0.024
OxD_{roGFP2}	Mitochondria			Cytoplasm		
	Control	OGD	RP	Control	OGD	RP
Pyramidal cell in OHSC	0.205 ± 0.064	0.039 ± 0.034	0.393 ± 0.027	0.074 ± 0.030	0.126 ± 0.032	0.145 ± 0.041
Astrocyte in OHSC	0.229 ± 0.061	0.167 ± 0.038	0.305 ± 0.057	0.065 ± 0.028	0.034 ± 0.011	0.152 ± 0.086
HeLa cell	0.238 ± 0.046	0.185 ± 0.057	0.221 ± 0.068	0.103 ± 0.006	0.109 ± 0.011	0.112 ± 0.029
$\ln([GSH]^2/[GSSG])$	Mitochondria			Cytoplasm		
	Control	OGD	RP	Control	OGD	RP
Pyramidal cell in OHSC	1.50 ± 0.59	-0.54 ± 0.47	2.65 ± 0.11	0.26 ± 0.54	0.59 ± 0.53	0.51 ± 0.61
Astrocyte in OHSC	1.83 ± 0.37	1.40 ± 0.36	2.24 ± 0.29	0.20 ± 0.56	-0.67 ± 0.64	0.22 ± 0.53
HeLa cell	1.91 ± 0.26	1.56 ± 0.40	1.79 ± 0.41	1.43 ± 0.11	1.48 ± 0.19	1.51 ± 0.44
E_{GSH}(mV)*	Mitochondria			Cytoplasm		
	Control	OGD	RP	Control	OGD	RP
Pyramidal cell in OHSC	-360.0 ± 7.6	-386.7 ± 3.4	-345.2 ± 1.5	-323.4±15.8	-312.2±15.4	-313.3 ± 7.8
Astrocyte in OHSC	-355.9 ± 4.8	-361.4 ± 4.7	-350.5 ± 3.6	-322.6±16.2	-329.7±10.9	-314.5±24.2
HeLa cell	-354.8 ± 3.4	-359.2 ± 5.2	-356.3 ± 5.3	-301.2 ± 1.5	-300.7± 2.4	-300.4± 5.7

Steady state values in control, OGD and RP from HeLa cells, pyramidal cells and astrocytes are summarized in this table, represented as means ± SEMs which were derived from 6 independent measurements. Their full data are shown in Figure 3-5. * E values assume pH = 7.00 in cytoplasm and pH = 8.00 in mitochondria.

APPENDIX D

4.0 THE DIFFERENTIAL SUSCEPTIBILITY BETWEEN CA1 AND CA3 PYRAMICAL CELLS TO OGD-RP DUE TO THEIR DIFFERENCE IN ROS MANAGEMENT

This Appendix contains information for section 4.0 *THE DIFFERENTIAL SUSCEPTIBILITY BETWEEN CA1 AND CA3 PYRAMICAL CELLS TO OGD-RP DUE TO THEIR DIFFERENCE IN ROS MANAGEMENT*

SUPPLEMENTAL DATA

Supplemental Figures

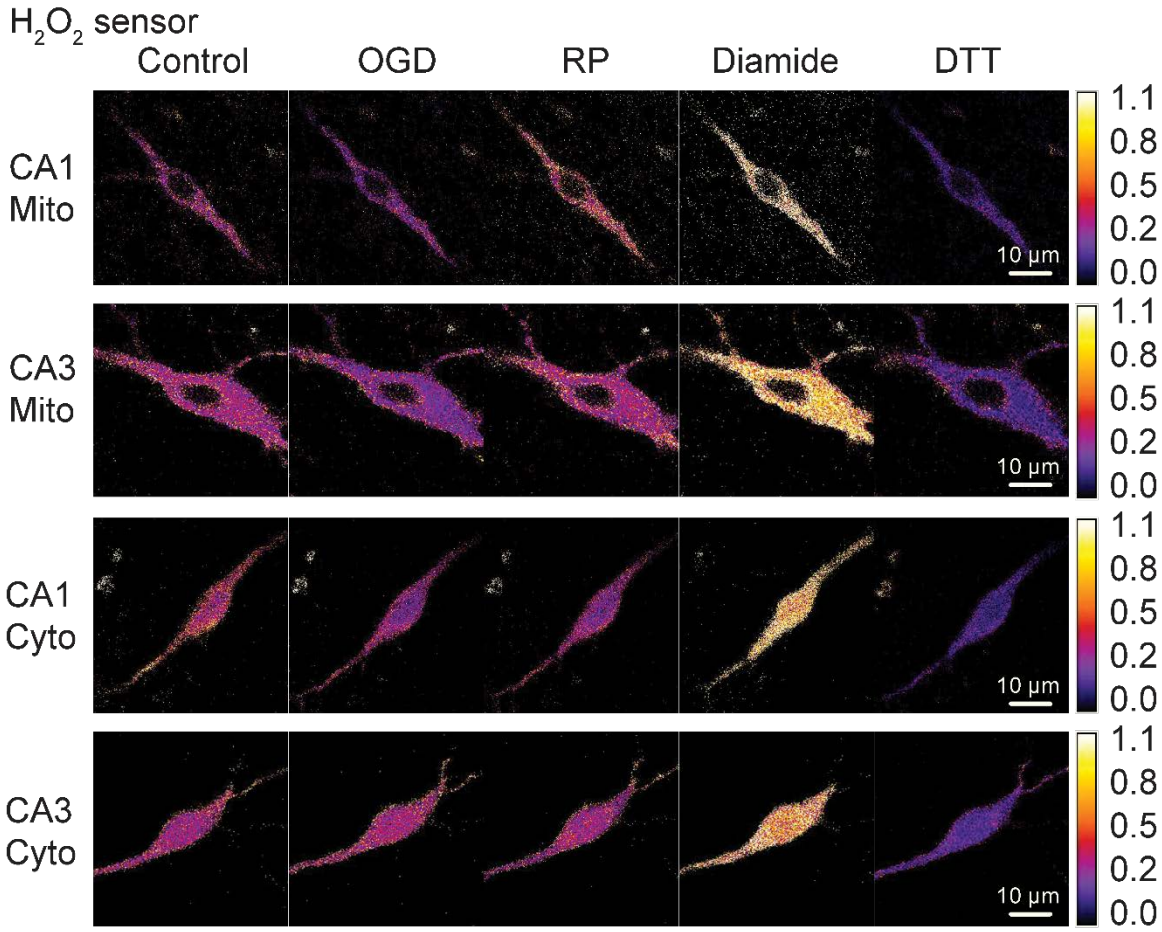

Figure. D-1. Ratiometric images of pyramidal cells expressing roGFP2-Orp1(Related to Fig. 4-1).

Ratiometric images of H_2O_2 sensor expressed in mitochondria (Mito) or cytoplasm (Cyto) of pyramidal cells in CA1 or CA3 are acquired according to the protocol described in Section 4.2. The value of $R_{405/488}$ ($0 < R_{405/488} < 1$), indicated in the calibration color bar, reflects the oxidation degree of the sensor. Cell are fully oxidized by diamide (shown in brightest color, $R_{405/488} = 1$) and fully reduced by DTT (shown in darkest purple, $R_{405/488} \approx 0.25$). Noticeable change in oxidation degree (reflected by color) is found in mitochondria, but not in cytoplasm during the OGD-RP experiment.

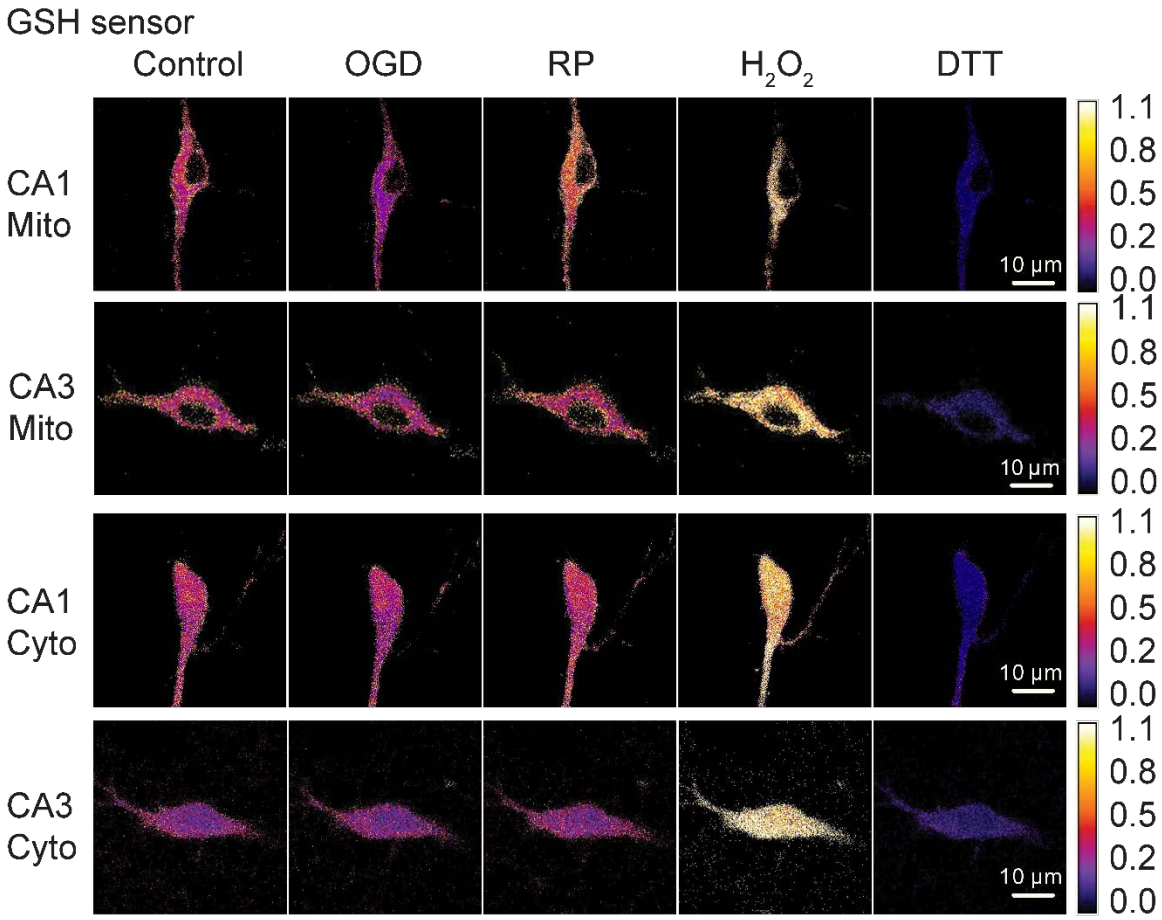

Figure. D-2. Ratiometric images of pyramidal cells expressing Grx1-roGFP2. (Related to Fig. 4-1)

Ratiometric images of GSH sensor expressed in mitochondria (Mito) or cytoplasm (Cyto) of pyramidal cells in CA1 or CA3 are acquired according to the protocol described in Section 4.2. The value of $R_{405/488}$ ($0 < R_{405/488} < 1$), indicated in calibration color bar, reflects oxidation degree of the sensor. Cell are fully oxidized by H_2O_2 (shown in brightest color, $R_{405/488} = 1$) and fully reduced by DTT (shown in darkest purple, $R_{405/488} \approx 0.18$). A larger change in oxidation degree (reflected by color) is found in mitochondria of CA1 than CA3 during the OGD-RP experiment.

a Shuttle scan between hippocampal area CA1 and CA3.

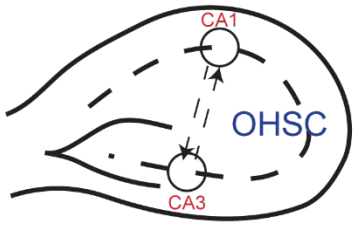

b Off-focus issue for imaging thiols or NAD(P)H in OHSC.

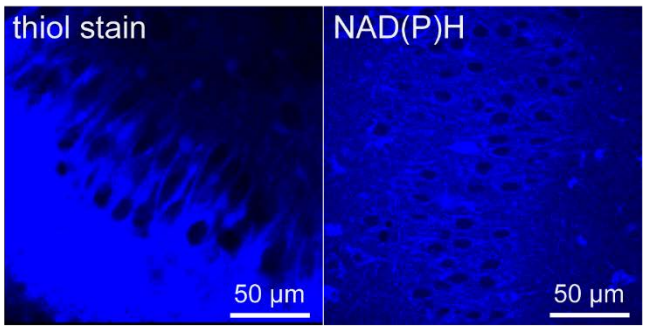

c Labelled single cell facilitates to maintain focusing on one cell layer.

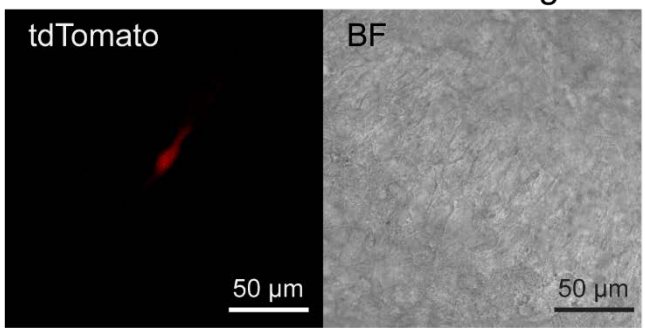

Figure. D-3. Optimizing NAD(P)H and thiols imaging. (Related to Fig. 4-2, 4-3)

(a) Scan shuttles between CA1 and CA3 to allow fluorescence signals from two areas to be acquired at the same time frame. This enables direct comparison between CA1 and CA3without calibration by using internal or external standards. (b) The autofocus (ATF) function was applied on the Leica confocal microscope aiming to limit the error in the z-direction within ± 1 µm over time. The algorithm of this function is to find the largest fluorescent area (FA) and highest fluorescence intensity (FI). Its application depends on the different FA and FI varying in different depths. However, The fluorescence images of NAD(P)H and thiols in OHSCs represent honeycomb patterns, which do not

show significantly difference of FA and FI in various depths, leading to the failure of the ATF function. (c) tdTomato was introduced to a single pyramidal cells in OHSC. The ATF function can easily maintain the focus on the equatorial plane (where largest FA and highest FI were found) of this labelled cell with z-axis shift < 1 μm.

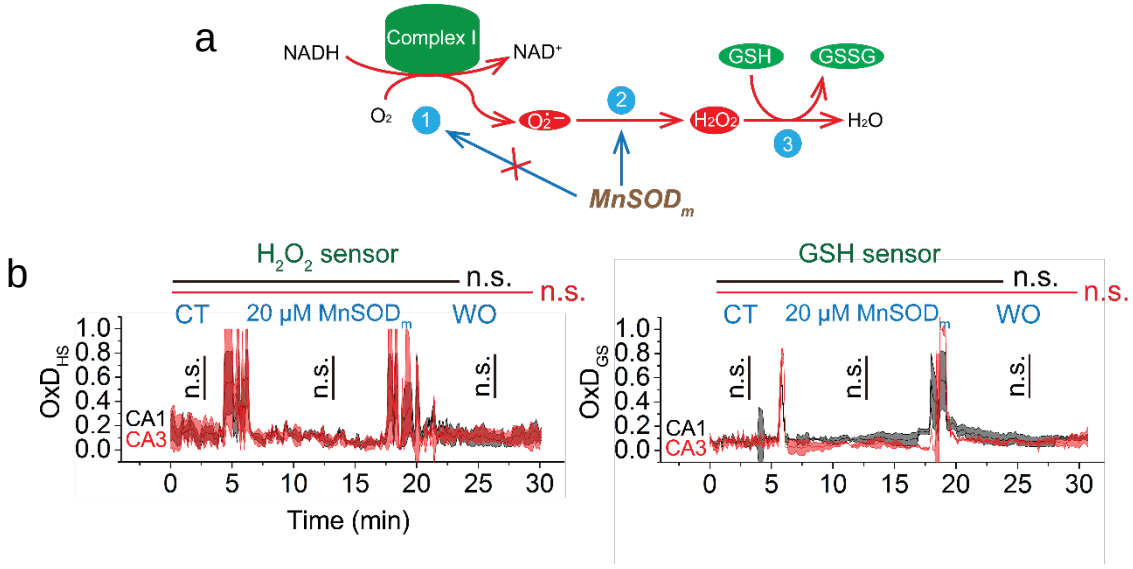

Figure. D-4. $MnSOD_m$ cannot affect complex I, but it affects the dismutation of superoxide. (Related to Fig. 4-4)

The ROS pathway is comprised of three steps: (1) superoxide generates at complex I under stimulation; (2) superoxide dismutates into H_2O_2; (3) H_2O_2 is removed by GSH system. (a) $MnSOD_m$ has no effect on step (1) in the ROS pathway, which is supported by data shown in (b). (b) OHSC is treated with control (CT)/ 20 μM $MnSOD_m$/wash out (WO) for 5 min/15 min/15 min. ACSF buffer is used in CT and WO. Each trace is represented in mean ± SEM, n= 6. No change is found in OxD of H_2O_2 (left) and GSH (right) during the treatment (comparisons among CT/20 μM $MnSOD_m$/WO are indicated by horizontal lines, black for CA1, red for CA3. One way ANOVA, no significant difference, n.s., $p > 0.05$, n = 6). No difference is found between CA1 and CA3 at each period (indicated by vertical lines with t-test results, n.s., $p > 0.05$, n=6).

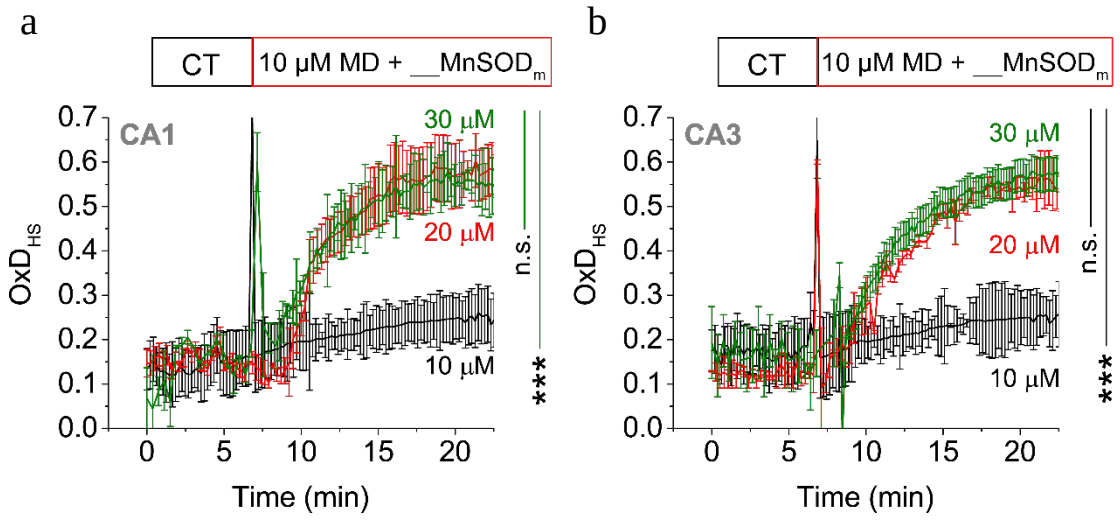

Figure. D-5. Determine [MnSODm]max. (Related to Fig. 4-4)

The maximum working concentration of $MnSOD_m$ for OHSC in superfusion is found at 20 μM. OHSC is first superfused with ACSF solution as a control (CT), then with menadione (MD) + MnSOD mimic ($MnSOD_m$). MD is used to trigger the superoxide formation, while $MnSOD_m$ works to achieve full conversion of superoxide to H_2O_2. The H_2O_2 system is recorded in OxD_{HS} in CA1 (a) and CA3 (b). 10 μM MD is used in all experiments. Three different concentrations of $MnSOD_m$ are tested here: 10 μM $MnSOD_m$, 20 μM $MnSOD_m$ and 30 μM $MnSOD_m$. No further change from 20 μM $MnSOD_m$ to 30 μM $MnSOD_m$ indicates that 20 μM is the proper concentration to apply $MnSOD_m$ in our experiment. All traces are represented in mean ± SEM (n=6). Curves of MD + $MnSOD_m$ were fitted into the first-order exponential equation and all of the fitted parameters were compared and analyzed with a t test with bootstrap and one way ANOVA with post hoc test (n.s, no significant difference, $p > 0.05$, ***$p<0.001$, n=6). The short vertical line indicates the comparison between 20 μM $MnSOD_m$ and 30 μM $MnSOD_m$. The comparison among 10 μM $MnSOD_m$, 20 μM and 30 μM $MnSOD_m$ is indicated by the long vertical line. Details of curve fitting and statistical analysis are described in Section 4.2.

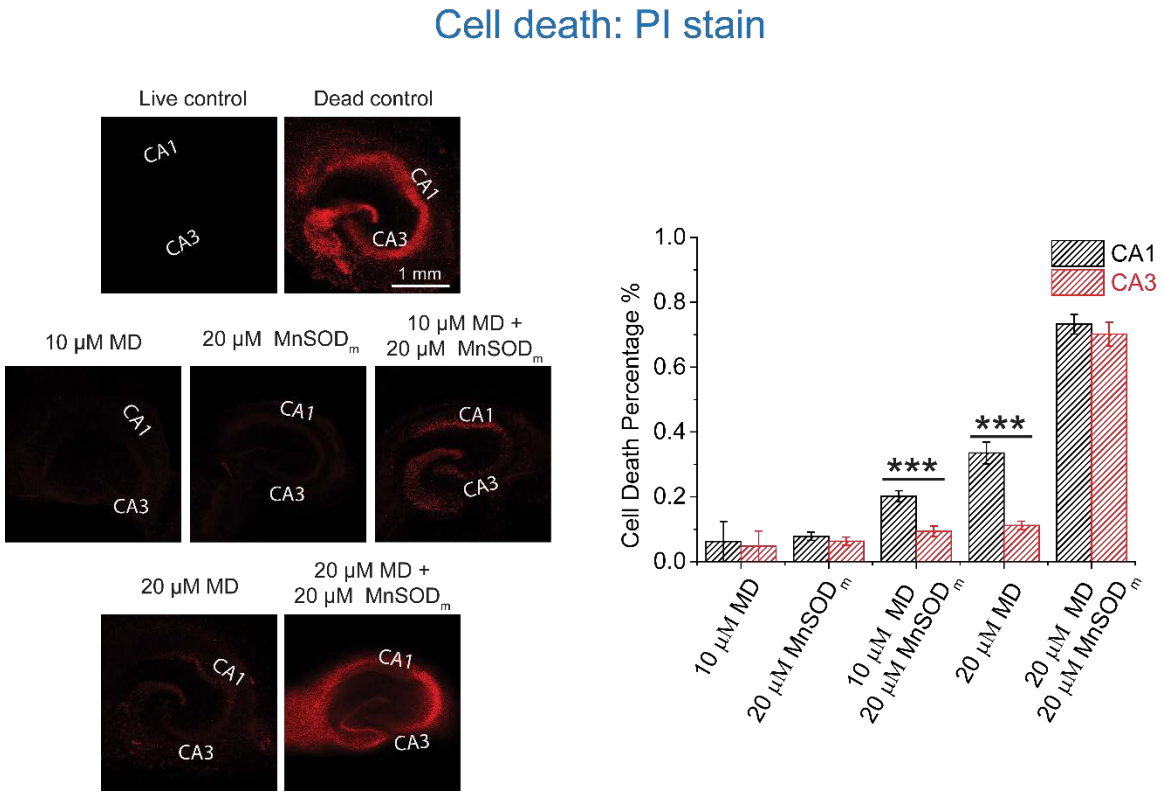

Figure. D-6. Differential cell death with the treatment of MD or MD + MnSODm. (Related to Fig. 4-4)

Differential mortality of pyramidale cells in areas CA1 and CA3 are found after the treatment of OGD-RP and 10 μM MD + 20 μM MnSODm. (left) Fluorescence images of OHSCs with different treatments. (right) Data of cell death under different treatments are represented and compared in CA1 and CA3 (One-Way ANOVA, ***$p < 0.001$, $n = 10$; no special sign is added if there is no significant difference). Cell death percentage is tested with PI stain (Section 4.2).

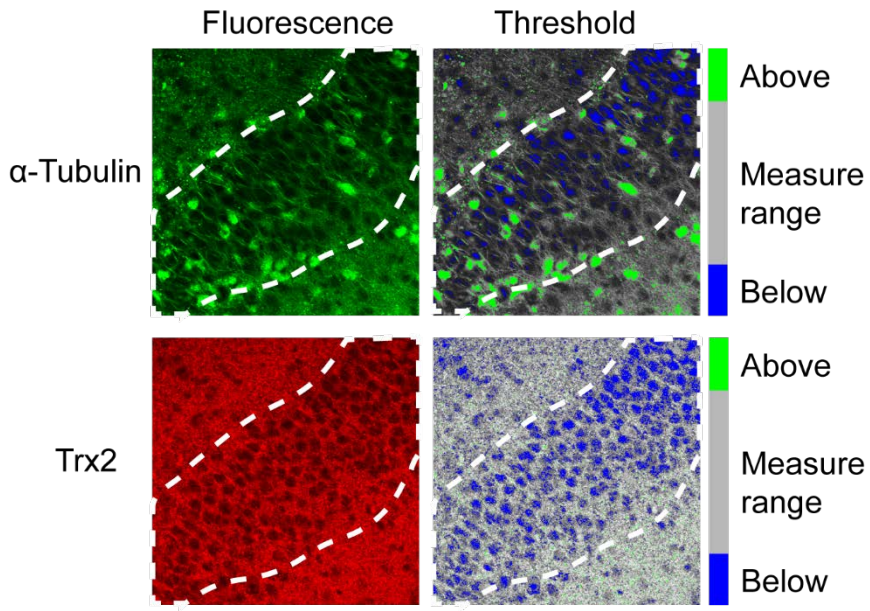

Figure. D-7. Quantitative measurement of the target protein in OHSC refering to the internal control via immunofluorescence. (Related to Fig. 4-6)

The content of Trx2 in subfield CA1 from OHSC was normalized to that of the internal standard, α-tubulin. (top) α-tubulin labelled with CF568 (Biotium, USA) was imaged with excitation 488 nm, emission 500-530 nm, shown in green. (bottom) Trx2 labelled with Alexa Fluor 488(Life Technologies, USA) was imaged at the excitation of 561 nm and the emission of 575-595 nm, shown in red. Fluorescent images (left column) were processed into the images with thresholds in the right column (the measureable area is shown in gray, areas of above and below are in green and blue, respectively). The region of interest (ROI) is outlined to only include the pyramidal cells in OHSC (white dashed line). Only pixels within the threshold in ROI will be counted. The sum of pixels was calculated for Trx2 and α-tubulin here, then the values of Trx2 was normalized by that of α-tubulin to represent the content of Trx2 in the pyramidal cell layer in OHSC.

(a) Peak analysis

Table D-1. Parameters of peak in Fig. 4-3.

Peak parameters	Peak 1	Peak 2	Peak 3
Emerging time (min)	7.41±0.52	11.7±0.80	6.34±0.36
Peak altitude (NFl)	1.07± 0.01	1.11±0.01	1.10±0.02
Ascending slope (NFl/min)	10.69±2.08 ($\times10^{-3}$)	20.2±3.7($\times10^{-3}$)	12.2±3.7($\times10^{-3}$)
Descending slope(NFI/min)	-5.26±3.21($\times10^{-3}$)	-12.5±1.79($\times10^{-3}$)	4.71±1.33($\times10^{-3}$)

*NFL, normalized fluorescent intensity of NAD(P)H

(b) Linear fitting

Table D-2. Data of steady OxD_{HS} in Fig. 4-1g for OGD-RP.

OxD_{HS} (mean ± SEM)	Control	OGD	RP
Mito CA1	0.447±0.018	0.250±0.039	0.423±0.028
Mito CA3	0.340±0.090	0.269±0.045	0.315±0.054
Cyto CA1	0.266±0.0274	0.342±0.044	0.186±0.023
Cyto CA3	0.260±0.038	0.260±0.037	0.200±0.019

Table D-3. Data of steady OxD_{GS} in Fig. 4-1h for OGD-RP.

OxD_{GS} (mean ± SEM)	Control	OGD	RP
Mito CA1	0.295±0.020	0.137±0.026	0.489±0.020
Mito CA3	0.317±0.073	0.120±0.031	0.241±0.035
Cyto CA1	0.234±0.038	0.157±0.028	0.191±0.023
Cyto CA3	0.302±0.075	0.110±0.031	0.227±0.036

Table D-4. Data of OxD in (I) to (III) in Fig. 4-4b, d for menadione treatment.

OxD (mean ± SEM)	(I) CT	(II) 10 μM MD	(III) WO
H_2O_2 CA1	0.078±0.032	0.079±0.018	0.077±0.010
H_2O_2 CA3	0.072±0.036	0.081±0.021	0.073±0.007
GSH CA1	0.104±0.020	0.115±0.025	0.106±0.036
GSH CA3	0.091±0.037	0.095±0.021	0.095±0.023

*only mitochondria is studied for the reason that only OxD_{HS} and OxD_{GS} in mitochondria change to OGD-RP.

(c) Nonlinear fitting to first order exponential equation

Table D-5. Data of fitted parameters for Fig. 4-4b(IV), 4-4c(II) and 4-4c(IV) for MD + $MnSOD_m$ treatment.

Fitting from OxD_{HS}	CA1			CA3		
	$k_1[H_2O_2]$	$k_2[Trx]_{Red}$	$[OxD_0]_{HS}$	$k_1[H_2O_2]$	$k_2[Trx]_{Red}$	$[OxD_0]_{HS}$
10 μM MD+20 μM $MnSOD_m$	0.196±0.015	0.136±0.054	0.069±0.047	0.186±0.019	0.137±0.016	0.085±0.067
20 μM MD	0.192±0.017	0.048±0.007	0.073±0.012	0.082±0.001	0.066±0.001	0.103±0.054
20 μM MD+20 μM $MnSOD_m$	0.252±0.011	0.013±0.003	0.103±0.045	0.252±0.011	0.011±0.002	0.103±0.045

*only mitochondria is studied for the reason that only OxD_{HS} and OxD_{GS} in mitochondria change to OGD-RP.

Table D-6. Data of fitted parameters for Fig. 4-4d(IV), 4-4e(II) and 4-4e(IV) for MD + $MnSOD_m$ treatment.

Fitting from OxD_{GS}	CA1			CA3		
	$k_1'[GSSG]$	$k_2'[GSH]$	$[OxD_0]_{GS}$	$k_1'[GSSG]$	$k_2'[GSH]$	$[OxD_0]_{GS}$
10 μM MD+20 μM $MnSOD_m$	0.274±0.014	0.083±0.010	0.083±0.016	0.091±0.006	0.117±00.012	0.109±0.006
20 μM MD	0.281±0.006	0.098±0.003	0.103±0.012	0.208±0.061	0.167±0.060	0.093±0.054
20 μM MD+20 μM $MnSOD_m$	0.321±0.010	0.071±0.002	0.101±0.080	0.318±0.042	0.077±0.016	0.099±0.076

*only mitochondria is studied for the reason that only OxD_{HS} and OxD_{GS} in mitochondria change to OGD-RP.

Table D-7. Data of fitted parameters for Fig. 4-5b for Trx inhibition assay.

Fitting from OxD_{HS}	CA1			CA3		
	$k_1[H_2O_2]$	$k_2[Trx]_{Red}$	$[OxD_0]_{HS}$	$k_1[H_2O_2]$	$k_2[Trx]_{Red}$	$[OxD_0]_{HS}$
No AF	0.200±0.010	0.136±0.054	0.069±0.047	0.187±0.019	0.138±0.039	0.085±0.067
AF	0.236±0.012	0.049±0.006	0.109±0.024	0.314±0.02	0.046±0.001	0.106±0.015

*only mitochondria is studied for the reason that only OxD_{HS} and OxD_{GS} in mitochondria change to OGD-RP.

Table D-8. Data of fitted parameters for Fig. 4-5c for Trx inhibition assay.

Fitting from OxD_{GS}	CA1			CA3		
	$k_1'[GSSG]$	$k_2'[GSH]$	$[OxD_0]_{GS}$	$k_1'[GSSG]$	$k_2'[GSH]$	$[OxD_0]_{GS}$
No AF	0.274±0.014	0.083±0.010	0.083±0.016	0.091±0.006	0.117±0.011	0.109±0.006
AF	0.274±0.004	0.065±0.003	0.081±0.015	0.290±0.006	0.065±0.003	0.106±0.008

*only mitochondria is studied for the reason that only OxD_{HS} and OxD_{GS} in mitochondria change to OGD-RP.

BIBLIOGRAPHY

1. McCann, S.K. & Roulston, C.L. NADPH oxidase as a therapeutic target for neuroprotection against ischaemic stroke: future perspectives. *Brain Sci.* **3**, 561-598 (2013).
2. Kim, J.Y., Kawabori, M. & Yenari, M.A. Innate Inflammatory Responses in Stroke: Mechanisms and Potential Therapeutic Targets. *Curr. Med. Chem.* **21**, 2076-2097 (2014).
3. Duval, D., Foll, I.D.-L., Vimard, F. & Gauberti, M. Neuroprotective effects of N-acetylcysteine: a review. *Brain Res. J.* **6**, 309-337 (2013).
4. Cornelius, C., *et al.* Traumatic Brain Injury: Oxidative Stress and Neuroprotection. *Antioxid. Redox Signaling* **19**, 836-853 (2013).
5. Rodriguez-Rodriguez, A., Egea-Guerrero, J.J., Murillo-Cabezas, F. & Carrillo-Vico, A. Oxidative Stress in Traumatic Brain Injury. *Curr. Med. Chem.* **21**, 1201-1211 (2014).
6. Abdul-Muneer, P.M., Chandra, N. & Haorah, J. Interactions of Oxidative Stress and Neurovascular Inflammation in the Pathogenesis of Traumatic Brain Injury. *Mol. Neurobiol.*, Ahead of Print (2014).
7. Larson, J., Drew, K.L., Folkow, L.P., Milton, S.L. & Park, T.J. No oxygen? No problem! intrinsic brain tolerance to hypoxia in vertebrates. *J. Exp. Biol.* **217**, 1024-1039 (2014).
8. Lasierra-Cirujeda, J., Coronel, P., Aza, M.J. & Gimeno, M. Beta-amyloidolysis and glutathione in Alzheimer's disease. *J. Blood Med.* **4**, 31-38 (2013).
9. Aliev, G., *et al.* Oxidative Stress Mediated Mitochondrial and Vascular Lesions as Markers in the Pathogenesis of Alzheimer Disease. *Curr. Med. Chem.* **21**, 2208-2217 (2014).
10. Butterfield, D.A., Di Domenico, F. & Barone, E. Elevated risk of type 2 diabetes for development of Alzheimer disease: A key role for oxidative stress in brain. *Biochim. Biophys. Acta, Mol. Basis Dis.* **1842**, 1693-1706 (2014).
11. Schapira, A.H.V. Mitochondria in the aetiology and pathogenesis of Parkinson's disease. *The Lancet Neurology* **7**, 97-109 (2008).
12. Guzman, J.N., *et al.* Oxidant stress evoked by pacemaking in dopaminergic neurons is attenuated by DJ-1. *Nature* **468**, 696-700 (2010).
13. Barnham, K.J., Masters, C.L. & Bush, A.I. Neurodegenerative diseases and oxidative stress. *Nat Rev Drug Discov* **3**, 205-214 (2004).
14. Lin, M.T. & Beal, M.F. Mitochondrial dysfunction and oxidative stress in neurodegenerative diseases. *Nature* **443**, 787-795 (2006).
15. Muller, M. & Leavitt, B.R. Iron dysregulation in Huntington's disease. *J. Neurochem.* **130**, 328-350 (2014).
16. Gil-Mohapel, J., Brocardo, P.S. & Christie, B.R. The Role of Oxidative Stress in Huntington's Disease: Are Antioxidants Good Therapeutic Candidates? *Curr. Drug Targets* **15**, 454-468 (2014).
17. Pandya, C.D., Howell, K.R. & Pillai, A. Antioxidants as potential therapeutics for neuropsychiatric disorders. *Prog. Neuro-Psychopharmacol. Biol. Psychiatry* **46**, 214-223 (2013).
18. Xu, Y., Wang, C., Klabnik, J.J. & O'Donnell, J.M. Novel Therapeutic Targets in Depression and Anxiety: Antioxidants as a Candidate Treatment. *Curr. Neuropharmacol.* **12**, 108-119 (2014).

19. Hassan, W., Silva, C.E.B., Mohammadzai, I.U., Teixeira da Rocha, J.B. & Landeira-Fernandez, J. Association of Oxidative Stress to the Genesis of Anxiety: Implications for Possible Therapeutic Interventions. *Curr. Neuropharmacol.* **12**, 120-139 (2014).
20. D'Amico, E., Factor-Litvak, P., Santella, R.M. & Mitsumoto, H. Clinical perspective on oxidative stress in sporadic amyotrophic lateral sclerosis. *Free Radical Biol. Med.* **65**, 509-527 (2013).
21. Chan, S.H.H. & Chan, J.Y.H. Brain Stem NOS and ROS in Neural Mechanisms of Hypertension. *Antioxid. Redox Signaling* **20**, 146-163 (2014).
22. Colamartino, M., Padua, L., Cornetta, T., Testa, A. & Cozzi, R. Recent advances in pharmacological therapy of Parkinson's disease: levodopa and carbidopa protective effects against DNA oxidative damage. *Health* **4**, 1191-1199, 1199 pp. (2012).
23. Mari, M., *et al.* Mitochondrial glutathione: Features, regulation and role in disease. *Biochim. Biophys. Acta, Gen. Subj.* **1830**, 3317-3328 (2013).
24. Kembro, J.M., Aon, M.A., Winslow, R.L., O'Rourke, B. & Cortassa, S. Integrating Mitochondrial Energetics, Redox and ROS Metabolic Networks: A Two-Compartment Model. *Biophys. J.* **104**, 332-343 (2013).
25. Niatsetskaya, Z.V., *et al.* The oxygen free radicals originating from mitochondrial complex I contribute to oxidative brain injury following hypoxia-ischemia in neonatal mice. *The Journal of neuroscience : the official journal of the Society for Neuroscience* **32**, 3235-3244 (2012).
26. Finkel, T. Signal transduction by reactive oxygen species. *J. Cell Biol.* **194**, 7-15 (2011).
27. Patel, J.C. & Rice, M.E. Classification of H2O2 as a Neuromodulator that Regulates Striatal Dopamine Release on a Subsecond Time Scale. *ACS Chem. Neurosci.* **3**, 991-1001 (2012).
28. Rice, M.E. H2O2: a dynamic neuromodulator. *Neuroscientist* **17**, 389-406 (2011).
29. Bao, L., *et al.* Mitochondria are the source of hydrogen peroxide for dynamic brain-cell signaling. *J. Neurosci.* **29**, 9002-9010 (2009).
30. Waypa, G.B., *et al.* Superoxide generated at mitochondrial complex III triggers acute responses to hypoxia in the pulmonary circulation. *Am. J. Respir. Crit. Care Med.* **187**, 424-432 (2013).
31. Mungai, P.T., *et al.* Hypoxia triggers AMPK activation through reactive oxygen species-mediated activation of calcium release-activated calcium channels. *Mol. Cell. Biol.* **31**, 3531-3545 (2011).
32. Herdegen, T. & Leah, J.D. Inducible and constitutive transcription factors in the mammalian nervous system: control of gene expression by Jun, Fos and Krox, and CREB/ATF proteins. *Brain Res. Rev.* **28**, 370-490 (1998).
33. Cheng, Y., *et al.* Caspase inhibitor affords neuroprotection with delayed administration in a rat model of neonatal hypoxic-ischemic brain injury. *J. Clin. Invest.* **101**, 1992-1999 (1998).
34. Banasiak, K.J., Xia, Y. & Haddad, G.G. Mechanisms underlying hypoxia-induced neuronal apoptosis. *Prog. Neurobiol. (Oxford)* **62**, 215-249 (2000).
35. Olmez, I. & Ozyurt, H. Reactive oxygen species and ischemic cerebrovascular disease. *Neurochemistry International* **60**, 208-212 (2012).
36. Krupinski, J., Kaluza, J., Kumar, P., Kumar, S. & Wang, J.M. Role of angiogenesis in patients with cerebral ischemic stroke. *Stroke* **25**, 1794-1798 (1994).

37. Laake, J.H., Haug, F.M., Wieloch, T. & Ottersen, O.P. A simple in vitro model of ischemia based on hippocampal slice cultures and propidium iodide fluorescence. *Brain Res Brain Res Protoc* **4**, 173-184 (1999).
38. Ahlgren, H., Henjum, K., Ottersen, O.P. & Runden-Pran, E. Validation of organotypical hippocampal slice cultures as an ex vivo model of brain ischemia: Different roles of NMDA receptors in cell death signalling after exposure to NMDA or oxygen and glucose deprivation. *Cell Tissue Res.* **345**, 329-341 (2011).
39. Noraberg, J., *et al.* Organotypic hippocampal slice cultures for studies of brain damage, neuroprotection and neurorepair. *Curr. Drug Targets: CNS Neurol. Disord.* **4**, 435-452 (2005).
40. Easton, J.D., *et al.* Definition and Evaluation of Transient Ischemic Attack: A Scientific Statement for Healthcare Professionals From the American Heart Association/American Stroke Association Stroke Council; Council on Cardiovascular Surgery and Anesthesia; Council on Cardiovascular Radiology and Intervention; Council on Cardiovascular Nursing; and the Interdisciplinary Council on Peripheral Vascular Disease: The American Academy of Neurology affirms the value of this statement as an educational tool for neurologists. *Stroke* **40**, 2276-2293 (2009).
41. Peters, O., *et al.* Increased Formation of Reactive Oxygen Species After Permanent and Reversible Middle Cerebral Artery Occlusion in the Rat. *J Cereb Blood Flow Metab* **18**, 196-205 (1998).
42. Fekete, Á., Vizi, E.S., Kovács, K.J., Lendvai, B. & Zelles, T. Layer-specific differences in reactive oxygen species levels after oxygen–glucose deprivation in acute hippocampal slices. *Free Radical Biology and Medicine* **44**, 1010-1022 (2008).
43. Abramov, A.Y., Scorziello, A. & Duchen, M.R. Three Distinct Mechanisms Generate Oxygen Free Radicals in Neurons and Contribute to Cell Death during Anoxia and Reoxygenation. *The Journal of Neuroscience* **27**, 1129-1138 (2007).
44. Choi, D.W. & Rothman, S.M. The role of glutamate neurotoxicity in hypoxic-ischemic neuronal death. *Annual review of neuroscience* **13**, 171-182 (1990).
45. Almeida, A., Delgado-Esteban, M., Bolaños, J.P. & Medina, J.M. Oxygen and glucose deprivation induces mitochondrial dysfunction and oxidative stress in neurones but not in astrocytes in primary culture. *Journal of Neurochemistry* **81**, 207-217 (2002).
46. Dringen, R., Pawlowski, P.G. & Hirrlinger, J. Peroxide detoxification by brain cells. *Journal of Neuroscience Research* **79**, 157-165 (2005).
47. Dringen, R., Kussmaul, L., Gutterer, J.M., Hirrlinger, J. & Hamprecht, B. The Glutathione System of Peroxide Detoxification Is Less Efficient in Neurons than in Astroglial Cells. *Journal of Neurochemistry* **72**, 2523-2530 (1999).
48. Drukarch, B., Schepens, E., Stoof, J.C., Langeveld, C.H. & Van Muiswinkel, F.L. Astrocyte-Enhanced Neuronal Survival is Mediated by Scavenging of Extracellular Reactive Oxygen Species. *Free Radical Biology and Medicine* **25**, 217-220 (1998).
49. Griffin, S., Clark, J.B. & Canevari, L. Astrocyte–neurone communication following oxygen–glucose deprivation. *Journal of Neurochemistry* **95**, 1015-1022 (2005).
50. Dringen, R. Metabolism and functions of glutathione in brain. *Progress in Neurobiology* **62**, 649-671 (2000).
51. Dringen, R., Kranich, O. & Hamprecht, B. The gamma-glutamyl transpeptidase inhibitor acivicin preserves glutathione released by astroglial cells in culture. *Neurochemical research* **22**, 727-733 (1997).

52. Dringen, R., Pfeiffer, B. & Hamprecht, B. Synthesis of the Antioxidant Glutathione in Neurons: Supply by Astrocytes of CysGly as Precursor for Neuronal Glutathione. *The Journal of Neuroscience* **19**, 562-569 (1999).
53. Pringle, A.K., *et al.* Neuroprotection by both NMDA and non-NMDA receptor antagonists in in vitro ischemia. *Brain Research* **755**, 36-46 (1997).
54. Wang, X. & Michaelis, E.K. Selective Neuronal Vulnerability to Oxidative Stress in the Brain. *Frontiers in Aging Neuroscience* **2**, 12 (2010).
55. Wang, X., *et al.* High intrinsic oxidative stress may underlie selective vulnerability of the hippocampal CA1 region. *Molecular Brain Research* **140**, 120-126 (2005).
56. Wang, X., *et al.* Genome-wide transcriptome profiling of region-specific vulnerability to oxidative stress in the hippocampus. *Genomics* **90**, 201-212 (2007).
57. Nikiforov, A., Dölle, C., Niere, M. & Ziegler, M. Pathways and Subcellular Compartmentation of NAD Biosynthesis in Human Cells: FROM ENTRY OF EXTRACELLULAR PRECURSORS TO MITOCHONDRIAL NAD GENERATION. *Journal of Biological Chemistry* **286**, 21767-21778 (2011).
58. Chan, S.H.H. & Chan, J.Y.H. Brain Stem NOS and ROS in Neural Mechanisms of Hypertension. *Antioxidants & Redox Signaling* **20**, 146-163 (2013).
59. Chen, Y. & Swanson, R.A. The glutamate transporters EAAT2 and EAAT3 mediate cysteine uptake in cortical neuron cultures. *Journal of Neurochemistry* **84**, 1332-1339 (2003).
60. Dringen, R., Kranich, O. & Hamprecht, B. The γ-Glutamyl Transpeptidase Inhibitor Acivicin Preserves Glutathione Released by Astroglial Cells in Culture. *Neurochem Res* **22**, 727-733 (1997).
61. Mailloux, R.J. & Harper, M.-E. Uncoupling proteins and the control of mitochondrial reactive oxygen species production. *Free Radical Biology and Medicine* **51**, 1106-1115 (2011).
62. Cornelius, C., *et al.* Traumatic Brain Injury: Oxidative Stress and Neuroprotection. *Antioxidants & Redox Signaling* **19**, 836-853 (2013).
63. Jones, D.P. Disruption of mitochondrial redox circuitry in oxidative stress. *Chemico-Biological Interactions* **163**, 38-53 (2006).
64. Murphy, M.P. Mitochondrial Thiols in Antioxidant Protection and Redox Signaling: Distinct Roles for Glutathionylation and Other Thiol Modifications. *Antioxidants & Redox Signaling* **16**, 476-495 (2011).
65. Lunt, S.Y. & Vander Heiden, M.G. Aerobic Glycolysis: Meeting the Metabolic Requirements of Cell Proliferation. *Annual Review of Cell and Developmental Biology* **27**, 441-464 (2011).
66. Rubi, B., del Arco, A., Bartley, C., Satrustegui, J. & Maechler, P. The Malate-Aspartate NADH Shuttle Member Aralar1 Determines Glucose Metabolic Fate, Mitochondrial Activity, and Insulin Secretion in Beta Cells. *Journal of Biological Chemistry* **279**, 55659-55666 (2004).
67. Fernie, A.R., Carrari, F. & Sweetlove, L.J. Respiratory metabolism: glycolysis, the TCA cycle and mitochondrial electron transport. *Current Opinion in Plant Biology* **7**, 254-261 (2004).
68. Venditti, P., Di Stefano, L. & Di Meo, S. Mitochondrial metabolism of reactive oxygen species. *Mitochondrion* **13**, 71-82 (2013).

69. Rydström, J. Mitochondrial NADPH, transhydrogenase and disease. *Biochimica et Biophysica Acta (BBA) - Bioenergetics* **1757**, 721-726 (2006).
70. Nakamura, M., Bhatnagar, A. & Sadoshima, J. Overview of Pyridine Nucleotides Review Series. *Circulation Research* **111**, 604-610 (2012).
71. Liu, Y.Q., Jetton, T.L. & Leahy, J.L. β-Cell Adaptation to Insulin Resistance: INCREASED PYRUVATE CARBOXYLASE AND MALATE-PYRUVATE SHUTTLE ACTIVITY IN ISLETS OF NONDIABETIC ZUCKER FATTY RATS. *Journal of Biological Chemistry* **277**, 39163-39168 (2002).
72. Lewis, Caroline A., *et al.* Tracing Compartmentalized NADPH Metabolism in the Cytosol and Mitochondria of Mammalian Cells. *Molecular Cell* **55**, 253-263 (2014).
73. Andreyev, A.Y., Kushnareva, Y.E., Murphy, A.N. & Starkov, A.A. Mitochondrial ROS metabolism: 10 Years later. *Biochemistry (Moscow)* **80**, 517-531 (2015).
74. Mailloux, R.J., McBride, S.L. & Harper, M.-E. Unearthing the secrets of mitochondrial ROS and glutathione in bioenergetics. *Trends Biochem. Sci.* **38**, 592-602 (2013).
75. Zelko, I.N., Mariani, T.J. & Folz, R.J. Superoxide dismutase multigene family: a comparison of the CuZn-SOD (SOD1), Mn-SOD (SOD2), and EC-SOD (SOD3) gene structures, evolution, and expression. *Free Radical Biology and Medicine* **33**, 337-349 (2002).
76. Hille, R. & Nishino, T. Flavoprotein structure and mechanism. 4. Xanthine oxidase and xanthine dehydrogenase. *The FASEB Journal* **9**, 995-1003 (1995).
77. Meitzler, J.L., *et al.* NADPH Oxidases: A Perspective on Reactive Oxygen Species Production in Tumor Biology. *Antioxid. Redox Signaling* **20**, 2873-2889 (2014).
78. Aon-Bertolino, M.L., *et al.* Thioredoxin and glutaredoxin system proteins—immunolocalization in the rat central nervous system. *Biochimica et Biophysica Acta (BBA) - General Subjects* **1810**, 93-110 (2011).
79. Yin, B., Barrionuevo, G. & Weber, S.G. Optimized Real-Time Monitoring of Glutathione Redox Status in Single Pyramidal Neurons in Organotypic Hippocampal Slices during Oxygen–Glucose Deprivation and Reperfusion. *ACS Chemical Neuroscience* (2015).
80. Greenwald, R.A. Superoxide dismutase and catalase as therapeutic agents for human diseases a critical review. *Free Radical Biology and Medicine* **8**, 201-209 (1990).
81. Wu, G., Fang, Y.-Z., Yang, S., Lupton, J.R. & Turner, N.D. Glutathione Metabolism and Its Implications for Health. *The Journal of Nutrition* **134**, 489-492 (2004).
82. Stanley, B.A., *et al.* Thioredoxin Reductase-2 Is Essential for Keeping Low Levels of H2O2 Emission from Isolated Heart Mitochondria. *Journal of Biological Chemistry* **286**, 33669-33677 (2011).
83. Brigelius-Flohe, R. & Maiorino, M. Glutathione peroxidases. *Biochim. Biophys. Acta, Gen. Subj.* **1830**, 3289-3303 (2013).
84. Cox, Andrew G., Winterbourn, Christine C. & Hampton, Mark B. Mitochondrial peroxiredoxin involvement in antioxidant defence and redox signalling. *Biochemical Journal* **425**, 313-325 (2010).
85. Peskin, A.V., *et al.* The High Reactivity of Peroxiredoxin 2 with H2O2 Is Not Reflected in Its Reaction with Other Oxidants and Thiol Reagents. *Journal of Biological Chemistry* **282**, 11885-11892 (2007).
86. Chae, H.Z., Kim, H.J., Kang, S.W. & Rhee, S.G. Characterization of three isoforms of mammalian peroxiredoxin that reduce peroxides in the presence of thioredoxin. *Diabetes Research and Clinical Practice* **45**, 101-112 (1999).

87. Trujillo, M., *et al.* Pre-steady state kinetic characterization of human peroxiredoxin 5: Taking advantage of Trp84 fluorescence increase upon oxidation. *Archives of Biochemistry and Biophysics* **467**, 95-106 (2007).
88. Takebe, G., *et al.* A Comparative Study on the Hydroperoxide and Thiol Specificity of the Glutathione Peroxidase Family and Selenoprotein P. *Journal of Biological Chemistry* **277**, 41254-41258 (2002).
89. Adimora, N.J., Jones, D.P. & Kemp, M.L. A Model of Redox Kinetics Implicates the Thiol Proteome in Cellular Hydrogen Peroxide Responses. *Antioxidants & Redox Signaling* **13**, 731-743 (2010).
90. Lillig, C.H., *et al.* New Thioredoxins and Glutaredoxins as Electron Donors of 3′-Phosphoadenylylsulfate Reductase. *Journal of Biological Chemistry* **274**, 7695-7698 (1999).
91. Condeelis, J. & Weissleder, R. In vivo imaging in cancer. *Cold Spring Harbor Perspect. Biol.* **2**, a003848 (2010).
92. Schuchmann, S., Kovacs, R., Kann, O., Heinemann, U. & Buchheim, K. Monitoring NAD(P)H autofluorescence to assess mitochondrial metabolic functions in rat hippocampal–entorhinal cortex slices. *Brain Research Protocols* **7**, 267-276 (2001).
93. Kann, O., Huchzermeyer, C., Kovács, R., Wirtz, S. & Schuelke, M. *Gamma oscillations in the hippocampus require high complex I gene expression and strong functional performance of mitochondria,* (2011).
94. Rocheleau, J.V., Head, W.S. & Piston, D.W. Quantitative NAD(P)H/Flavoprotein Autofluorescence Imaging Reveals Metabolic Mechanisms of Pancreatic Islet Pyruvate Response. *Journal of Biological Chemistry* **279**, 31780-31787 (2004).
95. Blacker, T.S., *et al.* Separating NADH and NADPH fluorescence in live cells and tissues using FLIM. *Nat Commun* **5**(2014).
96. Hung, Yin P., Albeck, John G., Tantama, M. & Yellen, G. Imaging Cytosolic NADH-NAD+ Redox State with a Genetically Encoded Fluorescent Biosensor. *Cell Metabolism* **14**, 545-554 (2011).
97. Zhao, Y., *et al.* Genetically Encoded Fluorescent Sensors for Intracellular NADH Detection. *Cell Metabolism* **14**, 555-566 (2011).
98. Chen, X.-P., Zhong, Z.-F., Xu, Z.-T., Chen, L.-D. & Wang, Y.-T. 2',7'-Dichlorodihydrofluorescein as a fluorescent probe for reactive oxygen species measurement: Forty years of application and controversy. *Free Radical Res.* **44**, 587-604 (2010).
99. Brandt, R. & Keston, A.S. Synthesis of diacetyldichlorofluorescin: A stable reagent for fluorometric analysis. *Analytical Biochemistry* **11**, 6-9 (1965).
100. Andoh, Y., *et al.* The Antioxidant Role of a Reagent, 2′,7′-Dichlorodihydrofluorescin Diacetate, Detecting Reactive-Oxygen Species and Blocking the Induction of Heme Oxygenase-1 and Preventing Cytotoxicity. *Journal of Biochemistry* **140**, 483-489 (2006).
101. Zhu, H., Bannenberg, G., Moldéus, P. & Shertzer, H. Oxidation pathways for the intracellular probe 2′,7′-dichlorofluorescin. *Arch Toxicol* **68**, 582-587 (1994).
102. Bonini, M.G., Rota, C., Tomasi, A. & Mason, R.P. The oxidation of 2′,7′-dichlorofluorescin to reactive oxygen species: A self-fulfilling prophesy? *Free Radical Biology and Medicine* **40**, 968-975 (2006).
103. Afri, M., Frimer, A.A. & Cohen, Y. Active oxygen chemistry within the liposomal bilayer: Part IV: Locating 2′,7′-dichlorofluorescein (DCF), 2′,7′-dichlorodihydrofluorescein

(DCFH) and 2′,7′-dichlorodihydrofluorescein diacetate (DCFH-DA) in the lipid bilayer. *Chemistry and Physics of Lipids* **131**, 123-133 (2004).
104. Østergaard, H., Henriksen, A., Hansen, F.G. & Winther, J.R. Shedding light on disulfide bond formation: engineering a redox switch in green fluorescent protein. *The EMBO Journal* **20**, 5853-5862 (2001).
105. Hanson, G.T., *et al.* Investigating Mitochondrial Redox Potential with Redox-sensitive Green Fluorescent Protein Indicators. *Journal of Biological Chemistry* **279**, 13044-13053 (2004).
106. Dooley, C.T., *et al.* Imaging Dynamic Redox Changes in Mammalian Cells with Green Fluorescent Protein Indicators. *Journal of Biological Chemistry* **279**, 22284-22293 (2004).
107. Björnberg, O., Østergaard, H. & Winther, J.R. Mechanistic Insight Provided by Glutaredoxin within a Fusion to Redox-Sensitive Yellow Fluorescent Protein. *Biochemistry* **45**, 2362-2371 (2006).
108. Robinson, K.M., Janes, M.S. & Beckman, J.S. The selective detection of mitochondrial superoxide by live cell imaging. *Nat. Protocols* **3**, 941-947 (2008).
109. Robinson, K.M., *et al.* Selective fluorescent imaging of superoxide in vivo using ethidium-based probes. *Proceedings of the National Academy of Sciences* **103**, 15038-15043 (2006).
110. Rothe, G. & Valet, G. Flow cytometric analysis of respiratory burst activity in phagocytes with hydroethidine and 2',7'-dichlorofluorescin. *Journal of Leukocyte Biology* **47**, 440-448 (1990).
111. Benov, L., Sztejnberg, L. & Fridovich, I. Critical evaluation of the use of hydroethidine as a measure of superoxide anion radical. *Free Radical Biology and Medicine* **25**, 826-831 (1998).
112. Zhao, H., *et al.* Detection and characterization of the product of hydroethidine and intracellular superoxide by HPLC and limitations of fluorescence. *Proceedings of the National Academy of Sciences of the United States of America* **102**, 5727-5732 (2005).
113. Zielonka, J. & Kalyanaraman, B. Hydroethidine- and MitoSOX-derived red fluorescence is not a reliable indicator of intracellular superoxide formation: Another inconvenient truth. *Free Radical Biology and Medicine* **48**, 983-1001 (2010).
114. Wang, W., *et al.* Superoxide Flashes in Single Mitochondria. *Cell* **134**, 279-290 (2008).
115. Schwarzländer, M., *et al.* Mitochondrial 'flashes': a radical concept repHined. *Trends in Cell Biology* **22**, 503-508 (2012).
116. Belousov, V.V., *et al.* Genetically encoded fluorescent indicator for intracellular hydrogen peroxide. *Nat Meth* **3**, 281-286 (2006).
117. Markvicheva, K.N., *et al.* A genetically encoded sensor for H2O2 with expanded dynamic range. *Bioorganic & Medicinal Chemistry* **19**, 1079-1084 (2011).
118. Bilan, D.S., *et al.* HyPer-3: A Genetically Encoded H2O2 Probe with Improved Performance for Ratiometric and Fluorescence Lifetime Imaging. *ACS Chemical Biology* **8**, 535-542 (2013).
119. Gutscher, M., *et al.* Proximity-based Protein Thiol Oxidation by H2O2-scavenging Peroxidases. *Journal of Biological Chemistry* **284**, 31532-31540 (2009).
120. Meyer, A.J. & Dick, T.P. Fluorescent Protein-Based Redox Probes. *Antioxidants & Redox Signaling* **13**, 621-650 (2010).
121. Sippel, T.O. New fluorochromes for thiols: maleimide and iodoacetamide derivatives of a 3-phenylcoumarin fluorophore. *Journal of Histochemistry & Cytochemistry* **29**, 314-316 (1981).

122. Sippel, T.O. Microfluorometric analysis of protein thiol groups with a coumarinylphenylmaleimide. *Journal of Histochemistry & Cytochemistry* **29**, 1377-1381 (1981).
123. Corrie, J.E.T. Thiol-reactive fluorescent probes for protein labelling. *Journal of the Chemical Society, Perkin Transactions 1*, 2975-2982 (1994).
124. Yang, J.-R. & Langmuir, M.E. Synthesis and properties of a maleimide fluorescent thiol reagent derived from a naphthopyranone. *Journal of Heterocyclic Chemistry* **28**, 1177-1180 (1991).
125. Wu, J., Ferrance, J.P., Landers, J.P. & Weber, S.G. Integration of a Precolumn Fluorogenic Reaction, Separation, and Detection of Reduced Glutathione. *Analytical Chemistry* **82**, 7267-7273 (2010).
126. Peng, H., *et al.* Thiol Reactive Probes and Chemosensors. *Sensors* **12**, 15907 (2012).
127. Penugonda, S., Wu, W., Mare, S. & Ercal, N. Liquid chromatography analysis of N-(2-mercaptopropionyl)-glycine in biological samples by ThioGlo™ 3 derivatization. *Journal of Chromatography B* **807**, 251-256 (2004).
128. Matsumoto, T., Urano, Y., Shoda, T., Kojima, H. & Nagano, T. A Thiol-Reactive Fluorescence Probe Based on Donor-Excited Photoinduced Electron Transfer: Key Role of Ortho Substitution. *Organic Letters* **9**, 3375-3377 (2007).
129. Yi, L., *et al.* A Highly Sensitive Fluorescence Probe for Fast Thiol-Quantification Assay of Glutathione Reductase. *Angewandte Chemie International Edition* **48**, 4034-4037 (2009).
130. Kim, G.-J., Lee, K., Kwon, H. & Kim, H.-J. Ratiometric Fluorescence Imaging of Cellular Glutathione. *Organic Letters* **13**, 2799-2801 (2011).
131. Rice, G.C., Bump, E.A., Shrieve, D.C., Lee, W. & Kovacs, M. Quantitative Analysis of Cellular Glutathione by Flow Cytometry Utilizing Monochlorobimane: Some Applications to Radiation and Drug Resistance in Vitro and in Vivo. *Cancer Research* **46**, 6105-6110 (1986).
132. Gutscher, M., *et al.* Real-time imaging of the intracellular glutathione redox potential. *Nat Meth* **5**, 553-559 (2008).
133. Srinivasan, U., Mieyal, P.A. & Mieyal, J.J. pH Profiles Indicative of Rate-Limiting Nucleophilic Displacement in Thioltransferase Catalysis. *Biochemistry* **36**, 3199-3206 (1997).
134. Shibata, N. & Kobayashi, M. The role for oxidative stress in neurodegenerative diseases. *Brain Nerve* **60**, 157-170 (2008).
135. Hald, A. & Lotharius, J. Oxidative stress and inflammation in Parkinson's disease: is there a causal link? *Experimental Neurology* **193**, 279-290 (2005).
136. Crespi, F. Hydrogen peroxide monitored in vivo, in situ and in real time in rat brain, is it a marker of central cholinergic dynamics? *Anal. Methods* **6**, 1174-1181 (2014).
137. Roberts, J.G., Toups, J.V., Eyualem, E., McCarty, G.S. & Sombers, L.A. In Situ Electrode Calibration Strategy for Voltammetric Measurements In Vivo. *Anal. Chem. (Washington, DC, U. S.)* **85**, 11568-11575 (2013).
138. Ross, A.E. & Venton, B.J. Sawhorse Waveform Voltammetry for Selective Detection of Adenosine, ATP, and Hydrogen Peroxide. *Anal. Chem. (Washington, DC, U. S.)* **86**, 7486-7493 (2014).
139. Kalyanaraman, B., *et al.* Measuring reactive oxygen and nitrogen species with fluorescent probes: challenges and limitations. *Free Radical Biol. Med.* **52**, 1-6 (2012).

140. Karlsson, M., Kurz, T., Brunk, U.T., Nilsson, S.E. & Frennesson, C.I. What does the commonly used DCF test for oxidative stress really show? *Biochemical Journal* **428**, 183-190 (2010).
141. Kristiansen, K.A., Jensen, P.E., Moller, I.M. & Schulz, A. Monitoring reactive oxygen species formation and localisation in living cells by use of the fluorescent probe CM-H(2)DCFDA and confocal laser microscopy. *Physiologia plantarum* **136**, 369-383 (2009).
142. Ostergaard, H., Tachibana, C. & Winther, J.R. Monitoring disulfide bond formation in the eukaryotic cytosol. *J. Cell Biol.* **166**, 337-345 (2004).
143. Hanson, G.T., *et al.* Investigating Mitochondrial Redox Potential with Redox-sensitive Green Fluorescent Protein Indicators. *J. Biol. Chem.* **279**, 13044-13053 (2004).
144. Cannon, M.B. & Remington, S.J. Re-engineering redox-sensitive green fluorescent protein for improved response rate. *Protein Sci.* **15**, 45-57 (2006).
145. Meyer, A.J., *et al.* Redox-sensitive GFP in Arabidopsis thaliana is a quantitative biosensor for the redox potential of the cellular glutathione redox buffer. *Plant J.* **52**, 973-986 (2007).
146. Gutscher, M., *et al.* Real-time imaging of the intracellular glutathione redox potential. *Nat. Methods* **5**, 553-559 (2008).
147. Funke, F., Gerich, F.J. & Müller, M. Dynamic, semi-quantitative imaging of intracellular ROS levels and redox status in rat hippocampal neurons. *NeuroImage* **54**, 2590-2602 (2011).
148. Grosser, E., *et al.* Oxidative burden and mitochondrial dysfunction in a mouse model of Rett syndrome. *Neurobiol. Dis.* **48**, 102-114 (2012).
149. Hasel, P., McKay, S., Qiu, J. & Hardingham, G.E. Selective dendritic susceptibility to bioenergetic, excitotoxic and redox perturbations in cortical neurons. *Biochim. Biophys. Acta, Mol. Cell Res.*, Ahead of Print (2015).
150. Breckwoldt, M.O., *et al.* Multiparametric optical analysis of mitochondrial redox signals during neuronal physiology and pathology in vivo. *Nat Med* **advance online publication**(2014).
151. Stoppini, L., Buchs, P.A. & Muller, D. A simple method for organotypic cultures of nervous tissue. *J Neurosci Methods* **37**, 173-182 (1991).
152. Engler, C., Kandzia, R. & Marillonnet, S. A One Pot, One Step, Precision Cloning Method with High Throughput Capability. *Plos One* **3**(2008).
153. Gogolla, N., Galimberti, I., DePaola, V. & Caroni, P. Preparation of organotypic hippocampal slice cultures for long-term live imaging. *Nat. Protocols* **1**, 1165-1171 (2006).
154. Woods, G. & Zito, K. Preparation of gene gun bullets and biolistic transfection of neurons in slice culture. *Journal of visualized experiments: JoVE* (2008).
155. Wills, Z.P., *et al.* The nogo receptor family restricts synapse number in the developing hippocampus. *Neuron* **73**, 466-481 (2012).
156. Haas, K., Sin, W.-C., Javaherian, A., Li, Z. & Cline, H.T. Single-Cell Electroporationfor Gene Transfer In Vivo. *Neuron* **29**, 583-591 (2001).
157. Fiacco, T.A. & McCarthy, K.D. Intracellular Astrocyte Calcium Waves In Situ Increase the Frequency of Spontaneous AMPA Receptor Currents in CA1 Pyramidal Neurons. *The Journal of Neuroscience* **24**, 722-732 (2004).
158. Tseng, Q., *et al.* Spatial organization of the extracellular matrix regulates cell–cell junction positioning. *Proceedings of the National Academy of Sciences* **109**, 1506-1511 (2012).
159. Meyer, A.J. & Dick, T.P. Fluorescent Protein-Based Redox Probes. *Antioxid. Redox Signaling* **13**, 621-650 (2010).

160. Schafer, F.Q. & Buettner, G.R. Redox environment of the cell as viewed through the redox state of the glutathione disulfide/glutathione couple. *Free Radical Biology and Medicine* **30**, 1191-1212 (2001).
161. Revsbech, N.P. An Oxygen Microsensor with a Guard Cathode. *Limnology and Oceanography* **34**, 474-478 (1989).
162. Galván, E.J., *et al.* Critical Involvement of Postsynaptic Protein Kinase Activation in Long-Term Potentiation at Hippocampal Mossy Fiber Synapses on CA3 Interneurons. *The Journal of Neuroscience* **30**, 2844-2855 (2010).
163. Huchzermeyer, C., Berndt, N., Holzhutter, H.-G. & Kann, O. Oxygen consumption rates during three different neuronal activity states in the hippocampal CA3 network. *J Cereb Blood Flow Metab* **33**, 263-271 (2013).
164. Shaner, N.C., *et al.* Improved monomeric red, orange and yellow fluorescent proteins derived from Discosoma sp. red fluorescent protein. *Nat. Biotechnol.* **22**, 1567-1572 (2004).
165. Fekete, A., Vizi, E.S., Kovacs, K.J., Lendvai, B. & Zelles, T. Layer-specific differences in reactive oxygen species levels after oxygen-glucose deprivation in acute hippocampal slices. *Free Radical Biol. Med.* **44**, 1010-1022 (2008).
166. Lash, L.H. Mitochondrial glutathione transport: Physiological, pathological and toxicological implications. *Chemico-Biological Interactions* **163**, 54-67 (2006).
167. Gerich, F.J., Hepp, S., Probst, I. & Muller, M. Mitochondrial inhibition prior to oxygen-withdrawal facilitates the occurrence of hypoxia-induced spreading depression in rat hippocampal slices. *J Neurophysiol* **96**, 492-504 (2006).
168. Bahar, S., Fayuk, D., Somjen, G.G., Aitken, P.G. & Turner, D.A. Mitochondrial and Intrinsic Optical Signals Imaged During Hypoxia and Spreading Depression in Rat Hippocampal Slices. *Journal of Neurophysiology* **84**, 311-324 (2000).
169. Schuchmann, S., Lückermann, M., Kulik, A., Heinemann, U. & Ballanyi, K. Ca2+- and Metabolism-Related Changes of Mitochondrial Potential in Voltage-Clamped CA1 Pyramidal Neurons In Situ. *Journal of Neurophysiology* **83**, 1710-1721 (2000).
170. Vogel, R., Wiesinger, H., Hamprecht, B. & Dringen, R. The regeneration of reduced glutathione in rat forebrain mitochondria identifies metabolic pathways providing the NADPH required. *Neuroscience Letters* **275**, 97-100 (1999).
171. Marí, M., Morales, A., Colell, A., García-Ruiz, C. & Fernández-Checa, J.C. Mitochondrial Glutathione, a Key Survival Antioxidant. *Antioxidants & Redox Signaling* **11**, 2685-2700 (2009).
172. Abramov, A.Y., Scorziello, A. & Duchen, M.R. Three distinct mechanisms generate oxygen free radicals in neurons and contribute to cell death during anoxia and reoxygenation. *The Journal of neuroscience : the official journal of the Society for Neuroscience* **27**, 1129-1138 (2007).
173. Park, W.H., Han, Y.W., Kim, S.H. & Kim, S.Z. An ROS generator, antimycin A, inhibits the growth of HeLa cells via apoptosis. *Journal of Cellular Biochemistry* **102**, 98-109 (2007).
174. Cheng, W.-H., *et al.* Cellular Glutathione Peroxidase Is the Mediator of Body Selenium To Protect against Paraquat Lethality in Transgenic Mice. *The Journal of Nutrition* **128**, 1070-1076 (1998).
175. Circu, M.L. & Aw, T.Y. Reactive oxygen species, cellular redox systems, and apoptosis. *Free Radical Biology and Medicine* **48**, 749-762 (2010).

176. Fang, Y.-Z., Yang, S. & Wu, G. Free radicals, antioxidants, and nutrition. *Nutrition* **18**, 872-879 (2002).
177. Lei, X.G. [19] - In Vivo Antioxidant Role of Glutathione Peroxidase: Evidence from Knockout Mice. in *Methods in Enzymology*, Vol. Volume 347 (eds. Helmut, S. & Lester, P.) 213-225 (Academic Press, 2002).
178. Markovic, J., *et al.* Glutathione Is Recruited into the Nucleus in Early Phases of Cell Proliferation. *Journal of Biological Chemistry* **282**, 20416-20424 (2007).
179. Millis, K.K., Weaver, K.H. & Rabenstein, D.L. Oxidation/reduction potential of glutathione. *The Journal of Organic Chemistry* **58**, 4144-4146 (1993).
180. Salvemini, F., *et al.* Enhanced Glutathione Levels and Oxidoresistance Mediated by Increased Glucose-6-phosphate Dehydrogenase Expression. *Journal of Biological Chemistry* **274**, 2750-2757 (1999).
181. Davis, W., Ronai, Z.e. & Tew, K.D. Cellular Thiols and Reactive Oxygen Species in Drug-Induced Apoptosis. *Journal of Pharmacology and Experimental Therapeutics* **296**, 1-6 (2001).
182. Daubeuf, S., *et al.* Enhanced resistance of HeLa cells to cisplatin by overexpression of γ-glutamyltransferase. *Biochemical Pharmacology* **64**, 207-216 (2002).
183. Furuichi, T., Liu, W., Shi, H., Miyake, M. & Liu, K.J. Generation of hydrogen peroxide during brief oxygen-glucose deprivation induces preconditioning neuronal protection in primary cultured neurons. *Journal of Neuroscience Research* **79**, 816-824 (2005).
184. Wüllner, U., *et al.* Glutathione depletion and neuronal cell death: the role of reactive oxygen intermediates and mitochondrial function. *Brain Research* **826**, 53-62 (1999).
185. Currais, A. & Maher, P. Functional Consequences of Age-Dependent Changes in Glutathione Status in the Brain. *Antioxidants & redox signaling* **19**, 813-822 (2012).
186. Gu, F., Chauhan, V. & Chauhan, A. Impaired synthesis and antioxidant defense of glutathione in the cerebellum of autistic subjects: Alterations in the activities and protein expression of glutathione-related enzymes. *Free Radical Biology and Medicine* **65**, 488-496 (2013).
187. Brodie, A.E., Potter, J. & Reed, D.J. Unique Characteristics of Rat Spleen Lymphocyte, L1210 Lymphoma and HeLa Cells in Glutathione Biosynthesis from Sulfur-Containing Amino Acids. *European Journal of Biochemistry* **123**, 159-164 (1982).
188. Sanford, A.L., *et al.* Voltammetric Detection of Hydrogen Peroxide at Carbon Fiber Microelectrodes. *Analytical Chemistry* **82**, 5205-5210 (2010).
189. Rahman, I., Kode, A. & Biswas, S.K. Assay for quantitative determination of glutathione and glutathione disulfide levels using enzymatic recycling method. *Nat. Protocols* **1**, 3159-3165 (2007).
190. Masters, J.R. HeLa cells 50 years on: the good, the bad and the ugly. *Nat Rev Cancer* **2**, 315-319 (2002).
191. Albrecht, Simone C., Barata, Ana G., Großhans, J., Teleman, Aurelio A. & Dick, Tobias P. In Vivo Mapping of Hydrogen Peroxide and Oxidized Glutathione Reveals Chemical and Regional Specificity of Redox Homeostasis. *Cell Metabolism* **14**, 819-829 (2011).
192. SchwarzlÄNder, M., *et al.* Confocal imaging of glutathione redox potential in living plant cells. *Journal of Microscopy* **231**, 299-316 (2008).
193. Dalby, B., *et al.* Advanced transfection with Lipofectamine 2000 reagent: primary neurons, siRNA, and high-throughput applications. *Methods* **33**, 95-103 (2004).

194. Hailer, N.P., Järhult, J.D. & Nitsch, R. Resting microglial cells in vitro: Analysis of morphology and adhesion molecule expression in organotypic hippocampal slice cultures. *Glia* **18**, 319-331 (1996).
195. Woods, G. & Zito, K. Preparation of Gene Gun Bullets and Biolistic Transfection of Neurons in Slice Culture. *Journal of Visualized Experiments : JoVE*, 675 (2008).
196. Llopis, J., McCaffery, J.M., Miyawaki, A., Farquhar, M.G. & Tsien, R.Y. Measurement of cytosolic, mitochondrial, and Golgi pH in single living cells with green fluorescent proteins. *Proceedings of the National Academy of Sciences* **95**, 6803-6808 (1998).
197. Banach-Latapy, A., *et al.* Redox-sensitive YFP sensors for monitoring dynamic compartment-specific glutathione redox state. *Free Radical Biology and Medicine* **65**, 436-445 (2013).
198. Balaban, R.S. Regulation of oxidative phosphorylation in the mammalian cell. *American Journal of Physiology - Cell Physiology* **258**, C377-C389 (1990).
199. Iijima, T., Mishima, T., Akagawa, K. & Iwao, Y. Mitochondrial hyperpolarization after transient oxygen-glucose deprivation and subsequent apoptosis in cultured rat hippocampal neurons. *Brain Research* **993**, 140-145 (2003).
200. Zhou, N., Gordon, G.R.J., Feighan, D. & MacVicar, B.A. Transient Swelling, Acidification, and Mitochondrial Depolarization Occurs in Neurons but not Astrocytes during Spreading Depression. *Cerebral Cortex* **20**, 2614-2624 (2010).
201. Campanella, M., *et al.* Regulation of Mitochondrial Structure and Function by the F1Fo-ATPase Inhibitor Protein, IF1. *Cell Metabolism* **8**, 13-25 (2008).
202. Gusdon, A.M. & Chu, C.T. To Eat or Not to Eat: Neuronal Metabolism, Mitophagy, and Parkinson's Disease. *Antioxidants & Redox Signaling* **14**, 1979-1987 (2010).
203. Ouyang, Y.-B., Voloboueva, L.A., Xu, L.-J. & Giffard, R.G. Selective Dysfunction of Hippocampal CA1 Astrocytes Contributes to Delayed Neuronal Damage after Transient Forebrain Ischemia. *The Journal of Neuroscience* **27**, 4253-4260 (2007).
204. Vaughn, A.E. & Deshmukh, M. Glucose metabolism inhibits apoptosis in neurons and cancer cells by redox inactivation of cytochrome c. *Nat Cell Biol* **10**, 1477-1483 (2008).
205. Petito, C.K., Feldmann, E., Pulsinelli, W.A. & Plum, F. Delayed hippocampal damage in humans following cardiorespiratory arrest. *Neurology* **37**, 1281 (1987).
206. Cummings, J.L., Tomiyasu, U., Read, S. & Benson, D.F. Amnesia with hippocampal lesions cardiopulmonary arrest. *Neurology* **34**, 679 (1984).
207. Zola-Morgan, S., Squire, L. & Amaral, D. Human amnesia and the medial temporal region: enduring memory impairment following a bilateral lesion limited to field CA1 of the hippocampus. *The Journal of Neuroscience* **6**, 2950-2967 (1986).
208. Brierley, J.B. & Cooper, J.E. CEREBRAL COMPLICATIONS OF HYPOTENSIVE ANAESTHESIA IN A HEALTHY ADULT. *Journal of Neurology, Neurosurgery & Psychiatry* **25**, 24-30 (1962).
209. Pulsinelli, W.A. & Brierley, J.B. A new model of bilateral hemispheric ischemia in the unanesthetized rat. *Stroke* **10**, 267-272 (1979).
210. Pulsinelli, W.A., Brierley, J.B. & Plum, F. Temporal profile of neuronal damage in a model of transient forebrain ischemia. *Ann Neurol* **11**, 491-498 (1982).
211. Kirino, T. Delayed neuronal death in the gerbil hippocampus following ischemia. *Brain Res* **239**, 57-69 (1982).

212. Bartsch, T., *et al.* Selective neuronal vulnerability of human hippocampal CA1 neurons: lesion evolution, temporal course, and pattern of hippocampal damage in diffusion-weighted MR imaging. *J Cereb Blood Flow Metab* **35**, 1836-1845 (2015).
213. Stanika, R.I., Winters, C.A., Pivovarova, N.B. & Andrews, S.B. Differential NMDA receptor-dependent calcium loading and mitochondrial dysfunction in CA1 vs. CA3 hippocampal neurons. *Neurobiology of Disease* **37**, 403-411 (2010).
214. Pellegrini-Giampietro, D.E., Zukin, R.S., Bennett, M.V., Cho, S. & Pulsinelli, W.A. Switch in glutamate receptor subunit gene expression in CA1 subfield of hippocampus following global ischemia in rats. *Proceedings of the National Academy of Sciences* **89**, 10499-10503 (1992).
215. Chan, P.H. Reactive Oxygen Radicals in Signaling and Damage in the Ischemic Brain. *J Cereb Blood Flow Metab* **21**, 2-14 (2001).
216. Mattiasson, G., Friberg, H., Hansson, M., Elmér, E. & Wieloch, T. Flow cytometric analysis of mitochondria from CA1 and CA3 regions of rat hippocampus reveals differences in permeability transition pore activation. *Journal of Neurochemistry* **87**, 532-544 (2003).
217. Kubo, T., *et al.* Characteristics of protective effects of NMDA antagonist and calcium channel antagonist on ischemic calcium accumulation in rat hippocampal CA1 region. *Brain Research Bulletin* **54**, 413-419 (2001).
218. Zhang, Q.-G., *et al.* Estrogen Attenuates Ischemic Oxidative Damage via an Estrogen Receptor α-Mediated Inhibition of NADPH Oxidase Activation. *The Journal of Neuroscience* **29**, 13823-13836 (2009).
219. Chan, P.H., *et al.* Overexpression of SOD1 in Transgenic Rats Protects Vulnerable Neurons Against Ischemic Damage After Global Cerebral Ischemia and Reperfusion. *The Journal of Neuroscience* **18**, 8292-8299 (1998).
220. Luetjens, C.M., *et al.* Delayed Mitochondrial Dysfunction in Excitotoxic Neuron Death: Cytochrome c Release and a Secondary Increase in Superoxide Production. *The Journal of Neuroscience* **20**, 5715-5723 (2000).
221. Morgan, M.J. & Liu, Z.-g. Crosstalk of reactive oxygen species and NF-[kappa]B signaling. *Cell Res* **21**, 103-115 (2011).
222. Zhao, Y., Patzer, A., Herdegen, T., Gohlke, P. & Culman, J. Activation of cerebral peroxisome proliferator-activated receptors gamma promotes neuroprotection by attenuation of neuronal cyclooxygenase-2 overexpression after focal cerebral ischemia in rats. *The FASEB Journal* **20**, 1162-1175 (2006).
223. Gasche, Y., *et al.* Early Appearance of Activated Matrix Metalloproteinase-9 After Focal Cerebral Ischemia in Mice[colon] A Possible Role in Blood-Brain Barrier Dysfunction. *J Cereb Blood Flow Metab* **19**, 1020-1028 (1999).
224. Haines, B. & Li, P.A. Overexpression of Mitochondrial Uncoupling Protein 2 Inhibits Inflammatory Cytokines and Activates Cell Survival Factors after Cerebral Ischemia. *Plos One* **7**, e31739 (2012).
225. Griendling, K.K., Sorescu, D. & Ushio-Fukai, M. NAD(P)H Oxidase: Role in Cardiovascular Biology and Disease. *Circulation Research* **86**, 494-501 (2000).
226. Rybnikova, E., Damdimopoulos, A.E., Gustafsson, J.-Å., Spyrou, G. & Pelto-Huikko, M. Expression of novel antioxidant thioredoxin-2 in the rat brain. *European Journal of Neuroscience* **12**, 1669-1678 (2000).

227. Valko, M., Rhodes, C.J., Moncol, J., Izakovic, M. & Mazur, M. Free radicals, metals and antioxidants in oxidative stress-induced cancer. *Chemico-Biological Interactions* **160**, 1-40 (2006).
228. Mitozo, P.A., *et al.* A study of the relative importance of the peroxiredoxin-, catalase-, and glutathione-dependent systems in neural peroxide metabolism. *Free Radical Biology and Medicine* **51**, 69-77 (2011).
229. inKudin, A.P., Augustynek, B., Lehmann, A.K., Kovács, R. & Kunz, W.S. The contribution of thioredoxin-2 reductase and glutathione peroxidase to H2O2 detoxification of rat brain mitochondria. *Biochimica et Biophysica Acta (BBA) - Bioenergetics* **1817**, 1901-1906 (2012).
230. Sheng, Y., *et al.* Superoxide Dismutases and Superoxide Reductases. *Chemical Reviews* **114**, 3854-3918 (2014).
231. Ono, T., *et al.* Xanthine oxidase is one of the major sources of superoxide anion radicals in blood after reperfusion in rats with forebrain ischemia/reperfusion. *Brain Research* **1305**, 158-167 (2009).
232. Lee, J.-M., Calkins, M.J., Chan, K., Kan, Y.W. & Johnson, J.A. Identification of the NF-E2-related Factor-2-dependent Genes Conferring Protection against Oxidative Stress in Primary Cortical Astrocytes Using Oligonucleotide Microarray Analysis. *Journal of Biological Chemistry* **278**, 12029-12038 (2003).
233. Shih, A.Y., Li, P. & Murphy, T.H. A Small-Molecule-Inducible Nrf2-Mediated Antioxidant Response Provides Effective Prophylaxis against Cerebral Ischemia In Vivo. *The Journal of Neuroscience* **25**, 10321-10335 (2005).
234. Yin, B., Barrionuevo, G. & Weber, S.G. Optimized Real-Time Monitoring of Glutathione Redox Status in Single Pyramidal Neurons in Organotypic Hippocampal Slices during Oxygen–Glucose Deprivation and Reperfusion. *ACS Chemical Neuroscience* **6**, 1838-1848 (2015).
235. Ahlgren, H., Henjum, K., Ottersen, O. & Rundén-Pran, E. Validation of organotypical hippocampal slice cultures as an ex vivo model of brain ischemia: different roles of NMDA receptors in cell death signalling after exposure to NMDA or oxygen and glucose deprivation. *Cell Tissue Res* **345**, 329-341 (2011).
236. Shaner, N.C., *et al.* Improved monomeric red, orange and yellow fluorescent proteins derived from Discosoma sp. red fluorescent protein. *Nat Biotech* **22**, 1567-1572 (2004).
237. Rajic, Z., *et al.* A new SOD mimic, Mn(III) ortho N-butoxyethylpyridylporphyrin, combines superb potency and lipophilicity with low toxicity. *Free Radical Biology and Medicine* **52**, 1828-1834 (2012).
238. Riccardi, C. & Nicoletti, I. Analysis of apoptosis by propidium iodide staining and flow cytometry. *Nat. Protocols* **1**, 1458-1461 (2006).
239. Eng, J., Lynch, R.M. & Balaban, R.S. Nicotinamide adenine dinucleotide fluorescence spectroscopy and imaging of isolated cardiac myocytes. *Biophysical Journal* **55**, 621-630 (1989).
240. Gogolla, N., Galimberti, I., DePaola, V. & Caroni, P. Staining protocol for organotypic hippocampal slice cultures. *Nat. Protocols* **1**, 2452-2456 (2006).
241. Jun, A.S., Brown, M.D. & Wallace, D.C. A mitochondrial DNA mutation at nucleotide pair 14459 of the NADH dehydrogenase subunit 6 gene associated with maternally inherited Leber hereditary optic neuropathy and dystonia. *Proceedings of the National Academy of Sciences* **91**, 6206-6210 (1994).

242. Martinet, W., *et al.* Western blot analysis of a limited number of cells: a valuable adjunct to proteome analysis of paraffin wax-embedded, alcohol-fixed tissue after laser capture microdissection. *The Journal of Pathology* **202**, 382-388 (2004).
243. Ornstein, D.K., *et al.* Proteomic analysis of laser capture microdissected human prostate cancer and in vitro prostate cell lines. *ELECTROPHORESIS* **21**, 2235-2242 (2000).
244. Espina, V., *et al.* Laser-capture microdissection. *Nat. Protocols* **1**, 586-603 (2006).
245. Ma, L.-H., Takanishi, C.L. & Wood, M.J. Molecular Mechanism of Oxidative Stress Perception by the Orp1 Protein. *Journal of Biological Chemistry* **282**, 31429-31436 (2007).
246. Stone, J.R. & Yang, S. Hydrogen Peroxide: A Signaling Messenger. *Antioxidants & Redox Signaling* **8**, 243-270 (2006).
247. Xiao, R., Lundström-Ljung, J., Holmgren, A. & Gilbert, H.F. Catalysis of Thiol/Disulfide Exchange: GLUTAREDOXIN 1 AND PROTEIN-DISULFIDE ISOMERASE USE DIFFERENT MECHANISMS TO ENHANCE OXIDASE AND REDUCTASE ACTIVITIES. *Journal of Biological Chemistry* **280**, 21099-21106 (2005).
248. Alluri, H., Anasooya Shaji, C., Davis, M.L. & Tharakan, B. Oxygen-Glucose Deprivation and Reoxygenation as an In Vitro Ischemia-Reperfusion Injury Model for Studying Blood-Brain Barrier Dysfunction. e52699 (2015).
249. Fontella, F.U., *et al.* Acute and repeated restraint stress influences cellular damage in rat hippocampal slices exposed to oxygen and glucose deprivation. *Brain Research Bulletin* **65**, 443-450 (2005).
250. Jarvis, C.R., Anderson, T.R. & Andrew, R.D. Anoxic Depolarization Mediates Acute Damage Independent of Glutamate in Neocortical Brain Slices. *Cerebral Cortex* **11**, 249-259 (2001).
251. Obeidat, A.S., Jarvis, C.R. & Andrew, R.D. Glutamate Does Not Mediate Acute Neuronal Damage After Spreading Depression Induced By O2/Glucose Deprivation in the Hippocampal Slice. *J Cereb Blood Flow Metab* **20**, 412-422 (2000).
252. Xie, M., Wang, W., Kimelberg, H.K. & Zhou, M. Oxygen and glucose deprivation-induced changes in astrocyte membrane potential and their underlying mechanisms in acute rat hippocampal slices. *J Cereb Blood Flow Metab* **28**, 456-467 (2007).
253. Silva-Adaya, D., Gonsebatt, M.E. & Guevara, J. Thioredoxin System Regulation in the Central Nervous System: Experimental Models and Clinical Evidence. *Oxidative medicine and cellular longevity* **2014**(2014).
254. Criddle, D.N., *et al.* Menadione-induced Reactive Oxygen Species Generation via Redox Cycling Promotes Apoptosis of Murine Pancreatic Acinar Cells. *Journal of Biological Chemistry* **281**, 40485-40492 (2006).
255. Hoegger, M., Lieven, C. & Levin, L. Differential production of superoxide by neuronal mitochondria. *BMC Neuroscience* **9**, 4 (2008).
256. Wyatt, K.M., Skene, C., Veitch, K., Hue, L. & McCormack, J.G. The antianginal agent ranolazine is a weak inhibitor of the respiratory Complex I, but with greater potency in broken or uncoupled than in coupled mitochondria. *Biochemical Pharmacology* **50**, 1599-1606 (1995).
257. Kim, H.-C., *et al.* An immunocytochemical study of mitochondrial manganese-superoxide dismutase in the rat hippocampus after kainate administration. *Neuroscience Letters* **281**, 65-68 (2000).
258. Kalyanaraman, B., *et al.* Measuring reactive oxygen and nitrogen species with fluorescent probes: challenges and limitations. *Free Radical Biology and Medicine* **52**, 1-6 (2012).

259. St-Pierre, J., Buckingham, J.A., Roebuck, S.J. & Brand, M.D. Topology of Superoxide Production from Different Sites in the Mitochondrial Electron Transport Chain. *Journal of Biological Chemistry* **277**, 44784-44790 (2002).
260. Abe, K. & Saito, H. Menadione Toxicity in Cultured Rat Cortical Astrocytes. *The Japanese Journal of Pharmacology* **72**, 299-306 (1996).
261. Huchzermeyer, C., *et al.* Gamma Oscillations and Spontaneous Network Activity in the Hippocampus Are Highly Sensitive to Decreases in pO2 and Concomitant Changes in Mitochondrial Redox State. *The Journal of Neuroscience* **28**, 1153-1162 (2008).
262. Kann, O., *et al. Metabolic dysfunction during neuronal activation in the ex vivo hippocampus from chronic epileptic rats and humans*, (2005).
263. Deponte, M. Glutathione catalysis and the reaction mechanisms of glutathione-dependent enzymes. *Biochimica et Biophysica Acta (BBA) - General Subjects* **1830**, 3217-3266 (2013).
264. Greetham, D., *et al.* Oxidation of the Yeast Mitochondrial Thioredoxin Promotes Cell Death. *Antioxidants & Redox Signaling* **18**, 376-385 (2013).
265. Trotter, E.W. & Grant, C.M. Non-reciprocal regulation of the redox state of the glutathione–glutaredoxin and thioredoxin systems. *EMBO reports* **4**, 184-188 (2003).
266. Winterbourn, C.C. & Hampton, M.B. Thiol chemistry and specificity in redox signaling. *Free Radical Biology and Medicine* **45**, 549-561 (2008).
267. Holmgren, A. Thioredoxin. *Annual Review of Biochemistry* **54**, 237-271 (1985).
268. Ng, C.F., Schafer, F.Q., Buettner, G.R. & Rodgers, V.G.J. The rate of cellular hydrogen peroxide removal shows dependency on GSH: Mathematical insight into in vivo H2O2 and GPx concentrations. *Free Radical Research* **41**, 1201-1211 (2007).
269. Arnér, E.S.J., Zhong, L. & Holmgren, A. Preparation and assay of mammalian thioredoxin and thioredoxin reductase. in *Methods in Enzymology*, Vol. Volume 300 226-239 (Academic Press, 1999).
270. Henderson, G.B., *et al.* Engineering the substrate specificity of glutathione reductase toward that of trypanothione reduction. *Proceedings of the National Academy of Sciences of the United States of America* **88**, 8769-8773 (1991).
271. Kwong, L.K. & Sohal, R.S. Age-Related Changes in Activities of Mitochondrial Electron Transport Complexes in Various Tissues of the Mouse. *Archives of Biochemistry and Biophysics* **373**, 16-22 (2000).
272. Lillig, C.H. & Holmgren, A. Thioredoxin and Related Molecules–From Biology to Health and Disease. *Antioxidants & Redox Signaling* **9**, 25-47 (2006).
273. Dikalov, S. Cross talk between mitochondria and NADPH oxidases. *Free Radical Biology and Medicine* **51**, 1289-1301 (2011).
274. Rui, C., *et al.* Protective effects of Lycium barbarum polysaccharide on neonatal rat primary cultured hippocampal neurons injured by oxygen-glucose deprivation and reperfusion. *J Mol Hist* **43**, 535-542 (2012).
275. Baitharu, I., *et al.* Withanolide A Prevents Neurodegeneration by Modulating Hippocampal Glutathione Biosynthesis during Hypoxia. *Plos One* **9**, e105311 (2014).
276. Van Elzen, R., *et al.* Integrated Proteomic Analysis Reveals a Substantial Enrichment of Protein Trafficking Processes in Hippocampus Tissue after Hypoxic Stress. *Journal of Proteome Research* **9**, 204-215 (2010).
277. Wang, K., *et al.* Thioredoxin Reductase Was Nitrated in the Aging Heart After Myocardial Ischemia/Reperfusion. *Rejuvenation Research* **16**, 377-385 (2013).

278. Cortassa, S., Aon, M.A., Winslow, R.L. & O'Rourke, B. A Mitochondrial Oscillator Dependent on Reactive Oxygen Species. *Biophysical Journal* **87**, 2060-2073 (2004).
279. Tanaka, N., *et al.* Expression of Keap1–Nrf2 system and antioxidative proteins in mouse brain after transient middle cerebral artery occlusion. *Brain Research* **1370**, 246-253 (2011).
280. Takagi, Y., *et al.* Redox Control of Neuronal Damage During Brain Ischemia After Middle Cerebral Artery Occlusion in the Rat: Immunohistochemical and Hybridization Studies of Thioredoxin. *J Cereb Blood Flow Metab* **18**, 206-214 (1998).
281. Zhang, F., *et al.* Pharmacological induction of heme oxygenase-1 by a triterpenoid protects neurons against ischemic injury. *Stroke* **43**, 1390-1397 (2012).
282. Parada, E., *et al.* The Microglial α7-Acetylcholine Nicotinic Receptor Is a Key Element in Promoting Neuroprotection by Inducing Heme Oxygenase-1 via Nuclear Factor Erythroid-2-Related Factor 2. *Antioxidants & Redox Signaling* **19**, 1135-1148 (2013).
283. Koide, Y., *et al.* A reversible near-infrared fluorescence probe for reactive oxygen species based on Te-rhodamine. *Chemical Communications* **48**, 3091-3093 (2012).
284. Markus, S., David, C.L., Mark, D.F. & Lee, J.S. The circularly permuted yellow fluorescent protein cpYFP that has been used as a superoxide probe is highly responsive to pH but not superoxide in mitochondria: implications for the existence of superoxide'flashes'. *Biochemical Journal* **437**, 381-387 (2011).
285. Zhou, M., Diwu, Z., Panchuk-Voloshina, N. & Haugland, R.P. A Stable Nonfluorescent Derivative of Resorufin for the Fluorometric Determination of Trace Hydrogen Peroxide: Applications in Detecting the Activity of Phagocyte NADPH Oxidase and Other Oxidases. *Analytical Biochemistry* **253**, 162-168 (1997).
286. Miller, E.W., Albers, A.E., Pralle, A., Isacoff, E.Y. & Chang, C.J. Boronate-Based Fluorescent Probes for Imaging Cellular Hydrogen Peroxide. *Journal of the American Chemical Society* **127**, 16652-16659 (2005).
287. Albers, A.E., Okreglak, V.S. & Chang, C.J. A FRET-Based Approach to Ratiometric Fluorescence Detection of Hydrogen Peroxide. *Journal of the American Chemical Society* **128**, 9640-9641 (2006).
288. Srikun, D., Miller, E.W., Domaille, D.W. & Chang, C.J. An ICT-Based Approach to Ratiometric Fluorescence Imaging of Hydrogen Peroxide Produced in Living Cells. *Journal of the American Chemical Society* **130**, 4596-4597 (2008).
289. Dickinson, B.C. & Chang, C.J. A Targetable Fluorescent Probe for Imaging Hydrogen Peroxide in the Mitochondria of Living Cells. *Journal of the American Chemical Society* **130**, 9638-9639 (2008).
290. Miller, E.W., Dickinson, B.C. & Chang, C.J. Aquaporin-3 mediates hydrogen peroxide uptake to regulate downstream intracellular signaling. *Proceedings of the National Academy of Sciences* **107**, 15681-15686 (2010).
291. Dickinson, B.C., Huynh, C. & Chang, C.J. A Palette of Fluorescent Probes with Varying Emission Colors for Imaging Hydrogen Peroxide Signaling in Living Cells. *Journal of the American Chemical Society* **132**, 5906-5915 (2010).
292. Dickinson, B.C., Peltier, J., Stone, D., Schaffer, D.V. & Chang, C.J. Nox2 redox signaling maintains essential cell populations in the brain. *Nat Chem Biol* **7**, 106-112 (2011).
293. Chung, C., Srikun, D., Lim, C.S., Chang, C.J. & Cho, B.R. A two-photon fluorescent probe for ratiometric imaging of hydrogen peroxide in live tissue. *Chemical Communications* **47**, 9618-9620 (2011).

294. Karton-Lifshin, N., *et al.* A Unique Paradigm for a Turn-ON Near-Infrared Cyanine-Based Probe: Noninvasive Intravital Optical Imaging of Hydrogen Peroxide. *Journal of the American Chemical Society* **133**, 10960-10965 (2011).
295. Masanta, G., *et al.* A mitochondria-localized two-photon fluorescent probe for ratiometric imaging of hydrogen peroxide in live tissue. *Chemical Communications* **48**, 3518-3520 (2012).
296. Yuan, L., Lin, W., Xie, Y., Chen, B. & Zhu, S. Single Fluorescent Probe Responds to H2O2, NO, and H2O2/NO with Three Different Sets of Fluorescence Signals. *Journal of the American Chemical Society* **134**, 1305-1315 (2012).
297. Kumar, M., Kumar, N., Bhalla, V., Sharma, P.R. & Qurishi, Y. A charge transfer assisted fluorescent probe for selective detection of hydrogen peroxide among different reactive oxygen species. *Chemical Communications* **48**, 4719-4721 (2012).
298. Miller, E.W., Bian, S.X. & Chang, C.J. A Fluorescent Sensor for Imaging Reversible Redox Cycles in Living Cells. *Journal of the American Chemical Society* **129**, 3458-3459 (2007).
299. Towne, V., Will, M., Oswald, B. & Zhao, Q. Complexities in horseradish peroxidase-catalyzed oxidation of dihydroxyphenoxazine derivatives: appropriate ranges for pH values and hydrogen peroxide concentrations in quantitative analysis. *Analytical Biochemistry* **334**, 290-296 (2004).
300. Albers, A.E., Dickinson, B.C., Miller, E.W. & Chang, C.J. A red-emitting naphthofluorescein-based fluorescent probe for selective detection of hydrogen peroxide in living cells. *Bioorganic & Medicinal Chemistry Letters* **18**, 5948-5950 (2008).
301. Dickinson, B.C., Srikun, D. & Chang, C.J. Mitochondrial-targeted fluorescent probes for reactive oxygen species. *Curr. Opin. Chem. Biol.* **14**, 50-56 (2010).
302. Lippert, A.R., Gschneidtner, T. & Chang, C.J. Lanthanide-based luminescent probes for selective time-gated detection of hydrogen peroxide in water and in living cells. *Chemical Communications* **46**, 7510-7512 (2010).
303. Van de Bittner, G.C., Dubikovskaya, E.A., Bertozzi, C.R. & Chang, C.J. In vivo imaging of hydrogen peroxide production in a murine tumor model with a chemoselective bioluminescent reporter. *Proceedings of the National Academy of Sciences* **107**, 21316-21321 (2010).
304. Robeson, J.L. & Tilton, R.D. Spontaneous Reconfiguration of Adsorbed Lysozyme Layers Observed by Total Internal Reflection Fluorescence with a pH-Sensitive Fluorophore. *Langmuir* **12**, 6104-6113 (1996).
305. Newton, G.L., Dorian, R. & Fahey, R.C. Analysis of biological thiols: Derivatization with monobromobimane and separation by reverse-phase high-performance liquid chromatography. *Analytical Biochemistry* **114**, 383-387 (1981).
306. Alhama, J., Romero-Ruiz, A. & López-Barea, J. Metallothionein quantification in clams by reversed-phase high-performance liquid chromatography coupled to fluorescence detection after monobromobimane derivatization. *Journal of Chromatography A* **1107**, 52-58 (2006).
307. Langmuir, M.E., Yang, J.-R., Moussa, A.M., Laura, R. & LeCompte, K.A. New naphthopyranone based fluorescent thiol probes. *Tetrahedron Letters* **36**, 3989-3992 (1995).

308. Cao, X., Lin, W. & Yu, Q. A Ratiometric Fluorescent Probe for Thiols Based on a Tetrakis(4-hydroxyphenyl)porphyrin–Coumarin Scaffold. *The Journal of Organic Chemistry* **76**, 7423-7430 (2011).
309. Lim, C.S., *et al.* Ratiometric Detection of Mitochondrial Thiols with a Two-Photon Fluorescent Probe. *Journal of the American Chemical Society* **133**, 11132-11135 (2011).
310. Long, L., Lin, W., Chen, B., Gao, W. & Yuan, L. Construction of a FRET-based ratiometric fluorescent thiol probe. *Chemical Communications* **47**, 893-895 (2011).
311. Wang, R., Chen, L., Liu, P., Zhang, Q. & Wang, Y. Sensitive Near-Infrared Fluorescent Probes for Thiols Based on Se-N Bond Cleavage: Imaging in Living Cells and Tissues. *Chemistry – A European Journal* **18**, 11343-11349 (2012).
312. Maity, D. & Govindaraju, T. A turn-on NIR fluorescence and colourimetric cyanine probe for monitoring the thiol content in serum and the glutathione reductase assisted glutathione redox process. *Organic & Biomolecular Chemistry* **11**, 2098-2104 (2013).
313. Reddie, K.G., *et al.* Fluorescent Coumarin Thiols Measure Biological Redox Couples. *Organic Letters* **14**, 680-683 (2012).
314. Xu, K., *et al.* A near-infrared reversible fluorescent probe for real-time imaging of redox status changes in vivo. *Chemical Science* **4**, 1079-1086 (2013).
315. Kosower, E.M., Pazhenchevsky, B., Dodiuk, H., Kanety, H. & Faust, D. Bimanes. 6. Reactive halogen derivatives of syn- and anti-1,5-diazabicyclo[3.3.0]octadienediones (9,10-dioxabimanes). *The Journal of Organic Chemistry* **46**, 1666-1673 (1981).
316. Niu, L.-Y., *et al.* BODIPY-Based Ratiometric Fluorescent Sensor for Highly Selective Detection of Glutathione over Cysteine and Homocysteine. *Journal of the American Chemical Society* **134**, 18928-18931 (2012).
317. Shao, N., *et al.* Design of Bis-spiropyran Ligands as Dipolar Molecule Receptors and Application to in Vivo Glutathione Fluorescent Probes. *Journal of the American Chemical Society* **132**, 725-736 (2010).
318. Lee, M.H., *et al.* Toward a Chemical Marker for Inflammatory Disease: A Fluorescent Probe for Membrane-Localized Thioredoxin. *J. Am. Chem. Soc.* **136**, 8430-8437 (2014).
319. Lee, M.H., *et al.* Mitochondrial Thioredoxin-Responding Off-On Fluorescent Probe. *J. Am. Chem. Soc.* **134**, 17314-17319 (2012).